

MATURITY MODELLING AND SOURCE ROCK EVALUATION OF UPPER OLIGOCENE SOURCE ROCKS (WITHIN AGBADA FORMATION), GREATER UGHELLI DEPOBELT, NIGER DELTA BASIN

Oladotun A. Oluwajana

Department of Earth Sciences, Adekunle Ajasin University, Akungba-Akoko, Nigeria

Received September 23, 2017; Accepted January 8, 2018

Abstract

Greater Ughelli depobelt of Niger Delta basin is an important petroleum province in Nigeria. Data/information on hydrocarbon generation potentials of Oligocene source rocks in the depobelt is limited. This present study utilized results of Rock-Eval pyrolysis and 1-D basin modelling of two wells to infer the timing of hydrocarbon generation and evaluate the deeply buried upper Oligocene source rocks within Agbada Formation. Total Organic Carbon contents of the shale samples within the studied wells range between 1.7 to 31.8 wt. % and suggest that the upper Oligocene source rocks could be considered as potential source rocks for hydrocarbon generation. The vitrinite kerogen composition of the upper Oligocene source rocks is the main organic matter with fewer component of exinite/vitrinite kerogen. The shale samples have poor to excellent source generative potential. Maturity models assumed that the deeply buried upper Oligocene source interval began hydrocarbon generation during Miocene and continue till date. The modelled present-day transformation ratios for upper Oligocene source rocks are low for enough hydrocarbons to be significantly expelled from the upper Oligocene source rocks. The results of this study provide basic information that improves understanding of the viability of the Oligocene-sourced play in the Greater Ughelli depobelt.

Keywords: Niger Delta Basin; generation; Oligocene; hydrocarbon; basin modelling.

1. Introduction

The study field lies in the Greater Ughelli depobelt (Figure 1) and one of the productive fields in the Niger Delta Basin. Greater Ughelli depobelt of the Niger Delta Basin has significant hydrocarbon potentials with oil and gas discoveries [1]. Quite a few studies had been undertaken on the source rocks of the Niger Delta basin [1-10].

Nwachukwu *et al.* [4] and Ekweozor *et al.* [6] have shown that the Agbada shale units have intervals that contain organic carbon contents sufficient to be considered good source rocks. However, published works particularly related to source rock characteristics, maturity histories and the timing of hydrocarbon generation of upper Oligocene source rocks within the Agbada Formation are limited. Oligocene source rocks have contributed to petroleum systems of some oil and gas fields in other parts of the world, as noted in offshore Sarawak Basin in Malaysia [11] and Yayu Basin, southwestern Ethiopia [12]. Source rocks of upper Oligocene age within the Agbada formation have not been considered to have contributed to oil and gas fields in the Greater Ughelli Depobelt.

This study presents the results of Rock-Eval pyrolysis and 1-D basin modelling study of *Giri* field in the Greater Ughelli depobelt using vitrinite reflectance data, rock-eval data and stratigraphic well data to evaluate the source rock characteristics of upper Oligocene source rocks and infer the maturity histories and time of hydrocarbon generation of the deeply buried upper Oligocene shale intervals. The evaluation of sedimentary rocks as effective source rocks of petroleum requires the determination of the amount and type of organic matter and the degree of conversion of the organic matter to petroleum hydrocarbons [13]. The outcome of this study provides information on the quantity, quality of the organic matter and hydrocarbon

generation potentials of upper Oligocene shale intervals in the Greater Ughelli depobelt of Niger Delta Basin.

2. Geological settings

The Niger Delta continental margin (Figure 1) is one of the largest deltaic systems in the world [9]. The sub-aerial part of the delta covers about 75,000 km² and extends more than 300 kilometers from apex to mouth [14]. The total sedimentary sequence was deposited in a series of mega-sedimentary belts (depobelts or mega-structures) in a succession temporally and spatially with southward progradation of the Delta [9]. The sedimentary fill is usually divided into three diachronous formations (Eocene-Recent); namely the undercompacted, overpressured marine Akata Formation, paralic Agbada Formation and continental fluviatile Benin Formation. The Akata Formation is typically overpressured and made up of prodelta shales with occasional turbidite sands. The Akata Formation represents muddy continental slope and rise environments and is the core unit in which shale diapirs form offshore [14].

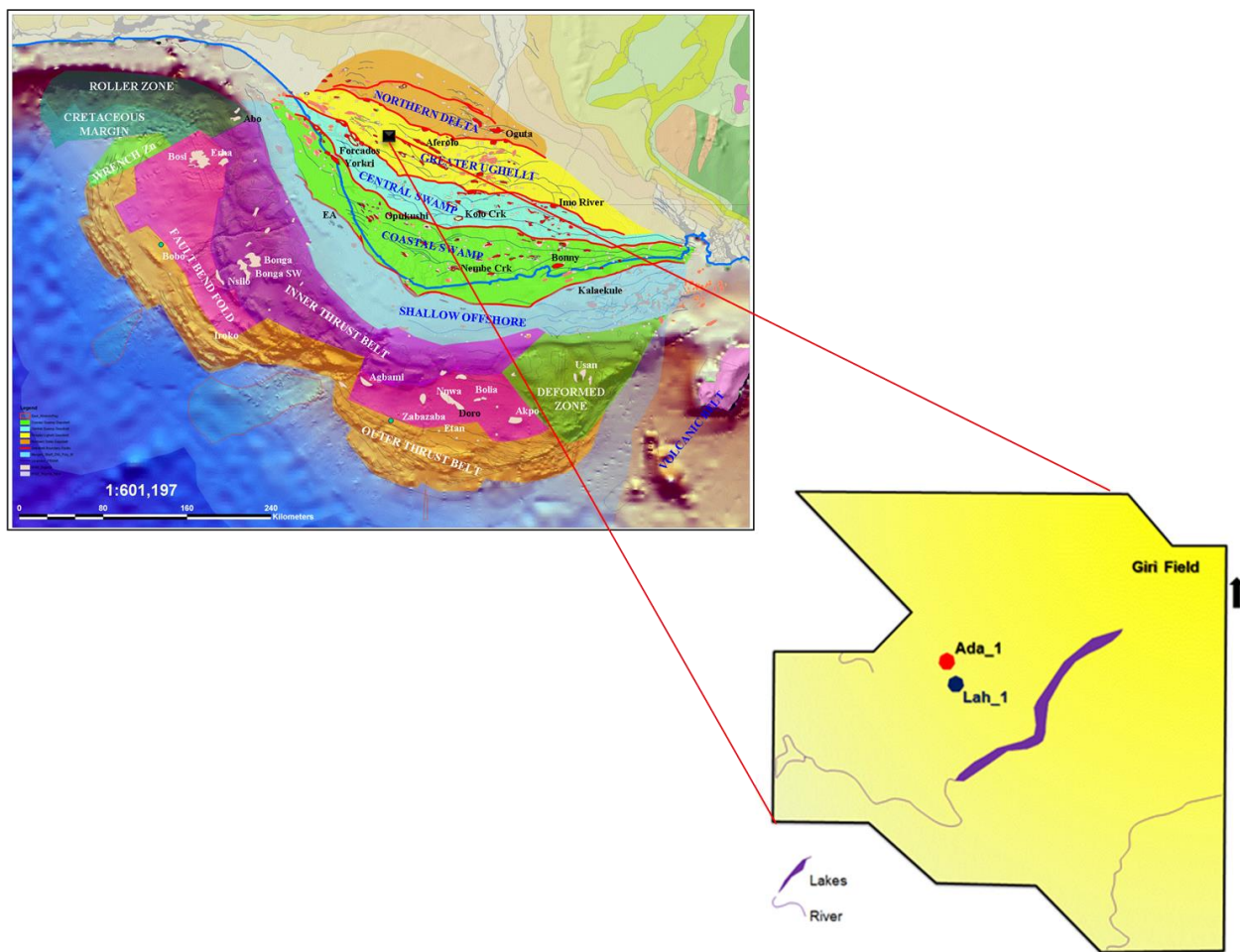


Figure 1. Location map of depobelts in the Niger Delta; showing the field where subsurface data were collected (Ada_1 and Lah_1 wells) (map modified from [15])

The Agbada Formation consists of paralic, mainly shelf deposits of alternating sands, shales and mudstone. The Benin Formation is predominantly non-marine upper delta plain sandstone (Figure 2). The Benin Formation is up to 2,000 m thick in the central onshore part of the delta and thins toward the delta margins [8]. The undercompacted, overpressured marine Akata Formation and paralic Agbada Formation are thought to have charged to varying degrees oil

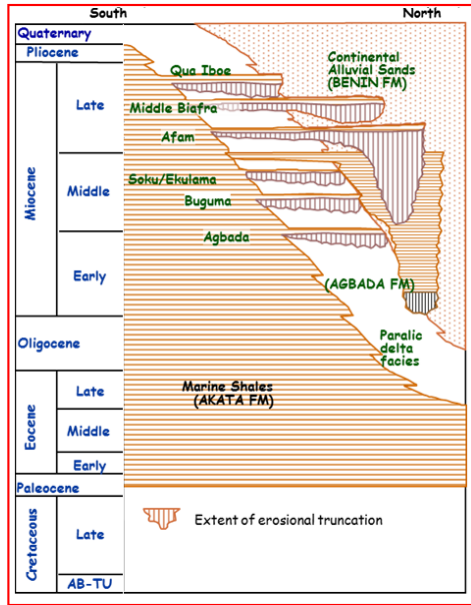


Figure 2. Regional stratigraphy of the Niger Delta showing different formations (modified from [19])

and gas in the Niger Delta [2]. Short *et al.* [16] defined the contact between the Agbada and Benin Formations as the highest shale bearing marine fauna in the Agbada Formation. However, the contact is more practically defined at the base of the massive sandstones typical of the Benin Formation and generally corresponds to the base of freshwater-bearing strata [8].

The progradation of the delta has been accompanied by formation of growth faults, associated rollover anticlines and mud diapirism [8]. Most hydrocarbon-bearing structures are along proximal margins of sub-basins where growth strata accumulated on blocks down-dropped across major syn-depositional faults and onlap adjacent anticlinal (rollover) closures [9]. Major growth faults exhibit throws of several hundred meters are arcuate in plain view, concave basinward and are generally several tens of kilometers in length [17]. All major oil and gas discoveries in the Niger Delta occur in Eocene to Pliocene sandstones of the Agbada Formation [8].

3. Materials and methods

Forty (40) ditch-cutting and sidewall samples from two wells in Greater Ughelli depobelt were analyzed by Shell Petroleum Development Company of Nigeria (SPDC). The two wells for proprietary reason were named as Ada_1 and Lah_1 wells. This study utilized Rock-Eval pyrolysis results and stratigraphic well data of the upper Oligocene source rocks within Agbada Formation. The results of the Total Organic Carbon (TOC) and Rock-Eval pyrolysis were presented in Table 1 and 2.

The sedimentation history of the basin is subdivided into a series of events of specified age and duration [18]. 1-D basin modelling was carried out using Schlumberger Petromod 2011 to basically infer the maturation and timing of hydrocarbon generation of the deeply buried upper Oligocene source rocks. The input data for the stratigraphic modelling included age, and thicknesses, lithology of different sedimentary layers, duration of deposition. Thickness and depth values of different sedimentary units are based on proprietary stratigraphic (well) penetration data from Shell Petroleum Development Company of Nigeria.

Paleobathymetry data are used in the reconstruction of the total subsidence that occurred within the basin [18]. Paleobathymetric values for the Niger Delta Basin used in this study were obtained from the proprietary Shell Petroleum Development Company chart and published reports [20-21]. Heat flow is considered to be an input parameter but it is challenging to define the heat flow values for the past. Therefore, the reconstruction of thermal histories of sedimentary basins is always simplified and calibrated against maturity profiles such as vitrinite reflectance [22]. The heat flow values were determined based on the tectonic history of the basins and were defined by streaming modelled and measured vitrinite reflectance data. Modelled vitrinite reflectance (calculated after Easy%R_o Sweeney and Burnham, 1990) has been related to measured data (Table 3) in order to calibrate the hydrocarbon generation levels. The hydrocarbon generation stages were calculated using reaction kinetics data based on [23].

The source rock parameters i.e. Total Organic Carbon content (TOC) and Hydrogen Index (HI) used in the construction of 1-D models were obtained from available well reports. Present-day TOC of 5.59 wt. % TOC and Hydrogen Index (HI) of 146mgHC/gTOC were applied during the modelling of Ada_1 well. TOC content of 3.66 wt. % TOC and Hydrogen Index (HI) of 128 mgHC/gTOC were applied during the development of Lah_1 well models.

Basin modelling, numerical simulation and calibration stages were the stages involved in the 1-D basin modeling. The basin modelling simulations were performed by applying forward modelling method. After calibration stage was achieved, the 1-D models of the two wells were simulated. Modelling results were presented visually.

4. Results and discussion

4.1. Organic matter richness

The Rock-eval pyrolysis results (Table 1 and 2) indicate that the Total Organic Carbon (TOC) contents of upper Oligocene shale samples in Ada_1 and Lah_1 wells range from 1.7 to 31.8 wt. % (average value of 5.59 wt. %) and 2.0 wt. % to 12.9 wt. % (an average value of 3.66 wt. %) respectively indicating good to very good source rocks (Figure 3).

Table 1. Geochemical results of Rock-Eval/TOC analysis of upper Oligocene shale samples in Ada_1 well

Well	Depth (m)	TOC (wt. %)	Rock-Eval pyrolysis						
			S ₁ (mg HC/g Rock)	S ₂ (mg HC/g rock)	S ₁ +S ₂ (mg HC/g Rock)	T _{max}	OI (mg HC/g Rock)	HI (mg HC/g rock)	PI (mg HC/g rock)
Ada_1	3093	13.9	1.22	26.35	27.57	412	45	190	0.04
Ada_1	3120	14.3	0.81	35.21	36.02	423	49	246	0.02
Ada_1	3235	31.8	2.46	69.9	72.36	414	35	220	0.03
Ada_1	3253	11.4	0.73	18.58	19.31	421	41	163	0.04
Ada_1	3267	15.8	0.8	29.96	30.76	422	42	190	0.03
Ada_1	3276	5	0.3	6.69	6.99	412	42	134	0.04
Ada_1	3285	2.5	0.28	3.37	3.65	418	52	135	0.07
Ada_1	3294	2.9	0.22	3.7	3.92	420	51	128	0.06
Ada_1	3331	8.1	0.58	12.73	13.31	415	42	157	0.04
Ada_1	3345	3.8	1.34	4.45	5.79	415	51	117	0.23
Ada_1	3358	19.7	2.52	66.69	69.21	415	38	338	0.04
Ada_1	3372	4.8	0.27	6.45	6.72	415	38	134	0.04
Ada_1	3450	3.4	7.08	12.25	19.33	415	65	360	0.37
Ada_1	3454	2.8	0.32	2.74	3.06	423	60	98	0.1
Ada_1	3596	2.2	0.1	1.3	1.4	422	66	59	0.07
Ada_1	3633	1.7	0.16	1.46	1.62	427	71	96	0.1
Ada_1	3637	1.7	0.32	2.04	2.36	425	82	120	0.14
Ada_1	3665	2.4	0	0	0	428	18	0	0
Ada_1	3683	2.4	0.2	1.36	1.56	424	35	57	0.13
Ada_1	3683	2.1	0.27	1.71	1.98	430	50	81	0.14
Ada_1	3701	2.6	0.38	2.07	2.45	421	49	83	0.16
Ada_1	3719	2.2	1.34	2.62	3.96	423	77	119	0.34
Ada_1	3747	2	1.15	2.212	3.36	426	95	106	0.36
Ada_1	3761	2.7	0.93	0.63	1.56	428	69	134	0.2
Ada_1	3779	2.3	1	3.72	4.72	428	82	162	0.21
Ada_1	3784	2	0.97	3.42	4.39	429	89	171	0.22
Ada_1	3793	2.1	0.83	4.34	5.17	428	70	207	0.18
Ada_1	3806	2.2	0.7	1.84	2.54	424	80	84	0.28
Ada_1	3851	2.1	1.42	3.37	4.79	427	105	160	0.3
Ada_1	3869	1.9	1.01	2.65	3.66	429	100	139	0.28
Ada_1	3870	2	1.21	2.61	3.82	427	87	131	0.32
Ada_1	3912	2.2	1.32	3.01	4.33	429	90	137	0.3

All the shale samples have TOC values exceeding 0.5 wt. % minimum thresholds required for potential source rock [24]. Organic matter richness of Agbada Shale as reported by [4] and [6] ranges from 0.2 to 6.5 wt. % and 0.4 to 4.4 wt. % respectively. Bustin [8] regarded upper Eocene to Oligocene as the richest source rock strata with the Agbada Formation.

The hydrogen index (HI) values of Ada_1 well and Lah_1 well ranged from 0 to 360 mg HC/g TOC and 41 to 255 mg HC/g TOC (Table 1 and 2), and are comparable to HI values of Agbada Shales obtained by [4] and [25].

Table 2. Geochemical results of Rock-Eval/TOC analysis of upper Oligocene shale samples in Lah_1 well

Well	Depth (m)	TOC (wt. %)	Rock-Eval pyrolysis						
			S ₁ (mg HC/g Rock)	S ₂ (mg HC/g Rock)	S ₁ +S ₂ (mg HC/g Rock)	T _{max}	OI (mg HC/g rock)	HI (mg HC/g rock)	PI (mg HC/g rock)
Lah_1	2872	2.3	0.35	1.46	1.81	427	26	63	0.19
Lah_1	2989	1.7	0.45	2.23	2.68	427	34	131	0.17
Lah_1	3068	12.9	1.64	34.2	35.84	426	10	255	0.05
Lah_1	3132	3	0.64	3.2	3.84	424	11	107	0.17
Lah_1	3195	2	0.28	1.29	1.57	430	29	65	0.18
Lah_1	3304	2	2.27	3.19	5.46	429	38	160	0.42
Lah_1	3393	2.8	0.64	5.55	6.19	431	28	198	0.1
Lah_1	3397	2.6	0.31	1.07	1.38	425	14	41	0.22

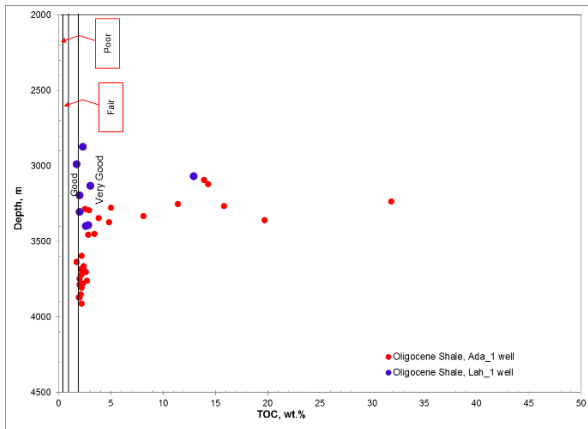


Figure 3. Organic richness of upper Oligocene source rocks in Ada_1 and Lah_1 wells

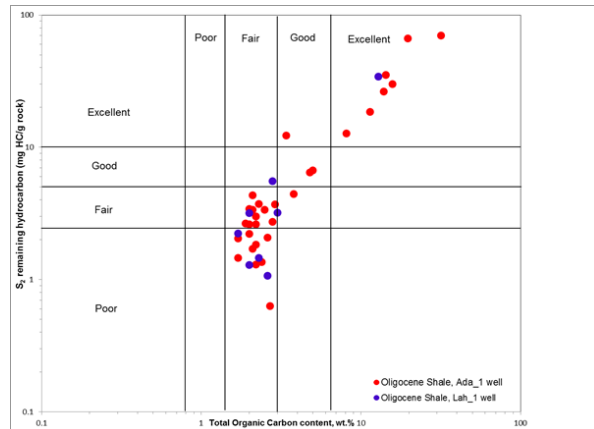


Figure 4. Crossplot of Total Organic Carbon (TOC) against Rock-Eval S₂ (generative hydrocarbons of the sample) values for the potential source rocks in the Agbada Formation

The plot of TOC content and S₂-generative hydrocarbons of the sample [28] showed that the upper Oligocene samples meet the accepted standards of a source with poor to excellent generative potential as classified by [26] (Figure 4).

4.2. Generating potentialities

The sum of the values S₁ (free hydrocarbons present in the sample) + S₂ (generative hydrocarbons of the sample) is regarded as generative potential. The generative potential of upper Oligocene shale samples in Ada_1 well ranges from 0 to 72.36 mg HC/g rock with average of 11.61 mg HC/g rock while (S₁+ S₂) values for Lah_1 well range from 1.38 to 35.84 mg HC/g rock (an average of 7.35 mg HC/g rock). The relationship between (S₁+ S₂) and TOC [27] suggests that the upper Oligocene shale samples in the two wells are considered as fair to excellent source potential (Figure 5). All Niger Delta source rocks have, or had, little or no oil-generating potential [8].

4.3. Type of organic matter

Petroleum is a generative product of organic matter disseminated in sediments; therefore the quality of hydrocarbon is directly related to the type of organic matter contained in any potential source rock [24]. The initial genetic type of organic matter of a particular source rock is essential for the prediction of oil and gas potential [28]. The kerogen type of the upper Oligocene shale samples in Ada_1 well and Lah_1 well were determined by using Rock-eval pyrolysis kerogen classification diagram constructed using crossplot of Hydrogen Index (HI) against T_{max} values [29]. The type of organic matter identified from the plot of Hydrogen Index (HI) against T_{max} ($^{\circ}\text{C}$) indicate the presence of mainly vitrinite kerogen composition of gas-prone Type III in shale samples recovered from Ada_1 well and Lah_1 well whereas few samples in the two wells are within the kerogen type II/III capable of generating mixed gas and oil but mainly gas (Figure 6). Van Krevelen-type diagram of the three pyrolyzed Agbada shales as reported by [4], indicates that they contain essentially Type III organic matter. The abundance of terrestrial organic matter in deltaic sediments has been documented [30].

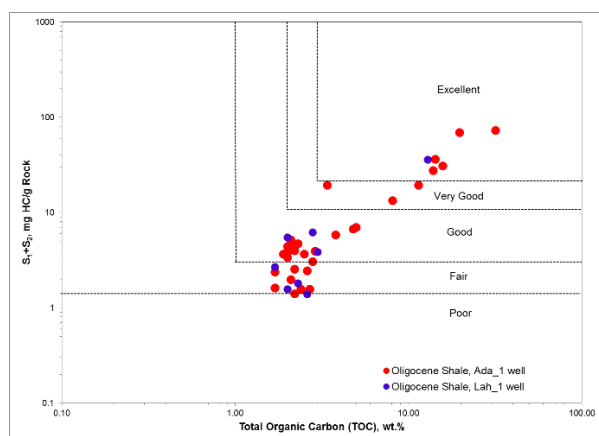


Figure 5. Plot of TOC against Rock-Eval S_1 (free hydrocarbons present in the sample) + S_2 (generative hydrocarbons of the sample) values for the potential source rocks in the two studied wells

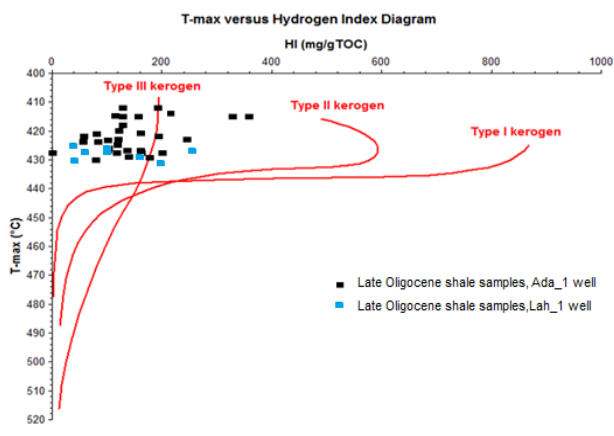


Figure 6. Diagram showing plot of Hydrogen Index (HI) against T_{max} ($^{\circ}\text{C}$) for selected upper Oligocene shale samples in Ada_1 well and Lah_1 well

4.4. Thermal maturity

T_{max} variation is a function of its thermal evolution [31]. The maturity windows represent an approximate range [36] as shown in figure 7. The thermal maturity of the upper Oligocene source rocks has been assessed by the plot of T_{max} against depth [31] (Figure 7) indicates that the upper Oligocene source samples are immature to marginally mature source rocks. This result is consistent with the work of [4].

Thermogenic oil is thought to be generated from marine and lacustrine source rocks at vitrinite reflectance values between 0.5 % R_o and 1.3% R_o , suggest oil generation window, while samples with values less than 0.5 % R_o are considered thermally immature [31-32]. Vitrinite reflectance greater than 1.3 % R_o indicates gas window maturity [32]. Vitrinite reflectance values of Ada_1 well range from 0.5 % R_o to 0.70 % R_o while vitrinite reflectance values of Lah_1 well range from 0.53 % R_o to 0.60 % R_o . The plot of vitrinite reflectance data (% R_o) versus depths [31] indicates that the vitrinite reflectance values of the two wells correspond to earliest part of the mature window (Figure 8). Nwachukwu *et al.* [4] identified mature Agbada shales in some wells in the western part of the Niger Delta basin.

Table 3. Vitrinite reflectance measurements of Eocene stratigraphic levels in the Ada_1 well and Lah_1 well

Well(s)	Depth (m)	Measured vitrinite reflectance values	Well(s)	Depth (m)	Measured vitrinite reflectance values
Ada_1	3253	0.5	Lah_1	2872	0.46
	3597	0.52		3068	0.5
	3858	0.7		3393	0.6

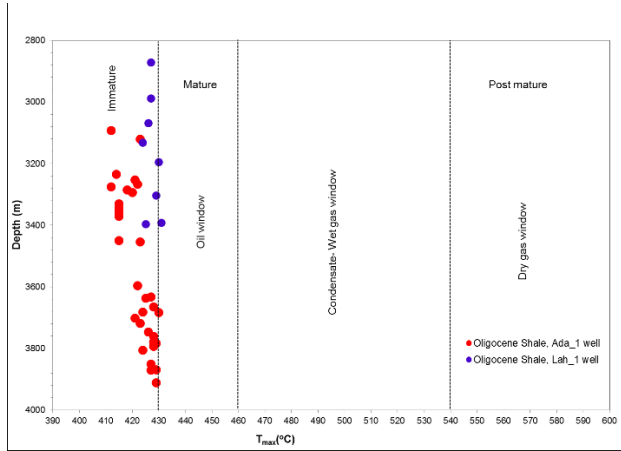


Figure 7. Plot of Depth versus pyrolysis T_{max} showing thermal maturity windows

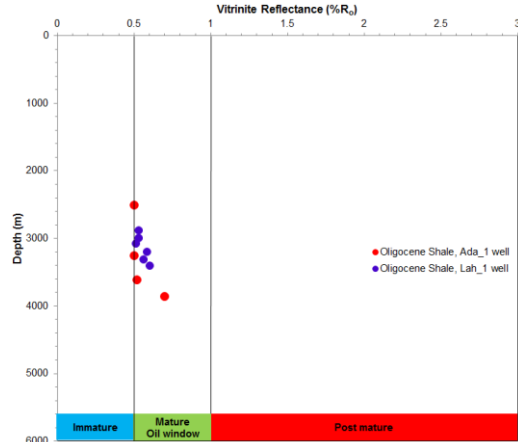


Figure 8. Plot of vitrinite reflectance data ($\%R_o$) versus depth showing thermal maturity stages of the upper Oligocene source rocks in the Ada_1 and Lah_1 wells

4.5. 1-D reconstructions using Schlumberger Petromod 2011

4.5.1. Heat flow history

Heat flow value ranging from 66 mWm^{-2} in the Aptian-Albian times to 88 mWm^{-2} during the Coniacian to early Santonian was calibrated for the 1-D models (Figure 9).

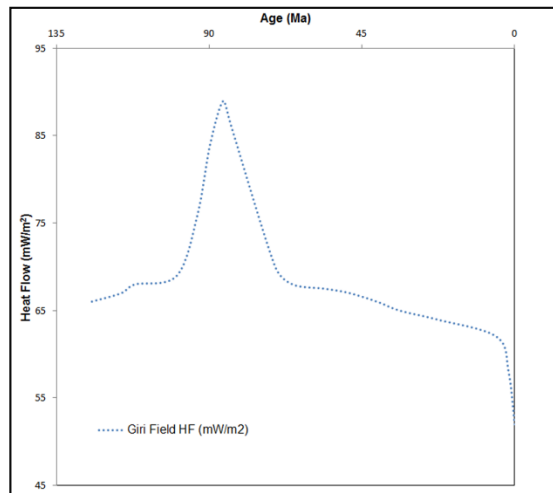


Figure 9. Heat-flow history used to model the most probable scenario for hydrocarbon generation in the Greater Ughelli (Niger Delta Basin)

Elevated heat flow value of 90 mWm^{-2} was assigned to the early Santonian phase of intense volcanic activity [10]. Late Turonian to Santonian times were marked by indication of active tectonic phase of folding, faulting, and uplifting [33]. This event was followed by gradual loss of thermal momentum associated with final cessation of mantle upwelling. Heat flow value of 45 mWm^{-2} was modelled as the present day values for the two wells. Heat flow values less than 80 mWm^{-2} observed during the Cenozoic, thus, suggest that the field located in Greater Ughelli depobelt is not geothermally active area. Rapid sedimentation may cause reduction in heat flow and thermal maturity [34]. Reduction in the values of heat flow during Cenozoic may be associated with rapid sedimentation in the Greater Ughelli depobelt.

4.5.2. Hydrocarbon generation phases

Kinetic models of [23] and [35] were used to establish the burial history and hydrocarbon generation potential of upper Oligocene Shale samples through 1-D charge modelling of Ada_1 and Lah_2 wells. Figure 10 shows a good and reasonable correlation between measured and calculated vitrinite reflectance values for the two wells. Maturity (vitrinite reflectance) values of the upper Oligocene source rock are low. The burial models showed that sedimentation rates were rapid in the two wells (Figure 11 and Figure 12).

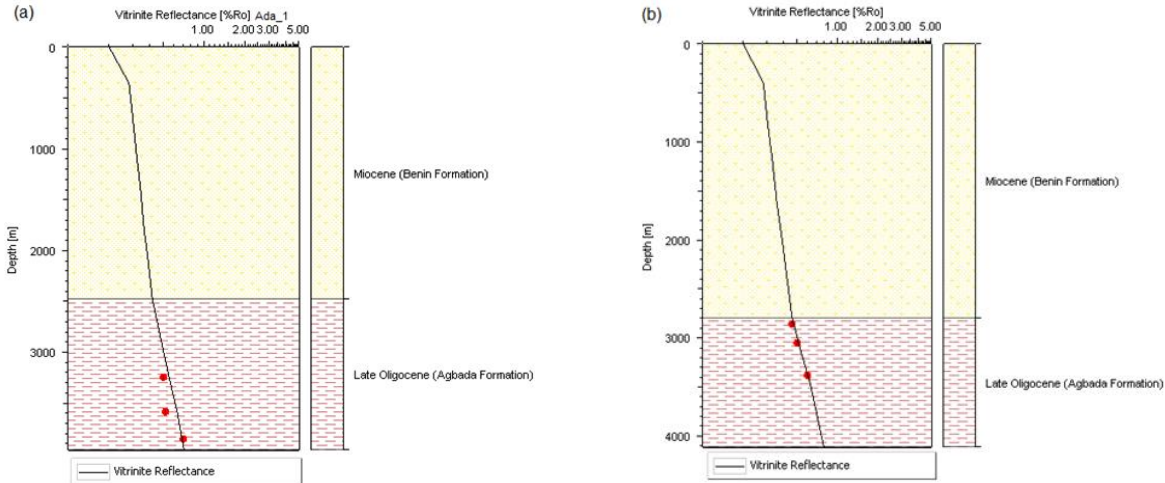


Figure 10. Correlation of measured and modeled vitrinite reflectance data for (a) Ada_1 well and (b) Lah_1 well

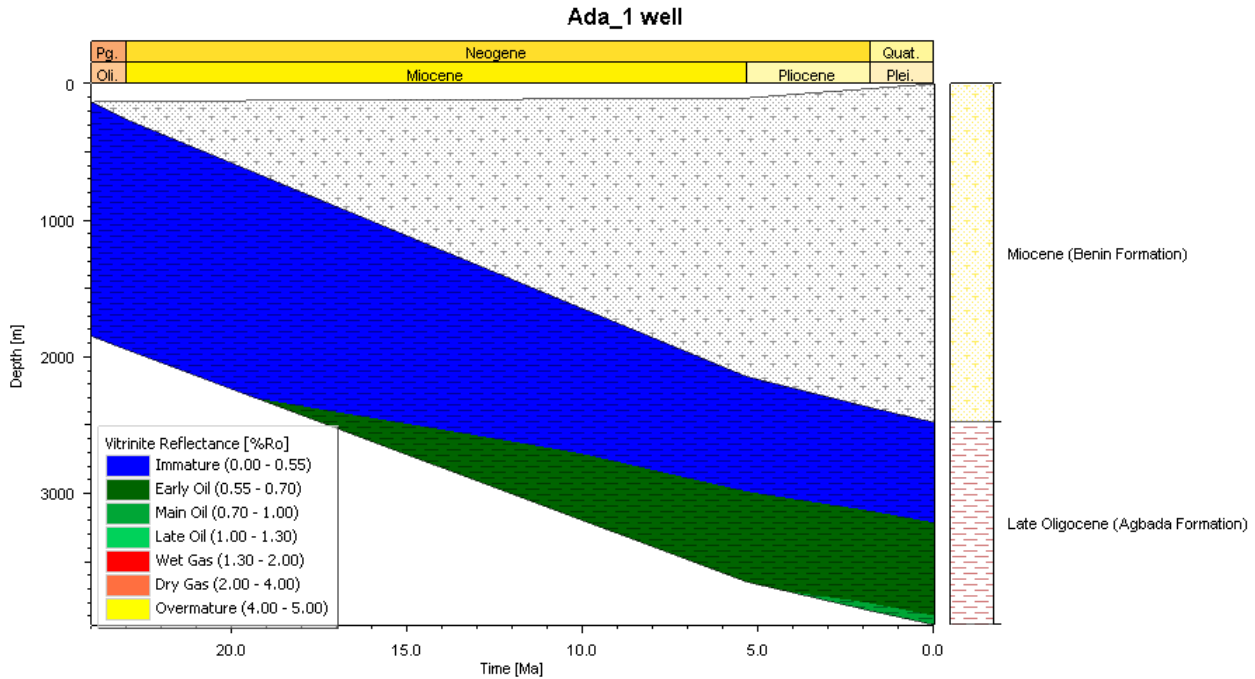


Figure 11. Burial history of the well Ada_1 showing the maturity overlay

Hydrocarbon generation from the upper Oligocene source rocks started during the Miocene (about 19.26 Ma). The top of the liquid hydrocarbon window in Ada_1 well was identified at 2,307 m and suggest that the upper Oligocene shale intervals in Ada_1 well are presently within immature to main oil window (Figure 11). The maturity model of Lah_1 well predicts that the hydrocarbon generation from the upper Oligocene source rocks occurred during the

Miocene (about 21.46 Ma) at present depth of 1,962 m. Upper Oligocene source rocks in Lah_1 well are currently within immature to main oil window (Figure 12).

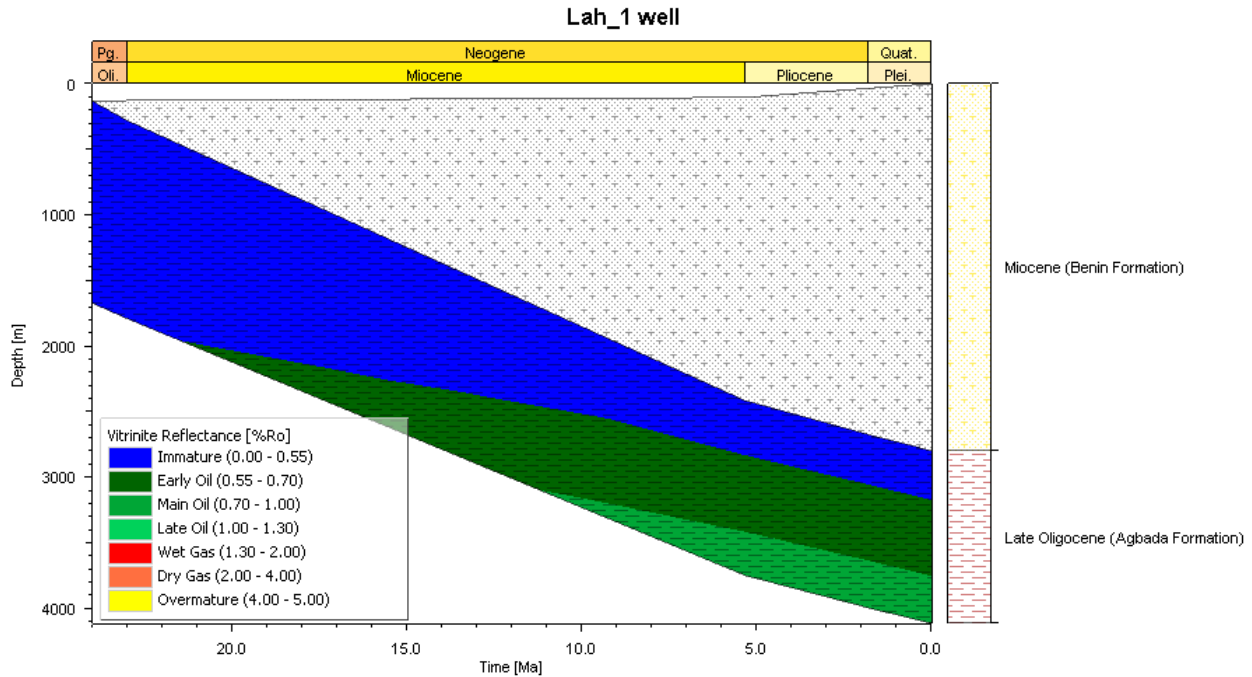


Figure 12. Burial history of the well Lah_1 showing the maturity overlay

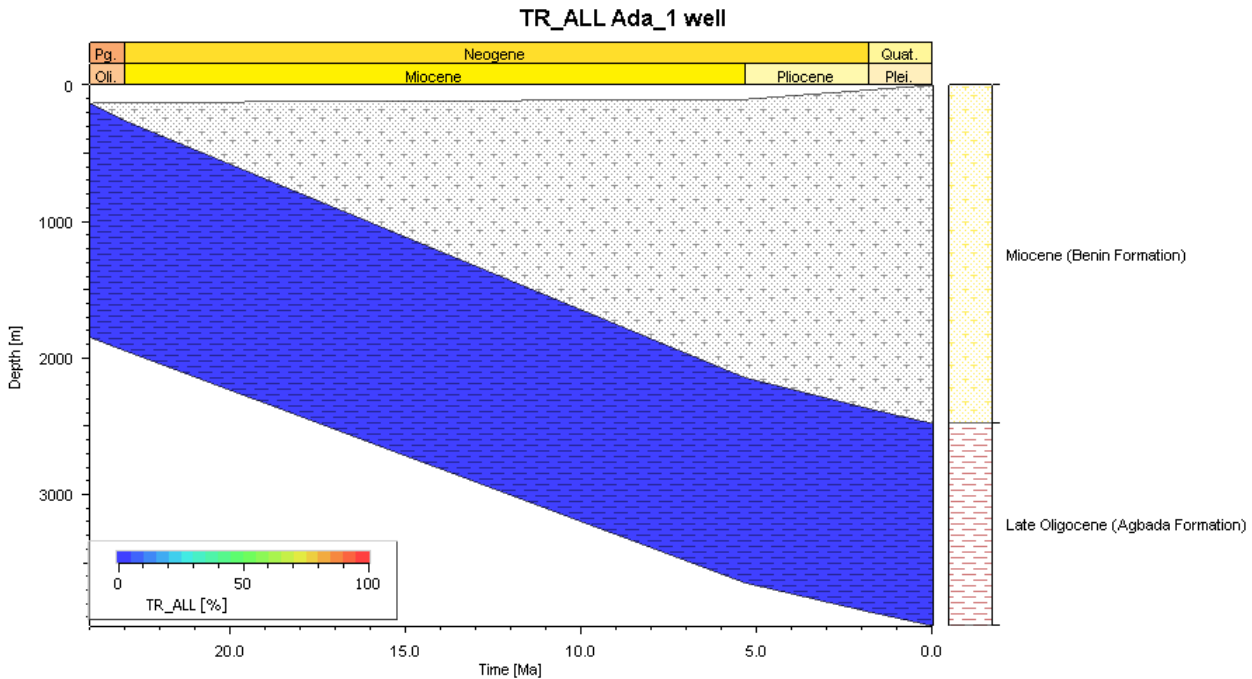


Figure 13. Transformation ratio (TR) distribution using burial history model of Ada_1 well

Oligocene source rock interval in Ada_1 well and Lah_1 well currently has transformation ratio of 0.12 % and 0.93 % respectively (Figure 13 and 14). The values of modelled present-day transformation ratio of deeply buried upper Oligocene source rocks in the two wells are less than 1%. Only small percent (<1%) of the organic material within upper Oligocene source rocks has been transformed. This transformation ratio is low for enough hydrocarbons to be

significantly expelled. The source rock intervals may have contributed to the charging of Miocene sandstone and unconsolidated sands of the Agbada Formation. Nwachukwu *et al.* [4] and Doust *et al.* [4] attributed the distribution of the top of the oil window to the thickness and sand/shale ratios of the overburden rock (Benin Formation and variable proportions of the Agbada Formation).

5. Hydrocarbon prospectivity

Thermal maturity of the deeply buried upper Oligocene source rocks in *Giri* Field is low ranging from immature to early mature. The studied Oligocene source rocks may have contributed to the hydrocarbon base of the Greater Ughelli depobelt of the Niger Delta. Hydrocarbon charge from Eocene source rocks, marine shales of the Akata Formation and underlying Cretaceous shales are also expected. Lambert-Aikhionbare *et al.* [7] derived a thermal maturity profile, showing that the shale within the Agbada Formation is mature enough to generate hydrocarbons. Petroleum in the Niger Delta is produced from sandstone and unconsolidated sands predominantly in the Agbada Formation. Interbedded shale within the Agbada Formation is expected to serve as the seal rock in the Niger Delta.

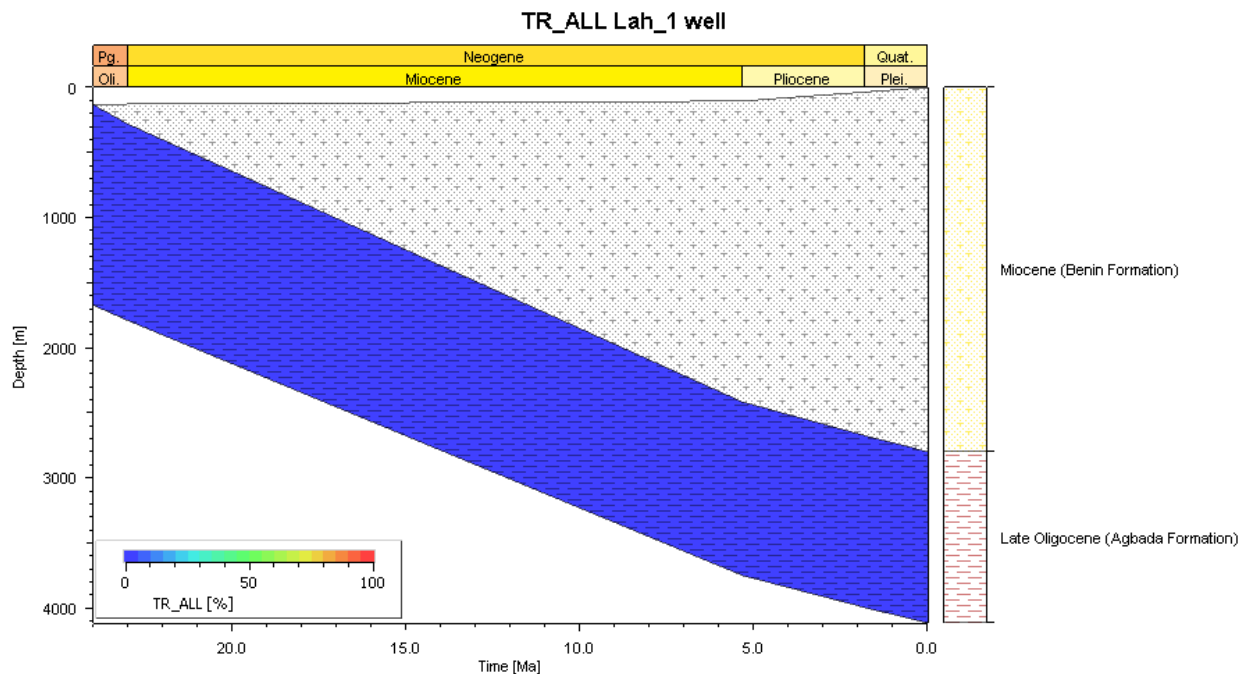


Figure 14. Transformation ratio (TR) distribution using burial history model of Lah_1 well

6. Conclusion

This study has established the importance of source rock evaluation and basin modeling in petroleum generation potential of a field within Greater Ughelli depobelt of Niger Delta Basin. The Total Organic Carbon (TOC) contents of upper Oligocene shale samples in the studied wells range from 1.7 to 31.8 wt.% indicating good to very good source rocks and could be considered as potential source rocks. The relationship between ($S_1 + S_2$) and TOC suggest that the upper Oligocene source rocks in the two wells can be regarded as poor to excellent source potential. The plot of Hydrogen Index (HI) against T_{max} (°C) showed that the upper Oligocene source rocks are capable of generating mainly gas and mixed hydrocarbon. Thermal maturity (vitrinite reflectance, % R_o) data indicates that the deeply buried upper Oligocene source rocks in the two wells are within immature to earliest part of the mature window.

1-D modelling of two wells in the Greater Ughelli depobelt assumed that the deeply buried upper Oligocene source rocks entered main oil (mature stage) window of hydrocarbon generation during Neogene. The transformation ratios of the deeply buried upper Oligocene

source rocks are low (<1%), thus, suggest that small amount of the organic material within upper Oligocene source rocks has been transformed. Upper Oligocene source rocks within the Greater Ughelli have not generated enough hydrocarbons for significant expulsion to occur.

The results of this study have shown that upper Oligocene source rocks are potential source rocks in the Greater Ughelli depobelt and may have contributed some hydrocarbon to the interbedded Agbada sandstones of Greater Ughelli Depobelt.

7. Acknowledgement

Geochemical data (TOC and Rock-Eval) on the two wells were obtained during the author's PhD research attachment with Onshore and Coastal Swamp Exploration Department of Shell Petroleum and Development Company of Nigeria (SPDC). I am grateful to Professor O. A. Ehinola for his contributions to my training as a petroleum geologist.

References

- [1] Ojo OJ, Akpabio I and Frielingdorf J. Burial and Thermal History Modeling and Petroleum System Analysis of the Northwest Niger Delta. *Comunicações Geológicas* 2012; 99:53-59.
- [2] Evamy BD. Haremboure J. Kamerling P. Knaap WA. Molloy FA. Rowlands PH. Hydrocarbon habitat of Tertiary Niger Delta. *American Association of Petroleum Geologists Bulletin* 1978; 62(1):1-39.
- [3] Weber KJ and Daukoru EM. Petroleum geology of the Niger Delta: Proceedings of the 9th World Petroleum Congress, Tokyo 1975; 2:202-221.
- [4] Nwachukwu JI and Chukwura PI. Organic matter of Agbada Formation, Niger Delta, Nigeria. *American Association of Petroleum Geologists Bulletin* 1986; 70:48-55.
- [5] Ekweozor CM. Okogun JI. Ekong DEU. Maxwell JR. Preliminary organic geochemical studies of samples from the Niger Delta, Nigeria: *Chemical Geology* 1979; 27:11-28.
- [6] Ekweozor CM. and Okoye NV. Petroleum source-bed evaluation of Tertiary Niger Delta. *American Association of Petroleum Geologists Bulletin* 1980; 64:1251-1259.
- [7] Lambert-Aikhionbare DO. and Ibe AC. Petroleum source-bed evaluation of the Tertiary Niger Delta: discussion: *American Association of Petroleum Geologists Bulletin* 1984; 68:387-394.
- [8] Bustin RM. Sedimentology and characteristics of dispersed organic matter in Tertiary Niger Delta: Origin of source rocks in a deltaic environment: *American Association of Petroleum Geologists Bulletin* 1988; 72:277-298.
- [9] Doust H. and Omatsola E. Niger Delta, in, Edwards JD., and Santogrossi PA., eds., *Divergent/passive Margin Basins*, American Association of Petroleum Geologists Bulletin, Memoir 48: Tulsa 1990; 239-248.
- [10] Odumodu CFR and Mode AW. Hydrocarbon maturation modeling of Paleocene to Lower Miocene source rocks in the Niger Delta Basin: implications for hydrocarbon generation. *Arabian Journal of Geosciences* 2016; 9:411. doi:10.1007/s12517-016-2427-5.
- [11] Gebregergis TM. and Yukoff IW. Burial and Thermal History model to evaluate source rock in Tatau province, offshore Sarawak Basin, Malaysia *American Association of Petroleum Geologists search and Discovery Article* 2011 #40706.
- [12] Wolela A. Sedimentation, organic maturity, and petroleum potential of the Oligocene–Miocene oil shale deposits, Yayu Basin, southwestern Ethiopia. *The American Association of Petroleum Geologists*, 2010; 94(5):643–663.
- [13] Shalaby MR. Abdullah WH. and Abu Shady AN. Burial History, basin modeling and organic geochemistry in the Western Desert, Egypt. *Geological Society of Malaysia Bulletin* 2008; (54):103-113.
- [14] Adeogba AA. McHargue TR. and Graham SA. Transient fan architecture and depositional controls from near-surface 3-D seismic data, Niger Delta continental slope. *American Association of Petroleum Geologists Bulletin* 2005; 89(5):627–643.
- [15] Ozumba B. Geology of the Niger Delta: An Overview for Geophysics Processors. Unpublished Shell Petroleum Development Company of Nigeria (SPDC) presentation for geologists in Nigeria 2003; 1-25.
- [16] Short KC. and Stauble AJ. Outline of Geology of Niger Delta. *American Association of Petroleum Geologists Bulletin* 196751:761-779.
- [17] Magbagbeola OA. and Willis BJ. Sequence stratigraphy and syndepositional deformation of the Agbada Formation, Robertkiri field, Niger Delta, Nigeria, *American Association of Petroleum Geologists Bulletin* 2007; 91(7):945-958.

- [18] Underdown R. and Redfern J. Petroleum Generation and Migration in the Ghadames Basin, North Africa: A two-dimensional basin-modeling study. *The American Association of Petroleum Geologists Bulletin*. 2008; 92(1):53-76.
- [19] Ozumba B. Niger Delta Regional Stratigraphy and Pore Pressure Prediction. Shell Petroleum Development Company of Nigeria (SPDC) presentation for geologists in Nigeria 2011; 1-30.
- [20] Hardenbol J. Thierry J. Farley MB. Jacquin T. Graciansky PC. Vail P. Mesozoic and Cenozoic Sequence Chronostratigraphic Framework of European Basins. PC. Graciansky, J. Hardenbol, T. Jacquin and P. R. Vail. Eds. Mesozoic-Cenozoic Sequence Stratigraphy of European Basins. SEPM Special Publication, 1998; 60.
- [21] Gradstein F. Ogg J. Smith A. A Geologic Time Scale. Cambridge University Press 2004; 589.
- [22] Yahi N. Schaefer RG. Littke R. Petroleum generation and accumulation in the Berkine basin, eastern Algeria. *The American Association of Petroleum Geologists* 2001; 85(8):1439-1467.
- [23] Vandenbroucke M. Behar F. Rudkiewicz JL. Kinetic modelling of petroleum formation and cracking : implications from the high pressure/high temperature Elgin Field (UK, North Sea). *Org. Geochem.* 1999; 30:1105-1125.
- [24] Tissot BP. Welte DH. Petroleum Formation and Occurrence: A new Approach to Oil and Gas Exploration Springer-Verlag, Berlin 1978; 538.
- [25] Akinlua A. Torto N. Geochemical evaluation of Niger Delta sedimentary organic rocks: a new insight *International Journal of Earth Sciences* 2011; 100:1401-1411.
- [26] Peters KE. Cassa MR. Applied source rock geochemistry. in: L.B. Magoon, W.G. Dow, (Eds.), *The Petroleum System-From Source to Trap*, The American Association of Petroleum Geologists Memoir 1994; 60:93-120.
- [27] Waples DW. *Geochemistry in Petroleum Exploration*. Boston, inter. Human Resources and Development Company 1985; 232.
- [28] El Nady MM. Ramadan FS. Hammad MM. Lotfy NM. Evaluation of organic matters, hydrocarbon potential and thermal maturity of source rocks based on geochemical and statistical methods: Case study of source rocks in Ras Gharib oilfield, central Gulf of Suez, Egypt. *Egyptian Journal of Petroleum* 2015; 24:203-211.
- [29] Espitalie J. Deroo G. Marquis F. Rock-Eval pyrolysis and its application, *Inst. Fr. Petrol.* 1985; 72.
- [30] Nwachukwu J. and Barker C. Organic matter: size fraction relationships for recent sediments from the Orinoco delta, Venezuela: *Marine and Petroleum Geology*, 1985; 2:202-209.
- [31] Bordenave ML. *Applied Petroleum Geochemistry*. Editions Technip, Paris. 1993.
- [32] Hakimi MH. and Abdullah WH. Modelling petroleum generation of Late Cretaceous Dabut Formation in the Jiza-Qamar Basin, Eastern Yemen *Marine and Petroleum Geology* 2015; 61:1-13.
- [33] Kogbe CA. Paleogeographic History of Nigeria from Albian Times. *Geology of Nigeria*, Elizabethan Publ. Co. Lagos, 1989; 257-274.
- [34] Frielingsdorf J. Sk. Aminul Islam, Martin Block, Md. Mizanur Rahman, Md. Golam Rabbani. Tectonic subsidence modelling and Gondwana source rock hydrocarbon potential, Northwest Bangladesh Modelling of Kuchma, Singra Hazipur wells *Marine and Petroleum Geology* 2008; 25(6): 553-564.
- [35] Sweeney JJ. and Burnham AK. Evaluation of a simple model of vitrinite reflectance based on chemical kinetics. *American Association of Petroleum Geologists Bulletin* 1990; 74:1559 – 1570.
- [36] Shalaby MR. Hakimi MH. Abdullah WH. Modeling of gas generation from the Alam El-Bueib Formation in the Shoushan Basin, northern western Desert of Egypt. *Int. J. Earth Sci.* 2013; 102:319-332.

To whom correspondence should be addressed: Dr. Oladotun A. Oluwajana, Department of Earth Sciences, Adekunle Ajasin University, Akungba-Akoko, Nigeria, oladotun.oluwajana@aaua.edu.ng

DERIVED ROCK ATTRIBUTE ANALYSIS AND INVERSION OF LAMDA μ RHO FOR FLUID AND LITHOLOGY PREDICTION IN NEMBE FIELD ONSHORE NIGER DELTA, NIGERIA

E. U. Aniwetalu¹, E.K. Anakwuba¹, J. N. Ilechukwu¹ and B. O. Omang²

¹ *Department of Geological Sciences, Nnamdi Azikwe University Awka, Nigeria*

² *Department of Mineral and Petroleum Resource Engineering Technology Federal Polytechnic, Auchi, Edo State Nigeria*

Received October 5, 2017; Accepted January 8, 2018

Abstract

Prediction of pore fluid and lithology using well log derived rock attributes alone are often associated with higher uncertainties. This could lead to inaccurate determination of formation properties. In this paper, integration of derived rock attributes and Prestack seismic inversion of Lamé parameters reduced the uncertainties. The goal was to effectively discriminate fluid and lithology in the reservoir and predict hydrocarbon charged sand zones that could be revived for further drilling decisions. To achieve this goal, elastic attributes were generated from the well logs and appropriate pair of these attributes was cross-plotted to discriminate fluid and lithology. To improve the confidence of delineating bypassed hydrocarbon zones away from the current producing zones, angle gather generated from the super gather of the prestack seismic data was inverted and data slices of lame impedances along the horizon of interest was extracted and analysed. The results of crossplot of velocity ratio versus Poisson's ratio and acoustic impedance successfully distinguished between fluids and lithology in the area. Gas and oil charged sand exhibit low velocity ratio, Poisson's ratio and acoustic impedance values. The results were also validated by the crossplot of LambdaRho versus MuRho from well logs. To delineate bypassed hydrocarbon away from well locations, data slices of the LambdaRho, and MuRho volumes were generated along HD2 reservoir. The results capture the hydrocarbon prospects at the known well locations and bypassed hydrocarbons away from the known locations which could be revived to increase production in the field.

Keywords: Lithology; Seismic inversion; Reservoir; Lambdah-Rho and Mu-Rho.

1. Introduction

Analysis of pore fluid and lithology are vital elements for effective exploration and production of hydrocarbon because of their importance in delineation of porosity, saturation and permeability in the reservoir. Accurate predictions of lithology and pore fluid in reservoirs that needed natural pressure gradient for extraction of hydrocarbon and those that simply required special recovery operations have continued to pose serious challenge to hydrocarbon exploration and development. But since hydrocarbon economic viability in the field is dependent on the quality and accuracy of the lithology and pore fluid, integrating well log derived attributes and inversion of Lamdah-Mu-Rho in the analysis of these important reservoir properties is hoped to create more confidence in their predictions. However, there has been a growing interest in determining lithology and pore fluid using well log data which is cheaper, and economical but also associated with higher uncertainties [1]. This could lead to erroneous prediction of lithology, pore fluid and delineation of other petrophysical properties such as porosity and permeability. Usually, at the location of a drilled well, we have measurements that give us an idea of the elastic and physical properties of the subsurface rocks [2]. But relying on this information alone for reservoir performance and developments analyses may not effectively give the expected results. Therefore, integrating prestack inversion of Lamdah-Mu-Rho (λ - μ - ρ) and derived well log attributes can offer more insight and confidence in reservoir studies. Goodway *et al.* [4]

proposed Lambda-Mu-Rho techniques as good tools for pore fluid discriminator which has its origin in the hard rock exploration areas of Canada. Hilterman [6] stated that this attribute ($\lambda-\rho$) is a good approximation of Gassmann's bulk modulus of pore fluid effect. Seismic inversion of these attributes provide additional look at the reservoir properties and its performance. The objective was to predict fluid, lithology and delineate hydrocarbon bearing sand intervals for new exploration and development using rock physics principle. Chopra *et al.* [9] stated that well log properties can be link to seismic data through rock physics studies so that one can infer their variation in a lateral and vertical sense.

2. Location and geologic setting

Nembe Field is located in the northern parts of Port Harcourt province in the Niger delta region of Nigeria (Fig.1).

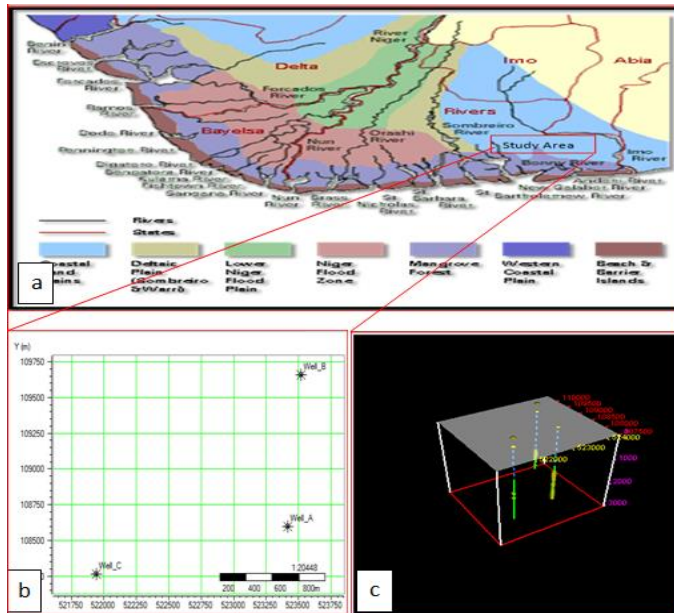


Fig.1. Location of the study area; (a) Map of Niger delta showing the location of the study area as modified after (b) The base map of the study area (c) The 3-D view of the well spots

Niger Delta is situated on the continental margin of Gulf of Guinea in equatorial West Africa, at the Southern end of Nigeria bordering the Atlantic Ocean between latitude 3° and 6° and longitude 5° and 8° [10]. The northern boundary is the Benin flank, an east-northeast trending hinge line south of the West Africa basement massif. The north-eastern boundary is defined by the outcrops of the cretaceous on the Abakaliki high and south east by the Calabar flank, a hinge line bordering the adjacent Precambrian. The offshore boundary of the Niger delta is defined by the Cameroun volcanic line to the east, the eastern boundary of the Dahomey basin. The province covers about 300,000km and includes the geologic extent of the tertiary Niger delta (Akaka- Agbada) petroleum system [12].

The sedimentary basin of the Niger delta encompasses a very large region

than the geographical extent of the modern delta as evidenced by the Niger- Benue drainage system [1]. It includes Cross river delta and extends eastwards into the continental margins of neighbouring Cameroon and Equatorial Guinea [8].

3. Materials and method

The data used in this study include suites of well logs and Pre-stack seismic data processed through super gather process to create a uniform offset distribution and to enhance signal to noise ratio. But since Pre-stack inversion perform better in incident angle domain; the super gather (offset) was converted to angle gather where we carried out subsequent processes. Well log correction such as media filtering was carried out on the well logs to minimise anomalous high frequency spikes while errors arising from gaps were corrected using spline interpolation which created interpolated new wells (new Vp and gamma ray log). Shear wave log was not available but was however generated empirically using Castagna relation which applying linear transforms to input p-wave log. Check shot correction was finally applied to improve the match between synthetic and seismic data by modifying the depth -time curve connected with sonic log. This was necessary because of the extrapolation of the initial Vp value to the surface by the program which usually overestimates the near surface velocity. In well log analysis, the

first step is usually to differentiate hydrocarbon charged sand from shale using gamma ray log. In absence of gamma ray log, P wave velocity logs can also perform similar functions (lithology prediction) but they are usually influenced by density, bulk and shear moduli. Kearey *et al.* [7] stated that velocity ratio is independent of density and can be used to derive Poisson's ratio which is much more diagnostic of lithology. These well log attributes (velocity ratio and Poisson's ratio) and other elastic rock parameters such as Lamdah-Rho and Mu-Rho were generated from well log using transform menu of E-log program (Fig.2). The generated well log attributes were crossplotted for quantitative analysis of well logs. The knowledge of the cross-plot populations were used to discriminate fluid and lithology at well locations. The trends of the cross-plot pattern was also used to determine the attribute(s) that have more robust indicator of pore fluid. To predict fluids and lithology (potential bypassed hydrocarbon zones) away from the well locations, Prestack seismic inversion of Lamdah-Mu-Rho was carried out basically to generate Acoustic Impedance, Shear Impedance and Density (Rho) volumes. Rock physic parameter such as LamdahRho ($\lambda\rho$) and MuRho ($\mu\rho$) volumes were generated. Lamdah-Rho was derived from the square of the difference of P-Impedance and S-Impedance ($P\text{-Impedance}^2 - S\text{-Impedance}^2$). MuRho was also derived from the square of S-Impedance ($S\text{-Impedance}^2$). Data slices were Created to predict the behaviour of hydrocarbon bearing intervals at known well locations and potential bypassed hydrocarbon away from the well locations.

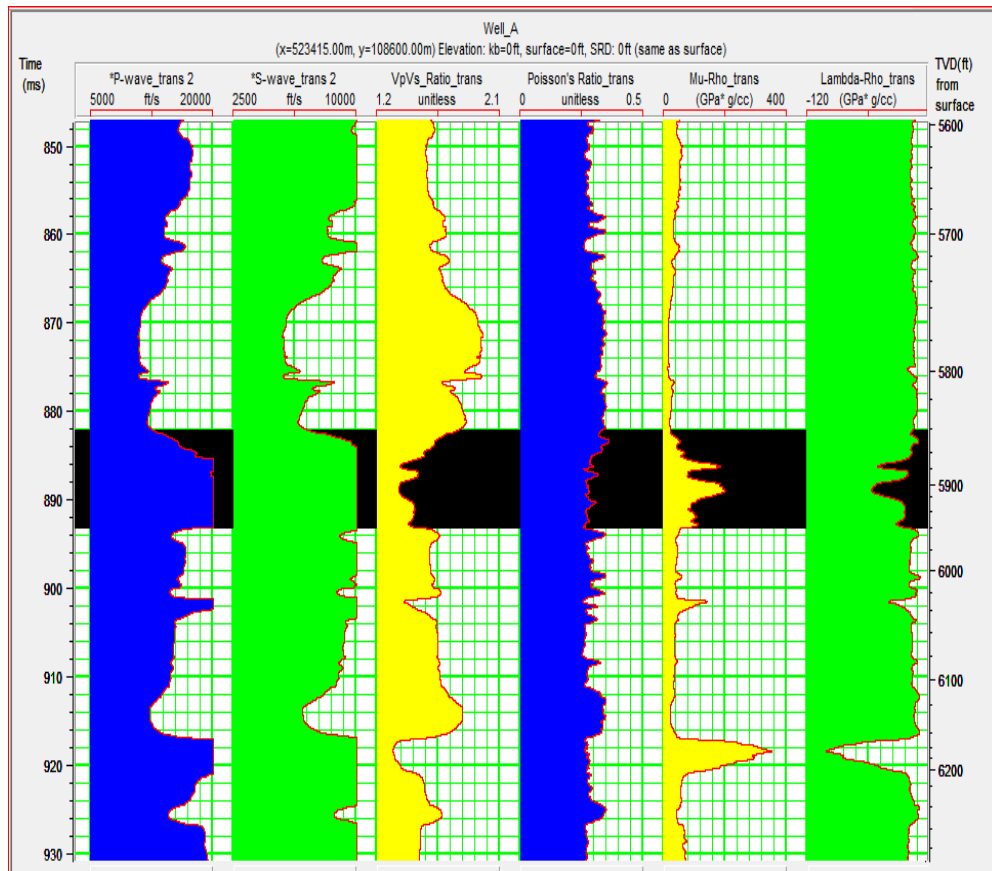


Fig.2. The generated well log attributes indicating HD2 reservoir

3. Results and discussion

Prediction of lithology and pore fluid saturation has been undertaken by analysing the cross-plot populations of the well log attributes (Velocity ratio, Poisson's ratio, LamdahRho and MuRho). The crossplot of Velocity ratio versus Poisson's ratio differentiate the reservoir into three distinct zones as indicated by green, yellow, blue and pink polygons (Fig.3). The green zone

represent gas sand, yellow zone is oil sand, blue zone is brine charged sand while the pink zone represents shale zone. The attribute cross-section presents fluids and lithology response to velocity and Poisson's ratio (Fig.4).

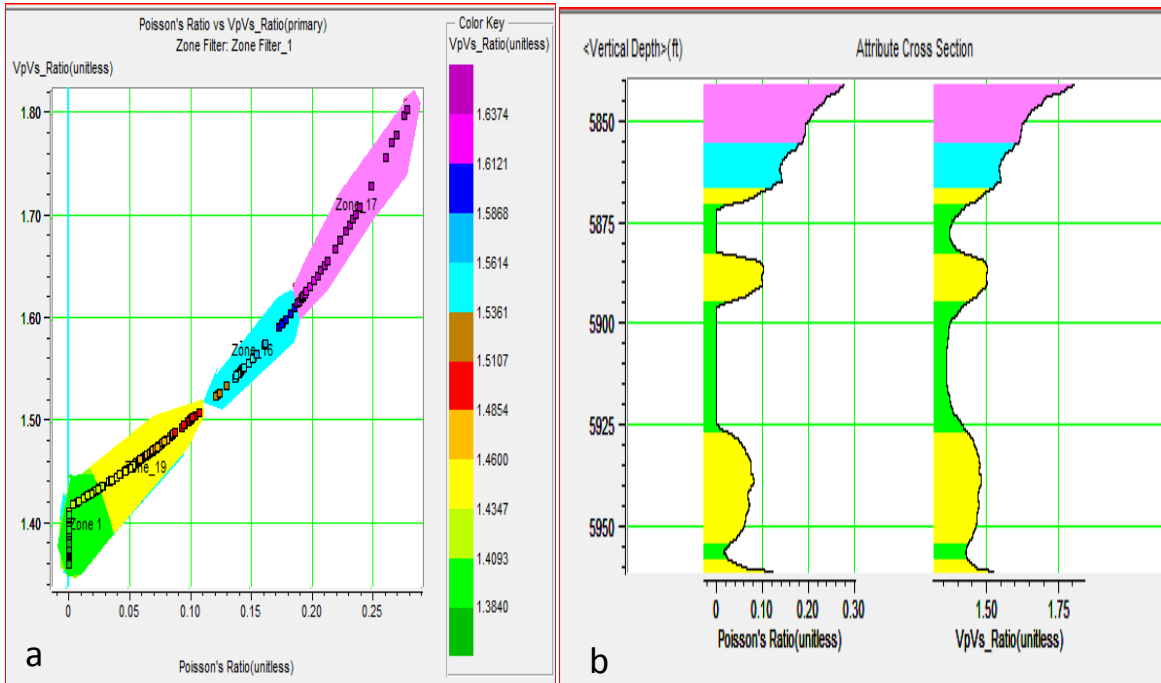


Fig.3. (a) Crossplot of velocity ratio and Poisson' ratio (b) Attribute Cross-Section showing hydrocarbon, Brine and Shale intervals

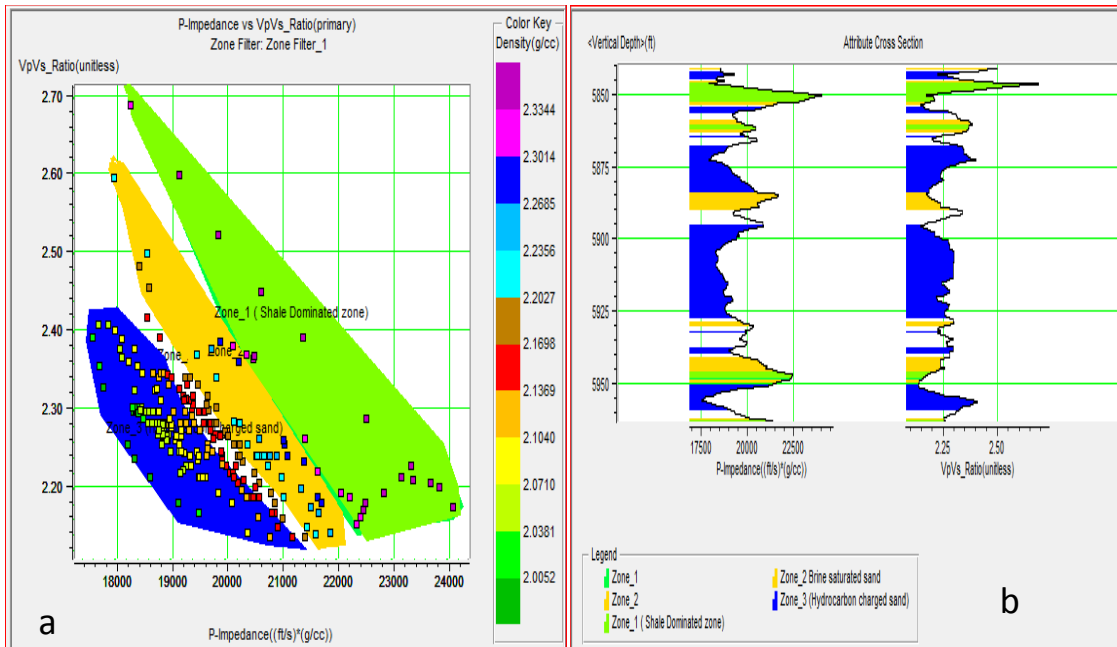


Fig.4. (a) Crossplot of velocity ratio and P-Impedance (b) Attribute Cross-Section showing hydrocarbon, Brine and Shale intervals

Gas and oil charged sand have lower poisons and velocity values while brine and shale are associated with higher values. The attribute cross-section of the velocity ratio revealed that shale has velocity ratio value above 1.75 (Fig.3b). This indicates that that velocity ratio may

not be used to discriminate shale and carbonate because both share similar range of velocity ratio values. The crossplot analysis of velocity ratio and acoustic impedance also discriminate lithology and pore fluid in a very similar manner (Fig.4). Low velocity ratios in blue polygon indicate hydrocarbon saturated zone and also correspond to low acoustic impedance. The brine saturated zone in yellow polygon and shale layer in green polygon both correspond to high velocity ratio and acoustic impedance. The acoustic impedance cross-section revealed that hydrocarbon saturated sand has low acoustic impedance, brine saturated sand exhibit relatively high acoustic impedance while shale has very high acoustic impedance (Fig.4). The results revealed that acoustic impedance and velocity ratio were not only used to delineate lithology but also to evaluate the presence of hydrocarbons in pores. Other well log attributes that sensitive to sedimentary rock's pore fluids are Lamé parameters. The use of relationship between lamé parameters such as λ (incompressibility), μ (rigidity), and ρ (Rho) in pore fluid and lithology discrimination was encouraged by [4]. The crossplot of these two attributes delineate gas saturated zone (green polygon), brine filled sand (blue polygon) and shale zone indicated in pink polygon (Fig.5).

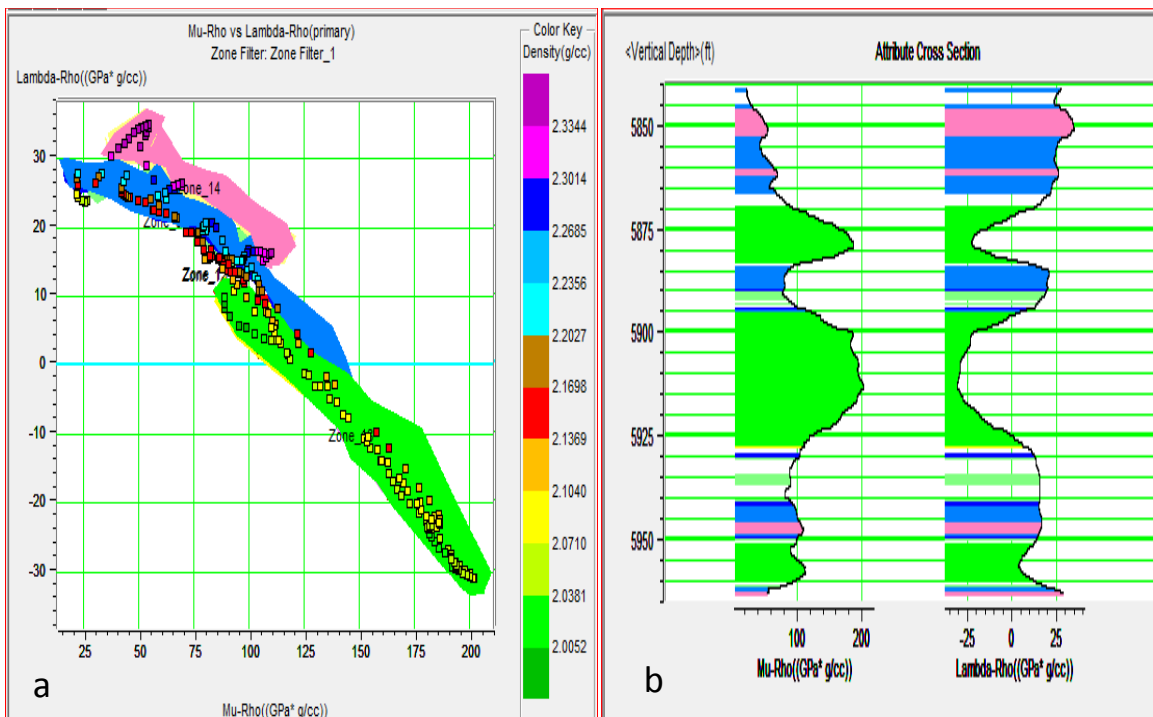


Fig.5. (a) Crossplot of LamdaRho ($\lambda * \rho$) and Mu-Rho ($\mu * \rho$) (b) Attribute Cross-Section MuRho ($\mu * \rho$) and LamdaRho ($\lambda * \rho$) showing Gas, Brine and Shale intervals

The interesting and unique result of the LamdaRho ($\lambda * \rho$) and MuRho ($\mu * \rho$) crossplots and their attribute cross-sections is that sand dominated zone indicates higher MuRho ($\mu * \rho$) values than shale. The high MuRho ($\mu * \rho$) values correspond to very low LamdaRho ($\lambda * \rho$) values which are indication of hydrocarbon filled sand sandstone (5b). The increase and decrease in $\lambda * \rho$ values in water and hydrocarbon filled sandstone respectfully is probably due to its response to the dense media. Hydrocarbon filled sand stone is less dense than water filled sandstone thus leading to decrease in $\lambda * \rho$ values. Various responses of the well attributes and their crossplot's populations revealed that $\lambda * \rho$, Velocity ratio, Poisson's ratio, acoustic impedance and density values are much lower in hydrocarbon saturated layer but characterised by higher ($\mu * \rho$) values (Fig.6). The study has shown that pore fluid and lithology of the well can be predicted by analysing the relationship that exists among the well log derived attributes. But to create much greater insight in fluid and lithology discrimination

beyond the well locations, Lambda-Mu-Rho inversion from the prestack 3D seismic data of the study area was undertaken (Fig. 7).

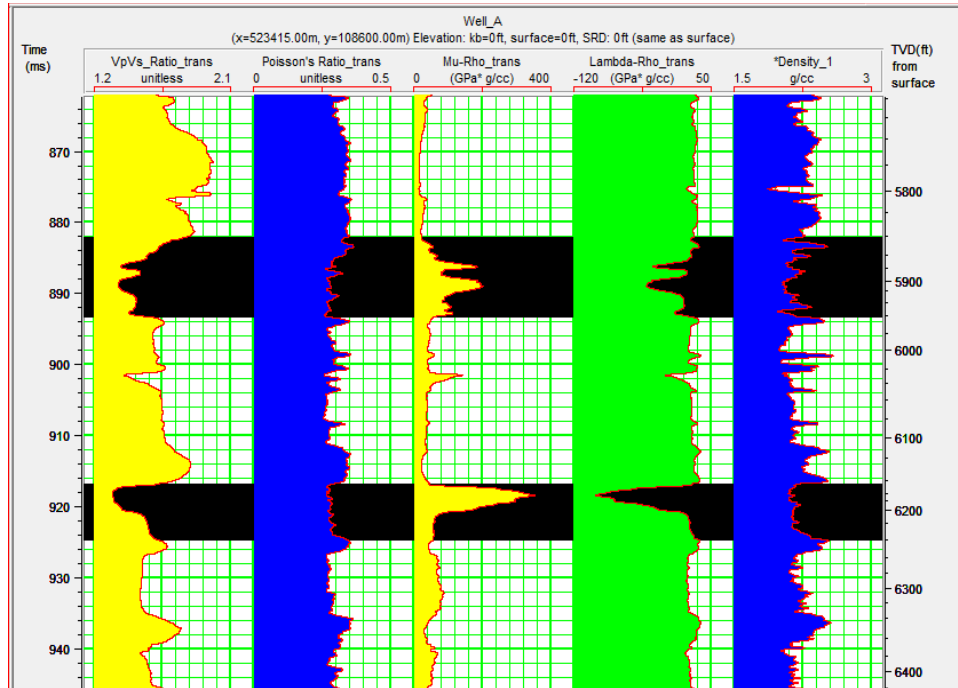


Fig.6. Generated well log attributes indicating their various responses to fluid and lithology

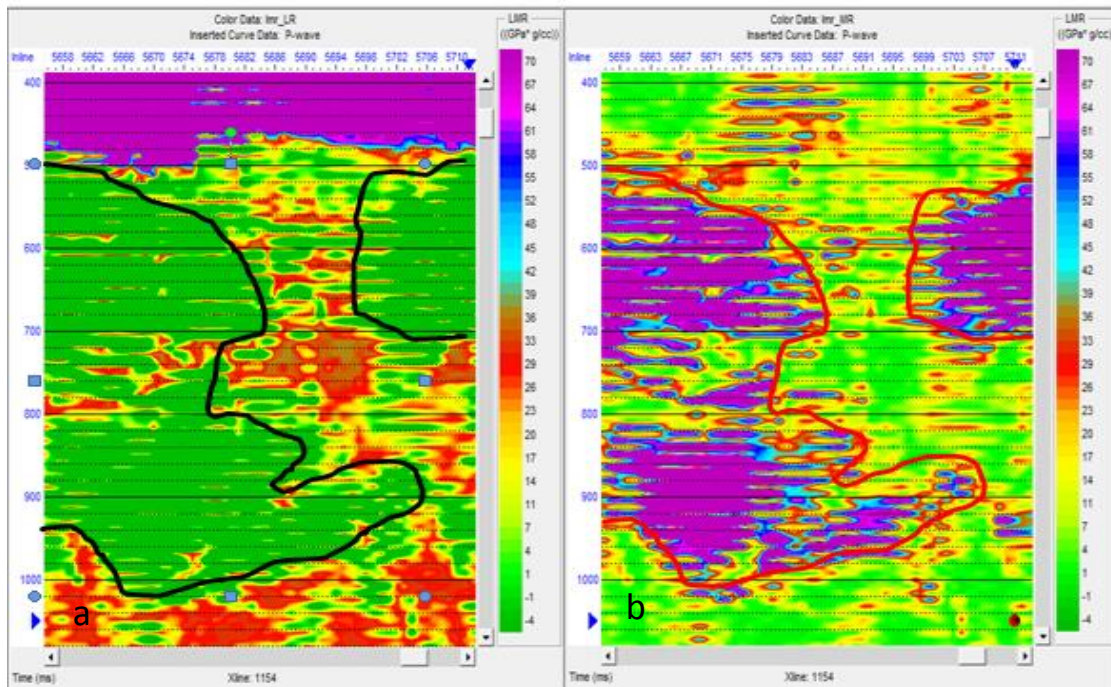


Fig.7. Lambda-Mu-Rho (LMR) inversion (a) Inverted LambdaRho volume (b) Inverted MuRho volume

In the inverted volume, sand dominated zones (green color bands) are characterised by lower $\lambda * \rho$ values (Fig.7a). The same zones are also characterised by higher $\mu * \rho$ values as indicated by pink color band (Fig.7b). This is an indication of hydrocarbon sand reservoirs. Data slices of $\lambda * \rho$ and $\mu * \rho$ were isolated to capture and delineate hydrocarbon charged sand channels

away from the well locations (Fig.8). Lower and higher $\lambda * \rho$ and $\mu * \rho$ values of data slices at the well locations are indication of the presence of hydrocarbon. This represents the Known hydrocarbon prospects that were predicted through well attribute cross-plots. The data slices of the $\lambda * \rho$ and $\mu * \rho$ were created from along the horizon (HD2) of interest. Very low values of LambdahRho ($\lambda * \rho$) were observed around the well locations (producing zones) in the central, far Northwestern and eastern parts of the slice (Fig.8a).

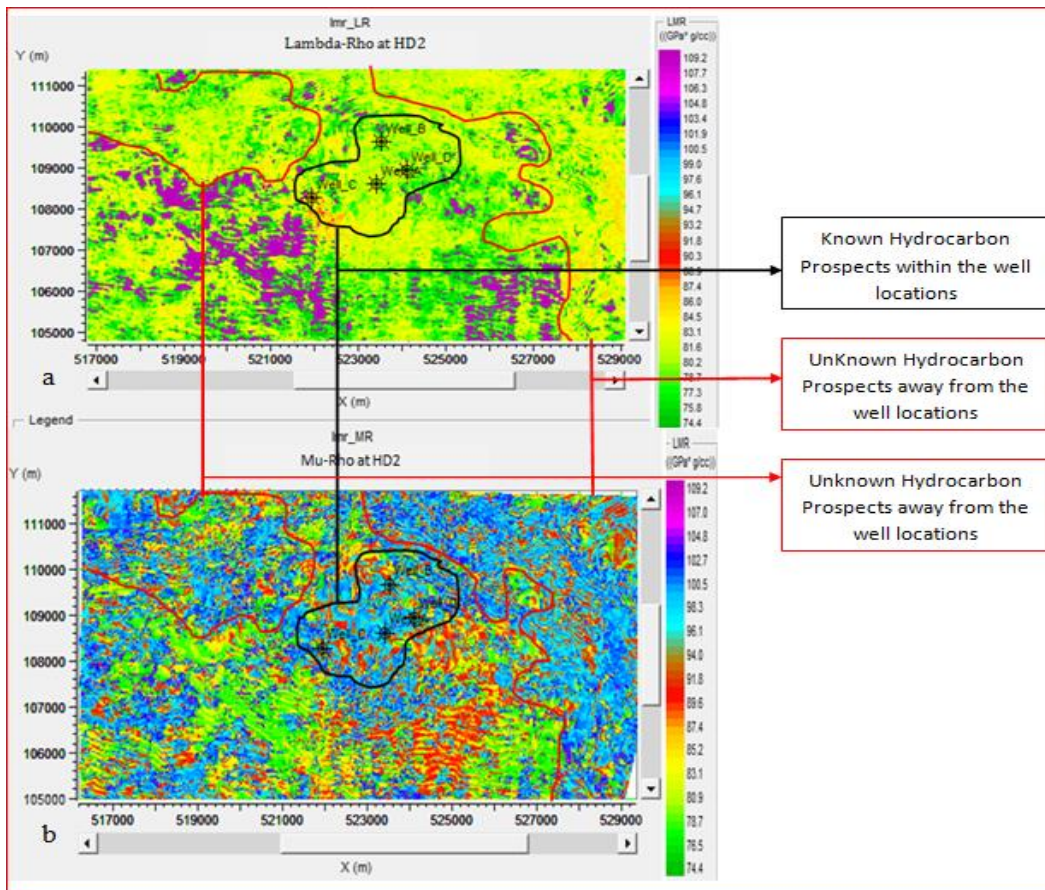


Fig. 8. HD2 reservoir data slices of the inverted (a) LambdahRho (b) MuRho

The lower values of LambdahRho outside the producing zones are the hydrocarbon sand-charged channels. This is unknown hydrocarbon prospect areas. This result was also validated by the data slice of the MuRho ($\mu * \rho$) extracted from the same horizon (Fig.8b). These unknown sand channels areas could be revived to increase more hydrocarbon production. However, derived well log attributes provide useful information on the reservoir condition through the distribution of the fluids and lithology. The knowledge of the lithology and porefluid content of the reservoir is very important in reservoir analysis and development. Hami-Eddine *et al.* [5] stated that the economic viability of a hydrocarbon field is reliant on the quality and accuracy of lithology and pore fluid. Although, the prediction of fluid and lithology using well log derived attributes alone are may not give useful information of the reservoir status beyond the well locations. This is one the major uncertainties associated with this traditional method of lithology and pore fluid prediction. But integration of the well log attribute and Prestack seismic inversion of the Lame parameters (Lambdah-Mu-Rho) offered unique results by providing vertical and lateral information of the reservoir condition beyond well locations. Like velocity ratio, Poison's ratio and P-impedance, Lame parameters derived from the well logs also aid in determination of lithology and pore fluid content of a formation. Goodway [3] proposed the use of relationship between lame parameters to differentiate lithology and gas sand. This is because of

their sensitivity to pore fluid and rock matrix. Mu-Rho (rigidity) is sensitive to rock matrix. Sand has higher Mu-Rho values than shale. LambdaRho (compressibility) is sensitive to pore fluid and useful in fluid discrimination. This knowledge was useful in the analysis of reservoir status and mapping of the hydrocarbon charge sand channels beyond the well locations.

4. Conclusion

The Cross-plots of the appropriate pairs well log derived attributes such as velocity ratio, Poisson's ratio, P-impedance and lame parameters have been used to delineate reservoir pore fluid and lithology contents. Clean sands exhibit Low velocity ratio values that range from 1 to 1.7 which is also associated with low Poisson's ratio and acoustic impedance values. Non reservoirs with streaks of shale have higher P-impedance and velocity ratio values with the range of 1.75 to 2.13. The cross-plot of Lamé parameters ($\lambda * \rho$ and $\mu * \rho$) also provide huge understanding of reservoir pore fluid and lithology by isolating hydrocarbon filled sand from brine filled sand. Hydrocarbon filled sand exhibit very low Lambda-Rho ($\lambda * \rho$) and high MuRho ($\mu * \rho$) values while brine filled sand showed relatively high $\lambda * \rho$ and low $\mu * \rho$ values. Prestack seismic inversion of the Lamé parameters was performed and data slices of Lamé impedances were extracted along the horizon of interest (HD2). With this, hydrocarbon charged sand within the (known) well locations and away from the well locations (unknown) were delineated with confidence. The unknown isolated sand channels can be revived to add to the current production output in study area.

Acknowledgements

We wish to express our gratitude to the Shell liaison Department at the University of Port Harcourt, Rivers State for providing the data used for this research.

References

- [1] Aniwetalu EU and Anakwuba EK. Quantitative Characterisation of Groundroll (Rayleigh Waves) in the Western Niger Delta, Nigeria. Archives of Applied Science Research, 2015; (4): 7-15.
- [2] Ekwe AC, Onuoha KM and Osayande N. Fluid and Lithology Discrimination Using Rock Physics Modelling And Lambdamurho Inversion: An Example from Onshore Niger Delta, Nigeria Search and Discovery Article, 2012: P.3-4.
- [3] Goodway W. AVO and Lamé' constants for rock parameterization and fluid detection. 2001: pp. 39-60.
- [4] Goodway W, Chen T, and Downton J. Improved AVO fluid detection and lithology discrimination using Lamé's petrophysical parameters: fluid stack' from P and S inversions: SEG Annual Meeting Expanded Technical Program Abstracts with Biographies, 1997; 67: 183-186.
- [5] Hami-Eddine K, Klein P, Loic R, Ribet B, Grout M. A new technique for lithology and fluid content prediction from prestack data: An application to carbonate reservoir. (2015): 1.
- [6] Hilterman FJ. Is AVO the seismic signature of the rock properties? Expanded abstract, SEG 59th Annual meeting, 2001.
- [7] Kearey P, Brooks M, Hill I. An Introduction to Geophysical Exploration. 3rd Edition. Blackwell Science: Oxford, UK., 2002:236 - 262.
- [8] Reijers TA. Stratigraphy and sedimentology of the Niger Delta. Geologos, 2011; 17(3): 133-162.
- [9] Chopra S and Sayers C. Special session: Rock physics: The Leading Edge, (2009): 15-16.
- [10] Short KC, and Stauble AJ. Outline of Geology of Niger Delta. AAPG Bull., 1967; .51: 761-779.
- [11] Obeng MC. Lithology and pore fluid prediction of a reservoir using density, compressional and shear wave logs: a case study of the Tano basin. MSc. Thesis, Kwame Nkrumah University of Science and Technology 2015; 25-29.
- [12] Obiekezie TN. Hydrocarbon exploration in ondo Field in the Niger Delta Basin Nigeria, Using a three Dimensional seismic reflection survey. Scientific Research and Essays, 2014; 6(17): 778-784.

To whom correspondence should be addressed: E. U. Aniwetalu, Department of Geological Sciences, Nnamdi Azikwe University Awka, Nigeria, emmymega4@gmail.com

PETROPHYSICAL ANALYSIS OF CHAD BASIN NIGERIA SANDSTONE FROM WELL LOGS

Cyril N. Nwankwo¹ and Sylvester A. Ugwu²

¹ Department of Physics, University of Port Harcourt, Nigeria

² Department of Geology, University of Port Harcourt, Nigeria

Received October 27, 2017; Accepted January 8, 2018

Abstract

The study evaluates the petrophysical properties of the reservoir sands of the Chad basin Nigeria in an attempt to evaluate its prospect for hydrocarbon accumulation. The sand units within the Fika, Gongila and Bima Formations from 12 exploratory Wells drilled in the area were delineated in order to estimate the rock properties such as porosity, permeability, water saturation, hydrocarbon saturation and net-to-gross (NGR) values. The interpretation of the computed values suggests that the sandstone units in the basin have the potential to accumulate and transmit hydrocarbons. The thicknesses of the sand units vary from 10 to 360 m, with an average porosity of 26.62% for all the Wells. The permeability of the rocks ranges from 75 to 5600 mD, suggesting good to excellent while the hydrocarbon saturation of the interstitial spaces are between 3.64 and 83.78 %. Although the overall average porosity and permeability are within limits required for hydrocarbon generation and accumulation, the hydrocarbon saturation values suggest that some of the reservoir units in the basin might contain hydrocarbon in non-commercial quantities.

Keywords: petrophysical; reservoir; well logs; sandstone; Chad basin.

1. Introduction

The Nigerian Government decision to renew exploration work in the Nigerian sector of the Chad Basin has necessitated detailed and systematic analysis of available data from previously drilled wells. This is geared towards achieving successful hydrocarbon production from the basin. At present, about 23 exploration wells that have no hydrocarbon of commercial quantity have been drilled in the area. However, a recent commercial discovery of oil and gas in neighboring countries where the basin extends has aroused interests of researchers from different disciplines [1-6].

The optimal method of producing hydrocarbon from reservoirs is the interest of any producing company. One of the ways of achieving this is through good petrophysical analysis or hydrocarbon reservoir properties modeling. A good reservoir system is made up of the reservoir, the trap and an impervious caprock overlying the reservoir. In Bornu Basin, the reservoirs have been identified as the sandstone facies in the Gongila and Fika formations and Bima Sandstone while the source rocks are mainly in the Gongila formation and in the Fika shale [1, 7-9]. For a rock to be a potential reservoir, porosity and permeability must exist in sufficient magnitude. The entrapment conditions must also be right, and it should be able to release the hydrocarbon at a reasonable rate when it is penetrated by a well.

Well logs data is a key tool used in investigating the fluid quality of reservoir sandstone. It provides accurate reservoir properties by analyzing petrophysical properties taken from a reservoir and thus, is widely used as benchmark or validation data in reservoir characterization [10-11]. Interpreting these measured data helps in evaluating formation properties like porosity, permeability, water saturation, and hydrocarbon that are usually not measured directly. In this study, we have tried to examine the average petrophysical properties of the reservoirs at different stratigraphic zones from 12 exploratory wells with a view of ascertaining if the

properties are good enough to support hydrocarbon generation, accumulation, and transmission. Knowledge of the distribution of these rock properties which occur at various scales [12] helps to determine the reservoir quality and in finding techniques that will give maximum fluid production.

In poorly explored regions like Bornu Basin, prediction of reservoir parameters (thickness, porosity, permeability, temperature when added to the knowledge of the geological development will be helpful to the explorationists in the area before the further commencement of drilling operations. Porosity is primarily related to depth, while the permeability also depends on porosity, mineralogy and grain size, which are controlled by the depositional environment.

2. Geologic Setting of Chad Basin

The Chad basin Nigeria is a broad sediment-filled depression stranding Borno, Bauchi, Plateau and Kano States of northern Nigeria. The area is located at longitude $11^{\circ} 45' E$ and $14^{\circ} 45' E$ and latitude $9^{\circ} 30' N$ and $13^{\circ} 40' N$ (Fig. 1). The origin of the Chad basin is attributed to the rift system that developed in the early Cretaceous when the African and South American lithospheric plates separated, and the Atlantic opened. The Basin developed at the intersection of many rifts, mainly in an extension of the Benue Trough. Obaje *et al.* [1] observed that Pre-Santonian Cretaceous sediments were deposited within the rift system.

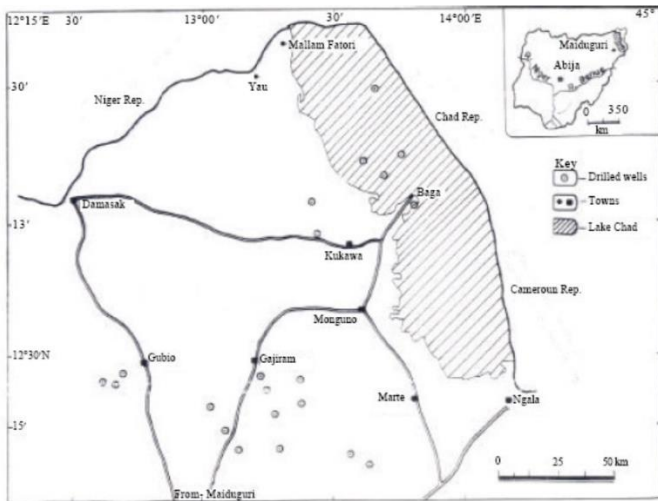


Fig. 1. Location map of the study area [13]

The lithostratigraphic units are the Chad, Fika, Gongila and Bima Formations. Bima Sandstone is the oldest rock and is adjudged the main reservoir rock. It is of Albian to early Turonian age and lies unconformably on the basement complex [9]. The translational Gongila Formation overlies the Bima. It consists of a sequence of sandstones, clays, shales and limestone layers. Its sandstone texture varies from fine to coarse-grained with the base defined by the first appearance of marine limestone above the Bima Sandstone. The Fika Formation overlies the Gongila Formation, and it consists of shale and thin limestone. The reservoirs are provided

by the sandstone facies of Fika and Gongila Formations and in the Bima Sandstone [9]. The Chad Formation is the youngest rock unit in the basin and is of Pleistocene age. The lithology consists of well developed fluvial sands, gravels, and grits with colour ranging from white, brown, yellow to grey.

3. Materials and methods

Wireline logs from twelve exploratory Wells drilled in Bornu Basin were analyzed for the purpose of evaluating the petrophysical parameters. The Wells considered, based on area spread and data completeness are Wadi-1, Krumta-1, Masu-1, Gaibu-1, Kanadi-1, Gubio-1, Herwa-1, Murshe-1, Mbeji-1, Kema-1, Tuma-1, and Ziyé-1. The well logs were mainly in hard copy which made the use of any geophysical software for the analysis difficult. A simple, quick look approach was therefore employed in deriving the petrophysical parameters from the logs. The lithologies penetrated by the wells were delineated with the use of gamma ray log. The signature of the log deflecting to the left, below the cutoff point formed the sand bed while shale formation showed prominent high gamma ray signature to the right.

Having identified the bed boundaries, constant log values were assigned to the reservoir sand beds. The values digitized from the logs at 10 m intervals are gamma ray counts from

the gamma ray log and interval transit time from the compensated sonic log. These values were then used to calculate the reservoir properties of each bed while the trends in the relationship between the parameters were achieved using the MS Excel. An inference of the potential and producibility of the formation as a suitable reservoir rock from various calculated parameters and cross plots was then made. The determined parameters in this study are porosity, permeability, and water saturation. The net to the gross sand ratio (NGR) was also considered for ease of analysis.

3.1. Determination of porosity

Evaluation of porosity was done using sonic log. For the sand porosity to be determined, the corresponding transit time Δt at any depth for each well was read and recorded from the sonic log. The percentage porosity for each well was calculated using the equation:

$$\phi = \left(\frac{\Delta t_{log} - \Delta t_m}{\Delta t_f - \Delta t_m} \right) \times \frac{100}{1} \quad (1)$$

where Δt_m is the transit time of the rock matrix; Δt_{log} is the transit time reading on the log and Δt_{fl} is the transit time of formation fluid. A value of $55.5 \mu s/ft$ and $189 \mu s/ft$ for Δt_m and Δt_{fl} respectively have been used for the computation.

3.2. Determination of compressional wave (Vp) and shear wave (Vs) velocities

The Vp was estimated from the sonic log which measures the time, Δt taken for the sound wave to travel through one foot of a formation. Δt recorded in a well log in $\mu s/ft$ is related to the Vp by

$$\Delta t = \frac{1}{V_p} \quad (2)$$

$$\text{or } \frac{1}{V_p} = \frac{1}{\Delta t} \times \frac{304800}{1} \text{ m/s} \quad (3)$$

The Vs was calculated from the compressional wave velocity by using the relation of [14] for sand and shale beds given respectively as

$$V_{sd} = (0.80416)V_p - 0.85588 \quad (4)$$

$$V_{sh} = (0.76969)V_p - 0.86735 \quad (5)$$

3.3. Determination of water saturation

Saturation of a formation defines the fraction of the rock's effective pore volume which is occupied by the particular fluid considered. Water saturation thus is the fraction of the volume occupied by Formation water. It is the fraction of the formation water in the undisturbed zone.

Water saturation was determined using [15] relation:

$$S_{W ud} = \frac{0.082}{\phi} \quad (6)$$

where $S_{W ud}$ is the water saturation and ϕ is the formation porosity.

It has been noted that for relatively small shale volumes, most shale models for estimating water saturation yield approximately similar results [16-17].

3.4. Determination of permeability

A number of methods for determining permeability from porosity are described in literature, including empirical approaches and various modelling techniques. In this study, permeability which measures the ease with which a formation allows fluid of certain viscosity to flow through it was estimated for the reservoir rock (sand bed) by employing the relation of [18] equation, which expresses permeability 'K' in terms of porosity and water saturation as:

$$K = 307 + 26552\phi^2 - 34540(\phi \times S_{W ud})^2 \quad (7)$$

The net-to-gross sand ratio (NGR), which is the proportion of clean sand within a reservoir unit was computed as the ratio of the net sand to the gross sand [6].

4. Results

The reservoir sands with higher thickness have been used in estimating the petrophysical parameters used in this analysis. The computed values from representative Wells (from lower Fika to Bima Formations) in the basin are shown in Tables 1 – 6. Plots of the porosities against depth shown in Figure 2 are poor to excellent for hydrocarbon accumulation. V_p is greater than V_s and linear throughout (Fig. 3), and the V_p/V_s ratio for all the wells is nearly constant which is indicative of dry sandstone.

Table 1. Petrophysical parameters for Wadi-1

Depth range (m)	Thickness (m)	V_p (m/s)	V_s (m/s)	Φ (%)	S_w (%)	S_h (%)	K (mD)	NGR
1460 - 1610	50	4541.80	3651.48	8.70	94.29	5.71	275.57	83.81
2000 - 2060	60	2767.39	2224.57	40.93	20.03	79.97	4522.66	86.25
2265 - 2410	145	3403.31	2735.95	25.51	32.14	67.86	1803.07	84.92
2710 - 2750	40	4549.25	3657.47	8.61	95.19	4.81	271.78	87.29
2915 - 3210	295	4354.29	3500.69	10.36	75.50	24.50	387.99	90.70

Table 2. Petrophysical parameters for Masu-1

Depth range (m)	Thickness (m)	V_p (m/s)	V_s (m/s)	Φ (%)	S_w (%)	S_h (%)	K (mD)	NGR
2000 - 2290	290	3467.36	2787.46	24.42	34.12	65.88	1682.45	91.27
2390 - 2450	60	4105.60	3300.71	58.42	41.58	79.97	597.96	93.71
2510 - 2590	80	4115.03	3308.28	58.95	41.05	67.86	588.51	92.13
2800 - 2845	45	4322.79	3475.36	72.93	27.07	4.81	410.41	91.71
2970 - 3085	115	3926.82	3156.94	49.49	50.51	24.50	803.72	91.28

Table 3. Petrophysical parameters for Kanadi-1

Depth range (m)	Thickness (m)	V_p (m/s)	V_s (m/s)	Φ (%)	S_w (%)	S_h (%)	K (mD)	NGR
1575 - 1620	45	2988.24	2402.16	34.83	23.54	76.46	3296.12	87.93
1740 - 1790	50	4549.25	3657.47	8.61	95.19	4.81	271.78	88.35
2185 - 2250	65	2796.33	2247.84	40.07	20.46	79.54	4338.99	86.14
2380 - 2500	120	4118.92	3311.41	13.86	59.17	40.83	584.65	90.88
2800 - 2890	90	4549.25	3657.47	8.61	95.19	4.81	271.78	92.78
2920 - 2980	60	4482.35	3603.67	9.36	87.58	12.42	307.54	92.38

Table 4. Petrophysical parameters for Gubio-1

Depth range (m)	Thickness (m)	V_p (m/s)	V_s (m/s)	Φ (%)	S_w (%)	S_h (%)	K (mD)	NGR
1785 - 1800	15	2848.60	2289.87	38.58	21.26	78.74	4026.14	98.37
2420 - 2470	50	2770.91	2227.40	40.82	20.09	79.91	4499.90	86.86
2765 - 2790	35	2745.95	2207.32	41.57	19.72	80.28	4663.78	90.84
2890 - 2945	55	2540.00	2041.71	48.31	16.97	83.03	6272.79	83.93
3165 - 3220	55	2605.13	2094.08	46.07	17.80	82.20	5709.64	89.44
3250 - 3280	50	2721.43	2187.61	42.32	19.38	80.62	4830.64	89.92

Table 5. Petrophysical parameters for Herwa-1

Depth range (m)	Thickness (m)	V_p (m/s)	V_s (m/s)	Φ (%)	S_w (%)	S_h (%)	K (mD)	NGR
1530 - 1560	30	2822.22	2268.66	39.33	20.85	79.15	4181.08	95.85
2100 - 2130	30	2673.68	2149.21	43.82	18.71	81.29	5173.30	88.95
3420 - 3690	270	4482.35	3603.67	9.36	87.58	12.42	307.54	92.46
3750 - 3810	60	4417.39	3551.43	10.11	81.09	18.91	346.27	87.93
4230 - 4260	30	4549.25	3657.47	8.61	95.19	4.81	271.78	88.45
4620 - 4700	80	4417.39	3551.43	10.11	81.09	18.91	346.27	83.93

Table 6. Petrophysical parameters for Ziye-1

Depth range (m)	Thickness (m)	Vp (m/s)	Vs (m/s)	Φ (%)	Sw (%)	Sh (%)	K (mD)	NGR
1630 - 1685	55	4233.33	3403.42	12.36	66.35	33.65	480.36	93.33
1910 - 1970	60	3810.00	3062.99	18.35	44.68	55.32	969.02	93.71
2330 - 2360	30	2770.91	2227.40	40.82	20.09	79.91	4499.90	93.71
2550 - 2660	110	2770.91	2227.40	40.82	20.09	79.91	4499.90	97.01
2720 - 2780	60	4292.96	3451.37	11.61	70.63	29.37	432.68	94.96
2840 - 2900	60	3958.44	3182.36	16.10	50.92	49.08	763.42	95.53
3110 - 3200	90	4762.50	3828.96	6.37	-	-	182.39	97.00

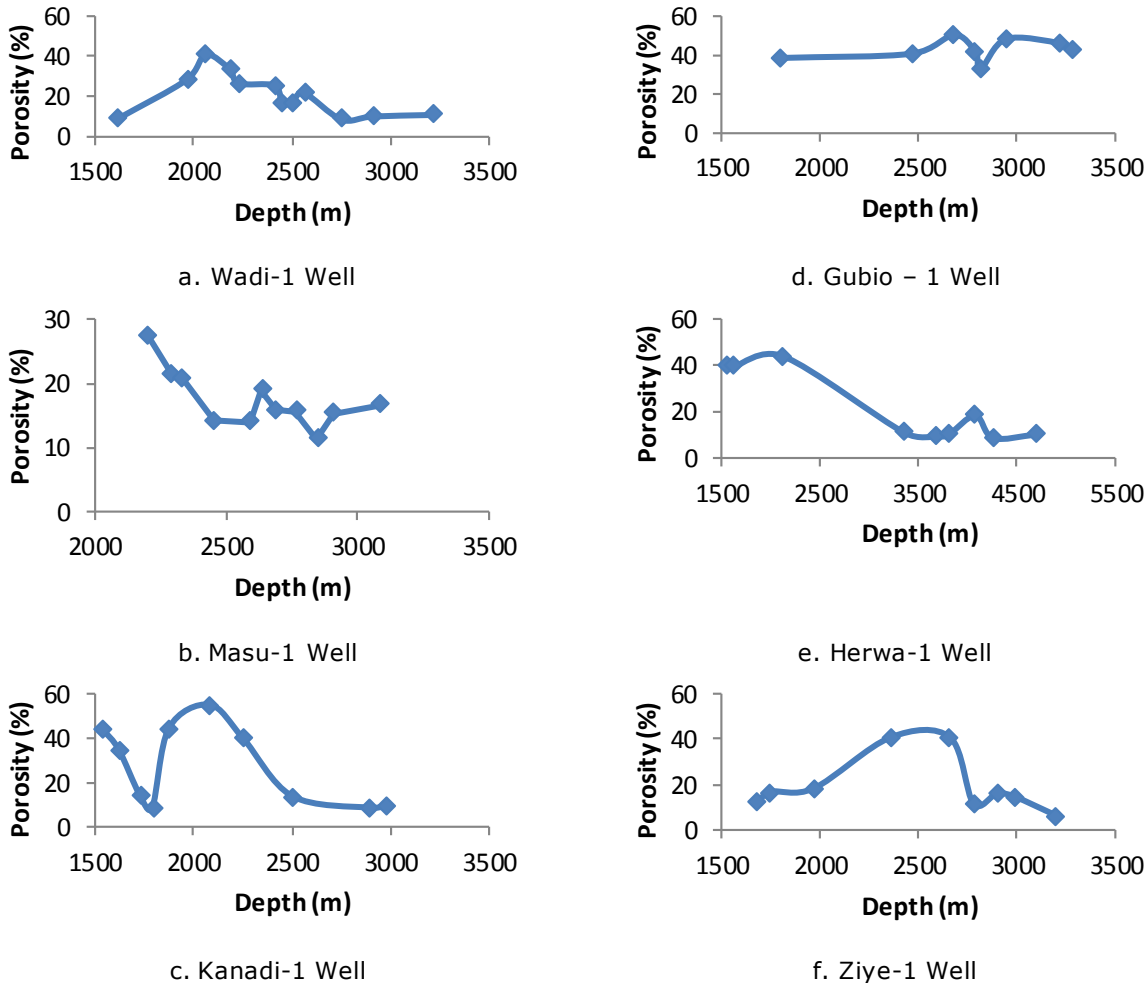


Fig. 2. Porosity - depth relationship between wells in Chad Basin

5. Discussion

The sand units vary in thickness from 10 to 360 m, with the thickness increasing in deeper depths. The gamma ray log readings within the various sand units (11–118 API) are fairly low to moderate which is an indication that the sands are shaly. The porosity and permeability of the reservoir sandstone generally decrease with increasing burial depth, as a result of mechanical compaction and diagenetic alterations [19]. Generally, the permeability reduction with burial depth is more pronounced for fine grained sandstones than for coarse grained; however, the presence of detrital clay, sorting and other elements related to variations in the deposi-

tional environments affect permeability. The presence of diagenetic cement may also result in substantial permeability reduction, as the cement reduces the size of the pore throats.

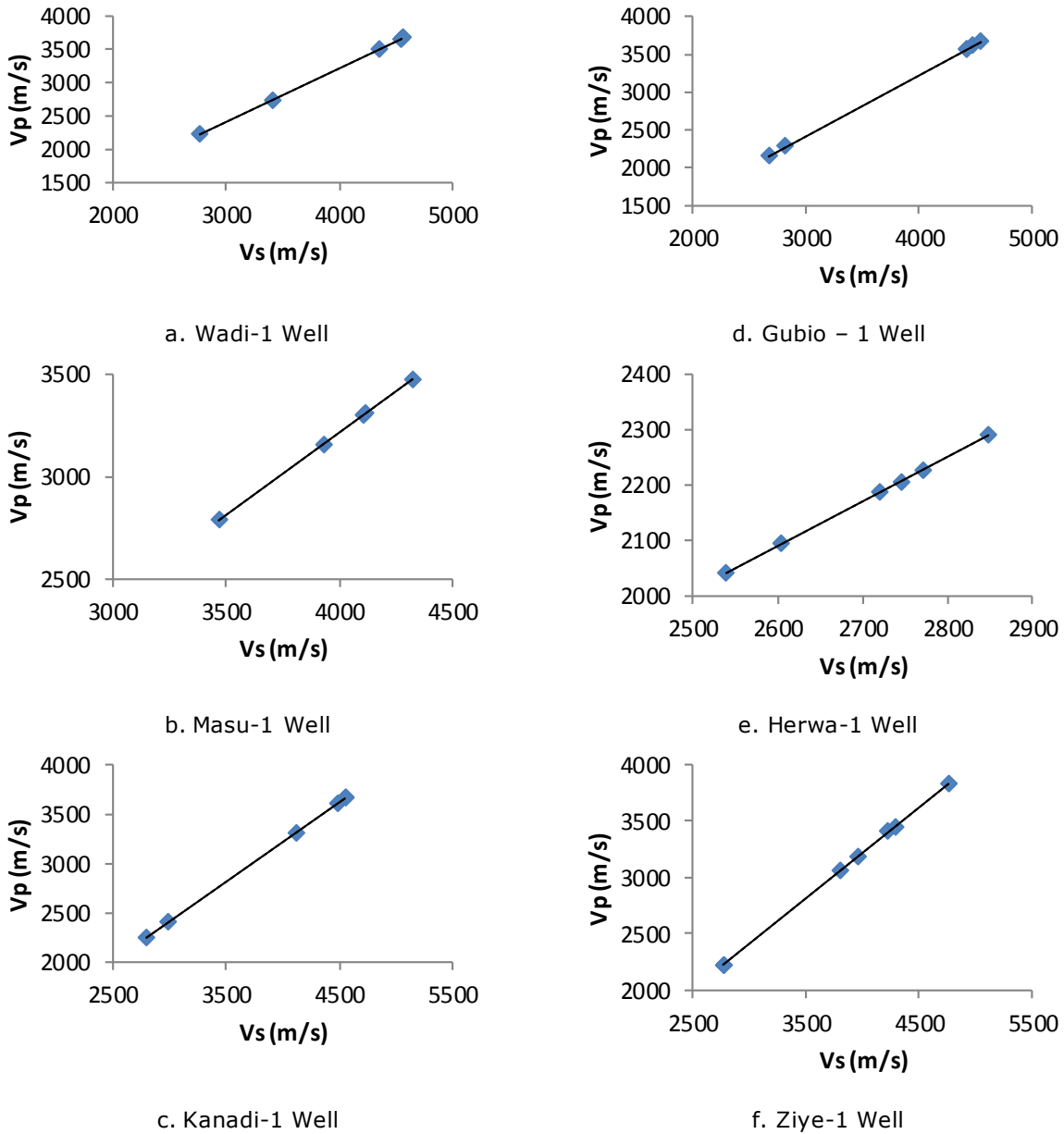


Fig. 3. Linear relationship between shear and compressional velocities

Porosity estimation and those of other parameters obtained in this study were based on sonic logs readings. A porosity range of 1.12 to 60.30% with a basin average of 26.62% was computed for the sand units. Permeability values range from 75 to 5600 mD are good to excellent for hydrocarbon production [20-21]. These computed values are an indication that fluids can flow through the rocks without causing structural changes. The average range of water saturation and hydrocarbon saturation are 16.22 and 96.36% and 3.64 and 83.78% respectively. The results show that some of the sand units are hydrocarbon bearing while some are water bearing. The hydrocarbon saturation values also suggest that many reservoir units in the basin might contain hydrocarbon in non-commercial quantities. However, the overall average porosity, permeability, and fluid saturations are within limits required for hydrocarbon generation and accumulation.

The sonic transit time log and the derived primary and shear velocities have proved to be a useful tool in predicting the rock properties of the study area. However, the [15] relation was ineffective in predicting reservoir fluids saturation when the transit time is less than 67 $\mu\text{s}/\text{ft}$. However, the general increases of both compressional and shear velocities with depth were not well pronounced in this study. This may be associated with heterogeneity nature of the lithology as seen from the calculated NGR values.

6. Conclusion

The overall computed porosities and permeabilities of the sand units are good enough to support the generation and accumulation of hydrocarbon. Depths with more likely water saturation in each of the wells are clearly delineated. A computed NGR value range of 78 to 99% for the basin is an indication of the presence of quality potential reservoir rocks. The hydrocarbon saturation obtained in some reservoir units suggests that the basin hydrocarbon potential might be of low to non-commercial quantities.

Acknowledgement

The authors are grateful to the Nigerian National Petroleum Corporation for releasing the data used in this study through its exploratory arm, NAPIMS Maiduguri.

References

- [1] Obaje NG, Attah DO, Opeloye SA, Moumount A. Geochemical evaluation of the hydrocarbon prospects of sedimentary basins in Northern Nigeria, *Geochem. J.* 40 (2006) 227- 243.
- [2] Ofoma AE, Chiaghanam OI, Amobi JO, Okogbue CO. Reservoir characterization of sand units penetrated by four Wells in the Nigerian sector of the Chad Basin and its Implication for Hydrocarbon Generation and Accumulation, *J Geol Geosci.*, 2014; 3: 183.
- [3] Okosun EA. A preliminary assessment of the petroleum potentials from southwest Chad Basin, Nigeria, *Bornu J. Geol.*, 2000; 2:2: 40 – 50.
- [4] Olugbemiro RO, Ligouis B, Abaa SI. The Cretaceous Series in the Chad basin, NE, Nigeria: source rock potential and thermal maturity. *Journal of Mining and Geology*, 1997; 20:1: 51-68.
- [5] Nwankwo CN, Ekine AS. Geothermal gradients in the Chad Basin Nigeria, from bottom hole temperature logs, *International Journal of Physical Science*, 2009; 4: 777-783.
- [6] Nwankwo CN, Nwosu LI. Effect of shale content on Sand Reservoir Quality: Case study of Chad Basin, Nigeria, Under review. 2016.
- [7] Adepelumi AA, Falebita DE, Olorunfemi AO, Olayoriju SI. Source-rock Investigation of the Turonian-Maastrichtian Fika Shale from Wireline-logs, Chad Basin, Nigeria, *Int. J. Petroleum Sci. Technol.* 2010; 4:1: 19-42.
- [8] Petter SW, Ekweozor CM. Petroleum Geology of Benue Trough and Southern Chad basin, Nigeria, *AAPG Bull.*,1982; 66:8: 1141-1149.
- [9] Nwankwo CN. Heat flow studies and hydrocarbon maturation modeling in the Chad basin Nigeria, Unpublished Ph.D Thesis, University of Port Harcourt, Port Harcourt Nigeria, (2007).
- [10] Mohaghegh S. Recent developments in application of intelligence in petroleum engineering, *Journal of Pet Tech*, 2005; 57(4): 86 – 91.
- [11] Mohaghegh S, Reeves S, Hill D. Development of an intelligent systems approach for reservoir candidate selection. *The Proc. of 2000 SPE/CERI Gas Tech Symp, Canada*, SPE 59767.
- [12] Mukerji T, Avseth P, Mavko G, Takahashi I, González E. Statistical rock physics: Combining rock physics, information theory, and geostatistics to reduce uncertainty in seismic reservoir characterization, *The Leading Edge*, 2001; 20:3: 313 – 319.
- [13] Ali S, Orazulike DM. Well logs-derived radiogenic heat production in the Sediments of Chad basin, NE, Nigeria, *Journal of Appl. Sci.*,2010; 10: 786-800.
- [14] Castagna JP, Greenberg ML. Shear-Wear Velocity Estimation in porous rocks, theoretical formulation, preliminary verification and applications, *Geophys. Prosp.*, 1993; 40: 195-209.
- [15] Udegbumam EO, Ndukwe K. Rock Property Correlation for hydrocarbon producing sand of the Niger Delta sand, *Oil and Gas J.* 1988.
- [16] Bussian AE. A comparison of shaly sand models, paper E, in 24th Annual Logging Symposium: Society of Professional Log Analysis. 1984.
- [17] Schlumberger (1987). *Log interpretation Principle/Application*, New York.

- [18] Owolabi OO, Longjohn TF, Ajiienka JA. An empirical expression for permeability in unconsolidated sands of eastern Niger Delta, *Journal of Petroleum Geology*, 1994;17(1): 111 – 116.
- [19] Olivarius M, Weibel R, Hjuler ML, Kristensen L, Mathiesen A, Nielsen LH, Kjoller C. Diagenetic effects on porosity-permeability relationships in red beds of the Lower Triassic Bunter Sandstone formation in the North German Basin. *Sed Geol*, 2015; 321: 139 – 153.
- [20] Wichtl FK. Log interpretation seminar (a course designed for modern basiclog evaluation practice), Schlumberger international, Houston, Texas. 1990.
- [21] Rider M. The geological interpretation of Well logs, Blackie Glasgow. 1986: 151 – 165

To whom correspondence should be addressed: Dr. Cyril N. Nuankwo, Department of Physics, University of Port Harcourt, Nigeria, cyril.nuankwo@uniport.edu.ng

EXPERIMENTAL STUDY OF HIGH LIQUID VISCOSITY OIL-GAS FLOWS USING ECT AND GAMMA RADIATION METHODS

Archibong Archibong-Eso^{1,2}, Yahaya D. Baba^{1,3*}, Aliyu Aliyu^{1,4}, Nonso Okeke¹, Abdulwahab Giwa³

¹ Oil & Gas Engineering Centre, Cranfield University, UK

² Cross River University of Technology, Calabar, Nigeria

³ Department of Chemical and Petroleum Engineering, Afe Babalola University, Ado-Ekiti, Nigeria

⁴ School of Mechanical Engineering, Pusan National University, 609-735, Busan, Republic of Korea

Received October 19, 2017; Accepted January 8, 2018

Abstract

Electrical capacitance tomography (ECT) and gamma ray densitometry have found applications in multiphase flows as both have been used to visualize flow patterns in the process, nuclear, chemical and oil-gas industries. However, liquid viscosity is often limited to about 10 cP in most of these applications. This study evaluates the suitability of ECT in the monitoring of multiphase flow consisting of heavy-oil (up to 7500 cP) and gas. Heavy-oil is of interest because of its huge reserves, increasing world energy demand, dwindling conventional-oil reserves, etc. The results obtained showed that ECT performed well in flow visualization and measurement of high-viscous oil/gas flows. Flow patterns identified included plug, slug, pseudo-slug (blow-through-slug) and annular flows. Liquid holdup measurements were found to be within $\pm 10\%$ and $\pm 5\%$ error in the static stratified and static annular test, respectively, based on the LBP algorithm while in dynamic test, it was considerably dependent on flow patterns and the LBP. Comparatively, high definition video recordings, pictures and gamma rays densitometer were used to validate the flow patterns identified by ECT.

Keywords: High viscosity oil; flow patterns; gamma rays; multiphase flow; liquid holdup.

1. Introduction

The foray of tomography into chemical and process industries is hinged on its several successes in medical applications. Multiphase flows exist widely in process and chemical industries such as nuclear, food, agro-allied, oil and gas, water, polymer, textile, etc. Prior knowledge of the behaviour of the phase distribution plays a significant role in process control, process equipment design, pumps and pumping systems design, quality control, safety assurance, process flow assurance, etc. The complex nature of multiphase flow, which is characterised by deformable phase interface, phase inversion, phase slip, as well as the variations of the phase distribution and the velocity profiles with temporal and spatial coordinates, makes it very difficult to measure its phase quantity and distribution (flow pattern or flow regime). Tomography thus becomes important as it can be utilized as a valuable tool in flow visualization. Of the various industrial tomography such as gamma, X-ray, microwave, ultrasonic, optical, electrical resistance tomography (ERT), electrical capacitance tomography (ECT) that are available for process industry applications, ECT is one of the most promising one due to its inherent simplicity, robustness, high speed capability, zero radiation emission, non-invasiveness, non-intrusiveness, low cost and ability to withstand wide range of operational temperatures and pressures [1].

ECT is a tomographic technique that involves the determination of the spatial permittivity distribution of dielectric materials within an object from external capacitance measurement using multiple sensor electrodes mounted on the periphery of the object [2]. The ECT system

typically consists of three units, namely the ECT sensing system, Data Acquisition System (DAS) and the Computing System. The ECT sensing system consists of an object (e.g., a pipe) and sensing electrodes, which are mounted on the object's periphery; this unit is used to obtain measurement values of the dielectric material within the object where they are mounted. Data Acquisition System (DAS) unit is used to acquire data obtained by the sensors and subsequently transfer the data in machine-readable form to the computing system. The computing system consists of a computer built to ECT manufacturer's specification and proprietary software, which comprises algorithms that aids real time and offline data reconstruction, tomographic image display and data analysis.

The ECT system was reportedly used in pipeline flow visualization at the University of Manchester in the early 1990s [3]. The success of earlier studies led to the subsequent use of ECT in visualizing multiphase flows in oil pipelines [1]. Nevertheless, visualization of multiphase flow using ECT techniques were concentrated on low viscous oils (less than 20 cP). Research work using ECT for applications higher than 1000 cP was not found in literature by the authors. Also, in multiphase flows, flow patterns for flows consisting of high-viscous liquids are significantly different from low-viscous liquids. Gokcal *et al.* [4] observed an increase in slug frequency and liquid holdup with a corresponding decrease in slug length as oil viscosity was increasing. Márquez and Trujillo [5] affirmed the difference in flow pattern at increased liquid viscosity when they noted in their work that slug region increased with increase in liquid viscosity. This study was concerned with high-viscous oil applications due to its increasing importance as a veritable energy source. Factors such as depleting conventional oil reserves, increase in world energy demand, technological advances (in heavy oil production), availability of huge heavy oil reserves and prevailing oil prices have combined to make heavy oil one of the leading sources of energy. Previous studies of ECT on multiphase applications are outlined below.

Gamio *et al.* [6] used an ECT system they designed to visualize two-phase flow consisting of oil and gas in a 7.62 cm pressurised test loop. Nitrogen gas and Exxsol D80 oil were respectively used as the gas and oil phases in the study. Different flow patterns were obtained though variations in the flow rates of oil and gas. Tomographic images were obtained for each flow condition and the results obtained were validated with video graphic images obtained through a transparent section in the flow loop as well as with the flow pattern map. Their work was based on oil with viscosity of 1.7 cP at 25 °C, and the study did not involve flow measurement such as liquid holdup.

Zhang and Wang [7] used a twin-plane dual modality (ECT/ERT) system developed by Tianjin University for the identification of oil-gas two-phase flow patterns. Only the ECT sensor outputs were used and the ECT sensor consisted of 12 electrodes mounted at the circumference of the pipe. A 0.6 m long horizontal test section with pipe internal diameter of 80 mm was used for the study. Nylon plastic pellets were used to stimulate each flow pattern. In the work, ECT identification of stratified flow, annular flow, core flow and full pipe flow patterns agreed with the Support Vector Machine (SVM), which is a technique based on statistical theory. However, this study reported very limited experimental data. The test was done under static conditions and the authors did not list the properties of the fluids used.

Baker *et al.* [8] used ECT to visualize the time varying cross sectional distribution transients in two-phase gas-liquid stratified/slug flow. The experiments were conducted in a 16.7 m long pipe with internal diameter of 0.038 m. Air and kerosene (viscosity of 3 cP at 25 °C) were used as the gas and liquid phase respectively. The maximum gas superficial velocity used was 12 m/s while the superficial velocity of the liquid was 0.5 m/s. An 8 electrode ECT sensor was used to visualize the cross sectional distribution of the phases in flow. Stratified and slug flows were clearly shown in the tomographic images obtained for both the high and low liquid superficial velocities. However, ECT images and visual observations via the transparent pipe section indicated either slug or stratified flows in disparity to annular flow predicted by the flow pattern map of [9]. Void fractions data obtained from ECT were found to be in agreement with those obtained from other studies in literature with similar fluid properties.

Isaksent *et al.* [10] used capacitance based tomography system for interface measurement in separation vessels. An eight-electrode capacitance sensor mounted circumferentially around a plexi-glass separator with a 60 cm long earthed screen surrounding the electrodes was used. The test fluids used were compressed air, tap and salt water as well as two types of oil (Exxol D80 and D100) with dielectric constant near 2.1. The tomography system was tested for both oil/air separation and oil/water/air separation. The oil/foam/air was conducted by creating enough foam inside the separator by means of high oil and gas flow rates which resulted in severe liquid motion. The tomographic system detected the foam thickness inside the separator above 5 to 10 cm. The reconstructed foam layer thickness was observed to give a good representation of the foam layer thickness inside the separator. The average absolute and maximum absolute errors were 0.3 and 2 cm, respectively. Water-oil-air test was also carried out for water conductivities of 4×10^{-3} S/m and 5 S/m (salt water). The absolute average error for both tap and salt water height and oil thickness were within 0.5 and 1.0 cm respectively.

Warsito and Fan [11] used a capacitance sensor array that comprised a twin plane sensor using 12 electrodes for each plane with each electrode measuring 5 cm in length to identify flow patterns in a gas-liquid two phase flow and a three phase gas-liquid-solid flow in a bubble column. For the gas-liquid fluid, air was used as the gas phase while Norpar 15 (paraffin) and Paratherm heat transfer liquids were used as the liquid phase. Norpar 15 has a density of 773 kg/m³ and a viscosity of 0.253 mPa·s. Paratherm has a density and a viscosity of 870 kg/m³ and 0.317 mPa·s respectively. Polystyrene beads with density and diameter of 1020 kg/cm³ and 2 mm, respectively, were used as the solid phase in the gas-liquid-solid system. The three-phase system was essentially a dielectrically two-phase system, enabling the measurement of the gas holdup alone in the gas-liquid-solid system independent of the other two phases. This is because the polystyrene beads have permittivity similar to that of Paratherm. The data acquisition system captured data at 100 frames per second. Iterative Linear Back Projection (ILBP) algorithm was used for the image reconstruction of the multiphase flow at 32 x 32 pixels per image. The study showed that ECT could be suitably applied in imaging gas-liquid as well as gas-liquid-solid flow systems with the image reconstruction method developed by the authors. It was observed that the technique used had no limitations on the maximum gas holdup but it proved difficult to measure small gas holdup due to the small signal-to-noise ratio.

Jeanmeure *et al.* [12] developed a design that enabled the use of ECT to directly identify flow patterns in a two-phase gas-oil flow. The study involved the flow identification and control in an air-kerosene flow in horizontal piping by using 8-electrodes ECT system and T-junction separator. This was done for a reduced set of interest of flow patterns with distinctive characteristics (annular and stratified flow). The method produced relatively fast images at 200 images per second and was used to detect slug flow to enable actions that will prevent undesirable effects on unit operation equipment downstream. The density and viscosity of the oil used in the test were 973.05 kg/m³ and 0.026 Pa·s respectively. The flow pattern identification was performed using the visual inspection of the flow in transparent pipe section and quantifying the fluctuations of the void fraction and dynamic pressure from the capacitance reading and pressure readings respectively using Probability Density Function (PDF) and Power Spectral Density (PSD) function of the time trace signal. The study concluded that capacitance sensors were very sensitive to flow regime change and could be used to identify the different flow patterns. This study was, actually, on low viscous oil, and tomographic images were not reported there.

Similarly, gamma radiation methods, being non-intrusive methods, have been frequently used for the measurement of component volume fractions in multiphase flow systems. For most applications, it is the attenuation of radiation (gamma-ray) that serves as the source for the measurements. Gamma densitometry has numerous advantages in terms of its higher penetration capabilities over other radiation attenuation methods (i.e., neutron beams) thereby making it a more ideal system for the measurement of phase fractions in large industrial systems.

From the literature reviewed above, it is obvious that most existing studies were based on low viscous oil, hence, a basis for this study to consider high-viscous flows using ECT. The capability of ECT in high-viscous flows (up to $\mu=7500$ cP) was thus investigated under static (bench) and dynamic (flowing) conditions. Tomographic images of ECT and temporal variations of liquid holdup measurements through time series plots were used to identify flow patterns. Gamma densitometer (a device for measuring the density of fluids in a completed well, pipeline or process equipment, using a radioactive source of gamma rays and a detector), visual observations and video recordings were used to validate the measurements of the ECT.

2. Experimental setup

In this study, two experimental test facilities in the Process and Systems Engineering (PASE) Laboratory were used for the dynamic (flowing) test, and the bench test was also conducted. Actually, 1 and 3-inch multiphase facility are similar in design with both having capabilities to operate under varieties of multiphase flows consisting of gas, water, oil and sand. The 3-inch multiphase facility (Figure 1) that was used in this work is described below.

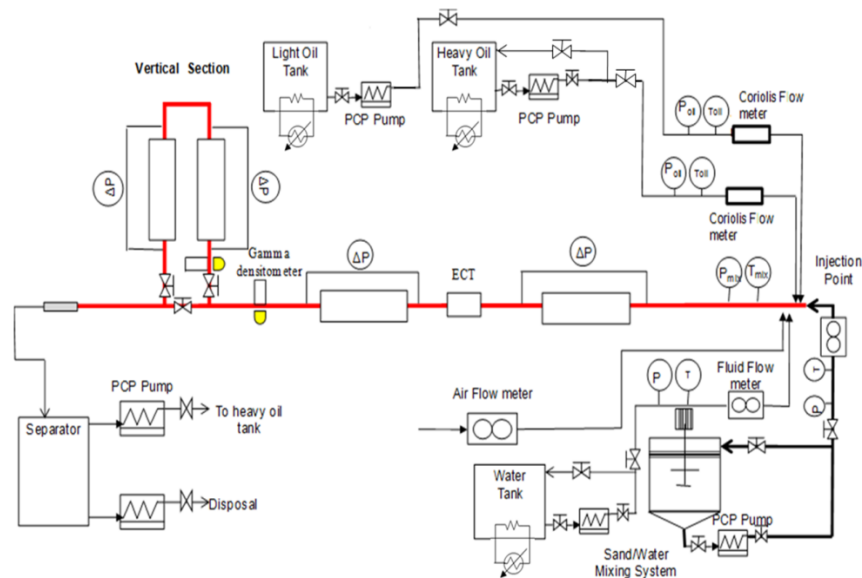


Figure 1. Schematics of the 3-inch multiphase facility at Cranfield University

The 3-inch multiphase facility is similar to the 1-inch facility. It is, actually, a scale up of the 1-inch facility. It is once through and consists of a 0.75 mm ID Perspex pipe with length of about 17 m. It has vertical and horizontal pipe sections, but for purposes of this study, emphasis will be laid on the horizontal section since this was the one used. The observation section of the facility was placed 150 pipe diameters upstream of the last injection point to ensure complete flow development in the horizontal section. Free air was received and compressed by an AtlasCopco® Screw Compressor with maximum discharge pressure and capacity of 10 barg and $400 \text{ m}^3 \cdot \text{hr}^{-1}$ respectively. Compressed air was discharged to a 2.5 m^3 air tank before it was delivered to the test section to avoid pulsating supply. At the tank, it was regulated to about 7 barg and fed to the test section where two gas flow meters, a 0.5-inch (Prowirl 72F15 DN15) vortex flow meter with range of $0\text{-}20 \text{ m}^3/\text{hr}$ and a 1.5-inch (Prowirl 72F40 DN40) vortex flow meter with range from $0\text{-}130 \text{ m}^3/\text{hr}$, both manufactured by Endress+Hauser, were used for air metering. Air was fed to the test section through a 2-inch steel pipe in-line with the horizontal test section.

A tank of capacity of 2 m^3 was used to store heavy-oil from where it was pumped using a variable speed progressive cavity pump with maximum capacity of $17 \text{ m}^3/\text{hr}$. Endress+Hauser's Promass 831 DN 80, coriolis flowmeter with range of $0\text{-}171 \text{ m}^3/\text{hr}$, was used in oil metering. The flow meter had three outputs: mass flow rate, density and viscosity.

A refrigerated bath circulator manufactured by Thermal Fisher was used for temperature control. Coils which were connected to the circulator were submerged in the oil tank, and hot or cold glycol was passed through the coils to regulate the oil temperature and, hence, its viscosity. The circulator temperature ranged from 0 to 50°C with an accuracy of $\pm 0.01^\circ\text{C}$. Data were acquired from the facility as raw voltage (0 – 10 V) using the data acquisition system, NI USB-6210, and they were converted to engineering units using Labview® version 8.6.1. The 3-inch ECT sensor was installed just after the viewing sections, which was about 155 pipe diameters downstream of the feeding point for oil and gas. The slurry and water systems are not described even though they are shown in the test facility schematics because they were not used in this study.

CYL 680, a mineral oil manufactured by Total® with density of 920 kg m^{-3} and viscosity of 3000 cP at 20 °C was used as the liquid phase (heavy-oil) in the dynamic test. CYL 680 and EDM 250, which is a dielectric oil type manufactured by Rustlick™ with viscosity 4 cP at 20 °C and density of 801 kg m^{-3} , were used in the bench test. For both tests, the gas used was atmospheric air, and it was compressed in the case of the dynamic test.

The ECT device used in this study was manufactured by Industrial Tomography Systems (ITS) in Manchester, United Kingdom. The system is made up of a sensing unit, data acquisition and a computing system. The sensing unit consists of a flexible copper laminate engraved with a predetermined electrode pattern and placed around steel pipe circumference with internal diameters of 1 and 3 inch respectively. Computer system and data acquisition software makes up the computing system. The software, Multi Modal Tomography Console (MMTC) has a VC++ Graphical User Interface (GUI), which was used to view the process of interest online and for tomography data management. Collated data could be viewed offline using another ITS proprietary software, Toolsuite V7. The Linear Back Projection (LBP) algorithm was used for image reconstruction in both software.

Furthermore, a gamma densitometer was used for phase fraction measurement. A fixed single-beam gamma densitometer manufactured by Neftemer Limited made up of a gamma source block and a Sodium Iodide (NaI) scintillation radiation detector was installed on the 3-inch facility. A 5.5 GBq Caesium-137 radioisotope was contained in the gamma radiation source block enclosed within a lead radiation protection shield protected by stainless steel. The radioisotope in the gamma densitometer was a dual-energy source emitting gamma rays in two broad photon energy levels. The 662-keV high-energy level was sourced from the gamma radiation transmission while the lower energy level range of 100 keV–300 keV was sourced from the scattered gamma radiation. Sodium iodide (NaI) scintillation radiation detector was used for the measurement of two separate sets of gamma attenuation data for the high and low energy levels with a sampling rate of 250 Hz. A detailed description of the gamma densitometer (see pictorial view in Figure 2) used for this investigation has been presented by [13].

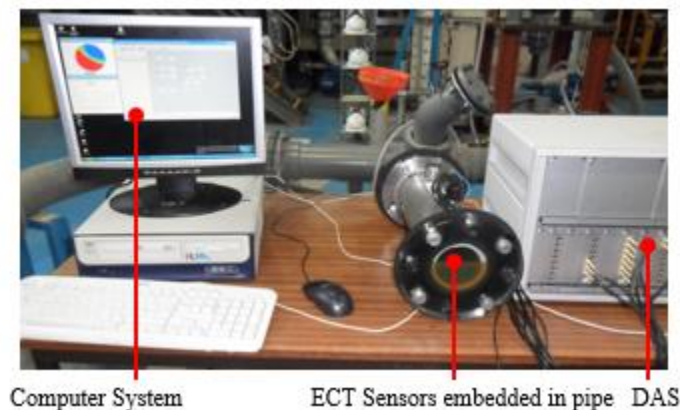


Figure 2. ECT static (bench) test experimental setup

In this study, the static (bench) and dynamic (flowing) test were conducted in the 1 and 3-inch facility using two ECT sensors of the same (test facility) size. In the static test, dielectric oil (4 cP at 25°C) and CYL 680 oil (3,000 cP at 25°C) were used with air as the gas phase. Liquid holdup measurements, tomographic images and raw capacitance signals were obtained from ECT for both sensors. The sensors were first calibrated by taking the capacitance readings for completely empty ECT sensor (full air) and recorded as the low reference since it is the low permittivity medium; the sensor was then filled with oil and recorded again to obtain the high reference since it was the high permittivity medium. The calibrated results were used as references for both the static and dynamic test. In the static test, emphasis was laid on the ability of the ECT to predict the liquid holdup measurement, visualize tomographic images and the raw capacitance measurement. In the ECT system, tomographic images were obtained essentially from the reconstruction of the raw capacitance data obtained by the sensors during sensing to pixel permittivity using some form of algorithm (in this case, the Linear Back Projection, LBP). In LBP, reconstruction was done in the Multi Modal Tomography Console (MMTC) software. A grey level was assigned to each of the 66 sensing areas. By superimposing the grey levels on the areas, the region where the object to be visualized was located became enhanced. 66 element vector with each value set as 1 for object presence and 0 for none presence was used to relate the 66 sensing areas. By multiplying the corresponding segment vector, V , with the 66-capacitance measurement values (m_1, m_2, \dots, m_n), the grey level, G was obtained. For a K number of segments, Equation (1) [14] was thus obtained.

$$\begin{pmatrix} G_1 \\ G_2 \\ \vdots \\ G_{K-1} \\ G_K \end{pmatrix} = \begin{pmatrix} V_1 \\ V_2 \\ \vdots \\ V_{K-1} \\ V_K \end{pmatrix} \begin{pmatrix} m_1 \\ m_2 \\ \vdots \\ m_{K-1} \\ m_K \end{pmatrix} \quad (1)$$

The equation thereby reduced to a matrix multiplication problem.

2.1. ECT referencing

Representative tomographic images results obtained in the 3-inch sensor for the air-oil system in both the heavy-oil and air are shown in Figure 3. The images show the first tomogram which is completely blue in colour indicating a completely empty sensor (100% air), that is, 0% liquid holdup to a completely filled sensor as shown in the last tomogram, and a total red colour indicating 100% liquid holdup (completely filled with oil). The two tomograms mentioned were subsequently used as the references.

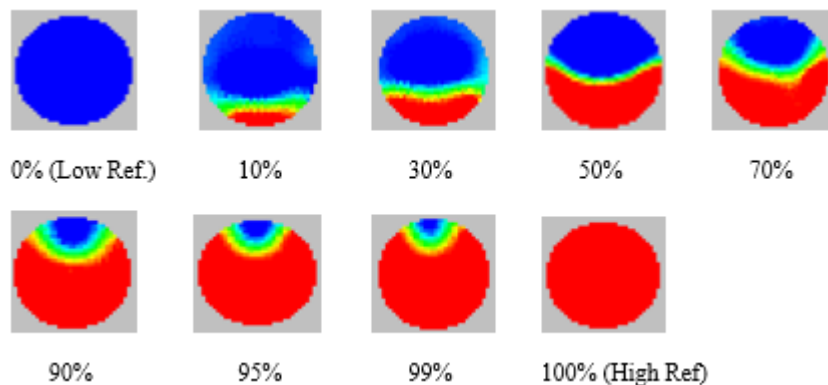


Figure 3. Tomographic images of different liquid holdup (%) for dielectric oil (viscosity: 3000 cP; ECT sensor: 3 Inch)

The tomographic images clearly indicated an increase in the red section (oil content) as the sensor was filled with oil during the bench test. The interface between the oil and air in the tomograms were indicated by a yellowish green colour; this region is normally considered as aerated oil. The tomographic images showed no noticeable effect of viscosity and pipe diameter difference on the ECT sensor. The test was conducted for both 4 cP (dielectric) and 3000 cP (CYL 680) oil with air as the gas phase using both the 1 and 3-inch sensors, and similar results were observed for all four cases studied.

It is worth noting that even though ECT displayed the tomographic images as a “representative” of the holdup value, the actual liquid holdup was obtained using the Maxwell’s expression (ITS, 2000) given in Equation (2).

$$\alpha = \frac{2\sigma + \sigma_2 - 2\sigma_{mp} - \frac{\sigma_{mp}\sigma_2}{\sigma_1}}{\sigma_{mp} - \frac{\sigma_2}{\sigma_1}\sigma_{mp} + 2(\sigma_1 - \sigma_2)} \quad (2)$$

In the equation above, α is the volume fraction of the dispersed material, σ_1 , σ_2 and σ_{mp} are the permittivity of the continuous phase, that of the dispersed phase and the reconstructed measured permittivity respectively.

3. Results and discussion

Results obtained from experimental investigations carried out in this study are presented in this section. Liquid holdup plots obtained in the study are shown in Figure 4 and 5. The solid line indicates an ideal case in which the measured and actual liquid holdup values are equal while the dotted line indicates the error margin from the ideal case. Liquid holdup measurement for 1 and 3-inch sensor at 3000 cP oil viscosity are shown in Figure 4. For both sensors, similar results were obtained and the effect of increase in size from a 1 to 3-inch sensor was not significant. About $\pm 10\%$ error margin was observed for both sensors thus showing no significant effect of increase in pipe diameter on ECT performance. ECT performance was also evaluated for the 4 cP oil under static condition; the results obtained were compared with the liquid holdup measurements for 3000 cP oil and they showed no significant effect as a result of the change in viscosity. The curved interface in the tomograms are related to the LBP algorithm used in image reconstruction.

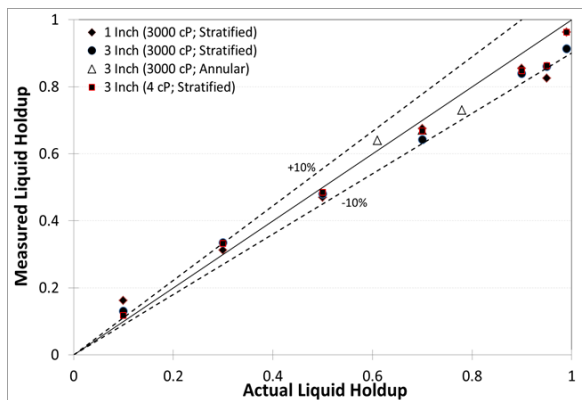


Figure 4. Liquid holdup comparison for 1 and 3-inch sensor ($\mu = 3000$ cP) oil

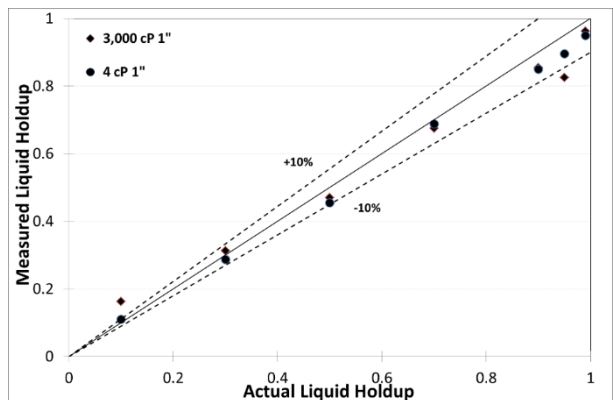


Figure 5. Viscosity comparison for 1-inch sensor

From Figures 4 and 5, it was observed that ECT could be used to predict the liquid holdup for actual liquid holdup values from 50% and above while overestimating liquid holdup values below 50%. In this case, the error margin was relatively lower at the lower liquid holdup values. This trend was observed for both 1 and 3-inch sensors as well as the two viscosities tested. Error margins at the liquid holdup values close to the high reference (full pipe) was seen to improve relatively to that in the mid liquid holdup values. This phenomenon is attributed to the LBP algorithm used in the image reconstruction and the fact that the sensor was

calibrated at the two terminals, the low and high reference; hence, relatively similar trends were noticed in literature for other sensing instrument such as gamma [15].

3.1. Flow pattern identification with ECT

Annular flow pattern was modelled on the bench (static) by inserting polyvinyl chloride (PVC) pipes of cylindrical shape with varying outer diameter (36 – 48 mm) into the oil filled sensor in the vertical position. The low reference used here was the PVC pipe inserted into the empty sensor while the high reference was oil. Figure 6 shows that for annular flow, the error margin ($\pm 5\%$) is well within that of the stratified static test, possible reasons for error difference were the sensor positioning and pipe material used.

Air-oil dynamic tests were conducted in the 1 and 3-inch multiphase facilities for viscosities of 1000, 3000 and 6000 cP. ECT was used to identify flow patterns and validated by visual observations in the sections that follow. Superficial gas and liquid velocities used in the study were 0.3 – 9 m/s and 0.06 – 0.1 m/s, respectively.

Some representative stacked tomographic images (time series of tomographic images taken from frames in consecutive sequence) for the 3-inch rig at 1000 cP, with V_{sg} values ranging from 0.3 – 9.0 m/s and a V_{so} value of 0.1 m/s are shown in Table 1. The images obtained provided information on the phase distribution in the pipeline during each flow condition. For V_{so} value of 0.1 and V_{sg} value of 0.3 – 0.5 m/s at 1000 cP, plug flow regime was observed. This flow pattern consisted of two characteristic tomographic images: one in which the tomogram showed a stratified layer of red at the bottom (indicating oil) with blue (gas) at the top section of the pipe. At certain intervals, this image almost changed completely to red (oil), and this period indicated the passage of the entire oil with negligible amount of gas, hence the plug body. In the stack images shown in Table 1, it is seen that oil (red colour) completely bridged to the top as the plug body was passing. This flow pattern was classified as plug flow based on the definition of [16], which states that plug flow is a limited case of slug but with the liquid plug being free of entrained gas bubbles. The yellowish-green and red colours observed at the pipe wall (in the stacked images) can be explained by the oil film coating on the walls of the pipe housing the sensor as a result of the high-viscous property of the oil.



Figure 6. Film and plug unit at $V_{so}=0.1$ m/s and $V_{sg}=0.3$ m/s, $\mu_l = 1000$ cP

A plot of the concentration (liquid holdup) time series was also analysed for flow patterns observed in the conditions stated above, and the plot showed intermittent behaviour, fluctuating from a low concentration of about 0.65 to as high as 1 in some cases. Plug/slug body were defined as such when the liquid holdup rose above 0.75 m/s. The low concentration value indicated the film region. Here, the combine flow of air and oil ensured that the liquid holdup value was relatively lower while the high concentration value indicated the passage of the plug body where very little air was contained in the flow and the liquid almost completely occupied the pipeline. The Probability Mass Function plot further confirmed the flow pattern obtained at the aforementioned flow conditions, which clearly showed a bi-modal distribution. ECT measurement was validated by a video recording, which was showing the plug flow pattern observed through physical inspection and recordings. Flow patterns observed at V_{so} value of 0.1 m/s and V_{sg} value of 0.3 -0.5 m/s at 1000 cP was found to be, actually, plug flow. It had two characteristic units that flowed intermittently. A film unit in which the less dense gas flowed on top of the denser liquid in a stratified pattern. This unit was disrupted at

certain intervals by long plug bodies flowing through. The plug was observed to cover the entire viewing section with no visible gas entrainment as shown in Table 1.

For V_{so} value of 0.1 and V_{sg} value of 0.7 – 2.0 m/s at 1000 cP, slug flow regime was observed. The tomographic images obtained were similar to those in plug flows differing only in the appearance of blue colour during intervals where the tomograms changed from stratified blue (at the top) and red (at the bottom) to a wholly red colour with little quantity of blue as presented in Figure 7.

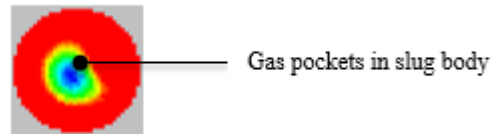


Figure 7. Tomogram showing gas entrained in liquid slug unit at $V_{so}=0.1$ m/s and $V_{sg}=1.0$ m/s with oil viscosity of 1000 cP

In the tomographic stack images in which the complete red image earlier seen in plug flow was not present, a dominant red colour was observed but with visible blue albeit small in size. This was attributed to the presence of entrained gas bubbles as the slug body passes. The slug body was shorter and more frequent as indicated in the stacked images at these flow conditions. The concentration time series plots and PMFs, however, did not show any significant difference between slug and plug flows. Based on the definition of Barnea *et al.* [16] this flow pattern was called slug flow. Video recordings showed a similar behaviour with plug flow differing in the slug body being shorter, more frequent and more energetic relative to the plug body. Gas bubbles were also observed in the slug unit as well as increased instability of the film region. The film region instability, change in slug length and increase in flow intensity were due to the increased kinetic energy of flow as a result of the increase in gas superficial velocity.

At V_{sg} values of 3 m/s in the 1000 cP test, flow regime observed in the stack images was a transition between the slug and wavy annular flow. The oil was seen to have insufficient energy to bridge the gas core thus forming a kind of wavy pattern around the gas as shown in Figure 8. This classification was chiefly subjective, but the PMF plot laid further credence to this as the hitherto, bimodal distribution in plug and slug flows merges partially with each other. This regime was defined as blow-through-slug or pseudo-slug based on the definition of Wong and Yau [17]. In the video recordings, a further increase in V_{sg} caused the gas kinetic energy to acquire even more momentum resulting in slugs requiring relatively larger energy to bridge the liquid film. It is similar to the wavy annular flow differing only in the fact that the gas velocity is not high enough to sweep the liquid to the top of the pipe.

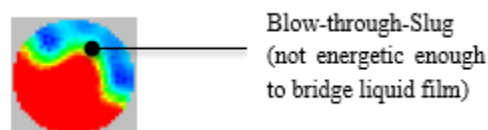


Figure 8. Tomogram showing Pseudo-Slug body at $V_{so}=0.1$ m/s and $V_{sg}=3.0$ m/s for oil viscosity of 1000 cP

Finally, at V_{sg} value of 7 – 9 m/s with oil viscosity of 1000 cP and 5 – 9 m/s, the stack tomographic images showed a wavy flow structure between the gas-oil interface, and the tomograms were similar to the pseudo-slug flow patterns but with relatively low penetration height into the gas zone. The concentration time series also showed a high fluctuation in behaviour with the PMF showing unimodal distribution. In the video recordings, the increased V_{sg} value caused increase in dissipated energy along the flow resulting in large amplitude of waves at the oil-gas interface. The top of the pipe wall was significantly wetted by oil with gas continually sweeping liquid at the interface to the top of the pipe. Most of the oil in flow, however, remained at the bottom of the pipe (due to gravity) with gas predominantly flowing at the centre and thin oil film at the top. The PMF, liquid holdup plot and the tomographic

images obtained from ECT showed promising results in the capability of ECT to visualize high-viscous oil and gas flows as validated by the video recordings obtained during the study.

Flow pattern maps from the study are shown in Figure 9 and 10. From the figures, an increase in viscosity was seen to result in a corresponding increase in the slug/plug flow pattern region. This was found to agree with the conclusion drawn by Márquez and Trujillo [4] and Gokcal *et al.* [4]. Also, an increase in the oil velocity had similar effects on the flow pattern within the range of superficial oil and gas velocities tested.

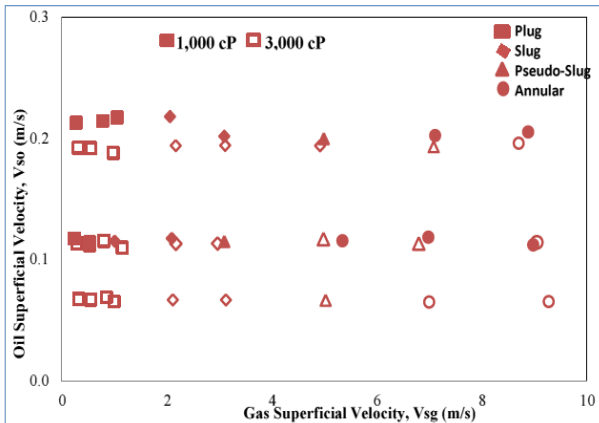


Figure 9. Flow pattern map for 1-inch multiphase facility

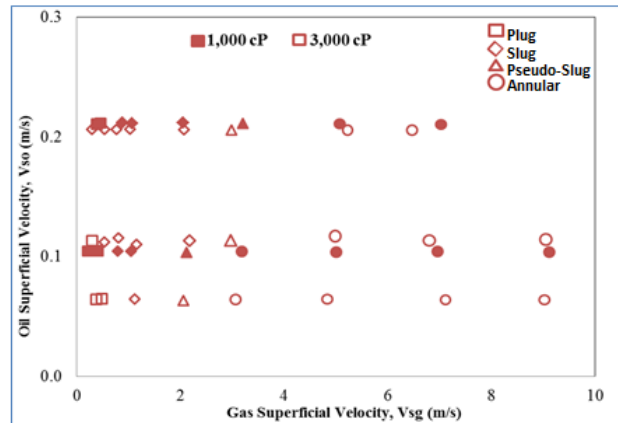


Figure 10. Flow pattern map for 3-inch multiphase facility

3.2. Validation of flow patterns obtained by ECT with gamma densitometer

A representative time series and PDF plots of the time varying liquid holdup measurement of ECT and Gamma densitometer measurements are presented in Table 2. Both data obtained from the 3-in pipe ID horizontal test facility are shown for 20 s each to facilitate a clear representation of the results.

At gas superficial velocity of 0.3 m/s, the ECT time series plots showed fluctuations in waveforms. This was an indication of the plug flow pattern in this flow condition. The crests of the waveforms indicated elongated liquid body passage, and each crest was observed to be a result of the sudden increase in the liquid holdup as the liquid bridged the entire pipe cross section. The troughs, which were indications of the film region passage, were characterized by relatively low liquid holdup values, which were explained by the increased void fraction as the liquid bridge hitherto prevalent in the elongated liquid body exited the observation section. Similar waveform characteristics were observed in the Gamma waveform signals shown in Table 2. PDF plots for this flow condition showed a bimodal distribution having two characteristic peaks with one at the higher holdup value indicating the slug liquid body while the other was representing the slug film.

At Vsg of 3.0 m/s, the flow pattern entered its transition region (pseudo-slug), and it was observed that both the ECT and gamma time series plots indicated less frequent crests, which was a result of the reduced intermittency in the flow. PDF plots from both ECT and Gamma indicated different modal distributions. This is as a result of the increased transient nature of the transition flow pattern and/or limitations of the single beam Gamma device used in this case, which was impeding its ability to capture clearly the features of the transition region.

For Vsg values of 9 m/s, both Gamma and ECT time series analysis shows a chaotic behaviour in the time series waveforms with no distinguishable crest or trough. The PDF, at this flow condition, showed a unimodal distribution which clearly suggested the non-intermittency of the flow pattern.

It can therefore be inferred that within the experimental test matrix and test conditions of this study, flow patterns identified by ECT were similar to those identified by Gamma densitometer.

Table 1. ECT results for oil viscosity 1000 cP oil superficial velocity 0.1 m/s with different gas superficial velocities (3-inch ECT sensor)

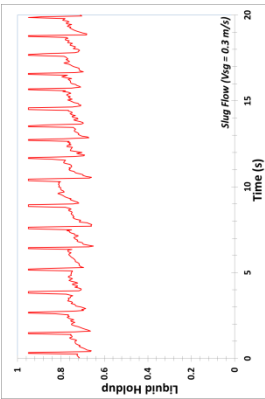
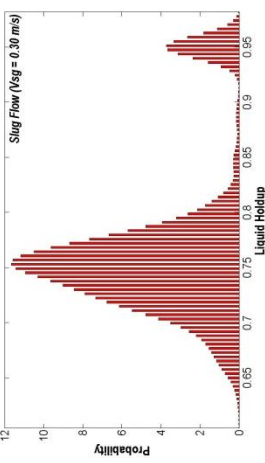
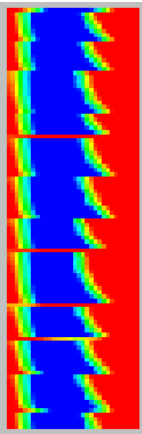
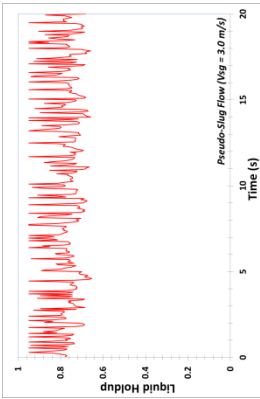
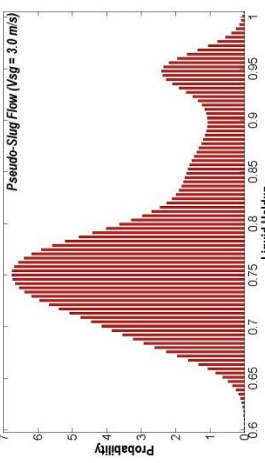
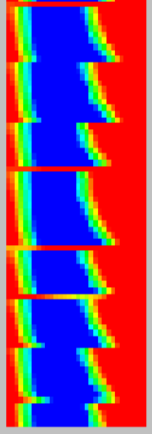
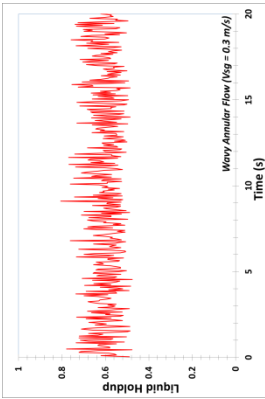
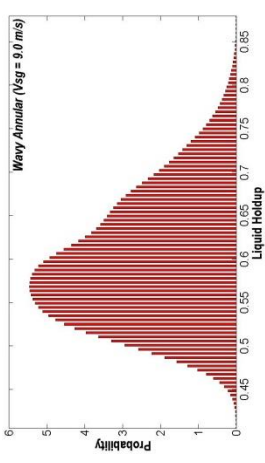
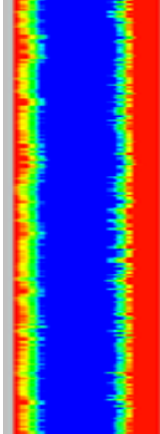
V _{sg}	ECT Time Series Plots	ECT PDF Plots	Stacked Images	Stacked Images
0.3 m/s	 <p>Slug Flow (V_{sg} = 0.3 m/s)</p>	 <p>Slug Flow (V_{sg} = 0.30 m/s)</p>	 <p>Plug Flow</p>	 <p>Plug Body Film Region</p>
3.0 m/s	 <p>Pseudo-Slug Flow (V_{sg} = 3.0 m/s)</p>	 <p>Pseudo-Slug Flow (V_{sg} = 3.0 m/s)</p>	 <p>Pseudo-Slug</p>	 <p>Pseudo-Slug Flow</p>
9.0 m/s	 <p>Wavy Annular Flow (V_{sg} = 9.0 m/s)</p>	 <p>Wavy Annular (V_{sg} = 9.0 m/s)</p>	 <p>Wavy Annular Flow</p>	 <p>Wavy Annular Flow</p>

Table 2. ECT results and Gamma Densitometer validation for oil viscosity 1000 cP oil superficial velocity 0.1 m/s with different gas superficial velocities (3-inch ECT sensor)

Vsg	ECT Time Series Plots	Gamma Time Series Plots	ECT PDF Plots	Gamma PDF Plots
0.3 m/s				
3.0 m/s				
9.0 m/s				

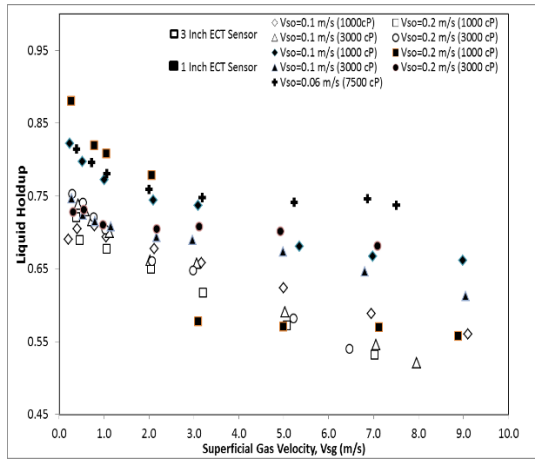


Figure 11. Plot of liquid holdup against Vsg at different Vso for 1- and 3-inch ECT sensor

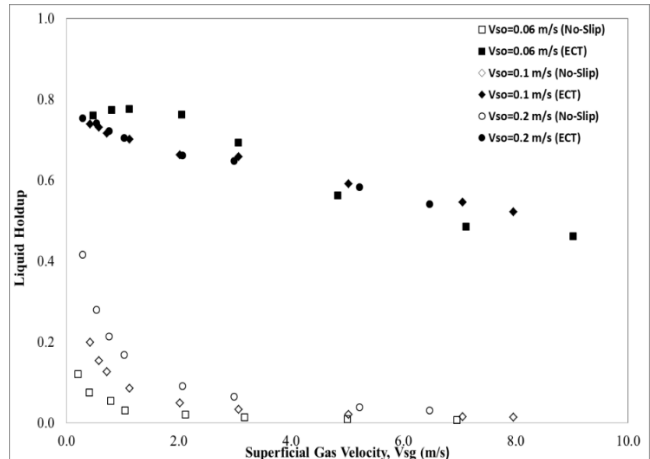


Figure 12. Plot of liquid holdup predicted by "No-Slip" equation and ECT sensor against Vsg (m/s) for the 3-inch test facility at oil viscosity of 3000 cP

Figure shows time averaged liquid holdup measurement obtained for 60 s from ECT in both the 1- and 3-inch test facility for viscosities ranging from 1000 – 7500 cP. The data plot showed a general trend of reduction in liquid holdup value as the gas superficial velocity was increasing. This was expected to be so in order to satisfy the continuity equation. As the gas superficial velocity was increased, the gas was observed to occupy more cross sectional area in the pipe resulting in a corresponding reduction of the liquid holdup in the cross sectional area of the pipe. An increase in the viscosity of the oil resulted in an increase in the liquid holdup at fixed Vsg and Vso. This was due to the fact that an increase in viscosity resulted in an increase in the shear stress (resistance to flow) of the oil. A reduction in the amount of entrained gas in the slug body (for slug flows) was also observed visually as well as from the time series trace in ECT. The gas kinetic energy hitherto sufficient to displace a particular amount of oil then became insufficient, thereby resulting in more liquid remaining in flow and thus increased liquid holdup. A comparison of the liquid holdup obtained from ECT to that of the "no slip" liquid holdup as shown in Figure was found to show a similar trend. However, the liquid holdup values were significantly different; this was due to the "no slip" assumptions in addition to the increased liquid viscosity tested.

4. Conclusion

ECT provided good tomographic images and liquid holdup measurements under static (bench) conditions. The results obtained showed that the measurement of ECT was accurate to within $\pm 10\%$ of the actual liquid holdup under stratified static conditions. Under dynamic (flowing) conditions, ECT was able to provide good tomographic images for the distribution of the phases in flows - plug, slug, pseudo-slug (blow-through-slug) and annular flows - that were observed. PMF plots of the liquid holdup data and the time series were used to further identify the different regimes. Flow patterns obtained were validated with the aid of video recordings and gamma ray densitometer. Liquid viscosity and pipe diameter had no significant effect under static conditions on ECT performance. However, for dynamic tests, increase in liquid viscosity led to a corresponding increase in the oil film coatings on the sensor walls. Shorter slugs and increased slug frequency with increase in liquid viscosity was clearly visualized by ECT. This was found to be in agreement with the studies performed by Márquez and Trujillo [5] and Gokcal et al. [4] for high viscous oil-gas flows.

Acknowledgement

The authors acknowledge the contribution of the Laboratory Manager, Technicians, Research Staff Members and Students in the Oil and Gas Engineering Centre of Cranfield University for their help and support rendered in the course of this research work.

References

- [1] Yang W and Peng L. Image Reconstruction Algorithms for Electrical Capacitance Tomography. *Meas. Sci. Technol.*, 1996; 14(1):
- [2] Dyakowski T. Process tomography applied to multi-phase flow measurement. *Meas. Sci. Technol.*, 1996; 7. 343–353.
- [3] Beck MS, Byars M, Dyakowski T, Waterfall R, He R, Wang SJ, Yang WQ. Principles & Industrial Applications of Electrical Capacitance Tomography. *Meas. Control*, 1997; 30(7): 197–200.
- [4] Gokcal B, Al-Sarkhi A, Sarica C, and Alsafran EM. Prediction of Slug Frequency for High Viscosity Oils in Horizontal Pipes,” in SPE Annual Technical Conference and Exhibition, 2009.
- [5] Márquez J and Trujillo J. Overview: Slug-Flow Characterization for Heavy-Oil Fields. in *Proceeding of SPE Latin American and Caribbean Petroleum Engineering Conference*, 2010, no. December, pp. 1–3.
- [6] Gamio J, Castro J, Rivera L, Alamilla J, Garcia-Nocetti F, and Aguilar L. Visualization of Gas-Oil Two-Phase Flows in Pressurized Pipes Using Electrical Capacitance Tomography. *Flow Meas. Instrum.*, 2005; 16: 129–131.
- [7] Zhang L and Wang H. Identification of oil-gas two-phase flow pattern based on SVM and electrical capacitance tomography technique. *Flow Meas. Instrum.*, 2010; 21(1): 20–24.
- [8] Baker G, Azzopardi B, and Clark W. Transients in stratified/slug flow – observations using electrical capacitance tomography. in *International Conference on Multiphase Technology*, 2003.
- [9] Taitel Y and Dukler AE. A model for predicting flow regime transitions in horizontal and near horizontal gas-liquid flow. *AIChE J.*, 1976; 22(1): 47–55.
- [10] Isaksent O, Dicot A, and Hammer EA. A Capacitance-Based Tomography System for Interface Measurement in Separation Vessels. *Meas. Sci. Tech*, 1994; 5: 1262–1271.
- [11] Warsito W and Fan L. Flow Structures in Gas-Liquid & Gas-Liquid-Solid Flow Systems Using Electrical Capacitance Tomography. *Chem. Eng. Sci.*, 2001; 56: 5871-5891.
- [12] Jeanmeure L, Dyakowski T, William B, and Zimmerman W. Direct Flow-Pattern Identification Using Electrical Capacitance Tomography. *Exp. Therm. Fluid Sci.*, 2002; 26: 763–777.
- [13] Archibong A, Zhao Y, and Yeung H. Comparison of electrical capacitance tomography & gamma densitometer measurement in viscous oil-gas flows. *AIP Conf. Proc.*, 2014; 1592(1).
- [14] Plaskowski A, Beck MS, Thorn R, and Dyakowski T. *Imaging industrial flows: Application of electrical process tomography*. Bristol and Philadelphia: Institute of Physics Publishing, 1995.
- [15] Åbro E and Johansen G. Improved void fraction determination by means of multibeam gamma-ray attenuation measurements *Flow Meas. Instrum.*, 1999; 10(2): 99–108.
- [16] Barnea D, Shoham O, Taitel Y and Dukler AE. Flow pattern transition for gas-liquid flow in horizontal and inclined pipes. Comparison of experimental data with theory. *Int. J. Multiph. Flow*, 1980; 6(1976): 217–225.
- [17] Wong T and Yau Y. Flow Patterns in Two-Phase Air-Water Flow. *Int. Commun. Heat Mass Transf.*, 1997; 24(1): 111–118.

To whom correspondence should be addressed: Yahaya D. Baba, Department of Chemical and Petroleum Engineering, Afe Babalola University, Ado-Ekiti, Nigeria, y.baba9550@gmail.com

DEMULSIFICATION OF WATER IN OIL EMULSION BY USING FATTY ALCOHOL AS DEMULSIFIER COMBINED WITH THERMAL METHOD

Marwa F. Abdul Jabbar and Rawan F. Abdulfatah

Chemical Engineering Department, College of Engineering, Al-Nahrain University, Baghdad, Iraq

Received October 5, 2017; Accepted January 8, 2018

Abstract

Emulsified water is generally present in crude oil as a result of the mixing occurring during production operation. The formation of emulsions conducts problems in production as well as in transportation. Therefore, they need to demulsify through demulsification process. In the present work, the chemical demulsification combined with thermal heating is used to treat Iraqi crude oil (Basrah oil) for separating the water from water in oil emulsions.

Many variables were studied to indicate their influence on water separation. They have been included chemical demulsifier concentration were (3- 8%), temperature (50 – 70°C), the water content of the emulsion (10 – 30%) and salt concentration (1-3%). All experiments were carried out on an emulsion prepared by mixing speed of (500 rpm) for (15 min). Also, viscosity and density were measured for samples before and after demulsification.

From the experimental results, there were noticed that the percentage water separation increased with increasing demulsifier concentration, temperature, water content and salt concentration. The best separation efficiency reached 66.7 % of initial water content present in the oil. Also, it was being seen the viscosity and density of emulsion decreased after treating by demulsification process.

Keywords: demulsification; demulsifies; crude oil; water in oil emulsion.

1. Introduction

Water naturally is existed in the crude oil and attributed as an oil field emulsion. This emulsion can happen at different stages include during drilling, producing, transporting and processing of crude oil [1].

An emulsion resulted when combined two immiscible liquids together. There are two main kinds of emulsion namely oil-in-water (o/w) and water-in-oil (w/o). While, in some cases, complex emulsions like oil-in-water-in-oil (o/w/o) and water-in-oil-water (w/o/w) emulsions can be existing. There are three major criteria that represent substantial role during the emulsification process [2]. First, the formation of an emulsion entails the availability of two immiscible liquids. Secondly, the emulsion is formed by stratifying mechanical energy to generate droplets. This is the most significant step in emulsification process. The third criterion is the existence of an agent handling fractional solubility in both phases which known as emulsifier [3].

Normal substances such as; resins, asphaltenes, carboxylic acids, and solids such as; waxes and clay stabilize these emulsions. The emulsions have stability, extending from slight minutes to a few years, relying on the type of the crude oil and the quantity of water [4].

The problems of formation water with crude oil including: the corrosion of pipe work, pumps, production equipment and downstream overhead distillation columns, cost for pumping or transferring water through pipeline or tankers, the poisoning of downstream refinery catalysts and the problems related to increasing viscosity of oil as a result of tiny dispersed water within crude oil. Therefore, there are a number of commercial and operating purposes of removing the emulsified water from the crude oil [5]. For economic and working purposes, it must separate total water from the crude oil emulsion before refining and transport. So as

to apart the water content of the produced crude oils, the emulsions have to be broken through demulsification method [6].

Demulsification is known as a process of breaking emulsions with the purpose to remove water from oil [7]. The methods that are ready for demulsification can be categorized as electrical, microwave, thermal and chemical demulsification. The most wide methods used for treating emulsions include using chemical additives combined with heat to conform separation processes of the emulsion. These chemical additives are commonly known as demulsifiers [5]. These demulsifiers are surface-active agents and achieve a high surface area at the crude water-oil interfaces. This makes in the variation of firm films of normal crude oil substances by a film that is helpful to water droplets to coalescence [8-9]. Demulsification of crude oil emulsions can happen by the destruction the central emulsion layer using consecutive additions of a demulsifying agent to the layer while heating and mixing with sequent settling [10].

The aim of the present work is to evaluate 2-ethylhexanol fatty alcohol (waste alcohol from butanol production) as demulsifier for breaking Iraqi crude oil emulsion. Demulsifier concentration, the water content of emulsion and salt concentration were studied. Also, the effect of temperature on demulsification performance and properties after demulsification were investigated.

2. Experimental work

2.1. Materials

In this study Basrah crude oil in Iraq was supplied by Al-Daura refinery with density and viscosity of being 0.911 g/cm^3 and 76.8 cP respectively while the API was 24. Fatty alcohol (2-Ethylhexanol) used as demulsifier and supplied from India. Fresh water used throughout the experiments and sodium chloride used to adjust the salinity of aqueous phase before added to the crude oil.

3. Method

3.1. Emulsion preparation

Water-in-oil emulsions were prepared by mixing crude oil and brine solution to obtain 30% (v/v) water content. In 500 mL beaker, the crude-oil was stirred at 25°C using mechanical stirrer at a rate of 500 rpm for 15 minutes to get a stable emulsion. This speed approach to that used by Al-Sabagh [11]. Emulsions were leaving two weeks to make sure that no separation took place, before the treatment.

3.2. Demulsification process



Fig. 1. Crude oil after separation process

The bottle test was used to evaluate the efficiency of the demulsifier to separate water-in-oil emulsions. The demulsifier was added to (200 mL) water-in-crude oil emulsion at a concentration (8%). The mixture was stirred for 3 minutes and placed in a (250 mL) graduated cylinder. Then, the cylinder was placed in a thermostatic water bath at 70°C . Water separation (in mL) was noticed periodically to record the amount of settled water as shown in Fig. 1. The water separation percentage has been calculated as illustrated in Eq.1 [12].

$$\text{Water separation\%} = \frac{\text{volume of water separated}}{\text{original volume of water}} * 100 \quad (1)$$

The emulsion was poured into separation funnel as shown in Fig. 2 to withdraw water to measure the density and viscosity of the remaining solution to compare with that of original emulsion and with crude oil. Viscosity was measured using Fungilab viscometer as shown in Fig. 3 while density measured by using pycnometer. The process is repeated for different water content, salt concentration, demulsifier concentration and temperature.



Fig. 2. Separation funnel for separate water and crude oil



Fig. 3. Viscometer Fungilab

4. Results and discussion

4.1. Effect of the demulsifier concentration

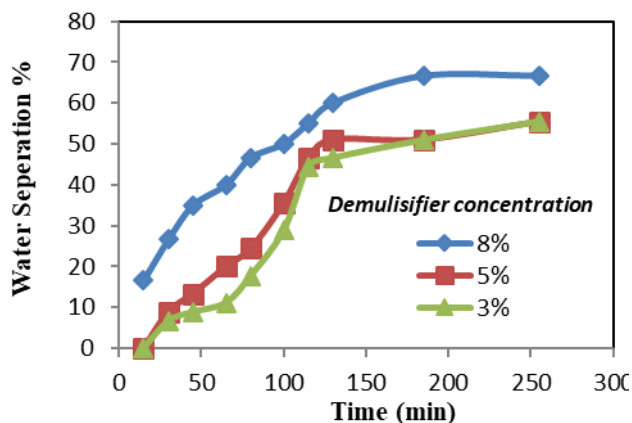


Fig. 4 Effect of the demulsifier concentration at constant temperature 70°C, water content 30% and salt content 3%

One of the most remarkable parameters prevailing the adsorption of demulsifiers at the interface is the demulsifier concentration that is shown in Fig. 4 at constant water content 30%, salt content 3%, and temperature 70°C. From this figure, it can be seen the separation efficiency, increased from 55% to 67% after 4h treatment as breaking agent increased from 3% to 8%. The increase of the demulsifier concentration led to an increase in the adsorption of the demulsifier molecules on the W/O interface, which displace the natural emulsifiers (asphaltene). This reduced the mechanical fixedness of the interfacial film, and

this fixedness keeps to decrease until being thinner, and then breakdown completely with more adsorption of the demulsifier agent on the interface [13].

4.2. Effect of the water content

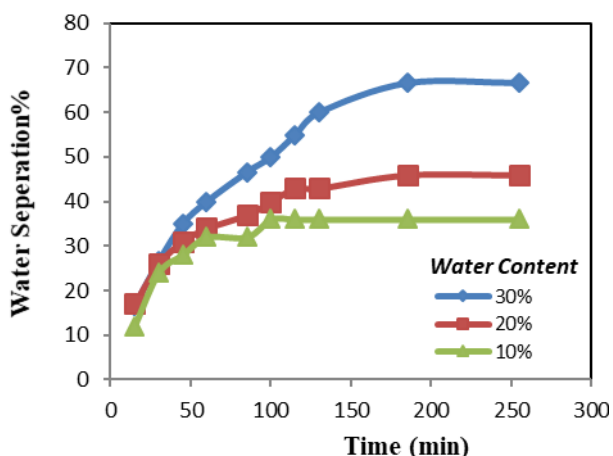


Fig. 5. Effect of water content at constant demulsifier concentration 8%, temperature 70°C and salt content 3%

The effect of the initial water content of emulsion on demulsification efficiency illustrated in Fig. 5. It can be observed the separated water increase from 36% to 67% as water content increasing from (10%-30%). This because the hardness of water/oil films reduced with increasing water content in the bulk till the interior pressure be greater than the exterior pressure at that moment, fast rupture of the water/oil interface happened, and the coherence of water droplets increased. The higher water content, the fewer interval between a drop and a drop becomes small, leading to the rapid combination [14].

4.3. Effect of salt content

In the petroleum industry, there is a wide difference in the salt content of the crude oils depending on most on the origin and may be, on the production wells or area within a field. The quantity of inorganic salts differs with the geologic formation.

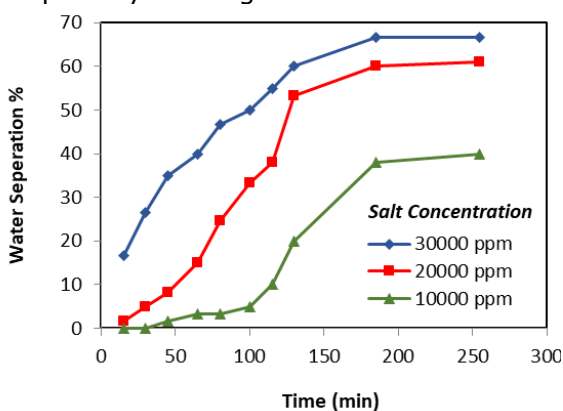


Fig. 6. Effect of salt content at constant demulsifier concentration 8%, temperature 70°C and water content 30%

It can be observed from Fig. 6 that water separation efficiency increases with increasing salt content. The addition of sodium chloride (inorganic salt) to the crude oil emulsion leads to an inverse action on emulsion stability; so that, the preferable separation of water was obtained for the sample governing the highest concentration of 3% NaCl (67% separation of total water) comparison to the lower concentration of NaCl (38% separation of total water) at time 3 hr. This phenomenon could be explicated by the pronounced variation in interfacial film behaviour. The salt ions result in an increase in relaxation of the forming film [15]. These results are in coincidence with those attained by Hajivand and Vaziri [16].

From the theory of diffuse ion, it is well known that for the same water content, when the salt concentration increases, this lead to increase the internal energy of the system [17]. Thus, the emulsions are not thermodynamically stable, and water droplets combine with each other to produce bigger droplets and increase the rate of coalescence.

4.4. Effect of the temperature

In the present study, the activity of temperature on the demulsification efficiency was investigated. The results showed in Fig. 7 and that by raising the temperature from 50°C to 70°C, this gave rise to better demulsification efficiency to reach 67% at higher temperatures while for low temperature (50°C) the separation was 39% at time 3h. The stability of emulsion can be decreased by conditions that reduced the film forming capacity of the crude oil. These films can be contracted by increasing the temperature through two ways [18].

The first, by enhancement the rate of coalescence by implying sufficient energy for the level of two droplets occurring previous to coalescence. The second, by giving rise to a reduction in the viscosity of continuous phase; which assisted the kinetic motion of the dispersed water droplets, hence increasing increased level leading to film relaxation, rupture of film and coalescence [19]. In other words, increasing the temperature results in decreasing the viscosity of the oil (continuous phase) and increase the occurrence of collision between the emulsified droplets "water." As a result, the difference in density between the oil and aqueous phase increases and hence makes water droplets to separate. Higher temperature, perhaps increases the solubility of emulsifiers, from the interface, into the oil phase, causing weaker film and a greater amount of water droplet coalescence and separation [11].

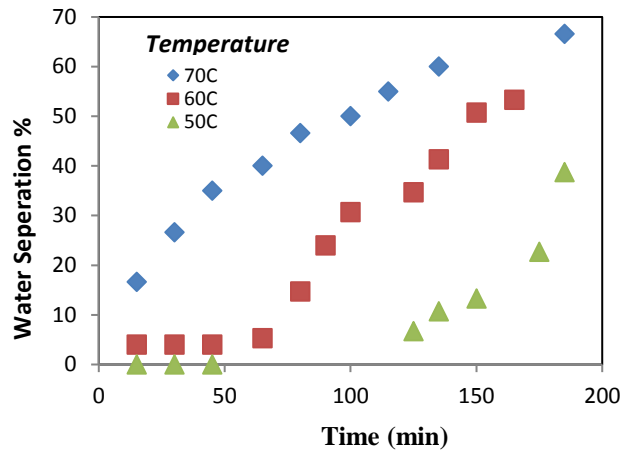


Fig. 7. Effect of temperature at constant water content 30%, salt content 3% and demulsifier concentration 8%

4.5. Viscosity and density of emulsion

4.5.1. Effect of the water content on viscosity and density

Fig. 8 illustrates the effect of water content on the viscosity of the emulsion at salt content 30000ppm and using demulsifier concentration 8%.

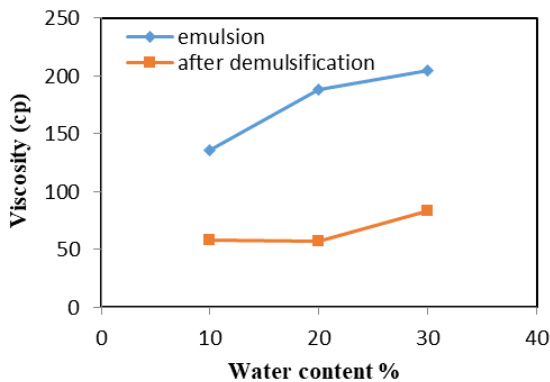


Fig. 8. Effect of water content on viscosity at salt concentration 3%, demulsifier concentration 8% and temperature 70°C

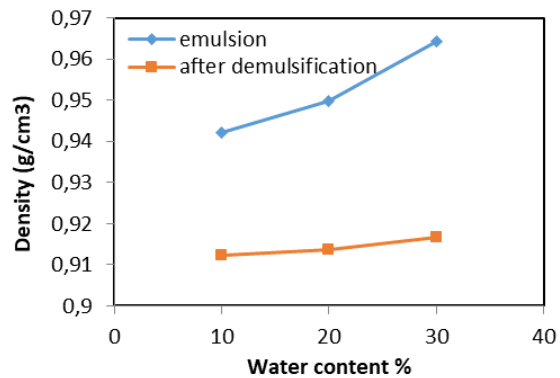


Fig. 9. Effect of water content on density at salt concentration 3%, demulsifier concentration 8% and temperature 70°C

From this figure two behaviors were shown, the first was that as water content increased from 10% to 30% the viscosity increased from 136 to 205cP (blue color) compared with the viscosity of oil alone was 76.8cp this because emulsions show non-Newtonian behavior. The second behavior was that the viscosity decreased after demulsification process as shown in the same figure to reach 87cp (red color) for water content 30%. The addition of demulsifier and implementation of heat will decrease the viscosity. As the results, the accumulation of

water droplets and mobility of water are increased causing collisions, coherence and then increase the rate of separation [20]. The same behavior was shown for density and illustrated in Fig. 9. It decreases from 0.9643 g/cm³ as an emulsion to reach 0.9167 g/cm³ after treating at water content 30%. Heat applied to emulsion will reduce the density of oil at a greater rate than that of water and therefore allows more settling of water. This is because the variety in densities of the two liquid phases may be increased [20].

4.5.2. Effect of salt content on viscosity and density

The same as the water content effect on emulsion, the salt content also effect on viscosity and density of emulsion as shown in Figs. 10 and 11. Fig. 10 illustrates the effect of salt content on the viscosity of the emulsion at constant temperature 70°C, demulsifier concentration 8% and water content 30%. From this figure, it was seen that viscosity decreased from 287 to 204cp as salt increased from 10000 to 30000ppm (blue color) but after demulsification, it decreased for all amounts. While the density increased from 0.948 to 0.962g/cm³ as the amount of salt increased from 10000ppm to 30000ppm as indicated in Fig. 11.

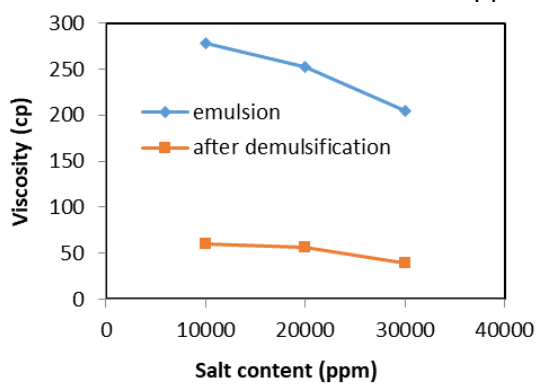


Fig. 10 Effect of salt content on viscosity at water content 30%, demulsifier concentration 8% and temperature 70°C

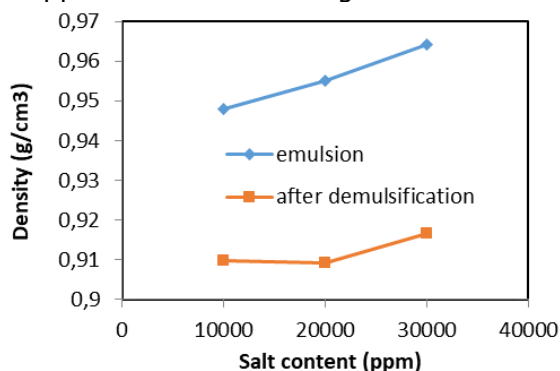


Fig. 11. Effect of salt content on density at water content 30%, demulsifier concentration 8% and temperature 70°C

5. Conclusions

- 1) Separation efficiency increases with increasing chemical demulsifier and temperature because the increase of the demulsifier concentration led to an increase in the adsorption of the demulsifier molecules on the W/O interface and the higher temperature might increase the solubility of emulsifiers.
- 2) Separation efficiency increases with increasing water content of emulsion.
- 3) Separation efficiency increases with increasing salt content of emulsions; this could be due to the destroying of the double charge layers by NaCl that delay the coalescence of water droplets.
- 4) The best demulsification efficiency was 67% that obtained at water content 30%, salt concentration 3%, demulsifier concentration 8% and temperature of 70°C.

References

- [1] Nuraini M, Abdurahman HN and Kholijah AMS. Effect of Chemical Breaking Agents on Water-in-Crude Oil Emulsion System. *International Journal of Chemical and Environmental Engineering*, 2011; 2(4): 250-254.
- [2] Zulkania A. Formation and Stability Study of Some Malaysian Crude Oil Emulsions. Master of Engineering. University Teknologi Malaysia, Skudai. Johor, 2004.
- [3] Ghannam MT. Water-in-Crude Oil Emulsion Stability Investigation. *Petroleum Science and Technology*, 2005; 23: 649-667.
- [4] Al-Sabagh AM, Kandile NG, El-Ghazawy RA and Noor El-Din MR. Synthesis and Evaluation of New Demulsifiers Incorporating Linear Alkyl Benzene Moiety for Treating Water-in-Oil Emulsion. *Journal of Dispersion Science and Technology*, 2013; 34: 996-1007.

- [5] Abdel-Azim AA, Abdel-Raouf ME, Abdul-Raheim RM, Maysor NE. Sugar-Based Ethoxylated Amine Surfactants as Demulsifiers for Crude Oil Emulsions: 2-Demulsification of Different Types of Crudes. *Brazilian Journal of Petroleum and Gas*, 2010; 4(4): 155-165.
- [6] Abdurahman HN, Yunus RM and Anwaruddin H. Water-in-Crude Oil Emulsions: Its Stabilization and Demulsification. *Journal of Applied Sciences*, 2007; 7(22): 3512-3517.
- [7] Fan Y, Simon S and Sjöblom J. Chemical Destabilization of Crude Oil Emulsion: Effect of Nonionic Surfactant as Emulsion Inhibitors. *Energy & Fuel*, 2009; 23(9): 4575-4583.
- [8] Al-Sabagh AM, Noor El-Din MR, and Mohamed HM. Effect of demulsifiers on surface active and rheological properties of water-in-oil emulsion in relation to the demulsification efficiency. *Egypt. J. Petrol.*, 2006; 15(1): 49-60.
- [9] Wu J, Xu Y, Dabros T, and Hamza H. Effect of EO and PO positions in nonionic surfactants on surfactant properties and demulsification performance. *Colloids Surf. A*, 2005; 252: 79-85.
- [10] Al-Sabagh AM, Nadia GK, and Noor El-Din MR. Functions of Demulsifiers in the Petroleum Industry Sep. *Sci. Technol*, 2011; 46(7): 1144-1163.
- [11] Al-Sabagh AM, Nasser NM, Khamis EA. Demulsification of Crude Oil Emulsions Using Ethoxylated Aliphatic Amine Polyesters as Novel Demulsifiers. *International Journal of Science and Research*, 2014; 3(12): 1171-1183.
- [12] Mosayebi A and Abedini R. Using Demulsifiers for Phase Breaking of Water/Oil Emulsion. *Pet Coal*, 2013; 55(1): 26-30.
- [13] Kim YH and Wasan DT. Effect of Demulsifier Partitioning on the Destabilization of Water-in-Oil Emulsions. *Industrial and Engineering Chemistry Research*, 1996; 35: 1141-1149.
- [14] Al-Sabagh AM, Maysor NE and Noor El-Din MR. Investigate the Demulsification Efficiency of Some Novel Demulsifiers in Relation to their Surface-Active Properties. *Journal of Dispersion Science and Technology*, 2007; 28(4): 547-555.
- [15] Binks BP. Surfactant Monolayers at the Oil-Water Interface. *Chemistry and Industry*, 1993; 14: 537-541.
- [16] Hajivand P and Vaziri A. Optimization of Demulsifier Formulation for Separation of Water from Crude Oil Emulsions. *Brazilian Journal of Chemical Engineering*, 2015; 32(01): 107 - 118.
- [17] Mohamed AMO, Gamala M, Zekri AY. Effect of Salinity and Temperature on Water Cut Determination in Oil Reservoirs. *J. Petro. Sci. Eng.*, 2003; 40: 177-188.
- [18] Eow JS and Ghadiri M. Electrostatic Enhancement of Coalescence of Water Droplets in Oil: A review of the Technology. *Chemical engineering Journal*, 2002; 85: 357-368.
- [19] Bhardwaj A, and Hartland S. Dynamics of Emulsification and Demulsification of Water in Crude Oil Emulsions. *Industrial and Engineering Chemistry Research*, 1994; 33(5): 1277-1279.
- [20] Kim YH. Study of Dynamic Interfacial Mechanisms for Demulsification of Water in Oil Emulsions. Ph.D. Thesis, Illinois Institute of Technology, 1995.

To whom correspondence should be addressed: Marwa F. Abdul Jabbar, Chemical Engineering Department, College of Engineering, Al-Nahrain University, Baghdad, Iraq marwa84_2007@yahoo.com

EXPLOITATION OF BITUMEN FROM NIGERIAN TAR SAND USING HOT-WATER/STEAM STIMULATION PROCESS

Shadrach Olise Ogiriki^{1*}, Marvelous Ayodele Agunloye², Afeez Olayinka Gbadamosi Abdulkashif¹, Olalekan Olafuyi³

¹ Department of Chemical and Petroleum Engineering, Afe Babalola University, Ado-Ekieta, Nigeria

² Department of Petroleum and Gas Engineering, University of Port Harcourt, Port Harcourt, Nigeria

³ Department of Petroleum Engineering, University of Benin, Benin City, Nigeria

Received October 18, 2017; Accepted January 8, 2018

Abstract

With the upward surge in global demand for energy, unconventional energy resources are being considered as options to quell the growing energy demand. These unconventional energy resources like oil sand, shale oil, shale gas, tight gas, are fast becoming alternatives to complement the conventional energy resources. Tar sand exploitation is being commercialized globally. With success stories from Canada, Venezuela and U.S.A., other countries tend to follow. Nigerian tar sands, which is similar to Canada's tar sand in terms of chemical composition, water wet nature, etc., has some characteristics which will yield enormous economic benefit when exploited. The possibility of producing heavy oil from the Nigerian tar sand deposits by steam stimulation was evaluated in this paper with respect to the technology (Cyclic Steam Stimulation), environmental impact and the economic analysis, with Canada's success stories used as reference point. The result of the study showed that heavy oil could be produced with steam stimulation process with little impact on the environment and with huge economic potentials.

Keywords: Bitumen; Tar sand; Cyclic Steam Stimulation; Oil Sand; Nigeria.

1. Introduction

The global demand for energy is rapidly increasing and conventional oil reserves will not be able to meet up the increasing energy demand. The need to exploit unconventional resources is being considered globally. Some of the unconventional resources include tar sand, shale oil, shale gas and tight gas. These resources (with tar sand inclusive) are termed unconventional because they cannot be exploited with the available technologies used in exploiting the "conventional crude oil and gas". Again, exploitation of these resources is quite expensive.

The problem associated with the exploitation of tar sand include:

- The best technology to exploit tar sand.
- Environmental implication of processes of exploiting tar sand
- Economic considerations.

Based on the stated challenges and the understanding of the thermal processes used in the exploitation of tar sand, this study is therefore concerned with the following:

1. Evaluation of the hot water/steam stimulation process applied in tar sand exploitation.
2. Environmental impact evaluation of the processes.
3. Economic evaluation of tar sand exploitation.
4. Tar sand market and prospect in Nigeria.

1.1. Concise description of tar sand and its origin

By definition, tar sands are sedimentary rocks (consolidated or unconsolidated) that contains bitumen (solid or semisolid hydrocarbons) or other heavy petroleum that, in natural

state, cannot be recovered by conventional petroleum recovery methods. Technically, tar sand is not a combination of tar and sand as the name implies, since tar is a viscous liquid; black in colour with adhesive properties, obtained by the destructive distillation of coal, wood, shale, etc., and such an origin for tar in tar sands are rarely implied. On the other hand, "bitumen" is the name given to viscous liquids or solid materials black or dark brown in colour having adhesive properties, consisting essentially of hydrocarbons derived from petroleum or occurring in natural asphalt and soluble in carbon disulphide. Bitumen is found mixed with other component such as clay, water, etc., in sand known as "tar sand" by name, which is a misnomer or an inappropriate term and should rightly have been called "bitumen sand" since it is bitumen and not tar from destructive distillation of coal that is intermingled with the sand deposits. Bitumen is simply the name of the oil found in tar sands and until recently, Alberta's bitumen deposits were known as tar sand but are now called "oil sands". A section of tar sand showing its composition is shown in Figure 1.

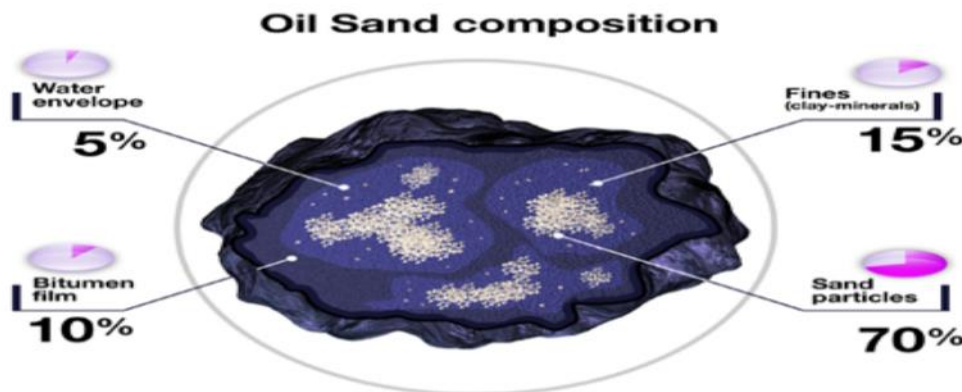


Figure.1. A Section of tar sand showing its oil composition

Tar sands is not only made up of bitumen but also consist of feldspar, Mica clay minerals in minor amount and quartz as the dominant mineral constituting over 90% of the entire assemblage of mineral grains. Tar sands are water wet by nature. In Nigerian, the tar sand belts fall within the Eastern Dahomey basin which is a coastal sedimentary basin filled with over 2500 metres of cretaceous and younger sediments unconformity overlying the block faulted basement complex rocks. The basin sedimentary fill was subdivided into three intervals by Durham Pickett [1] namely:

- Sand and sandstone at the base.
- Alternating sand and shale.
- Upper shales which correspond to the three formations of Ise, Afowo and Ararom respectively [2].

The grain size of the tar bearing sands vary from fine to coarse grained. The quartz sand forms a bulk of the material with either the bitumen i.e. Oil wet (as in the case of some US deposits - Utah), or water wet (as for the Athabasca in Canada and Okitipupa in Ondo State of Nigeria), forming the continuous phase, generally depending on the grade of the oil sand.

The microscopic examination of the Athabasca tar sand shows that the thin film of water is about 10mm thick. The similarity of the grain/water relationship of both the Nigerian and Canadian tar sand makes it characteristically easy to derive comparative studies on processing Nigerian tar sand from the Canadian experience. Although, the Nigerian tar sand has been discovered since the dawn of the past 2 decades, they have largely remained unexploited due to the availability of the conventional oil in the neighbouring oil rich Niger Delta of the country.

According to Adegoke *et al.* [3], the lithology, hydrocarbon contents area and spatial distribution of the bituminous sands have been well documented. Adegoke *et al.* [3] recom-

mended that bitumen be exploited by open cast mining in areas where the bituminous sands outcrop or where they are overlain by less than 50 – 75 metres of over burden while heavy oil be exploited by the use of in-situ techniques in all areas south of the tar sand mine zone, especially where the over burden thickness is in excess of 100 meters.

The work presented by this paper is aimed primarily at giving the technical, environmental and economic evaluations (benefits and implications) of exploiting Nigerian Tar sand using hot water/steam stimulation.

2. Properties of Nigerian tar sand

Oil sand (tar sand) consists of an initiate mixture of bitumen, water, quart sand and clays and other minerals which is either oil or water wet. The case of oil sands in Utah in U.S.A is oil-wet but the oil sands in Canada and Okitipupa in Ondo State of Nigeria are water-wet. This makes the Nigerian and Canada tar sand similar. The Nigerian and Canadian tar sand are also similar in the area of mean value of chemical composition as shown on Table 1 [4].

Table 1. Chemical composition of Nigerian and Canadian oil sands

Element	Nigeria's composition (%)	Canada's composition (%)
Carbon	85	83.4
Hydrogen	10.7	10.4
Nitrogen	0.5	0.4
Oxygen	1.7	1.0

Other similarities between Nigeria and Canada tar sand properties on the bases of characteristics is in the area of having similar texture parameter, oil saturation, chemistry and water-wet nature of grains. However, the Nigerian tar sand are more asphaltenic and lesser in trace metals. Table 2 shows the comparison of the metal compositions of Nigeria and Athabasca tar sands.

Table 2. Metal composition of Nigeria's and Athabasca's tar sands

Element	Nigeria's Composition (ppm)	Athabasca's Composition (ppm)
Vanadium	35	75
Nickel	33	198

The close similarity of the characteristics of the tar sands of Nigeria and Athabasca suggest that the Canadian experience can be used as a model for the development of Nigerian tar sand. The similarities make it characteristically easy to derive comparative studies on processing of the Nigerian deposits, easy determination of similar techniques for exploitation and draws the difference from those oil wet deposits of California, New Mexico and Utah.

3. Cyclic steam stimulation process

The Cyclic Steam Stimulation (CSS) is the simplest and the most direct of the steam stimulation processes. Steam is injected into the formation of bitumen or tar sand deposits and allowed to soak. The pressure of the steam dilates or fractures the formations while the heat reduces the viscosity of the bitumen. The bitumen is then pumped to the surface through the same injection well. This process is repeated in a cyclic fashion. The CSS could be divided into three (3) different stages.

Stage 1: This is the called the steam injection stage or phase. In this stage, steam is being injected at high pressure into the formation. The high pressure is to fracture the formation while the heat from the steam is to reduce the viscosity of the bitumen.

Stage 2: This is known as the soak period. This is the time interval that is allowed for the bitumen's viscosity to reduce. This is as a result of the heat from the steam. Most often, a period of one to three months is given for the soak period.

Stage 3: Finally, the bitumen with reduced viscosity is then pumped, alongside the condensed water from the steam, to the surface and processed as heavy crude. This stage is known as the Bitumen Production phase.

Figure 2 is a diagrammatic representation of the stages for the CSS process in a vertical well. All the three stages are carried out in a single vertical well and the process recovers 15 to 25% of original oil in place. Finally, the bitumen with reduced viscosity is then pumped, alongside the condensed water from the steam, to the surface and processed as heavy crude. This stage is known as the bitumen production phase.

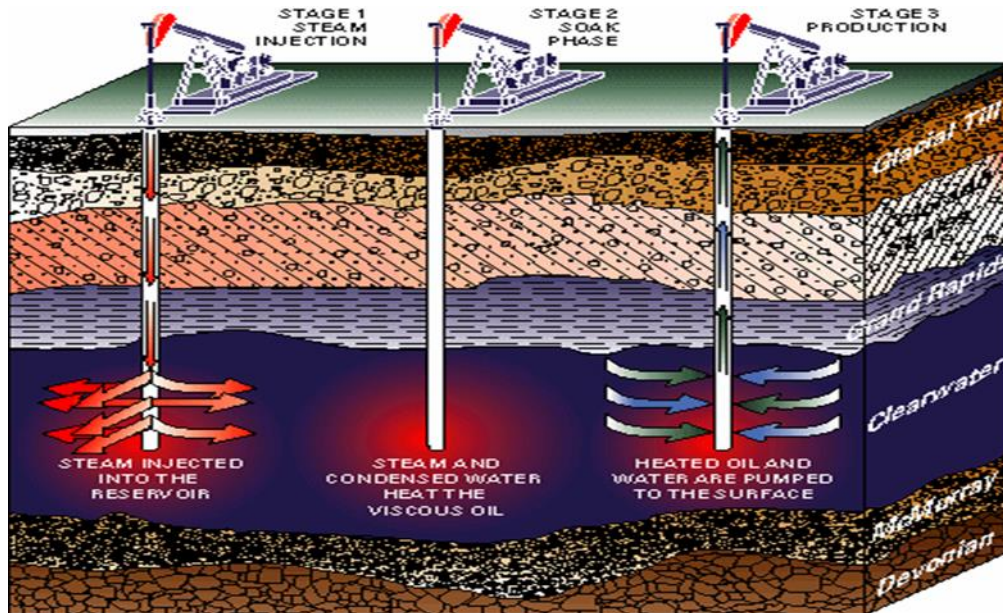


Figure 2. Cyclic steam stimulation showing the three different stages (Source: IMPERIAL OIL)

3.1. Production operations and control

The CSS operation requires close monitoring geared at controlling the downhole process, to avoid operational issues and maximize efficiency and recovery. The temperature and pressure of the well should be constantly monitored to balance the steam/liquid interface of the well. Optimum CSS requires that liquid does not accumulate over the well—reducing production rates—but avoiding steam production because it jeopardizes the integrity of the well [5].

3.2. Performance and challenges

The CSS process has some advantages that could help limit environmental impact. Some of these are as follows:

1. The application of this process (CSS) reduces access road construction compared to mining processes.
2. Up to a maximum of 32 wells can be drilled in a single cluster on 2-acre spacing.
3. Utilities (pipelines, flow lines, power lines), including mud cycling plants are economically positioned on a lease to reduce well cost and site clean-up problems.
4. Decreases rig time required per hole since wells are shallow.
5. Minimum tear-down of rig component after each well.

3.3. Limitations

The limitations of the CSS include the following:

1. Low initial formation injectivity.
2. Poor heat conductivity due to low reservoir thermal conductivity.
3. Inadequate control of the movement of the injected steam.
4. Tendency of the injected steam to override (wash off) the section of the bitumen deposit that is to be heated.

4. Environmental consideration

The selection of boiler technology is related to the choice of fuel for steam generation. Natural gas-fueled boilers are the simplest and most economical option. Unfortunately, with the quantities of steam needed for a large-scale development project, the cost of natural gas, whose price may fluctuate considerably in the future, could have a very serious impact on project economics. For other technologies, such as Circulating Fluidized Bed (CFB) boilers designed to burn liquid or solid heavy fuels, feedwater must be free of dissolved minerals, requiring advanced water treatment that adds to operating costs.

Despite the high concentrations of carbon, nitrogen and sulfur compounds, residuum is being considered by some companies as an alternative to natural gas. Use of these heavy fuels would considerably aggravate the problem of carbon dioxide (CO₂) emissions and generate substantial quantities of sulfur dioxide (SO₂) and nitrogen oxide (NO₂), creating a major and negative environmental impact. To counter these problems, specific surface equipment would have to be installed for sweetening (removing the sulfur) and denitrification of the combustion gases, and even for capturing, transporting and storing the CO₂. The cost of such installations, coupled with the cost of feedwater treatment, would diminish or perhaps cancel out any cost gains on the fuel.

However, the latter options can only be envisaged if there is a sufficient quantity of residual from the deep conversion process. To assemble the pieces of this huge and complex puzzle, research and development must therefore make the right trade-offs between economic and environmental criteria. The key to that effort is developing sufficiently reliable tools so that the latest advances can be taken into consideration in industrial decisions.

5. Economic analysis of tar sand

The CSS process cycle could take from four months to 2 years, this long gestation period means that the extraction requires long term investment and the cost implications has to be carefully studied. A thorough and in-depth cost-benefit analysis is required before a project can be fully sanctioned.

5.1. Economic drivers for tar sands exploitation

The nature and composition of tar sands pose a specific challenge to its economic viability. As a developing fuel source, its production and processing costs are still significantly high. Thus, the break-even costs are relatively higher than for conventional fuels especially for new steam driven in-situ projects due to the nature of projects as well as specialist technology required. A full-scale development project would require heavy investment with the potential of leaving operators vulnerable to demand and price fluctuations.

The major economic drivers for tar sands exploitation include:

- Conventional Oil prices
- Extraction Methods and Costs
- Heavy oil Refining infrastructure
- Available market for bitumen product
- Available supply of energy feedstock
- Government subsidies and incentives

With today's oil prices just above US\$50/bbl, most projects will either not be economical or investors will have to accept a lower rate of return until prices pick up. However, higher oil

prices will drive investment and thus as oil prices expectedly recover, so will the profitability of oil sands projects.

Cost effective and energy efficient extraction technologies can encourage exploitation as seen recently in the case of shale gas in the United States. Better methods have helped drive down operating cost and thus lower the breakeven cost for most investments thereby increasing the profit margin even in the midst of low oil prices.

Government can help promote investment by subsidizing the industry, proving incentives, providing subsidies to importers of heavy machinery used in the extraction process including reduced taxation of oil sands project.

5.2. Tar sands supply costs

Available estimates for the cost of extracting bitumen from the oil sands are based on a 'supply cost' approach. According to the Canadian Energy Research Institute's (CERI) "The bitumen supply cost is the constant dollar price needed to recover all capital expenditures, operating costs, royalties, taxes, and earn a specified return on investment" [6].

CERI's supply cost estimates take into account a 10% real rate of return, taxes, royalties, operating costs and other variables. In its Energy Report for 2015, it stated that the supply cost for SAGD and, surface mining and extraction were calculated hypothetically. Excluding transportation and blending costs, crude bitumen produced by SAGD and mining projects are US\$45.08/bbl and US\$53.94/bbl respectively. Figure 3 shows the breakdown of Bitumen/SCO supply cost in Canada. On the other hand, Wood Mackenzie, a financial institution, in its February 2015 analysis stated that the breakeven for crude bitumen supply cost for in-situ projects is US\$41/bbl and that of mining is US\$47/bbl for WTI crude oil. Considering the price of crude oil in the international market as at April 08, 2016, where WTI sells at US\$37.26/bbl and Brent sells at US\$39.43/bbl, investors would have to consider ways to cut cost so as to produce at profitable margins. For intending investors in the Nigeria Bitumen, the Federal Government of Nigeria would have to provide incentives to make bitumen production profitable so as to attract capitals and investors. These might be in the form of infrastructural facilities to access the bitumen deposits, tax exemptions and/or probably create free trade zones for bitumen production.

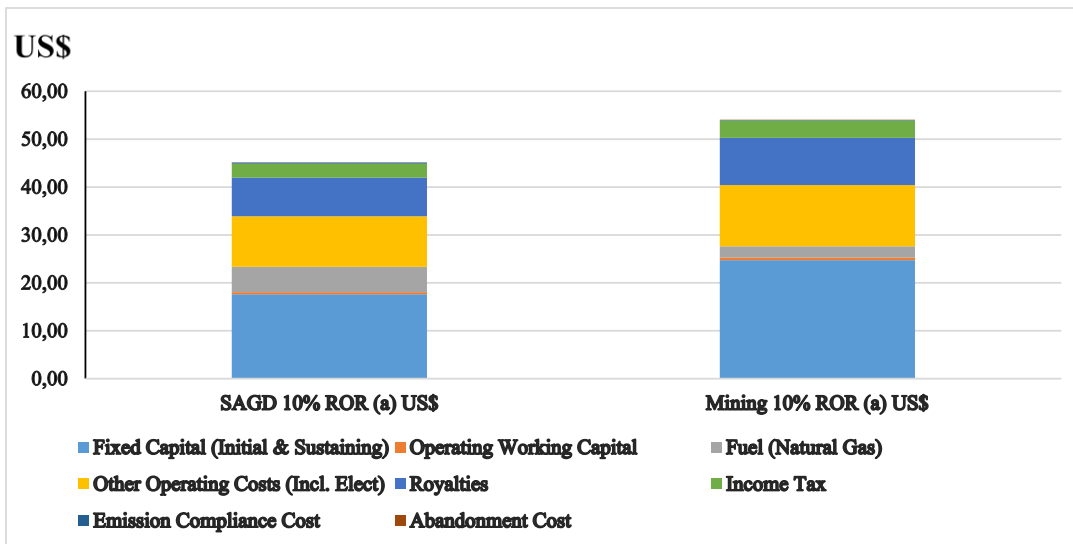


Figure 3. Breakdown of Bitumen/SCO Supply Cost (Source: CERI)

5.3. Economic impact and sensitivity analysis

The analysis of Canadian tar sands undertaken and published by CERI in February 2017 [7], suggests that the supply cost is most sensitive to changes in initial capital expenditure and

the assumed discount rate. An increase in any of these two will result in a significant increase in the supply cost and vice versa. This is very critical as capital costs are one of the very few parameters that have an impact on project economics directly under the control of operators. The impact is felt more for a stand-alone mining project than for in-situ steam projects. The non-energy operation costs also significantly affect the profitability of mining projects. However, these costs have shown steady decline on year-on-year basis.

Another important cost element is the energy related costs, given that oil sands projects are very energy-intensive, consuming large quantities of natural gas, electricity and chemicals as feedstock. These are very dependent on the market prices of these commodities.

Research based on the capital and operating of pilot projects as at 2016 show that the in-situ extraction method offers a more economical way of extracting bitumen from tar sands compared to a stand-alone mining project. This is also evident from the illustration in Figure 3.

6. The Nigerian tar sand prospect

From the experience of exploiting tar sand in Canada, Nigerian tar sand can as well be exploited with great economic benefit. Though, there might be little differences as regards factors like policies, socio-cultural values and prices of materials, Nigerian tar sand can successfully be exploited using the cyclic steam stimulation process.

6.1. Tar sand market prospect and application in Nigeria

The only source of bitumen at present in Nigeria is the Kaduna Refinery which processes heavy crude. This is insufficient for domestic needs, thus, Nigeria imports bitumen to supplement her internal production. Extracted bitumen from the tar sand belt can be used as feedstock for the Kaduna Refinery and for setting up other bitumen processing units to meet both domestic and West African sub-regional needs. The bitumen is uniquely aromatic and naphthenic in composition, thus can be used for the manufacture of naphthenic base stocks for industries specializing in critical application products. Heavy and extra-heavy crude can be extracted from the Nigerian tar sands. This can be upgraded to Synthetic Crude Oil (SCO) or Syncrude specification tailored as feed stock to refineries.

Sulphur and phenol can be derived from the Nigerian tar sand. Laboratory tests have shown that specification grade grease within National Lubricating Grease Institute (NLGI) are suitable as lubricants for plain and roller bearings and as sealant can be made from the Nigerian tar sand's oil.

Certain basic facilities favourable for conducting business exist in the country and these include:

- A fairly developed infrastructure such as road network, deep ocean ports and jetties.
- A network of gas and oil pipelines
- Improved communication system
- Dynamic banking community
- Relaxed foreign exchange for capital raising
- Large local and sub-regional market for bitumen sales
- Existing joint venture opportunities
- A large community of geoscientists and engineers
- A commitment to privatization

Above all, the government of Nigeria must recognize the fact that an enabling political environment must be put in place to attract foreign investment into the country. To this effect, Nigeria should continuously strive to improve on its political and economic stability, accountability in government spending and divesting of government concerns under a democratic setting.

6.2. Tar sand project possibilities in Nigeria

Three Potential Project Types (PPT) are envisaged for the tars and resources in Nigeria.

1. Small scale project: asphalt concrete (strip mining)

- Suitable for small-size scale prospect, using specification bitumen as a major component for road asphalt.
 - Short-term execution period of three (3) years using strip-mining techniques.
 - Production level: 150,000 metric tons/year.
 - Bidders will obtain Exploration Prospecting Lease (EPL) and later Mining Lease (ML) or Quarrying Lease (QL).
2. Medium-sized project: synthetic crude production (In-situ mining)
- Mining at depths below 150m using enhanced oil recovery technique (EOR)
 - Time frame 5years for development
 - Suitable for companies having foreign partners with technological know-how.
 - Successful bidders will be granted EPL
 - Projected production 10,000bbls/day
3. Large-size project: mega mining project (open mining)
- Focus on tar sands activity within 30-50m of overburden
 - Open cast mining method
 - Major experienced companies to invest in exploitation and full feasibility evaluation prior to commencement
 - Requires periods of about 15years to develop
 - Expected to produce modules of 50,000bpd of synthetic crude for export
 - Processing by water/solvent extraction method.

7. Conclusions

The conclusion drawn from this work are as follows:

1. The close similarity of the characteristics of the tar sands of Nigeria and Athabasca suggest that the Canadian experience can be used as a model for the development of Nigerian tar sand
2. With success stories of the application of CSS with minimal environmental impact on the immediate surroundings, Nigeria can therefore, make good application of this method (CSS) to exploit her huge tar sand deposits.
3. The exploitation of Nigerian tar sand is of huge economic benefit to the Nigerian economy, especially with the upward trend of crude oil demand in the international market.
4. CSS have minimal impact on the environment. The major issues to deal with as regards CSS is mainly recycling the produced condensed water and treating the residual gases can be handled
5. That CSS recovery method for oil sand is economical and environmentally friendly and is therefore recommended as one of the recovery methods to exploit Nigerian Tar Sand.

References

- [1] Durham KN, and Picket CR. Lekki Borehole Programme; Oil Mining Lease 47 unpubd. Report. Tennessee Nig. Inc. (1966).
- [2] Omatsola ME, Adegoke OS. Tectonic evolution and Cretaceous stratigraphy of the Dahomey basin. Nigeria Journal Mining and Geology, 1981; 18 (01).
- [3] Adegoke OS, Ako BD, Enu EI. Geotechnical Investigation of the Ondo State bitumen geology consultancy unit, University of Ile-Ife 1980.
- [4] Montgomery DS. Bitumen chemistry related to oil production and upgrading. University of Alberta 1981, Edmonton, Alberta, Canada.
- [5] Edmunds NR. Investigation of SAGD steam trap control in two and three dimensions. SPE Int. Conf. on Horizontal Well Technology, Calgary, Canada, Nov. 4-7 1998.
- [6] CERI Study No. 152 (2015): Canadian Oil Sands Supply Costs and Development Projects, 2015-2035
- [7] CERI Study No. 163 (2017): Canadian Oil Sands Supply Costs and Development Projects, 2016-2036

To whom correspondence should be addressed: Shadrach Olise Ogiriki, Department of Chemical and Petroleum Engineering, Afe Babalola University, Ado-Ekiti, Nigeria, shadrachogiriki@abuad.edu.ng

EFFICIENT ESTIMATION OF MAXIMUM FLOW RATES THROUGH CHOKES DURING PETROLEUM PRODUCTION OPERATION

Alireza Rahimzadeh¹, Arash Kamari², Amir H. Mohammadi^{3,4}

¹ Department of Petroleum Engineering, PETROPARS Ltd, Farhang Blvd, District 2, Tehran, Iran

² Department of Geology, Kansas State University, 108 Thompson Hall, Manhattan, KS 66506, USA

³ Institut de Recherche en Génie Chimique et Pétrolier (IRGCP), Paris Cedex, France

⁴ Discipline of Chemical Engineering, School of Engineering, University of KwaZulu-Natal, Howard College Campus, King George V Avenue, Durban 4041, South Africa

Received October 6, 2017; Accepted March 3, 2018

Abstract

One of the challenging subjects in petroleum production engineering is to calculate flow rates through chokes and orifices accurately. Variety of empirical correlations and analytical models have been developed so far, and most of them have acceptable results just in their domain of measured data. Lack of a method which gives the decent match with measured data is a necessity regardless of the type of the fluids and input parameters ranges. This article presents advanced methods to estimate the gas flow rate through choke. The database includes around 1600 data with a wide range of input parameters. The methods are included feed-forward artificial neural network (ANN), least square support vector machine (LSSVM), decision tree (DT) analysis. Based on the results, decision tree with less than 1% error makes the perfect modelling of choke flow rate. ANN and LSSVM with 2% error have reliable results. Besides, a model has been developed based on gene expression programming (GEP) which shows correct results just in low gas flow rates.

Keywords: Choke; DT; ANN; LSSVM; GEP; ANFIS; Gas Rate.

1. Introduction

In the petroleum production engineering, chokes and orifices are instruments which are used to regulate the flow rate of producing wells and they are usually installed after well head. There are two general types of chokes: positive chokes and adjustable chokes [1]. The reasons for having a choking device in the production system are to [2]: 1) protect reservoir and surface equipment from pressure fluctuations; 2) avoid sand problems due to high drawdown; 3) control flow rate to avoid water or gas coning; 4) produce the reservoir at the most efficient rate.

There are two types of flow in surface chokes: critical and subcritical. During critical flow, fluid velocity in choke restriction is higher than sonic velocity, and in this situation, the flow rate is independent of downstream pressure. Mach number for the fluid is greater than or equal to one for critical flow [1]. In opposite, the flow rate in the subcritical state is a function of downstream and upstream pressure both.

In this work, a literature review has been done to analyse different empirical and analytical models. Afterwards, based on the available data, choke multiphase flow modelling will be done by three advanced regression methods including decision tree (DT) modelling, Feed-Forward neural network analysis (ANN) and least square support vector machine (LSSVM) approach. Additionally, a new model, which has been developed based on gene expression programming (GEP) and incorporates the main input variables to calculate choke flow rate is presented. For the first time, decision tree algorithm as one of the powerful models has been applied to

estimate gas flow rate through well head chokes, and which shows highly accurate results in comparison to existing models including empirical correlations, analytical models and also ANN and LSSVM.

2. Literature review of the existing models and correlations

There are various equations and models which predict volume flow rate of chokes and orifices. In this section, the most well-known ones will be reviewed. Perkins developed an analytical model encounter isentropic (adiabatic with no friction loss) flow of multiphase hydrocarbons and water in chokes. It has been derived based on the general energy equation which is valid for critical and subcritical flow [3]. Based on this model, Rahimzadeh *et al.* developed a choke multiphase flow model for a gas condensate reservoir. The model was accuracy evaluated by incorporating a gas condensate field DST and production test data. Nomination of well potential after clean up and well stimulation, appropriate design of the production test and well production allocation in platforms; are some of the main applications of this work. In this paper, in addition to analytical modelling, a new empirical correlation which incorporates the water content has been derived which is showed in the following [2].

$$Q = 0.0253 \times \frac{P_{wh} \times Size^{1.845} \times (1 - \frac{BSW}{100})^{0.1374}}{0.0878} \quad (1)$$

where Q = Gas Rate, MMSCF/D; Pwh = Well Head Pressure, psia; Size = Choke Size, in; BSW = Water Cut (W/W+O), %; CGR = Condensate Gas Ratio, STB/MMSCF

Sachdeva derived a choke model for prediction of critical and subcritical multiphase flow rates, which was evaluated using measurement field data. The accuracy of the model has been concluded based on real data [4]. Guo *et al.* used a comprehensive data base of oil and gas condensate wells to improve choke flow model performance, which was found that by optimizing the discharging coefficient, the accuracy of prediction is enhanced [5].

There are various empirical correlations which basically use the same parameters with the different coefficients which were tuned based on specific databases. Osman *et al.* derived an empirical correlation of choke flow for a gas condensate reservoir which is located in Middle East [6]. The correlation is presented as follows:

$$P_1 = 767.2 \times Q_g \times \frac{LGR^{0.5598}}{S^{1.8298}} \quad (2)$$

where P₁ is well head pressure (psia), LGR is the liquid-gas ratio (STB/MSCF), Q_g is gas flow rate (MSCF/day), and S is choked size in 64th inches [6].

Most of the empirical correlations can be presented in the following form. They tried to assign a proper relationship between wellhead pressure and flow rate

$$P_{wh} = \frac{A_1 Q_L GLR^{A_2}}{d^{A_3}} \quad (3)$$

where P_{wh} is well head pressure (psia), GLR is the gas-liquid ratio (SCF/STB), Q_L is oil flow rate (STB/day), and d is choked size (inch).

Gilbert was the first to present such a relationship based on field data collected from the Ten Section field of California. Ros also presented relationships that are often used. Baxendell and Achong also modified the correlation coefficients. Table 1 summarizes the parameters for each equation [7-10].

Table 1. Empirical correlations coefficients

Model	A ₁	A ₂	A ₃
Gilbert	3.86 × 10 ⁻³	0.546	1.89
Ros	4.26 × 10 ⁻³	0.500	2.00
Baxendell	3.12 × 10 ⁻³	0.546	1.93
Achong	1.54 × 10 ⁻³	0.650	1.88

Ashford *et al.* developed mathematical models and empirical correlations to analyse dynamic behavior of multiphase flow through orifices, and most of them were tested with field data. Validity in both critical and subcritical flow regimes were evaluated as well. Pressure drops in choke were related to fluid properties and choke sizes. Some of them incorporate temperature as an input parameter. As mentioned earlier, optimization of discharge coefficient in these models is used to increase the accuracy of prediction [11-12]. Al-Attar *et al.* compared available equations of multiphase flow through chokes. This assessment was made based on statistical analysis of more than 100 well tests [13].

Fortunati determined accurate liquid flow rate based on the corrected velocity of the mixture in downstream of chokes. This model was applicable for critical and subcritical flow [14]. One of the missing parameters in most of the empirical correlation is water quantity. Safar Beiranvand *et al.* [15] presented a new form of the empirical equation which uses basic sediment and water (BS&W) as a new input parameter along with other conventional inputs such as well head pressure, gas oil ratio and chokes size. Having optimized, relevant coefficients of input parameters were shown based on Iranian oil field which includes production data from different wells [15].

Advanced models such as neural network and support vector machine have been reported to calculate choke flow rates in some articles. Al-Khalifa used Artificial Neural Network technique as a practical tool to estimate flow rates through chokes and selection of optimal orifice dimensions. This model gives precise answers in comparison to measured field data and works in wide range of input parameters [18]. ZareNezhad studied the performance of gas condensate flow through chokes by use of the neural network. The network was trained using Levenberg-Marquardt back-propagation method, and transfer function which was applied was a hyperbolic tangent sigmoid function [19]. Gorjaei *et al.* derived a least square support vector machine (LSSVM) algorithm to forecast liquid flow rate in two-phase flow in surface chokes. Particle swarm optimization (PSO) is applied to improve tuning constraints of LSSVM model. Model inputs include choke upstream pressure, the gas liquid ratio (GLR) and choke size which are surface measurable variables [20]. In a similar work, Nejatian *et al.* developed a model using Least-Squares Support Vector Machine (LSSVM) method to estimate choke flow coefficient in both nozzle and orifice type chokes in subsonic gas flow [21].

3. Development of New Models

To develop reliable models, a comprehensive dataset is required. The database collected covers different variables viz. choke size (24-72, 1/24 inch), well head pressure (896-3787, psia), BSW (0-15, %), gas rate (5-94, MMscf/d), oil rate (58-4307, bbl/d), and water rate (0-179, bbl/d). In the DST operation, the wells are producing at a series of different stabilized flow rates in different chock sizes, typically with a sequence of increasing flow rates. In the mean while measuring the stabilized bottom hole flowing pressure at the sand face, wellhead pressure, water content, oil and water rate are executed. In this study, 1597 test points were taken with acceptable ranges for different input parameters.

All the models including DT, ANN and LSSVM and also GEP based model were coded in MATLAB software to analyze the data and recognize the patterns. The statistical error parameter used in this study is average absolute relative deviation (AARD).

$$AARD\% = \frac{1}{n} \sum_{i=1}^n E_i\% \quad \text{where} \quad E_i\% = ABS \left[\frac{X_{exp} - X_{rep./pred}}{X_{exp}} \right] \times 100 \Rightarrow i = 1, 2, 3, \dots, n \quad (4)$$

To validate the accuracy of the models with data which were not used in training the models, about eighty percent of database was separated for training and the rest was assigned for testing the ANN, LSSVM and DT approaches.

A significant information that can be obtained from data mining tasks is the decision tree (DT). A decision tree is a method to recognize dominant patterns in data series as tree structures. The objective of using the decision tree is to obtain an accurate representation of

the relationship between input and output parameters. One of the main advantages of DT is visualization of structure; unlike neural networks, it is not a "black box." The tree is composed of a root node, a set of internal nodes, and a set of terminal nodes (leaves). Each node of the decision tree structure makes a binary decision that splits either one class or some of the classes from the remaining classes [22-23]. The regression DT toolbox available in the MATLAB software was used to develop a model for comparing the predicted values with the other methods. Input parameters of the DT model are BSW which expresses the ratio of water rate in total liquid rate, choke size (1/64 in), well head pressure (psi) and CGR is condensate to gas ratio (STB/MMscf). The output parameter is Q_g which stands for choke gas flow rate (MMscf/d). In the following, the results are presented. The AARD value of the model is 0.4 %. Same input variables were employed for the development of a reliable model on the basis of adaptive neuro-fuzzy inference system (ANFIS) algorithm. ANFIS was proposed by Jang in 1993 [24] which is accounted as a smart hybrid methodology composed and or combined with both fuzzy logic and artificial neural network. The AARD obtained for estimation of choke flow rate by using ANFIS is 43 %.

Neural Network is an information processing method based on the biological nervous systems, such as the brain, process information. They simulate the human brain in the following two ways:

1. A neural network obtains patterns through learning.
2. A neural network's pattern is stored within inter-neuron connection strengths known as synaptic weights.

Neural networks are used to large numbers of worldwide problems. Their prime gain is that they can recognize appropriate patterns for complex problems in comparison to conventional methods. The most common neural network model is the multi-layer perceptron (MLP). This type of neural network is known as a supervised network because it needs a measured output in order to learn. The goal of this type of network is to make a model that properly maps the input to the output using imported data so that the model can then be used to estimate output in case of lack of measurements [25-26]. The tanh-axon transfer function and Levenberg-Marquardt back propagation was used to establish ANN model. By optimization of the model based on the lowest AARD value, the number of hidden neurons in hidden layer was assumed 20.

Input parameters of the ANN model are BSW which expresses the ratio of water rate in total liquid rate, choke size (1/64 in), well head pressure (psi) and CGR, which is condensate to gas ratio (STB/MMSCF). The output parameter is Q_g which stands for choke gas flow rate (MMscf/d). In the following, the results of modelling by ANN model are reported. The AARD value of the model is 1.8 %.

LS-SVM is a modified version of SVM and a more simple method than SVM. The LS-SVM allows to handle linear and nonlinear multivariable problems and explains the multivariable problems comparatively fast way to analyze the structure. In this version, one finds the solution by solving a set of linear equations instead of a quadratic programming problem for classical SVMs [27-28]. To achieve optimum values of algorithm parameters (γ and σ^2), the LSSVM model is linked with an optimization approach known coupled simulated annealing (CSA). Having optimized, the values obtained by the CSA-LSSVM algorithm for the estimation of gas flow rates of choke are 0.526941 and 472.5468 for σ^2 and γ , respectively [29]. Input parameters of the LSSVM model are BSW which express the ratio of water rate in total liquid rate, choke size (1/64 in), well head pressure (psi) and CGR, which is condensate to gas ratio (STB/MMscf), as mentioned earlier. The output parameter is Q_g which stands for choke gas flow rate (MMscf/d), as mentioned earlier. The AARD value of the model is 1.7 %. Figure 1 illustrates a comparison between the values estimated by DT, ANFIS, LS-SVM, and ANN and the actual data of gas production rate. As clear from the figure, DT has the best performance among all models developed in this study.

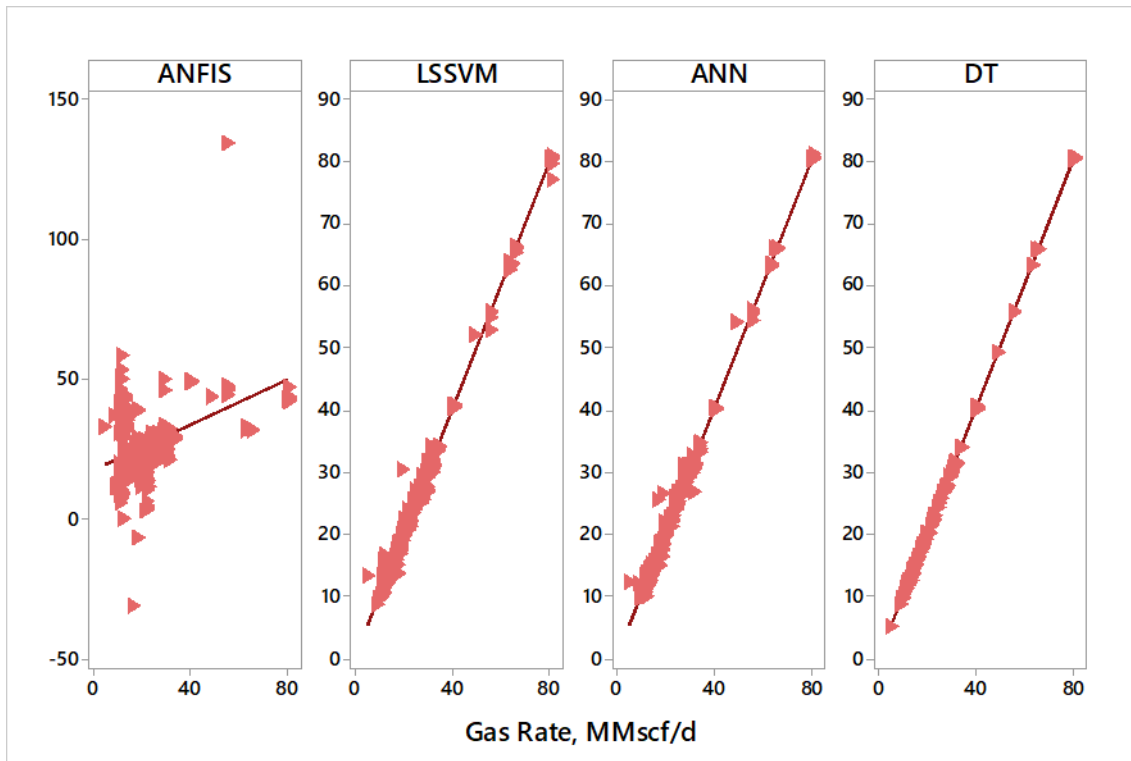


Figure 1. The crossplots for the values etimated by ANFIS, DT, ANN, and LS-SVM models versus the actual data of gas production rate

4. Development of a Model by GEP Approach

As previously pointed out, there is still a necessity to propose reliable methods for estimating gas production rates covering wide ranges of variables. An overview of previously reported studies reveals that BSW, choke Size, CGR and WHP are most effective variables for accurate determination of gas rates from the choke. Therefore, a simple method with four variables is proposed on the basis of gene expression programming in this study for the determination of gas rates from choke for one of Iranian gas condensate reservoirs. It is worthwhile to note that most of previously reported empirically derived correlations do not consider the BSW parameter for developing the model to estimate well choke flow. During development of the method by gene expression programming algorithm, the average absolute relative deviation was considered as an error function to measure the accuracy of the newly proposed model. Furthermore, some simple functions including +, -, /, and log were used to develop the equation. The final form of the method is as follow:

$$Q_g = 0.33217 BSW + 0.66434 S + \ln(CGR + WHP) + \frac{47.698 (BSW + 47.698)(BSW+WHP)^{\frac{1}{3}}}{CGR - WHP} - 3.063 \quad (5)$$

where Q_g stands for choke gas flow rate (MMscf/day), BSW expresses the ratio of water rate in total liquid rate, and S is the choke size (1/64 in), WHP denotes well head pressure (psi), and CGR is condensate to gas ratio (STB/MMSCF).

The results are presented in the following figure. The AARD value of the model is 14 %. Figure 2 indicates the cross plot of the values estimated by the newly proposed method versus the actual data of gas production rate. The results show an acceptable accuracy by applying this method.

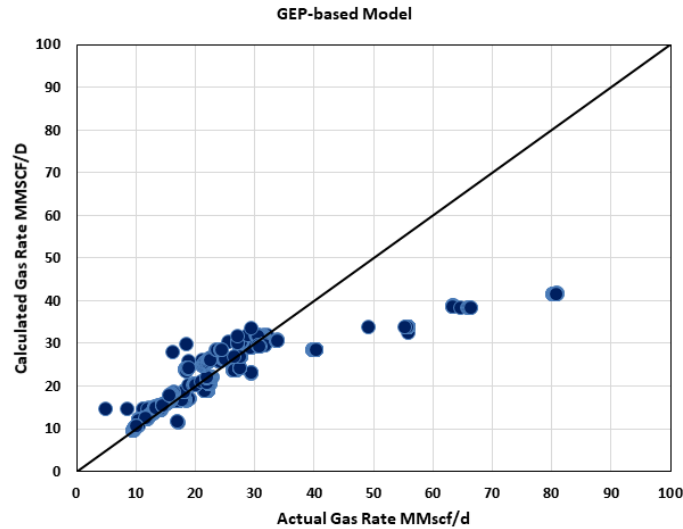


Figure 2. The crossplot for the values predicted by the newly proposed GEP-based method versus the actual data of gas production rate

5. Conclusion

The objective of this study was to find an appropriate modelling approach for choke multiphase flow performance. Three advanced methods were proposed to analyze the data and export reliable patterns to estimate gas flow rate. Besides, a GEP based model was presented to analyze the data. The AARD values for ANN, LSSVM, ANFIS and GEP models are 1.8%, 1.7%, 43% and 14%, respectively. A decision tree with AARD of 0.4 % is the best and accurate technique to estimate gas flow rate in comparison to other approaches. Regarding the model developed by gene expression programming, it shows a good match at low flow rates. Additionally, the accuracy of the GEP based model is decreased with increasing the rate.

References

- [1] Carroll III JA. 1990. Multivariate production systems optimization, Stanford University.
- [2] Rahimzadeh A and Mohammadmoradi P. Development of Choke Multiphase Flow Modeler. International Petroleum Technology Conference 2014.
- [3] Perkins TK. Critical and subcritical flow of multiphase mixtures through chokes. SPE Drilling & Completion, 1993;8(04): 271-276.
- [4] Sachdeva R, Schmidt Z, Brill J and Blais R. Two-phase flow through chokes, SPE Annual Technical Conference and Exhibition 1986. Society of Petroleum Engineers.
- [5] Guo B, Al-Bemani A and Ghalambor A. Improvement in Sachdeva's multiphase choke flow model using field data. Journal of Canadian Petroleum Technology, 2007; 46(05).
- [6] Osman ME and Dokla ME. Gas condensate flow through chokes, European Petroleum Conference 1990. Society of Petroleum Engineers.
- [7] Achong IB. Revised Bean and Performance Formula for Lake Maracaibo Wells. Shell Internal Report 1961.
- [8] Baxendel, PB. Bean Performance-Lake Wells. Shell Internal Report 1957.
- [9] Gilbert W. Flowing and gas-lift well performance, Drilling and production practice. American Petroleum Institute 1954.
- [10] Ros N. An analysis of critical simultaneous gas/liquid flow through a restriction and its application to flowmetering. Applied Scientific Research, 1960; 9(1): 374-388.
- [11] Ashford F. An evaluation of critical multiphase flow performance through wellhead chokes. Journal of Petroleum Technology, 1974; 26(08): 843-850.
- [12] Ashford F and Pierce P. Determining multiphase pressure drops and flow capacities in down-hole safety valves. Journal of Petroleum Technology, 1975; 27(09): 1,145-1,152.
- [13] Al-Attar H and Abdul-Majeed G. Revised bean performance equation for East Baghdad oil wells. SPE Production Engineering, 1988; 3(01): 127-131.

- [14] Fortunati F. Two-phase flow through wellhead chokes, SPE European Spring Meeting 1972. Society of Petroleum Engineers.
- [16] Safar Beiranvand M and Babaei Khorzough, M. Introducing a new correlation for multiphase flow through surface chokes with newly incorporated parameters. SPE Production & Operations, 2012; 27(04): 422-428.
- [18] Al-Khalifa MA and Al-Marhoun MA. Application of Neural Network for Two-Phase Flow through Chokes, SPE Saudi Arabia Section Technical Symposium and Exhibition 2013. Society of Petroleum Engineers.
- [19] Zarenezhad B and Aminian A. An artificial neural network model for design of wellhead chokes in gas condensate production fields. Petroleum Science and Technology, 2011; 29(6): 579-587.
- [20] Gorjaei RG, Songolzadeh R, Torkaman M, Safari M and Zargar G. A novel PSO-LSSVM model for predicting liquid rate of two phase flow through wellhead chokes. Journal of Natural Gas Science and Engineering, 2015; 24: 228-237.
- [21] Nejatian I, Kanani M, Arabloo M, Bahadori A and Zendehboudi S. Prediction of natural gas flow through chokes using support vector machine algorithm. Journal of Natural Gas Science and Engineering, 2014; 18: 155-163.
- [22] Osei-Bryson K-M. Evaluation of decision trees: a multi-criteria approach. Computers & Operations Research, 2004; 31(11): 1933-1945.
- [23] Sethi IK and Chatterjee B. Efficient decision tree design for discrete variable pattern recognition problems. Pattern Recognition, 1977; 9(4): 197-206.
- [24] Jang J-SR. ANFIS: adaptive-network-based fuzzy inference system. Systems, Man and Cybernetics, IEEE Transactions on, 1993; 23(3): 665-685.
- [25] Arulampalam G and Bouzerdoum A., A generalized feedforward neural network architecture for classification and regression. Neural Networks, 2003; 16(5): 561-568.
- [26] Rafiq M, Bugmann G and Easterbrook D. Neural network design for engineering applications. Computers & Structures, 2001; 79(17): 1541-1552.
- [27] Ding L-Z and Liao S. Approximate Model Selection for Large Scale LSSVM, ACML. Citeseer, 2011. pp. 165-180.
- [28] Ekici BB. A least squares support vector machine model for prediction of the next day solar insolation for effective use of PV systems. Measurement, 2014; 50: 255-262.
- [29] Vasan A and Raju KS. Comparative analysis of simulated annealing, simulated quenching and genetic algorithms for optimal reservoir operation. Applied Soft Computing, 2009;9(1): 274-281.

To whom correspondence should be addressed: Amir H. Mohammadi, Discipline of Chemical Engineering, School of Engineering, University of KwaZulu-Natal, Howard College Campus, King George V Avenue, Durban 4041, South Africa
amir_h_mohammadi@yahoo.com

EFFECT OF SALINITY ON FLOW PROPERTIES OF DRILLING FLUIDS: AN EXPERIMENTAL APPROACH

Emine Avci

Department of Petroleum and Natural Gas Engineering, Faculty of Engineering and Natural Sciences, Iskenderun Technical University, 31200, Iskenderun-Hatay, Turkey

Received November 6, 2017; Accepted March 3, 2018

Abstract

This work presents an investigation of the effect seawater on laboratory prepared water-based mud recommended to be used in drilling formation. The properties measured are plastic viscosity, yield point, mud weight, fluid loss, gel strength, cake thickness and pH. As a result, it is found that the seawater significantly affects the rheological properties of drilling mud. It is indicated that seawater-based muds have considerably lower viscosity, yield point than those of fresh water-based muds. However, the fluid loss, the mud cake thickness and the mud weight of seawater-based muds are higher than those of fresh water-based muds.

Keywords: *Bentonite; Drilling mud; Salinity; Seawater; Rheology.*

1. Introduction

The extraction of fossil fuels from offshore fields largely increased in the last five decades [1-2]. Drilling fluid, also called drilling mud, is the most significant component in the drilling process. Drilling fluids perform several functions including controlling formation pressures, maintaining hole integrity and stability, cooling and lubricating the drill bit and the drill string, cleaning the bottom hole, and suspending cuttings in the annulus when circulation is stopped or carrying them to the surface during drilling [3-4]. Therefore, the success of the drilling operations largely depends on the performance of the drilling fluids. Drilling mud should have certain rheological properties in order to perform these functions. This indicate that the factors which affect the rheological properties of the drilling mud require investigation. Traditionally, muds have been classified into three categories according to the base fluid used in their preparation. These are: oil, air and water. About 5-10% of the wells drilled use oil muds and a much smaller percentage use air. Most air-drilled wells are relatively shallow in hard, competent formations [5]. Most of the world's drilling operations use water-based muds and they mainly consist of water and bentonite [6]. Many offshore wells are drilled using a seawater system because of ready availability [7]. There are many studies in the literature considering the effects of a great deal factors, such as temperature, pressure, contaminants and various additive on the rheological properties of the drilling mud during the drilling. The aim of this study to investigate the effect of seawater used in offshore drilling operations on the rheological properties of bentonite-based drilling mud at ambient temperature.

2. Material and method

Initially, four different mud samples were prepared using seawater obtained from Iskenderun Bay which is seen in Figure 1. Seawater was mixed with 20 g, 30 g, 40 g and 50 g bentonite concentrations using a five-spindle multi-mixer (model 9B) for 20 minutes and these samples were labeled as S1, S2, S3 and S4, respectively. After mixing, each bentonite dispersion was poured in a covered container and left for 16 h to provide that the bentonite achieve the exact hydration at ambient temperature. In order to compare, four bentonite mud samples were also prepared with deionized water with same bentonite concentrations following the

same procedure, then these samples were also labeled as D1, D2, D3 and D4, respectively. Table 1 shows the concentrations of materials used and label names given in the prepared drilling muds. Prior to measurement, the samples were stirred for 5 min at high shear rate (11,000 rpm).



Figure 1. Map of the area obtained seawater

The rheological measurements were made on these samples prepared such as viscosity, yield point using OFI Testing Equipment, Inc. 8 Speed Viscometer (Model 800). The viscometer has 8 speeds (600 rpm, 300 rpm, 200 rpm, 100 rpm, 60 rpm, 30 rpm, 6 rpm and 3 rpm) as recommended by API to measure the rheological properties of drilling mud samples. Plastic viscosity (PV) and yield point (YP) were calculated from 300 and 600 rpm readings using following formulas from API Recommended practice of Standard procedure for field testing drilling fluids [8-9]:

$$PV (\mu_p) = \theta_{600} - \theta_{300} \text{ (cP)} \tag{1}$$

$$YP = \theta_{300} - \mu_p \text{ (lb/100ft}^2\text{)} \tag{2}$$

Filtration loss of the prepared samples were measured by using OFI Testing Equipment, Inc. Filter Press model (140-75) under a pressure of 6.894 bar (100 psi) for 30 min. Mud weights of the samples were measured by using the OFI Testing Equipment, Inc. mud balance model (900). Also pH and cake thickness values of drilling mud samples were measured using pH paper and vernier caliper, respectively. All of these studies carried out at room temperature.

Table 1. Types and concentrations of materials used in the formulated drilling muds

Drilling Fluid samples	Material amount	Drilling Fluid samples	Material amount
S1	Bentonite: 20 g Seawater: 500 mL	S3	Bentonite: 40 g Seawater: 500 mL
D1	Bentonite: 20 g Deionized water: 500 mL	D3	Bentonite: 40 g Deionized water: 500 mL
S2	Bentonite: 30 g Seawater: 500 mL	S4	Bentonite: 50 g Seawater: 500 mL
D2	Bentonite: 30 g Deionized water: 500 mL	D4	Bentonite: 50 g Deionized water: 500 mL

3. Result and discussions

The comparative rheological properties of mud prepared using seawater and mud prepared using deionized water are shown in Figure 2 for S1 and D1 samples. This figure shows that the shear stress values of the S1 sample are considerably lower than the shear stress values of D1 sample at all shear rates (Figure. 2A). The fluid loss through the mud cake to the formation of S1 sample is over 70 percent more than that of D1 sample in 30 min period (Figure. 2B). From fig. 2C, it can be noticed that the mud weight and cake thickness of the S1 sample are higher than those of D1 sample, while the plastic viscosity, yield point and pH values of the S1 sample are lower than those of D1 sample (Figure. 2C).

Figure 3 shows comparative rheological properties for S2 and D2 samples. From Figure 3, it can be observed that the tendency of rheological properties of S2 and D2 samples is quite similar to that of S1 and D1 samples. This indicates that the shear stress values (Figure 3A), the plastic viscosity, the yield point, pH values of sample S2 (Figure 3C) are lower than those of D2 sample; on the other hand, the fluid loss (Figure 3B), density and cake thickness values (Figure 3C) of S2 sample are higher than those of D2 sample.

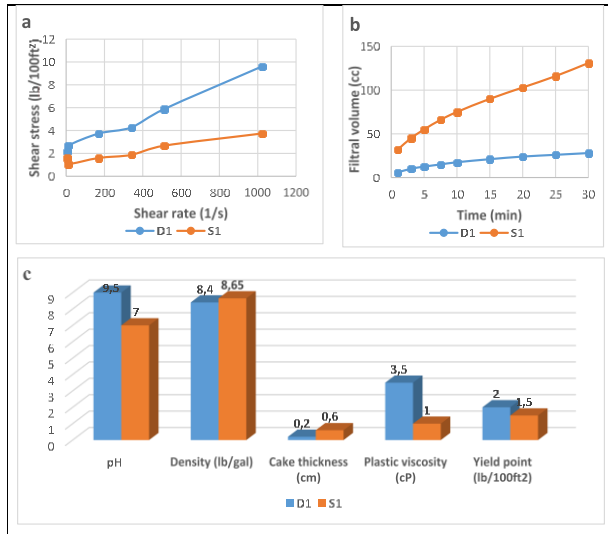


Figure 2. Comparison of rheological properties for S1 and D1 samples, a) Shear rate-shear stress relations b) Time-fluid loss relation, c) pH, density, cake thickness, plastic viscosity, yield point values

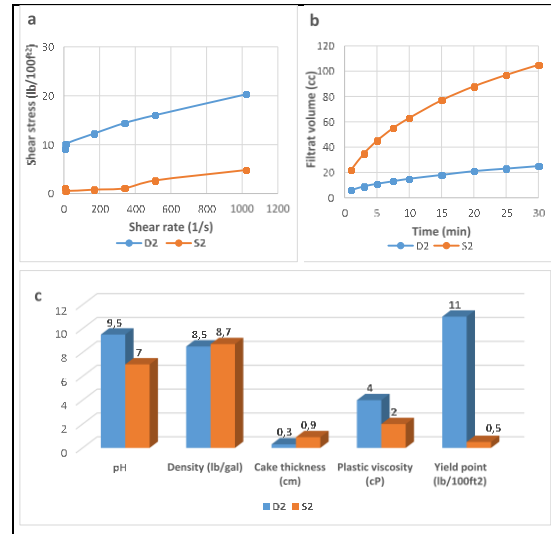


Figure 3. Comparison of rheological properties for S2 and D2 samples, a) Shear rate-shear stress relations b) Time-fluid loss relation, c) pH, density, cake thickness, plastic viscosity, yield point values

From Figure 4, it can be indicate that the tendency of rheological properties of S3 and D3 samples is similar to those of S1-D1 and S2-D2 samples as well. This indicate that the shear stress (Figure 4A), the plastic viscosity, the yield point, pH values (Figure 4C) of S3 sample are lower than those of D3 sample, while the fluid loss (Figure 4B), density and cake thickness (Figure 4C) of S3 are higher than those of D3 sample. However, it can be observed that there is an advanced difference particularly in yield point values.

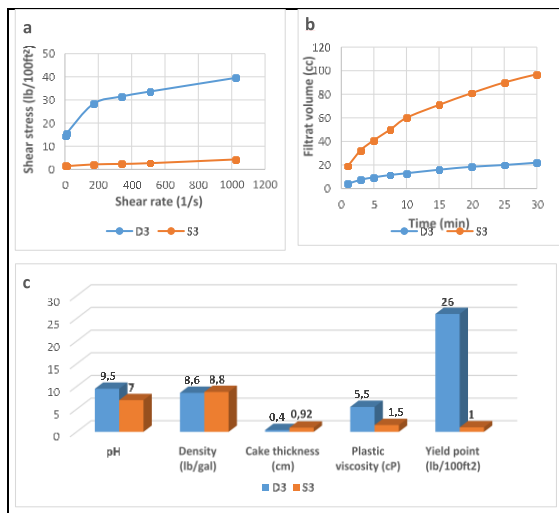


Figure 4. Comparison of rheological properties for S3 and D3 samples, a) Shear rate-shear stress relations b) Time-fluid loss relation, c) pH, density, cake thickness, plastic viscosity, yield point values

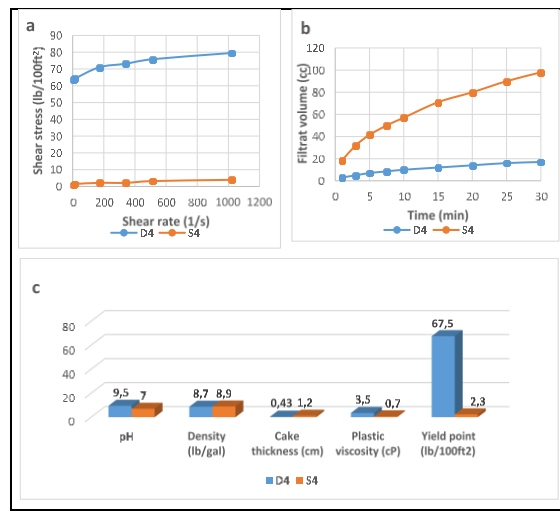


Figure 5. Comparison of rheological properties for S4 and D4 samples, a) Shear rate-shear stress relations b) Time-fluid loss relation, c) pH, density, cake thickness, plastic viscosity, yield point values

Figure 5 shows that the comparative rheological properties for S4 and D4 samples. It can be also noticed that the inclination of rheological properties of S4-D4 samples is similar to those of S1-D1, S2-D2 and S3-D3 samples. This indicate that the shear stress (Figure 5A), the plastic viscosity, the yield point, pH values (Figure 5C) of S4 sample are lower than those of D4 sample, while the fluid loss (Figure 5B), the density and the cake thickness (Figure 5C)

of S4 sample are higher than those of D4 sample. However, it can be noticed that the the difference between the values of S4 and D4 samples is higher than the values of the other samples (S1-D1, S2-D2, S3-D3).

4. Conclusions

Drilling fluid should have stable rheological properties during drilling operations. Based on this study, it is found that seawater dramatically affects the rheological properties of drilling mud. It is indicated that as bentonite concentration increased, both mud cake thickness and mud weights increased, whereas the fluid loss decreased and pH values remained steady for both types of mud and the differences of values related to seawater and fresh water-based increased. Also, it was observed that the viscosity, the yield point of seawater-based drilling mud were quite low compared to fresh water-based mud. Nevertheless, the fluid loss, the mud cake thickness and the mud weight were higher than those of fresh water-based mud. All of these are undesired consequence for drilling mud. Therefore, the use of seawater to prepare mud will immensely affect drilling performance and well cost.

References

- [1] Ghisel RG (editor). Fifty years of off shore oil, gas development. Hart Publications 1997: Houston, TX.
- [2] Terlizzi A, Bevilacqua S, Scuderi D, Fiorentino D, Guarnieri G, Giangrande A, Frascetti S. Effects of offshore platforms on soft-bottom macro-benthic assemblages: a case study in a Mediterranean gas field. *Marine Pollution Bulletin*, 2008; 56(7): 1303-1309.
- [3] Rooki R, Ardejani FD, Moradzadeh A, Mirzae, H, Kelessidis V, Maglione R and Norouzi M. Optimal determination of rheological parameters for herschel-bulkley drilling fluids using genetic algorithms (GAs). *Korea-Australia Rheology Journal*, 2012; 24(3) 163-170.
- [4] Sami NA. Effect of magnesium salt contamination on the behavior of drilling fluids. *Egyptian Journal of Petroleum*, 2016; 25(4), 453-458.
- [5] Caenn R, Chillingar GV. Drilling fluids: State of the art. *Journal of petroleum science and engineering*, 1996; 14(3-4): 221-230.
- [6] Kafashi S, Rasaei M, Karimi G. (2017). Effects of sugarcane and polyanionic cellulose on rheological properties of drilling mud: An experimental approach. *Egyptian journal of petroleum*, 2017; 26(2): 371-374.
- [7] Warren B, van der Horst PM, van't Zelfde TA. (2001). U.S. Patent No. 6,281,172. Washington, DC: U.S. Patent and Trademark Office.
- [8] Recommended Practice, 1988. Standard procedure for field testing drilling fluids, 12th ed. vol. 13 B (RP13B). API, Washington, USA, pp. 7 -9.
- [9] Mahto V, Sharma VP. Rheological study of a water based oil well drilling fluid. *Journal of Petroleum Science and Engineering*, 2004; 45(1): 123-128.

To whom correspondence should be addressed: Emine Avci, Department of Petroleum and Natural Gas Engineering, Faculty of Engineering and Natural Sciences, Iskenderun Technical University, 31200, Iskenderun-Hatay, Turkey, emine.avci@iste.edu.tr

GAS PROCESS SYSTEM EMPIRICAL TOOL FOR PREDICTING HYDRATE FORMATION

Emeka Emmanuel Okoro¹, Evelyn Bose Ekeinde², Kevin Igwilo¹ and Adewale Dosunmu²

¹ *Petroleum Engineering Department, Covenant University Ota, Nigeria*

² *Petroleum Engineering Department, University of Port Harcourt, Nigeria*

Received November 22, 2017; Accepted March 3, 2018

Abstract

The rapid formation of gas hydrates, promoted by typical high pressure/ low temperature operating conditions in deep water installations, is considered one of the most difficult problems with flow assurance. Understanding the conditions for the formation of hydrates is necessary to overcome the problems associated with hydrates. Ideally, the conditions for the formation of gas hydrates are determined experimentally in the laboratory; but this data is not always available. Therefore, correlation is used to determine the conditions for gas hydrate formation. Several models have been proposed that require more complex and longer computations to predict the conditions for the formation of gas hydrate over the years. In this study, it is crucial to develop a reliable and easy-to-use method for oil and gas practitioners'. The proposed correlation extends over a wide range of pressure (2000 to 25000kPa) and molecular weights (16 to 27). Consistent and accurate results of the proposed pressure range, temperature, and molecular weight are presented. Statistical error analysis is used to appraise the efficiency and accuracy of the correlation coefficient for estimating the formation of gas hydrate. This will guide designer and operator to select the optimal correlation for a particular application.

Keywords: Gas hydrate; Gas process system; hydrate prediction; correlations; Instability in Pipeline.

1. Introduction

Natural gas is becoming more important all over the world, as an important source of energy and as raw material for the processing industry. The increase in demand for natural gas in the energy matrix throughout the world has caused a great demand for exploration and production of the offshore proven reserves. The offshore industry is developing from shallow water fixed platforms to the development of deepwater field with floating facilities. This has created new problems for the prevention of hydrate during transportation and processing of natural gas in the subsea environment [1]. Hydration requires a condition that consists of having water in the pipeline; the pressure must be high, with a temperature that is low and the existence of methane, carbon dioxide [2].

The exploration deeper waters have rendered transporting of hydrocarbons and water mixture to onshore facilities through a single multiphase pipeline the only practical way. Currently, the responsibilities of processing the fluids on-site are considered very strict due to the cost of building and maintaining the complex offshore platforms with processing facilities [3]

In 1934, Hammerschmidt [4] discovered that the obstacle to the gas pipeline was not due to the formation of ice, but due to the formation of natural gas clathrate hydrate. History had it that, this discovery was the determining factor in raising a practical interest for oil and gas companies [1]. Gas hydrates are one of the serious economic and safety challenges in oil and gas industry in the exploration, extraction, production, transportation, and processing of natural gas and liquid. Hydrate formation can block pipelines and processing equipment. Formation of gas hydrates can occur during process operation and shut in periods. It can be very complex, difficult and expensive to remove them.

Hydrate plugging of hydrocarbon production conduits causes serious operational problems that can lead to significant and considerable economic losses. The ability to model and predict the emergence of hydrate plugging would help to improve design and operation of the facility in order to reduce the extent of such events. Methods for preventing and eliminating hydrates have been studied and developed using various approaches [5].

The purpose of this study is to develop a tool that can predict the conditions for the production of hydrates. The predicted conditions are compared with published used empirical methods.

2. Literature review

There are different approaches which can be applied to mitigation a plug of gas hydrates such as dehydration, heat management, and chemical inhibition [6]. Three methods have been used in the field; and among these methods, chemical inhibition is the most common to prevent and reduce gas hydrate formation [7].

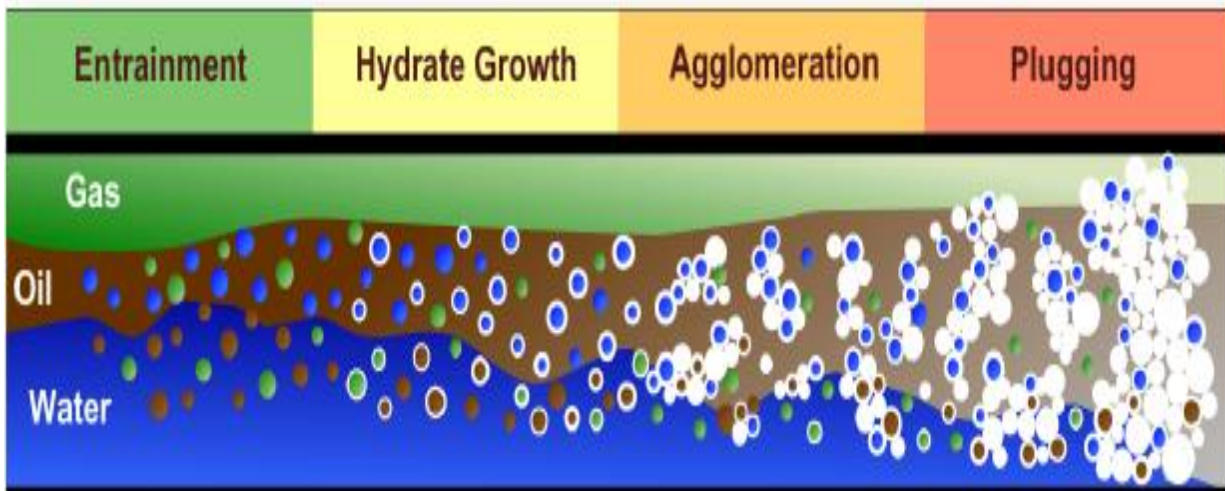


Figure 1. A conceptual model for hydrate formation (Source: Turner [8])

When speaking about the formation of hydrate, the vital elements relates to economics [9]. Since these problems can interfere with the process operations; thus, its higher value is directly related to economics. According to Obanijesu *et al.* [10], intensifying and improving research to explore more opportunities to avoid, identify, prevent or eliminate hydrate occurrence in the pipeline is a worthwhile investment as a consequence is catastrophic.

According to Huijie [11], the thermodynamics of hydrate formation has been extensively studied by researchers for many years, and data on some thermodynamic inhibitors have been acquired. These data can be useful for testing industrial design applications and predictive models. Several methods have been published for predicting hydrate formation in the presence of inhibitors.

The methods are mostly based on using cubic equations of state for the fluid phase. The statistical associated fluid theory has been investigated extensively since proposed and is very advantageous over traditional cubic equation of state. Salam *et al.* [12] in their study on prediction of hydrate formation conditions, outline some of the improvement that has been done on methods of hydrate formation prediction.

Bhangole *et al.* [13] extended van der Waals and Platteuw's to predictions of hydrate formation in the reservoir. They developed a model for pore-freezing that can be used to envisage gas hydrate equilibrium for pure CH₄, CO₂, and mixed CH₄-CO₂ system for any pure size distribution. They used Equation of State developed for bulk gas hydrate equilibrium conditions based on van der Waals-Platteuw's model. The model was implemented with FORTRAN code, and it can calculate gas hydrate saturation equilibrium at any given pressure, temperature; and also calculate hydrate equilibrium condition for salt in a mixed CH₄-CO₂ gas hydrate

system. Another model applied to an offshore and deep water environment is the work of Mohammadi and Tohidi [14]. They developed a model to predict the hydrate free zone in mixed salt and chemical inhibitors for deep water and offshore applications.

Prevention of formation of hydrate is of paramount important because this definitely saves 5-8% of total plant cost and several methods have been adopted in the prediction of hydrate free zone when designing transportation of gas. Gas has a different composition which makes their behavior and hydrate formation condition differs [12].

To optimize the cost of cleaning or remediation, the accuracy of forecasting conditions for the production of natural gas hydrates is very vital. The best way to determine the conditions for the formation of hydrate is to experimentally measure the formation of the composition of interest at high pressure and low temperature.

From a practical view, it will be almost impossible to establish the gas hydrate formation conditions for an infinite number of specific gas composition needed. Also, the experimental activities are both expensive and time consuming relative to industrial needs. It is necessary to form the prediction methods that will help for interpolation between the measured ones. Therefore, an accurate and simplified model is desirable for predicting natural gas hydrate conditions [19].

Several empirical correlations to predict hydrate formation conditions have been published by different researchers' [15-18]. It is obvious that a model that can predict hydrate plugging in a given production system will become a valuable tool. The results would be useful in both design and operations.

3. Methodology

In this study, correlations to determine the conditions for gas hydrate formation based on gas gravity method was programmed. The tool was assessed to match existing experimental data published in the literature under different system conditions. In the industry, precise forecasting tools are now required for hydrate plugging. Knowledge of the risk of hydrate plugging with greater accuracy will help to develop a system and also provide operational support.

In this study, over 30 data point was collected in three-phase equilibria of various gas systems. Data also include those published in some literature, and a review of the literature showed that pressure, temperature and specific gravity are common correlation variables.

3.1. Development of the new Tool

An accurate and simplified model is desirable for predicting natural gas hydrate. Among the thermodynamic models in the literature, only a few examples can predict reliable hydrate-formation conditions for the complex systems with a minimal error.

The proposed model was developed using the statistical analysis software and experimental data points (from literature) to find the top correlations midst the variables. Multiple regressions provided a powerful method used to correlate the formation temperature of hydrate with pressure, specific gravity and water-vapour pressure.

3.2.1. The new and existing correlations

In this study, the following method was used to develop this new correlation. Firstly, the hydrate formation temperatures were correlated as a function of pressure for various molecular weights. The calculated coefficients of these polynomials are correlated as a function of molecular weight. Already developed polynomials were applied to calculate the new coefficients so as to predict the condition for hydrate formation for natural gases.

Bahadori et al. correlation [20]

$$\ln T = a + b \left(\frac{1}{p}\right) + c \left(\frac{1}{p}\right)^2 + d \left(\frac{1}{p}\right)^3 \quad (1)$$

where, $a = A_1 + B_1M + C_1M^2 + D_1M^3$; $b = A_2 + B_2M + C_2M^2 + D_2M^3$; $c = A_3 + B_3M + C_3M^2 + D_3M^3$; $d = A_4 + B_4M + C_4M^2 + D_4M^3$.

The coefficients are given in the literature [20] .

Kobayashi correlation [21] ,

$$T = 1 \left/ \begin{matrix} A_1 + A_2 \ln r_g + A_3 \ln P + A_4 (\ln r_g)^2 + A_5 (\ln r_g)(\ln P) + A_6 (\ln P)^2 + A_7 (\ln r_g)^3 + \\ A_8 (\ln r_g)^2 (\ln P) + A_9 (\ln r_g)(\ln P)^2 + A_{10} (\ln P)^3 + A_{11} (\ln r_g)^4 + \\ A_{12} (\ln r_g)^3 (\ln P) + A_{13} (\ln r_g)^2 (\ln P)^2 + A_{14} (\ln r_g)(\ln P)^3 + A_{15} (\ln P)^4 \end{matrix} \right. \quad (2)$$

where: $A_1 = 2.7707715 \times 10^{-3}$; $A_2 = -2.782238 \times 10^{-3}$; $A_3 = -5.649288 \times 10^{-4}$;
 $A_4 = -1.298593 \times 10^{-3}$; $A_5 = 1.407119 \times 10^{-3}$; $A_6 = 1.785944 \times 10^{-4}$
 $A_7 = 1.130284 \times 10^{-3}$; $A_8 = 5.9728235 \times 10^{-4}$; $A_9 = -2.3279181 \times 10^{-4}$
 $A_{10} = -2.6840758 \times 10^{-5}$; $A_{11} = 4.6610555 \times 10^{-3}$; $A_{12} = 5.5542412 \times 10^{-6}$
 $A_{13} = -1.4727765 \times 10^{-5}$; $A_{14} = 1.3938082 \times 10^{-5}$; $A_{15} = 1.4885010 \times 10^{-6}$
 Also, $r_g = M_g/29$

Berg correlation [22]

For $0.555 \leq r_g < 0.58$

$$T = -96.03 + 25.37 \ln P - 0.64(\ln P)^2 + \frac{r_g^{-0.555}}{0.025} \left[80.61P + \frac{1.16 \times 10^4}{P+596.16} - (-96.03 + 25.37 \ln P - 0.64(\ln P)^2) \right] \quad (3)$$

For $0.58 < r_g \leq 1.0$

$$T = \frac{80.61P - 2.1 \times 10^4 - \frac{1.23 \times 10^3}{r_g^{-0.535}} - \left(1.23 \times 10^4 + \frac{1.71 \times 10^3}{r_g^{-0.509}} \right)}{P - \left(-260.12 - \frac{15.18}{r_g^{-0.535}} \right)} \quad (4)$$

3.3. This study correlation

The hydrate formation temperature **T** is a functional relationship between the operating pressure **P** and gas gravity γ_g of the mixture. In this study non-linear regression analysis was used to develop such relationship. The model utilized is

$$T = a_1 + P/\gamma_g \dots \dots \dots \quad (5)$$

The least-square minimization to solve equation 5 was formulated as follow. An objective function **f(c)** is defined by the error function given as:

$$f(c) = \sum_{i=1}^N r_i^2 \quad (6)$$

where the vector **c** = [a₁, a₂, a₃ ..., a₁₆] represents 16 independent variables called regression constants. The elements or **r** are dependent variables called residues.

The residue expresses the relative difference between the experimental hydrate formation temperature (**p, γ_g , T**) and the study's simulated hydrate temperature (**p, γ_g , T**). The residue for **N** number of data points is defined by

$$r_i = \frac{[(p,\gamma_g,c)_i - (p,\gamma_g,T)_i]}{(p,\gamma_g,T)_i}, i = 1, 2, 3, \dots, N \quad (7)$$

The requirement non-linear optimization is to find the update

$$c_{i+1} = \mathbf{arg\ Min}\{F(c)\} \quad (8)$$

To ensure convergence to a realistic constant, the non-linear optimization is controlled to enforce the descent direction such that the objective function at an iteration stage is greater than the objective function at the next iteration stage. That is,

$$f(c_{k+1}) < f(c_k) \quad (9)$$

Once, the descent direction is located, a step size that would give a good decrease in the objective function is chosen. Thus, the derivation of the hydrate formation model for this study;

$$\ln T = A_1 + A_2 \gamma_g + A_3 \gamma_g^2 + A_4 \gamma_g^3 + A_5 P^{-1} + A_6 \gamma_g P^{-1} + A_7 \gamma_g^2 P^{-1} + A_8 \gamma_g^3 P^{-1} + A_9 P^{-2} + A_{10} \gamma_g P^{-2} + A_{11} \gamma_g^2 P^{-2} + A_{12} \gamma_g^3 P^{-2} + A_{13} P^{-3} + A_{14} \gamma_g P^{-3} + A_{15} \gamma_g^2 P^{-3} + A_{16} \gamma_g^3 P^{-3} \quad (10)$$

The coefficients of A₁ to A₁₆ are given in table 1.

Table 1 Tuned coefficients used to predict hydrate formation in this study

Coefficients	120kpa<P<40000 kPa	120kpa<P<5000 kPa	5000kpa<P<40000 kPa
	$\gamma_g > 0.79$	$\gamma_g < 0.79$	$\gamma_g < 0.79$
A1	6.4185	-4.181	7.096
A2	-2.552493	42.688	-6.322
A3	2.991437	-61.17434	9.5033
A4	-1.158472622	28.998521	-4.6997603
A5	-8642.6	45280	-125800
A6	29705.57	-198998	550710
A7	-34452.406	287958.4	-801136.6
A8	13279.8105	-137602.738	385346.2
A9	11590000	-83170000	921900000
A10	-40165000	365400000	-4068700000
A11	46549350	-529914100	5955962000
A12	-17899087.1	253645600	-2882535910
A13	-4020000000	5858000000	-2.105E+12
A14	13893900000	-28022700000	9.3177E+12
A15	-16004230000	43176940000	-1.36864E+13
A16	6124077900	-21652554200	6.64571E+12

3.4. Error analysis

The statistical error analyses were applied to test the performance and accuracy of the proposed hydrate formation correlations and table 4 data was used for this process. The criteria adopted in this study was average percent relative error.

Table 2. Experimental data used for comparison (Source: Bahadori and Vuthaluru [23])

Pressure (kPa)	Gas molecular weight	Experimental temperature	Pressure (kPa)	Gas molecular weight	Experimental temperature
3157.8	16	274.82	4757.38	20.3	288.71
4136.85	16	277.59	23442	20.3	297.04
5515.81	16	280.37	496.42	23.2	272.04
1723.69	17,4	277.59	1930.53	23.2	283.15
3309.48	17.4	283.15	11721.09	23.2	294.26
6756.86	17.4	288.71	758.42	26.1	277.59
18098.74	17.4	294.26	1585.79	26.1	283.15
2688.96	18,85	283.15	17926.37	26.1	297.04
14134.25	18,85	294.26	413.69	29	274.82
827.37	20.3	274.82	1344.48	29	283.15
2344.2	20.3	283.15	3033.69	29	288.71

4. Results and discussion

The type of hydrate data applied is the formation pressures and temperatures. This type of data is most significant for natural gas applications. We summarized the most accessible experimental data of this type, which were compiled as a basis for comparing reputable correlations such as Berg, Bahadori, and Kobayashi correlations. The experimental data on

hydrate formation conditions were compared with those calculated by the proposed correlation and included in the program.

Using software for statistical analysis, we applied a regression model to the experimental data points to find the best correlations among the variables. The data points include several samples ranging from gas mixtures to non-hydrocarbon and pure hydrocarbon components. To confirm the correlations accuracy and compare the predicted results with the experimental data, a statistical error analysis was used for these correlations.

The resulting predictive tool will improve the design process of production facilities and estimate hydrate plugging risk in any specific scenario.

4.1. Comparison of new correlation with existing correlations

As a basis for comparison, several authoritative correlations were selected; Berg [22], Kobayashi *et al.* [21], and Bahadori *et al.* [23]. Using the same hydrate conditions, the results of the proposed new correlations were compared with the existing correlation. Figure 2 shows a comparison of the proposed method and existing correlation results. It was deduced that the proposed correlation shows a higher yield in comparison with other existing correlations and estimates the conditions for the formation of hydrates.

Figure 2. Proposed new correlation and existing correlations

Pressure [kpa]	Molar Weight	Temperature (K)					RUN	Error	
		Experimental Temperature	Study (2017)	Bahadori (2009)	Kobayashi (1987)	Berg (1986)		Study	
3157.8	16	274.82	276.388	270.3238499	276.7638	254.76		Study	0.82462
4136.85	20	277.59	285.971	282.9295528	291.9577	200.813		Bahadori	0.8346
5515.81	16	280.37	286.537	285.772696	282.298	260.846		Kobayashi	0.85419
								Berg	9.55322
3309.48	17	283.15	281.36	276.1457197	283.5376	189.902			
6756.86	17.4	288.71	300.198	296.238329	290.7906	203.386			
18098.7	17.4	294.26	294.182	295.447175	293.8896	229.803			
2688.96	18.85	283.15	275.4	275.2947253	287.5313	191.518			
14134.3	18.85	294.26	294.757	297.3329057	294.582	229.443			
2344.2	26	283.15	295.828	268.917811	289.5894	196.569			
4757.38	20.3	288.71	288.277	284.7554211	292.9642	204.174			
23442	20.3	297.04	296.556	296.7332495	288.9319	248.761			
11721.1	23.2	294.26	294.596	292.8311869	293.43	231.706			
17926.4	26.1	297.04	296.186	295.2819701	285.2685	246.558			

From the study, we can agree that empirical expressions are a vital tool in predicting gas hydrate stability in different systems. Figure 2 illustrates that the proposed new correlation gives the accurate results in all pressure ranges and specific gas gravities when the temperature at which hydrate will form a certain pressure is predicted. This consistency was not matched by any of the correlations used in the survey range.

Figure 3. Proposed new correlation and existing correlations - another hydrate predictions

Pressure [kpa]	Molar Weight	Temperature (K)					Error
		Experimental Temperature	Study (2017)	Bahadori (2009)	Kobayashi (1987)	Berg (1986)	
3021.2	16	274.82	275.087	269.4604347	276.3253	254.268	Study 0.70187
3833.21	20	277.59	284.145	281.6952026	291.4776	199.368	Bahadori 0.71784
4968.99	16	280.37	284.843	275.8663379	281.2711	259.723	Kobayashi 0.85625
3299.89	17	283.15	281.284	276.0964311	283.5121	189.866	Berg 9.03223
5988.12	17.4	288.71	297.48	295.1658945	289.9556	200.857	
16923.4	17.4	294.26	293.81	295.3878128	293.989	227.756	
3921.8	18.85	283.15	286.531	282.3128871	290.3204	197.455	
14331.5	18.85	294.26	294.823	297.3056068	294.5442	229.866	
22222	26	283.15	296.675	296.0862807	280.9572	252.789	
4977.72	20.3	288.71	289.118	285.3494313	293.2018	205.147	
25557	20.3	297.04	296.946	296.9100416	287.5872	251.325	
10453.3	23.2	294.26	294.157	292.112665	294.061	228.314	
18036.5	26.1	297.04	296.202	295.307787	285.1549	246.74	

5. Conclusion

The proposed correlation holds for a wide range of temperatures, pressure (2000 to 25000kPa) and molecular weights (16 to 27). Consistent and accurate results of the proposed pressure range, temperature, and molecular weight were presented. For all conditions, statistical error analysis was used to estimate the efficiency and accuracy of the correlation coefficient for estimating the formation of gas hydrate. The tool will guide the operator to select the best correlations for their particular applications. The results of the hydrate formation conditions estimated by the previous correlations were compared with the experimental data. From this comparative study, we can conclude that;

1. The current study and Kobayashi correlation results close to the experimental results at the investigated range of temperature, pressure and molecular weight.
2. The composition of the gas system plays a very important role in determining the temperature or pressure of hydrate formation. This means that two gas systems with the same specific gravity can form hydrate under different conditions.
3. The predicted results are in most cases are approximately the same with the experimental data; thus, the gas hydrate model developed in this study can be used to establish a flow assurance strategy.

Acknowledgement

The authors wish to express their thanks to Department of Petroleum Engineering, Covenant University, and the entire Management of Covenant University Canaan Land Nigeria; for their support and enabling the environment to embark on this study.

References

- [1] Akpabio MG. Hydrate prevention is subsea Natural Gas production. Faculty of Science and Technology, Institute of Petroleum Technology; Department of petroleum Engineering and Applied Geophysics. Norwegian University of Science and Technology 2012.
- [2] Ahsan S. Preventing Hydrate formation in Gas Transporting Pipe Lines with Synthetic Inhibitors. International Journal of Chemistry; 2013; [01], ISSN 2306-6415.

- [3] Montini M, Humphrey AI, Watson MJ and Johnson AE. A probabilistic approach to prevent the formation of Hydrates in Gas production systems. 7th International conference on Gas Hydrates 2011, Edinburgh, Scotland, United Kingdom.
- [4] Hammerschmidt EG. Formation of gas hydrate in natural gas transmission lines, 1934. *Ind. Eng. Chem.*, 1934; 26: 851-855.
- [5] Nakarit C. Gas Hydrate formation and control by the use of chemicals. Faculty of Science and Technology, Department of Mathematics and Natural Science. University of Stavanger 2012, Norway.
- [6] Sloan ED and Koh CA. Clathrate hydrates of natural gases. Boca Raton, Fla.: CRC Press. XXV,2008; 721 s.
- [7] Mokhatab S, Poe WA and Speight JG. *Handbook of Natural Gas Transmission and Processing*. Gulf Professional Publishing 2006, MA, USA. p.16, 19, 33.
- [8] Turner D. Clathrate hydrate formation in water-in-oil dispersions. Ph.D. Thesis. 2005 Colorado School of Mines. Golden, Colorado, USA.
- [9] Jonassen AH. Distribution of Hydrate inhibitors in processing of Gas condensate. Petroleum Geoscience and Engineering, Norwegian University of Science and technology 2013.
- [10] Obanijesu EO, Pareek V, Gubner R and Tade MO. Hydrate formation and its influence on Natural gas pipeline internal corrosion. *NAFTA*, 2011; 62(5-6):164 – 173.
- [11] Huijie W. Measurement and prediction of Gas Hydrate equilibrium conditions in the presence of inhibitors. Faculty of Graduate Studies, Chemical and Biological Engineering; University of British Columbia 2005.
- [12] Salam KK, Arinkoola AO, Aranomi DO and Ayansola YE. (2013): Prediction of Hydrate formation conditions in Gas pipelines. *International Journal of Engineering Sciences*, 2013; 2(8); 327 - 331.
- [13] Bhangole AY, Zhu T, Mc Grail BP and White MD. A model to predict gas hydrate equilibrium and gas hydrate in the process media including mixed CO₂ –CH₄ Hydrates”, paper SPE 99759 paper presented at the 2006 SPE/DOE symposium on improved oil recovery held in Tulsa, Oklahoma, 22-26 April 2006, Pp. 1-7.
- [14] Jadhawar P, Mohammadi AH, Yang J and Tohidi B. Subsurface Carbon Dioxide Storage through Clathrate Hydrate Formation, in *Advances in the Geological Storage of Carbon Dioxide*, Amsterdam 2006: Springer, p. 111
- [15] Carson DB and Katz DL. Natural gas hydrates, *Trans., AIME* 1942; 146: 150.
- [16] Katz DL. Predictions of conditions for hydrate formation in natural gases, *Trans. AIME*, 1945; 160: 140-144.
- [17] Paez JE, Blok R, Vaziri H and Islam MR. Problems in hydrates: mechanisms and elimination methods’, SPE paper No. 67322, SPE production operations Symposium, 26-28 March 2001, Oklahoma City.
- [18] Carroll JJ. An examination of the prediction of hydrate formation conditions in sour natural gas’, GPA Europe, Spring Meeting Dublin, May 19-21 2004, Ireland.
- [19] Hoseini-Nasab SM, Vafaei M, Mohamedi A and Izadpanah AA. Development of new Empirical correlation for predicting Hydrate formation conditions. *Proceedings of the 7th International Conference on Gas Hydrates*, Edinburgh, Scotland, United Kingdom; July 17 – 21 2011.
- [20] Bahadori A, Vuthaluru HB, Mokhatab S, and Tade MO. Predicting hydrate forming pressure of pure alkanes in the presence of inhibitors. *Journal of Natural Gas Chemistry*, 2009; 17, 249-255.
- [21] Kobayashi R, Kyoo YS, Sloan ED., in: Bradley HB. et al. Eds., *Phase Behavior of Water Hydrocarbon Systems*, Petroleum Engineering Handbook, SPE, Dallas, Richardson, TX, 1987, pp. 25-13.
- [23] Bahadori A and Vuthaluru HB. A novel correlation for estimation of hydrate forming condition of natural gases. *Journal of Natural Gas Chemistry*, 2010; 18(4): 453-457.

To whom correspondence should be addressed: Emeka Emmanuel Okoro, Petroleum Engineering Department, Covenant University Ota, Nigeria,

VARIATIONS IN SURFACE POTENTIAL CHARACTERISTICS OF SELECTED SHALES FROM CENTRAL LUCONIA, OFFSHORE SARAWAK- MALAYSIA

*EvelynLove Fosu-Duah**, *Eswaran Padmanabhan*, *José Antonio Gámez Vintane*

Universiti Teknologi PETRONAS, Department of Geoscience, 32610 Perak Darul Ridzuan, Tronoh-Malaysia

Received November 3, 2017; Accepted January 8, 2018

Abstract

Surface potential measurements deduced from electrophoretic mobility were made on organic shale from the potential source rocks from Central Luconia, offshore Sarawak basin, Malaysia, with the aim of determining the ionic binding properties of the rocks. Variations in zeta potential were attributed to protonation and deprotonation reactions occurring on amphoteric sites (Al-OH and Si-OH) of kaolinite, which is the dominant clay mineral phase among the shales. Dissolution of Al³⁺ from the crystal lattices of muscovite and contribution from illite were also considered as surface potential variants in specific samples. The influence of shale chemical composition and organic matter content on surface charge characteristics was studied by correlating results from total organic content analyses, X-ray fluorescence spectroscopy, and isoelectric points. Organic matter showed no relationship with isoelectric points, but an enhancement of isoelectric points was observed with increasing Al₂O₃ and Si/Al ratios.

Keywords: Isoelectric Point; Kaolinite; Organic Matter; Shale; Zeta Potent.

1. Introduction

Zeta potential (ζ) is the potential difference generated due to the differences in particle/ion concentration at the boundary of hydrodynamic shear or slipping plane [1]. It holds information on the electric double layer (Figure 1) of charged particles [2]. The sign of these measurable electric data is similar to that of excess charge particles moving with the adhered layer of counter ions, and the magnitude is proportional to the particle charge [2]. The theory of zeta potential is detailed by Müller [3] so that only a brief background is given here.

Generally, particulate shales possess surface charges generated through mechanisms such as differential ion adsorption from the electrolyte solution, differential ion dissolution from a crystal lattice, surface anisotropy, isomorphous substitution and ionization of surface functional groups; the so-called Nernst potential. The degree of surface potential generation is known to be dependent, to a greater degree, on solution conductivity, electrolyte concentration, and pH, but it seems that the effect of pH is mostly the subject of scientific discussion [6]. The dependence of surface potential on solution pH is important for the present study because shales are composed of admixtures of clay minerals that bear surface variable charges.

The net charge on the shale particles affects the distribution of surrounding ions which results in an increase in the concentration of counter ions. The region of the extent of this charge distribution influence is termed the electric double layer (EDL) [2-3]. The EDL consists of an inner stern layer and an outer diffuse layer. Particle movement in solution due to an applied voltage causes the diffuse layer to shorn off. Hence particles obtain charge due to the loss of the counter ions. The potential difference at the plane of shear; zeta potential is the subject of interest in this research.

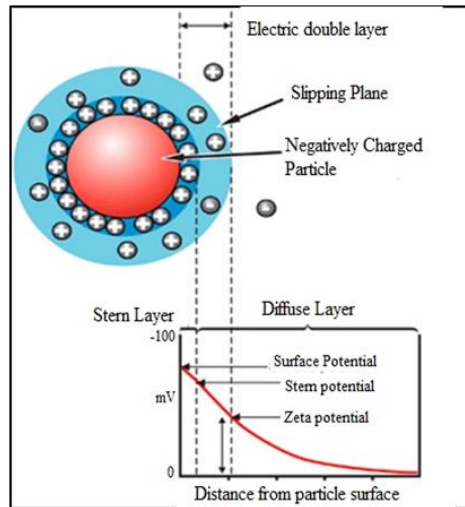


Figure 1. Schematic Representation of EDL and ζ modified after [4-5]

The measured magnitude of zeta potential is a good index of the magnitude of electrostatic repulsive interaction between shale particles as such can be used to predict and control the stability of the shale particles in dispersion [7]. Generally, the dividing line between stable and unstable suspensions is generally within the range of $+30 \text{ mV} \geq \zeta \geq -30 \text{ mV}$. All particles that fall outside this range are considered stable. The point of least stability is when ζ is zero, and the pH of occurrence is termed the isoelectric point (IEP) [7]. ζ is mostly deduced from electrophoretic mobility (EM) [7]. Besides its experimental accessibility, the parameter is known to be intricately related to many geological processes. Zeta potentials do not only influence organic matter (OM) accumulation in source rocks [9-10], but their interactions in aqueous solutions control gas adsorption and fluid flow rate [11] through reservoirs. Thus, as it is also well-known, the zeta potential is the most important factor controlling the distribution of hydrocarbons in pores [12].

The zeta potential of shale particles is seldom well-defined. The heterogeneities in surface potential in aqueous media are caused by complexities in the crystal structures and chemical composition of the mineralogical components of the shale. Foreign surface-bound materials such as organic matter can be an additional source of heterogeneities to surface potential. The layered silicates also account for most variable surface potential in shales [13] due to the presence of charges on their lamellae [6,14-15]. Measured surface potential due to clay minerals in shale is mostly high in magnitude as compared to that from other reservoir rocks such as coarse siliciclastics and carbonate materials, which might probably explain the occurrence of large quantities of hydrocarbon as 'sorbed gas' in unconventional shale settings [16-21]. The type of clay mineral present has also been pointed out to be a major influence on the sign and magnitude measured in the shale particles.

El-Swaify [22] and later Nmegbu and Spiff [23] found the inextricable relationship between physicochemical properties of particulate matter in geological suspensions and zeta potential. For example, the sign and magnitude of zeta potential is known to govern important properties such as adsorption, flocculation, coagulation and aggregation [6, 24] a brilliant idea which has been successively exploited and applied in effective hydrocarbon evaluation [12] and oil gangalia displacement (Sensu Gu *et al.* [25] and Nmegbu and Spiff [23]). Zeta potential studies have also been used to estimate the amount of excess conductivity due to clay minerals in hydrocarbon estimation studies using resistivity logging [26-27].

Although all these aspects are well documented and published, no paper deals with the zeta potential generated on the surfaces of shales from Central Luconia of the Sarawak basin of Malaysia. In this regard, this study is aimed at characterizing and determining the variations of the zeta potential generated by selected shales from Central Luconia.

2. Materials and methods

Powders of five onshore samples labelled CL1 to CL5 from offshore Central Luconia (Cycle III) were used for the study. Samples were recovered from well named "E15-1" E at shaly intervals in an otherwise carbonate succession.

Mineralogical compositions were derived from X-ray diffraction (XRD) patterns measured on randomly oriented powders. Analyses were performed on the fine fraction from representative shale samples of uniform crystallite sizes achieved through milling with a Fristch - Pulveristte 2 mill and procedures detailed by Macedo and Bryant [28]. Diffractograms were recorded in the 2θ in the range of 3° to 60° with a scan speed of $1^\circ/20/\text{mm}$. All reported mineral compositions relate to the crystalline content of the analyzed samples. Fourier Transform Infrared (FTIR) spectroscopy was achieved on an Agilent Technologies Cary 660 Series FTIR Spectrometer. Samples of 2 mg and 0.5 mg were dispersed in PIKE MIRACLE diamond attenuated total reflectance spectroscopy (ATR) to record optimal spectra in the regions of 4000 to 500 cm^{-1} with a resolution of 4 cm^{-1} and 64 scans. Mineral morphologies were determined by Field Emission Scanning Electron Microscopy (FESEM).

The chemical composition of the shales was determined by X-ray fluorescence (XRF) spectroscopy using a Bruker S8 Tiger wavelength dispersive X-ray fluorescence spectrometer. Total organic carbon (TOC) was determined on bulk and fractionated sediment samples using an Analytikjena carbon analyser.

Zeta potential (ζ) measurements of the samples were made with an Anton Paar Surpass™ Electrokinetic Analyzer (SEA) at $25 \pm 0.1^\circ\text{C}$. The instrument is equipped with an attract software which automatically converts electrophoretic mobility of streaming potential of particles to ζ using the Helmholtz-Smoluchowski equation (1).

$$\zeta = \frac{4\pi V}{\varepsilon} \text{EM} \quad (1) \quad [29]$$

where, EM = electrophoresis mobility; V = viscosity of the suspension; ε = dielectric constant; Π = constant; and ζ = zeta potential.

The procedure measures how fast charged particles move under the influence of an applied electric field. The bigger the charge particles carry; the faster particles move.

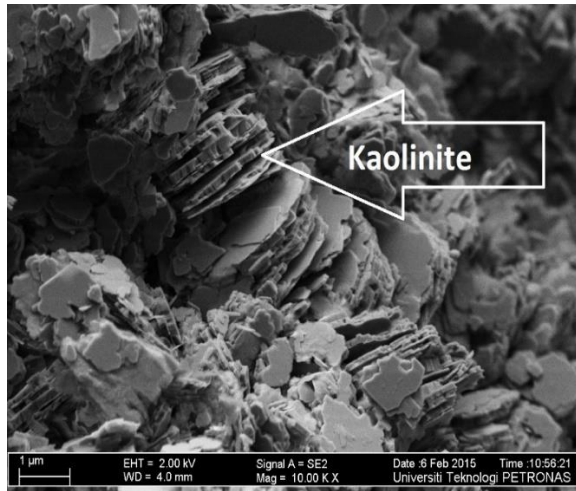
Stock dispersions were diluted to ~ 0.05 g/L solid content, and the salt concentration of dilute systems was adjusted to a constant concentration of KCl (0.001M). Values of pH of dilute dispersions were determined directly and adjusted with HCl and KOH between $2 < \text{pH} < 10$ before the introduction of samples into the capillary cell. A titration unit in the Surpass™ electrophoretic measuring system, which adjusted the pH of the sample suspension to pre-programmed values and to selected rates of titration, made isoelectric (IEP) identification possible with commensurate precision with a single sample.

3. Results and discussion

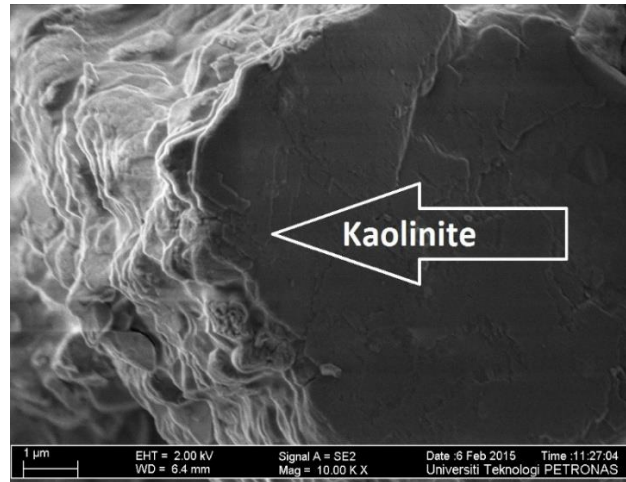
A summary of results from XRF, TOC and zeta potential analysis of the five samples are presented in Table 1. Sample mineralogy after XRD, and ATR-FTIR analyses are presented in Table 2. Figures 2a-e give a visual representation of each sample mineralogy in FESEM micrographs. Sample values of SiO_2 and Al_2O_3 are indicated in Figure 3.

Table 1. Chemical composition and pertinent physical properties of shale samples

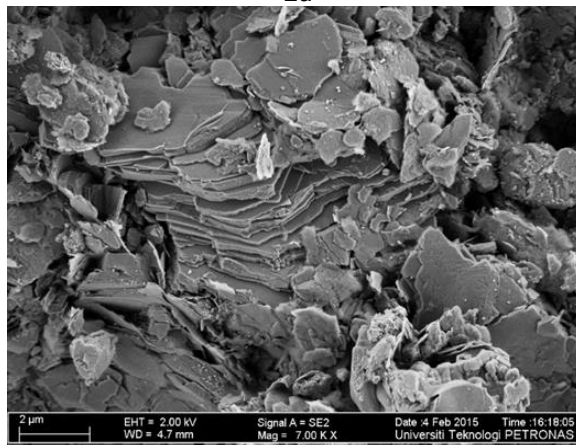
Sample ID	Sample composition after XRF			TOC (%)	IEP
	SiO_2 (%)	Al_2O_3 (%)	$\text{SiO}_2:\text{Al}_2\text{O}_3$		
CL1	52.31	18.10	0.3480	0.47	5.47
CL2	54.60	18.50	0.3388	0.72	3.10
CL3	51.80	17.90	0.3456	2.36	5.05
CL4	51.40	17.80	0.3463	0.94	4.18
CL5	51.20	18.05	0.3525	0.67	5.60



2a



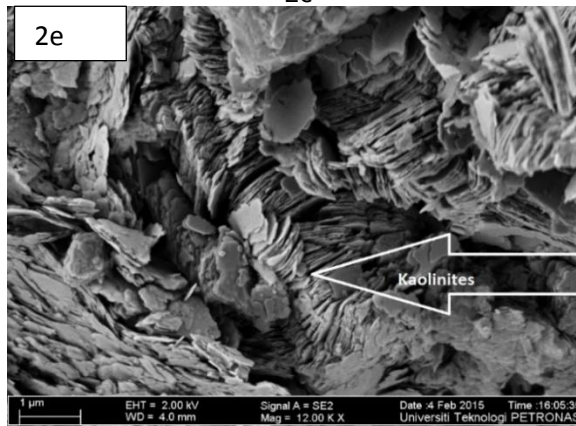
2b



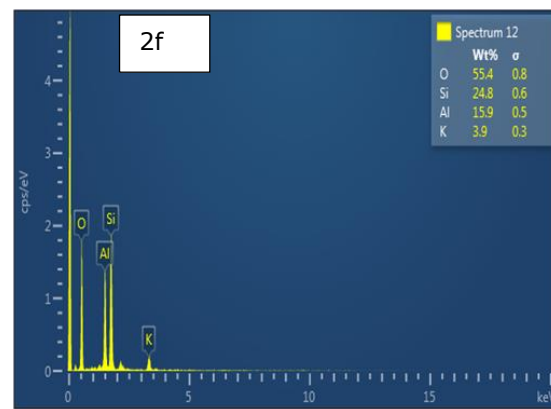
2c



2d



2e



2f

Figures (2a-e) FESEM micrographs showing the dominance of the clay mineral kaolinite in samples C1 to C5. (2f): Representative EDS spectra of the dominant clay mineral in the studied samples

Table 2. Summary of mineralogical results after XRD and ATR-FTIR

Sample ID	Illite	Kaolinite	Muscovite	Quartz
CL1		✓	✓	✓
CL2		✓	✓	✓
CL3	✓	✓		✓
CL4		✓	✓	✓
CL5		✓	✓	✓

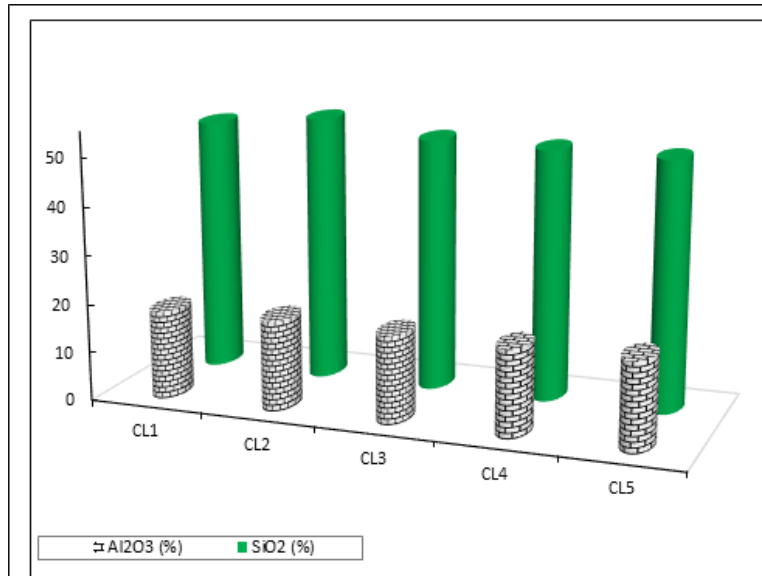


Figure 3. Distribution of Al₂O₃ and SiO₂ in the shale samples

3.1. Mineralogy

The mineralogical composition of all five samples is fairly uniform and composed of quartz and clay minerals. Among the latter, the presence of kaolinite is the majority in all samples, followed by muscovite/illite (Table 1). The dominance of kaolinite as the major clay mineral phase is concluded after the intensity readings of XRD and FTIR peaks. This is confirmed by visual observations on FESEM micrographs (Figures 2a to 2e).

3.2. Chemical composition

Geochemically, the SiO₂ content of the shales range from 51.20% to 54.60%, with an average of 52.26% (Figure 3). Thus the average SiO₂ in the shales studied herein is below that given by Pettijohn [30] (58.50%) and Gromet *et al.* [31] (64.82%). Al₂O₃ concentrations are within the range of 17.80% and 18.50%. Sample CL2 reported the highest percentage of Al₂O₃, while CL4 reported the least (Table 2; Figure 3). The average Al₂O₃ concentration in the studied Central Luconia shale samples under investigation is relatively higher than that reported by both Pettijohn [30] and Gromet, *et al.* [31], which are 15.40% and 17.05% respectively.

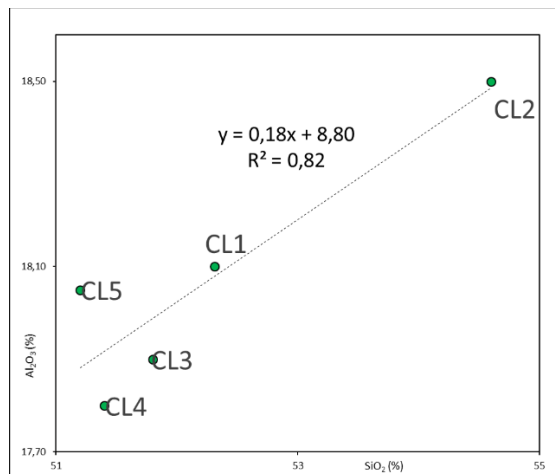


Figure 4. Relationship between SiO₂ and Al₂O₃ in the samples

Obviously, after Table 2, SiO₂ is the most abundant chemical constituent of the studied Central Luconia shale samples, which is consistent with the work by Gromet *et al.* [31]. In general, according to Pettijohn [30], SiO₂ exists in shales as a part of clay minerals, as undecomposed detrital silicates and as free silica. Al₂O₃, like SiO₂, may also exist either as a part of clay minerals or as free aluminium hydroxide minerals (e.g., gibbsite). However, in this study, the strong positive correlation ($R^2 = 0.82$) between SiO₂ and Al₂O₃ (Figure 4) is a strong indicator that these major oxides are associated with the aluminosilicates [32]. This is consistent with the occurrence of clay minerals identified by XRD, FTIR, and FESEM (Figure 2a to 2e) analyses, among which kaolinite is the dominant phase.

3.3. Electrochemistry-Zeta potential

Zeta potential (ζ) values have been estimated from the five shale samples after the electro-phoretic mobility, using the equation (1) over a pH range of 2 to 10. Those values have been used to characterize the development of surface potential on amphoteric sites on mineral constituents. Values are represented as a function of pH in Figures 5a-b. Marked changes in the development of ζ were observed in all the shales as a function of pH, with absolute negative ζ decreasing with decreasing suspension pH. The reverse is true for basic conditions. Zeta potential (ζ) reported in the shales is within the range of +37 mV to -30 mV. The average positive and negative ζ reported for the five samples are +25.51 mV and -17.6 mV respectively. Samples CL2 and CL5 reported the least negative ζ (-10 mV). The highest positive zeta potential of +37 mV was recorded in sample CL3 (Figure 5a). The zeta potential values presented herein are within the range of values reported for shale in the literature [33-34].

All the samples reported a distinguished pH identified as the isoelectric point (IEP) where the measured ζ recorded in the shale equals to zero. The range of IEP measured in the samples is between 3.10 and 5.60. The lowest and highest IEP were measured in samples CL2 and CL5 respectively. An average IEP of 4.68 is herein calculated for the shale.

The dependence of ζ -generation on pH is often attributed to the protonation and deprotonation of potential-determining ions on the surfaces of organic matter [35] and mineral surfaces [36-37].

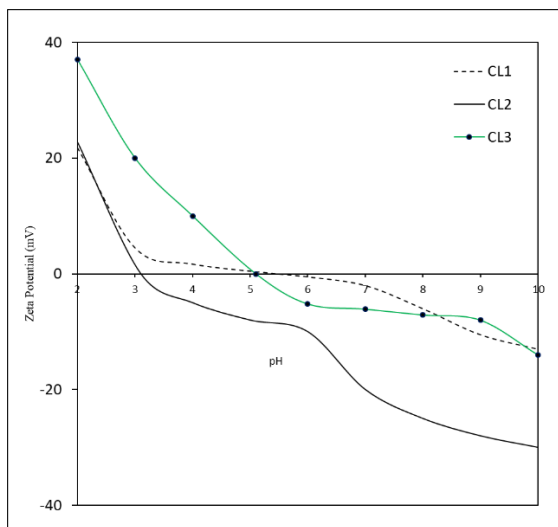


Figure 5a. ζ of CL1 to CL3 as a function of pH

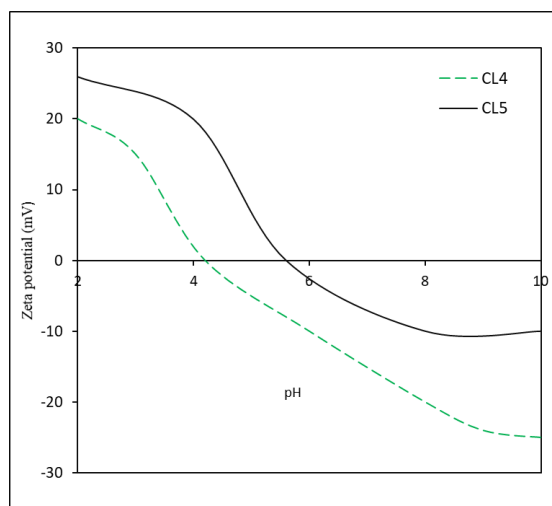
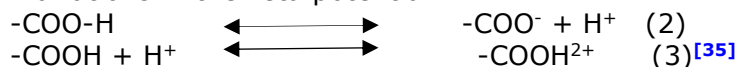


Figure 5b. ζ of CL4 and CL5 as a function of pH

For geological materials that differ remarkably by mainly organic matter content (Table 2), Wada and Okamura [35] showed that protonation and dissociation reactions involving carboxylic (-COOH) functional groups such as those presented in equations (2) and (3) respectively account for variations in the zeta potential.



Although protonation constants of -COOH functional groups are mostly greater than 4 (thus incapable of such acidic IEP values reported in Table 1), it is however possible for complex multifunctional macro-molecules like shale organic matter to interact with neighbouring sites which may alter dissociation constants and account for low IEP values like those reported in this study (Table 2) [38].

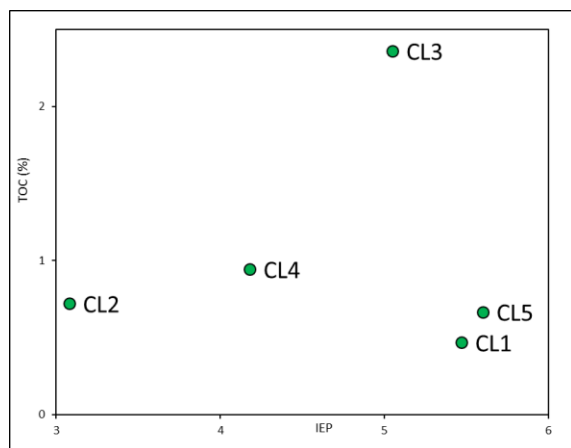


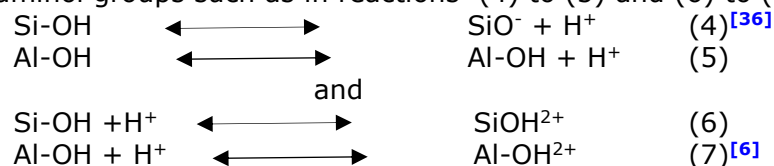
Figure 6. Relationship between of TOC (%) and IEP

Organic matter has been suggested by numerous authors to lower IEP [39-41]. Others like Fox [42], Appel *et al.* [43] and Fosu-Duah [34], and Fosu-Duah *et al.* [44] have also reported a positive correlation between TOC and IEP. Although the influence of the amount of organic matter present is clearly known to materially affect the development of ζ in geological materials, it is irrelevant to this study. This is supported by the lack of correlation between the two parameters as shown in the scatter plot in Figure 6.

The ζ and acidic IEP values of the shales may, therefore, be a reflection of the silicic mineral composition of the shales such as quartz, muscovite/illite and kaolinite (Table 2).

These minerals have characteristically acidic IEP values [39,43]. However, in terms of surface chemistry, aluminosilicates are the most reactive mineral constituents of shales [45], given that deprotonation and protonation of H^+ and OH^- are likely to occur on the amphoteric sites of the clays [46].

According to Parks [47], Tombácz and Szekeres [36] and then Eslinger and Pevear [48], negative and positive charges in geological materials arise from the significant contribution of amphoteric edges and basal (OH) (O face) sites through deprotonation and protonation from silanol and aluminol groups such as in reactions (4) to (5) and (6) to (7).



Various heterogeneities like the type of clay mineral and concentration account for variations in the magnitude of the zeta potential recorded in the samples. Since kaolinite is the major clay phase in the shale, it is likely that the surface electrical reactions are dominated by protonation and dissociation reactions which occur on the surfaces of this clay mineral. It is also noteworthy to mention that, dissolution of Al^{3+} from the crystal lattices of muscovite and/or a contribution from the silanol and aluminol groups of illite may also account for some variations in the zeta potential of these samples.

3.03.1 Isoelectric points (IEP)

Heterogeneous geological material like shale must have a reflection of its mineralogical suite on the zeta potential properties such as IEP. Several studies have demonstrated this using binary system (silicon-aluminium; [47]) and can be extrapolated to multicomponent mixtures [34]. Recalling from Table 2, the IEPs reported for the samples seem to fall within the range of values mostly assigned in literature to kaolinitic samples [34,43,50]. This may support the earlier suggestion that kaolinite which is the commonest and abundant clay mineral in the studied shales are probably the main variant of zeta potential properties. On the basis of mineralogical composition, Parks [51] suggested that the IEP can be predicted semi quantitatively proceeding from simple oxides. For example, aluminosilicates like kaolinite should have an intermediate IEP value between that of pure Al_2O_3 and SiO_2 , the particular IEP value being dependent on the Si/Al ratio given. This implies that the IEP of each shale is the weighted average of the chemical components' isoelectric points [33,51]

In this study, the relatively low IEP (3.10) of sample CL2 may, therefore, be a reflection of the relatively low $SiO_2:Al_2O_3$ ratio reported (Table 2). Nevertheless, deviations from the norm can also be found. For instance, sample CL3, when compared against CL4, shows an

unexpected lower $\text{SiO}_2:\text{Al}_2\text{O}_3$ ratio (0.3456 vs. 0.3463) and a higher IEP (5.05 vs. 4.18). This discrepancy may, however, point to factors other than just the $\text{SiO}_2:\text{Al}_2\text{O}_3$ ratio. Hu and Liu [52], Hu *et al.* [53] and Miller, *et al.* [15] suggested that heterogeneities of the structural layers of clay minerals significantly affect the surface zeta potential characteristics. Although the IEPs of CL1, CL3, CL4 and CL5 (Table 2) are within the acidic range, these values suggest the pronounced contribution of the aluminol components of the shale; most of these components might be due to kaolinite, which is the major clay phase in the shale. This is supported by the positive correlation ($R^2 = 0.81$) between IEP and Al_2O_3 (Figure 7). (Recalling from the geochemical analyses, Al_2O_3 is shown to be mainly associated with the clay mineral constituents; Figure 4).

An increase in the $\text{SiO}_2:\text{Al}_2\text{O}_3$ ratio has been shown to be positively correlated with IEP in many publications [15,34,52,54] but there is still a controversy on the ability of the aluminol components of clays to shift IEP values from those of pure clays into higher ones, and the conditions at which this occurs [55-56]. For instance, the works of Angove *et al.* [50], Hu and Liu [52], Miller *et al.* [15] and, Gupta [29] support the positive correlation between $\text{SiO}_2:\text{Al}_2\text{O}_3$ ratio and IEP values, in very much the same way as we found in this study ($R^2 = 0.81$, Figure 8). However, the conclusions of Miller *et al.* [15] and Hu and Liu [52] that the aluminol components of aluminosilicates have insignificant influence on their surface charge characteristics – even though there is an equivalent exposure of both silanol and aluminol sheets, especially in kaolinite – contradicts that of Angove *et al.* [56] who reported an IEP value of 7.3 for pure kaolinite. An explanation for this contradiction was given by Gupta [29], who claimed that the technique of deducing zeta potentials from electrophoretic mobility is mostly compromised by the heterogeneities shown by the clay minerals.

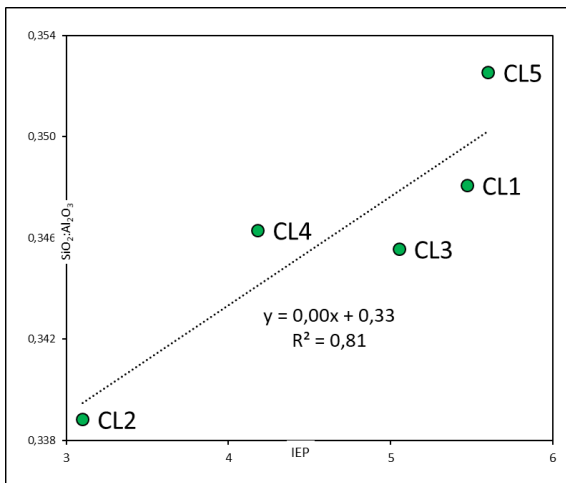


Figure 7. Relationship between $\text{SiO}_2:\text{Al}_2\text{O}_3$ and IEP

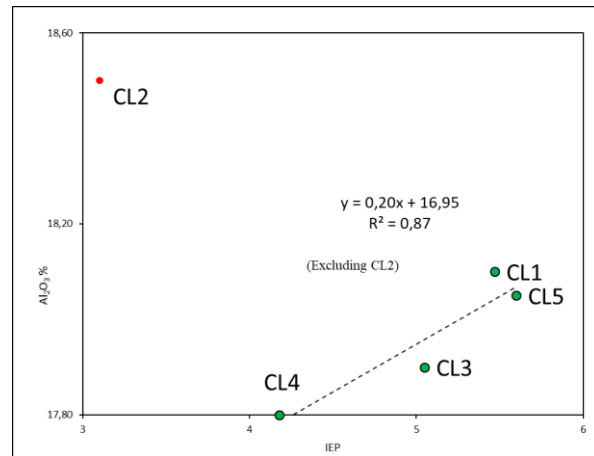


Figure 8. Relationship between Al_2O_3 (%) and IEP

In this study, the positive correlation between four of the samples ($R^2 = 0.87$; excluding sample CL2 Figure 8) suggests that the amount of Al_2O_3 has a significant influence on the surface potential of the Central Luconia shale. This might explain the relatively high IEPs of CL1, CL3 and CL5 (Table 2) which are closer to that of pure Al_2O_3 (IEP \sim 8, [57]). It may also suggest an equal contribution of SiO_2 and Al_2O_3 to the surface charge characteristics of the shale despite the relatively high percentages of the former. If this is true, then IEP of samples CL1, CL3 and CL5 are thus equal to the mean of the IEPs of pure SiO_2 (\sim 3) and Al_2O_3 (\sim 8) which is \sim 5.5 (similar to those reported for CL1, CL3 and CL5 in Table 2), which is consistent with the work by Parks [47].

4. Conclusions

The study of the surface charge characteristics has shown that zeta potential (ζ) generations in Central Luconia on the average range from +25.51 mV to -17.6 mV. An average IEP of 4.68 has been assigned to the shale.

- The influence of organic matter on surface charge characteristics is insignificant. Shale chemical composition is the main variants of surface potential specifically the activities on the amphoteric sites of clay minerals.
- The gradual change in the magnitude of the zeta potential observed as a function of pH is a good indication that the expulsion and sorption capacities of the shale can be managed.

The relatively high average positive zeta potential of the shales in comparison with the negative zeta potential indicates that the shale have high anion sorption capacities.

Acknowledgements

The donors of the Research Fund (0153ab-A33 offered to A.P. Dr. Eswaran Padmanabhan), administered by the Research and Information Office (RIO) are highly acknowledged for financially supporting this research.

References

- [1] Lyklema H. Liquid-fluid interfaces. in Fundamentals of interface and colloid science. vol 3, J Lyklema, Ed., ed: Academic Press, 2000, pp. 3-5.
- [2] Hunter RJ. Zeta potential in colloid science: Principles and applications. London: Academic Press, 1988.
- [3] Müller RH. Zeta potential und partikeladung in der laborpraxis. Wissenschaftliche Verlagsgesellschaft GmbH. Stuttgart, 1996.
- [4] Binazadeh M. Effect of secondary structure on surface adsorption of peptides. Ph.D., University of Alberta, 2013.
- [5] Binazadeh M, Xu M, Jiang K., Zolfaghari A, Dehghanpour H. Effect of electrostatic interactions on water uptake of gas shales: The interplay of solution ionic strength, electrostatic double layer, and shale zeta potential. Society for Petroleum Engineers, vol. 14, 2015.
- [6] Tombácz E and Szekeres M. Colloidal behavior of aqueous montmorillonite suspensions: The specific role of pH in the presence of indifferent electrolytes. Applied Clay Science, 2004; 27: 75-94, 10.
- [7] Kim J-K and Lawler DF. Characteristics of zeta potential distribution in silica particles. Bulletin of the Korean Chemical Society, 2005; 26:1083-1089.
- [8] Parks GA and Bruyn PLD. The zero point of charge of oxides. The Journal of Physical Chemistry, 1962; 66: 967-973, 1962.
- [9] Hedges JI and Kei, RG. Sedimentary organic matter preservation: An assessment and speculative synthesis. Marine Chemistry, 1995; 49: 81-115.
- [10] Stumm W and Morgan J. Aquatic chemistry. 3 ed. New York: John Wiley and Sons, 1996.
- [11] Jenne EA. Controls on Mn, Fe, Co, Ci, Cu, and Cn concentrations in soils and water—the significant role of hydrous Cn and Fe oxides; in Gould. in Trace inorganics in water, advances in chemistry, AC Society, Ed., ed Washington, 1968, pp. 337-387.
- [12] Basu S, Nandakumar K, and Masliyah JH. A study of oil displacement on model surfaces. Journal of colloid and interface science, 1996; 182: 82-94, 1996.
- [13] Marcano-Martinez E and McBride MB. Comparison of the titration and ion adsorption methods for surface charge measurement in oxisols. Soil Science Society of America Journal, 1989; 53: 1040-1045.
- [14] Schuylenborgh V. Clay minerals vol. 17, 1982.
- [15] Miller JD, Nalaskowski J, Abdul B, and Du H. Surface characteristics of kaolinite and other selected two layer silicate minerals. The Canadian Journal of Chemical Engineering, 2007; 85: 617-624.
- [16] Krauskopf KB and Bird DK. Introduction to geochemistry. 3 ed. New York, 1995.
- [17] Zhang P and Austad T. Wettability and oil recovery from carbonates: Effects of temperature and potential determining ions. Colloids and Surfaces A: Physicochemical and Engineering Aspects, 2006; 279: 179-187.
- [18] Ji L, Zhang T, Milliken KL, Qu J, and Zhang X. Experimental investigation of main controls to methane adsorption in clay-rich rocks. Applied Geochemistry, 2012; 27: 2533-2545.

- [19] Gasparik M, Bertier P, Gensterblum Y, Ghanizadeh A, Krooss BM, and Littke R. Geological controls on the methane storage capacity in organic-rich shales. *International Journal of Coal Geology*, 2014; 123: 34-51.
- [20] Fosu-Duah E, Padmanabhan E, and Vintaned JAG. Micro-scale hydrocarbon distribution in organic-rich shales: A case study in the union springs formation, Marcellus subgroup (USA). *Pet Coal*, 2017; 59(5):641-652.
- [21] Fosu-Duah EL, Padmanabhan E, and Gámez Vintaned JA. Variations in specific surface area of some oligocene-miocene shales. *Journal of Scientific Research and Development*, 2016; 3: 33-43.
- [22] El-Swaify SA. Changes in the physical properties of soil clays due to precipitated aluminum and iron hydroxides: II. Colloidal interactions in the absence of drying. *Soil Science Society of America Journal*, 1976; 40: 516-520.
- [23] Nmegbu CGJ and Spiff J. Chemical flocculation of microorganisms in the reservoir during meor. *International Journal of Engineering and Advanced Technology*, 2014; 3: 46-49.
- [24] Elliott HA and Sparks DL. Electrokinetic behavior of a paleudult profile in relation to mineralogical composition. *Soil Science*, 1981; 132: 402-409, 1981.
- [25] Gu G, Xu Z, Nandakumar K, and Masliyah J. Effects of physical environment on induction time of air-bitumen attachment. *International Journal of Mineral Processing*, 2003; 69: 235-250.
- [26] Waxman MH and Smits LJM. Electrical conductivities in oil-bearing shaly sands. *Society of Petroleum Engineers Journal*, 1968; 8: 107-122.
- [27] Clavier C, Coates G, and Dumanoir J. Theoretical and experimental bases for the dual-water model for interpretation of shaly sands. *Society of Petroleum Engineers Journal*, 1984; 24: 153-168.
- [28] Macedo J and Bryant R. Morphology, mineralogy, and genesis of a hydrosequence of oxisols in Brazil. *Soil Science Society of America Journal*, 1987; 51: 690-698.
- [29] Gupta V. Surface charge features of kaolinite particles and their interactions. Ph.D. Thesis, Department of Metallurgical Engineering, The University of Utah, Utah, 2011.
- [30] Pettijohn FJ. *Sedimentary rocks*: Harper & Row Limited, 1975.
- [31] Gromet LP, Haskin LA, Korotev RL, and Dymek RF. The "north American shale composite": Its compilation, major and trace element characteristics. *Geochimica et Cosmochimica Acta*, 1984; 48: 2469-2482.
- [32] Fu X, Wang J, Tan F, Feng X, Wang D, and Song C. Geochemistry of terrestrial oil shale from the lunpola area, northern Tibet, China. *International Journal of Coal Geology*, 2012; 102: 1-11.
- [33] Fosu-Duah EL, Padmanabhan E, and Gámez Vintaned JA. Electrophoretic behavior of some shales from the setap formation, sarawak basin, Malaysia. *International Journal of Applied Engineering Research*, 2016; 11: 337-341.
- [34] Fosu-Duah EL. Surface characteristics and charging potential of selected shales from the setap formations, onshore and offshore Sarawak, Malaysia. MSc. Thesis, Department of Geoscience, Universiti Teknologi PETRONAS, Perak, 2016.
- [35] Wada K and Okamura Y. Electric-charge characterisation of ando a1 and buried a1 horizon soils. *Soil Science*, 1980; 31: 307-314.
- [36] Tombácz E and Szekeres M. Surface charge heterogeneity of kaolinite in aqueous suspension in comparison with montmorillonite. *Applied Clay Science*, 2006; 34: 105-124.
- [37] Breeuwsma A and Lyklem, J. Interfacial electrochemistry of haematite (α -Fe₂O₃). *Discussions of the Faraday Society*, 1971; 52: 324-333.
- [38] Hochella, MF. Atomic structure, microtopography, composition, and reactivity of mineral surfaces. in *Mineral-water interface geochemistry*. MF Hochella and AF White, Eds., ed: *Reviews in mineralogy*, 1990: 23: 87-132.
- [39] Raj V and Peech M. Electrochemical properties of some oxisols and alfisols of the tropics. *Soil Science Society of America Journal*, 1972; 36: 587-593.
- [40] Morais FI, Page AL, and Lund LJ. The effect of pH, salt concentration, and nature of electrolytes on the charge characteristics of Brazilian tropical soils. *Soil Science Society of America Journal*, 1976; 40: 521-527.
- [41] Hendersho, WH and Lavkulich LM. The effect of sodium chloride saturation and organic matter removal on the value of zero point of charge. *Soil Science*, 1979; 128: 136-141.
- [42] Fox RL. Some highly weathered soils of Puertrorico, 3. Chemical properties. *Geoderma*, 1982; 27: 139-176.
- [43] Appel C, Ma LQ, Rhue RD, and Kennelley E. Point of zero charge determination in soils and minerals via traditional methods and detection of electroacoustic mobility. *Geoderma*, 2003; 113: 77-93.

- [44] Fosu-Duah E, Padmanabhan E, and Gamez-Vintaned,JA. Characteristic zeta potential of selected oligocene-miocene shales from the setap formation, onshore Sarawak-Malaysia. *International Journal of Applied Engineering Research*,2017; 12: 6360-6368.
- [45] Nanda J, Patil A, and Waikar J. Evaluation of reactive clay in Indian shale. *Halliburton Technology Offshore World*,2014: 1-3.
- [46] Naidu R, Morrison RJ, Janik L, and Asghar M. Clay mineralogy and surface charge characteristics of basaltic soils from Western Samoa. *Clay Minerals*,1997; 32: 545-556.
- [47] Parks GA. Aqueous surface chemistry of oxides and complex oxide minerals. in *Equilibrium concepts in natural water systems*. ed: American Chemical Society, 1967: 67:121-160.
- [48] Eslinger E and Pevear DR. Clay minerals for petroleum geologists and engineers. *Society for Sedimentary Research (short course notes)*, 1988; 22: 1-24.
- [49] Smoilik TJ, Harman M, and Fuerstenau DW. Surface characteristics and flotation behaviour of aluminosilicates. *Transactions of the American. Institute of Mining Metallurgical and Petroleum Engineering*, 1966; 235: 367-375.
- [50] Fosu-Duah E, Padmanabhan E, and Gamez-Vintaned JA. The isoelectric points of selected black shales from the setap formation-Sarawak basin. in *ICIPEG*, 2017: 539-544.
- [51] Parks GA. The isoelectric points of solid oxides, solid hydroxides, and aqueous hydroxo complex systems. *Chemical Reviews*,1965; 65: 177-198.
- [52] H Y, and Liu X. Chemical composition and surface property of kaolins. *Minerals Engineering*, 2003; 16: 1279-1284.
- [53] Hu Y, Wei S, Hao J, Miller JD, and Fa K. The anomalous behavior of kaolinite flotation with dodecyl amine collector as explained from crystal structure considerations. *International Journal of Mineral Processing*, 2005; 76: 163-172.
- [54] Angove MJ, Johnson BB, and Wells JD. The influence of temperature on the adsorption of Cadmium(ii) and Cobalt(ii) on kaolinite. *Journal of Colloid and Interface Science*,1998; 204: 93-103.
- [55] Tewari PH and Lee W. Adsorption of co(ii) at the oxide-water interface. *Journal of Colloid and Interface Science*, 1975; 52: 77-88.
- [56] Angove MJ, Johnson BB, and Wells JD. Adsorption of Cadmium (ii) on kaolinite. *Colloids and Surfaces A: Physicochemical and Engineering Aspects*, 1997; 126: 137-147.
- [57] Kosmulski M. *Surface charging and points of zero charge*. New York: CRC Press, 1956.

To whom correspondence should be addressed: EvelynLove Fosu-Duah, Universiti Teknologi PETRONAS, Department of Geoscience,32610 Perak Darul Ridzuan, Tronoh-Malaysia, love.duah@gmail.com

CHARACTERIZATION OF SOURCE ROCKS AND DEPOSITIONAL ENVIRONMENT, AND HYDROCARBON GENERATION MODELLING OF THE CRETACEOUS HOIHO FORMATION, GREAT SOUTH BASIN, NEW ZEALAND

Liyana N. Oslı, Mohamed R. Shalaby and Md. Aminul Islam*

Department of Geology, Faculty of Science, Universiti Brunei Darussalam, Jalan Tungku Link, BE 1410, Brunei Darussalam

Received December 12, 2017; Accepted February 10, 2018

Abstract

The Hoiho Formation in the Great South Basin (GSB) of New Zealand has been analysed for source rock characterization, hydrocarbon generation modelling, and interpretation of paleodepositional environment. Rock-Eval pyrolysis results from wells indicate the presence of excellent organic matter quality and quantity. The Hoiho Formation is dominantly of kerogen type II-III (oil and gas prone) and kerogen type III (gas prone). High values are also recorded for total organic carbon (TOC), hydrocarbon volume generated during pyrolysis (S₂) and hydrogen index (HI). Based on the maximum pyrolysis temperature and vitrinite reflectance values in Kawau-1A, Toroa-1 Tara-1 wells, it can be concluded that the Hoiho Formation is thermally mature only at the Central Graben of the basin, where these three wells are positioned at. Conversely, thermally immature source rock of the Hoiho Formation is recorded in the Hoiho-1C well. Important biomarkers and their derivatives, such as regular steranes, Pristane and Phytane confirm that Hoiho source rock was originally from a terrestrial source. One-dimensional basin modelling was applied to reconstruct the burial and thermal maturity histories of the formation. The top of oil window was reached at approximately 29 Ma, 53 Ma and 57 Ma at Kawau-1A, Toroa-1 and Tara-1 wells respectively.

Keywords: *Hoiho Formation; source rock characterization; burial history; Great South Basin; New Zealand.*

1. Introduction

The primary objective of this study is to describe and understand the source rock of the Hoiho Formation in the Great South Basin of New Zealand by focusing on the geochemical properties of the formation. This involves characterizing the source rock, studying the paleo-depositional environment, and producing hydrocarbon generation models. Despite not being commercially-productive, the Great South Basin hosts source rocks of high potential, including the Hoiho Formation. Because very little study has been done on this formation, it is therefore of a great interest to the authors of this paper to analyse this formation.

The Great South Basin (GSB) has a total area of 100,000 km² and is one of the largest basins in New Zealand (Fig.1), containing sediments of Late Cretaceous and Early Tertiary age that fill a series of grabens and half-grabens [1-5]. This deepwater basin was created in the Cretaceous and had experienced mild tectonism [2].

Extensive studies on the hydrocarbon potential of the Great South Basin have been conducted, such as those undertaken by Keuhnert [6], Gibbons and Jackson [7], Anderton *et al.* [8], Cook *et al.* [4], and Killops *et al.* [9]. This basin has been targeted for drilling, despite not having commercial hydrocarbon production [10]. Formations of interest for hydrocarbon exploration belong to Paleocene and Cretaceous, in which the lithology of source rocks are primarily coal and black marine shale [11].

One of the formations that displays a high potential as a source rock is the Hoiho Formation. This Formation is part of the Cretaceous Hoiho Group that represents the oldest sediments

and the main source of petroleum in the Great South Basin [4,12]. The Hoiho Formation contains syn-rift deposits consisting of organic rich clast-supported coaly sandstone.

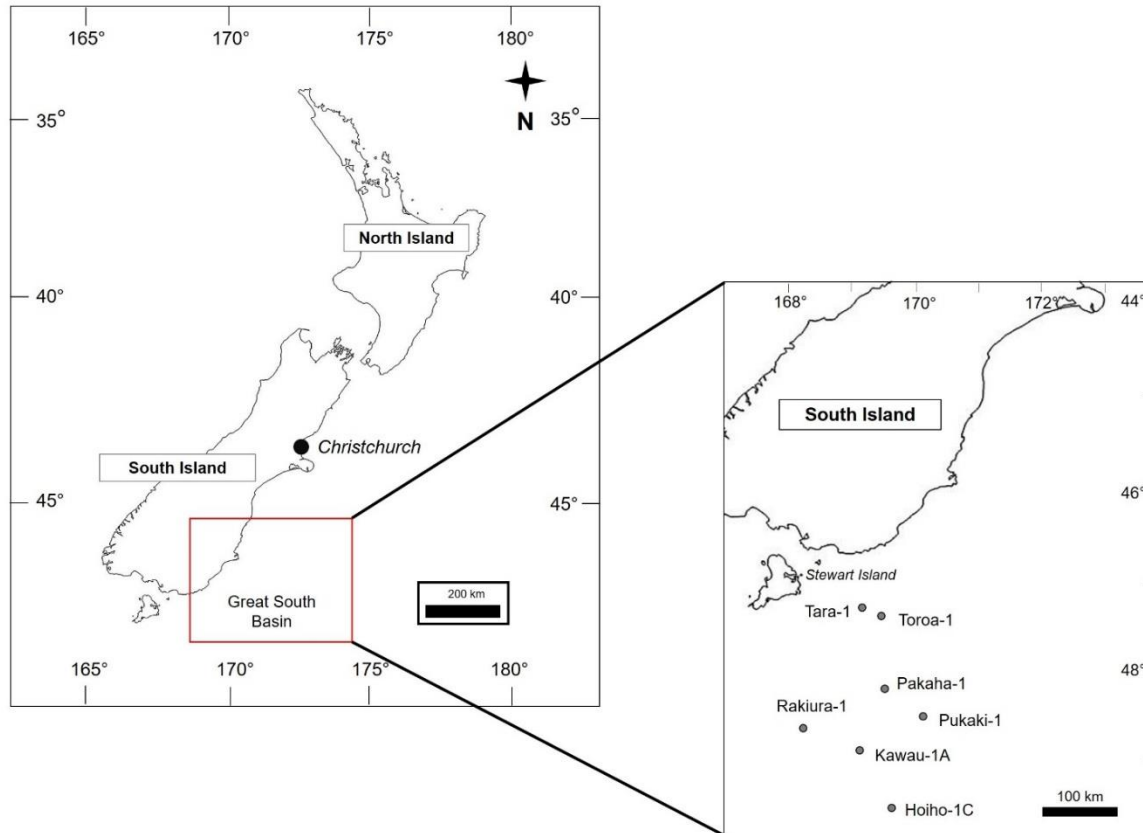


Figure 1. Map of New Zealand showing the location of the Great South Basin and the study area (modified after Schiøler *et al.* [1])

Only four out of eight wells drilled in the Great South Basin suggested hydrocarbon generation [13]. Killops *et al.* [9] concluded that wells Kawau-1A, Toroa-1, and Pakaha-1 encountered gas condensate in Cretaceous sands. The Hoiho-1C well, drilled in 1978, encountered two source rocks but did not display any hydrocarbon show. Wells Tara-1 and Takapu-1 experienced several mechanical difficulties during drilling but later reported the absence of hydrocarbon, while the Tara-1 well showed gas at the top of the Cretaceous formations that were drilled. The Rakiura-1 well also failed to penetrate a good source rock, as the sands encountered were either of poor quality or immature. In the Great South Basin, the Pukaki-1 well is the most recent well drilled and recorded only minor methane [11]. Hydrocarbon quality in the wells of the Great South Basins has also been studied through Rock-Eval pyrolysis, in which the kerogen analysed was observed to be mainly humic in coaly sediments, affirming the dominance of gas condensate as encountered by the Kawau-1A, Toroa-1, Pakaha-1 and Tara-1 wells.

Rock-Eval pyrolysis for the Hoiho Formation is generally limited. Gibbons and Jackson [7] has stated that the predictions of oil potential in the Great South Basin are over-optimistic, as pyrolysis was performed on samples from the Kawau-1A and Toroa-1 wells only. Similarly, Rock-Eval data obtained from the Pukaki-1 and Rakiura-1 wells are also limited. Therefore, this paper aims to re-evaluate the Hoiho Formation as a source rock by using the data from four wells for Rock-Eval pyrolysis: the Hoiho-1C, Kawau-1A, Tara-1 and Toroa-1 wells (Fig. 2). Assessment of the Hoiho Formation also includes generating one-dimensional models to understand the formation's burial and thermal maturity histories and characterizing the paleo-depositional environment using biomarkers.

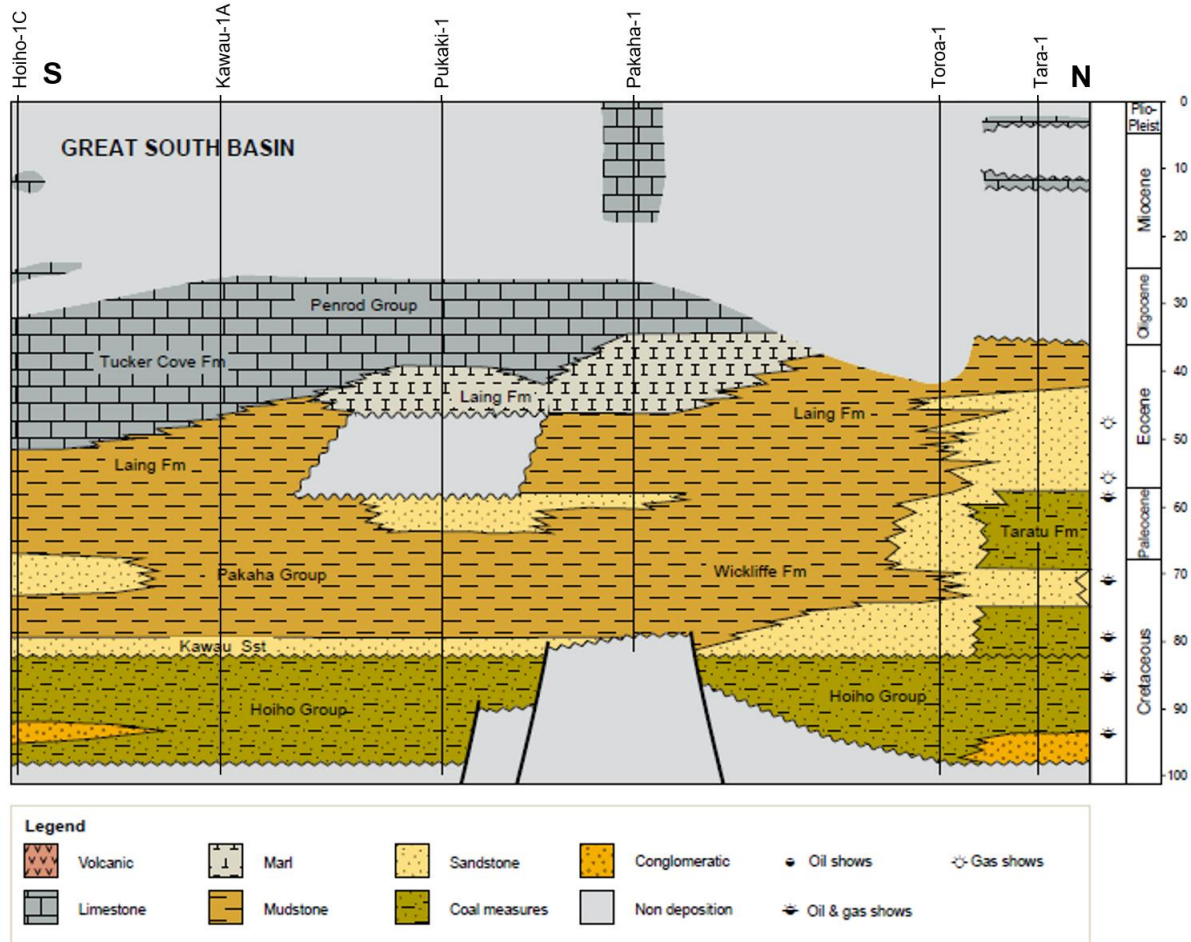


Figure 2. Stratigraphy of the Great South Basin (Modified after New Zealand Petroleum and Minerals, [10])

2. Geological settings and stratigraphy

The geological setting and stratigraphy of the Great South Basin has been studied by several authors, including McMillan and Wilson [14], Schiøler *et al.* [1] and Constable *et al.* [15]. The eastern part of New Zealand, where the Great South Basin is located, underwent more intense tectonic activities than the western margin. In the Cretaceous, there was a shift from a compressional to an extensional regime in the eastern New Zealand. Subduction of the Phoenix plate halted at approximately 105 -100 Ma from central New Zealand to the eastern tip of the Chatham Rise, and rifting initiated that eventually led to the separation of New Zealand from Gondwana [16]. This change caused widespread uplift and erosion creating a wide angular unconformity, called the Albian Unconformity, which extends throughout the whole of New Zealand.

It is also in the Cretaceous that the major tectonic episodes that initiated the formation of the Great South Basin began [10]. Initiation of rifting in the mid-Cretaceous created NW-SE trending grabens and half-grabens that underwent sedimentation [15]. Continuous sedimentation in the form of non-marine conglomerates, sandstone, mudstone, and coal from fluvial and lacustrine environments occurred during this period [10,15-16]. These rift-related sediments deposited in grabens and half-grabens make up the Hoiho Group (Fig. 2), which rests unconformably on the basement rocks of the Great South Basin. The basement rocks of the Great South Basin are primarily over thickened crust that generates high elevation blocks [17].

After this thick succession of fluvial and lacustrine sediments was deposited, accommodation space in the grabens began to decrease, allowing for marine influence. It is for this

reason that the Hoiho Group is thought to be overlain by delta plains that may host potential sand reservoirs and coaly source rocks [15]. As rifting waned, a basal transgressive sandstone called the Kawau Sandstone was deposited that hosts condensate gas in the Kawau-1A well [1,4] (Fig. 2). New Zealand completely separated from eastern Gondwana in the Late Cretaceous, which is marked by a marine transgression throughout New Zealand that peaked in the Oligocene [16]. This separation resulted in the formation of the Tasman Sea.

Rifting in the Great South Basin was followed by thermal subsidence that continued from Late Cretaceous to Paleogene [15]. Sediments deposited during this time include sandstone, greensand, and mudstone. Further subsidence of the basin initiated the deposition of carbonates and calcareous mudstone as the basin became a deep marine environment [9-10]

Throughout the Paleocene, there was a shift in the shoreline to the west [9]. In the western margin of the basin, a prograding delta began to form during the period of thermal subsidence. Upon the final opening of the Solander and Emerald sub-basins in approximately 45 Ma, supply of sediment to the delta terminated and transgressive sedimentation began (Fig. 2). In the Oligocene-Miocene, the western margin of the Great South Basin was affected by plate tectonics, as movement along the Alpine Fault was initiated [15,18].

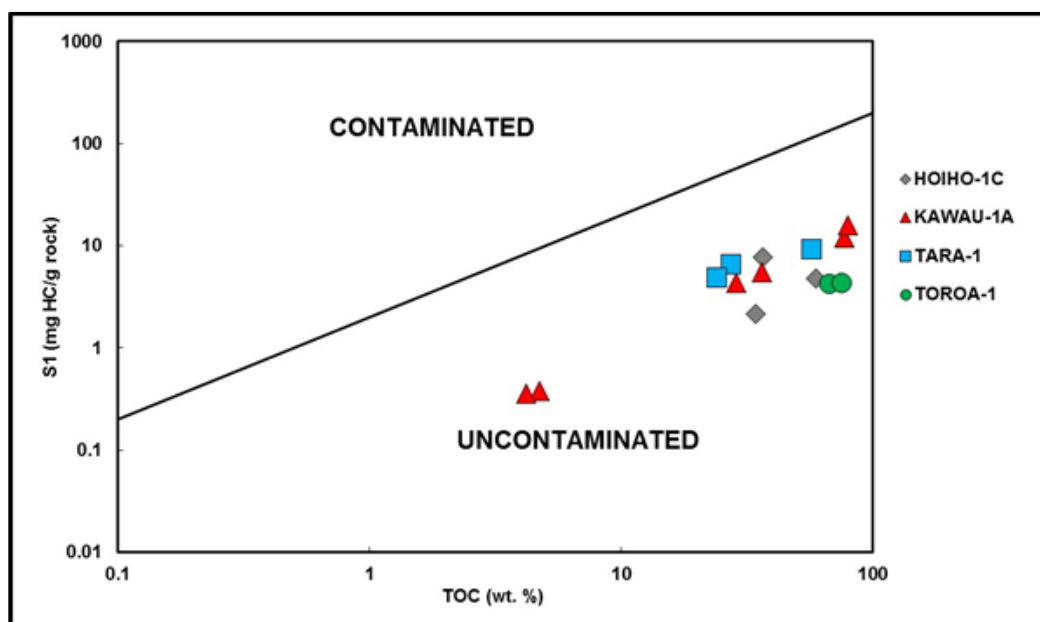


Figure 3. A cross-plot of S_1 versus TOC to indicate the origin of hydrocarbon in the Hoiho Formation (Fakhri et al. [54])

Compressional stresses from mountain-building along the Alpine Fault became amplified, and the western margin of the basin was folded into anticlines and synclines, creating uplift in this part of New Zealand [10]. A thick prograding marine sequence is found in this part of the basin and trends north east [1,16]. After the Miocene, thick successions illustrating marine progression were deposited in the western Great South Basin. In the eastern part of the basin, there was an accumulation of Neogene age pelagic sediments [9].

3. Data and methods

All data sets were provided and permitted for publishing by the Ministry of Business, Innovation and Employment (MBIE) of New Zealand together with GNS Science. Twenty-seven drill cutting samples belonging to the Hoiho Formation from the Hoiho-1C, Kawau-1A, Tara-1 and Toroa-1 wells were used to Rock-Eval pyrolysis.

Rock-Eval 2 and 6 are used in this study with the aim of investigating the hydrocarbon potential, maturity, and type of organic matter [19-20]. Pyrolysis results include the volume of free hydrocarbon or bitumen available in the source rock before pyrolysis (S_1), the volume of

hydrocarbon generated during pyrolysis (S_2), amount of carbon dioxide emitted (S_3), Total organic carbon (TOC), vitrinite reflectance (R_o), and maximum pyrolysis temperature (T_{max}). The Hydrogen Index (HI) and Oxygen Index (OI) were calculated using the given data [20-21]. Other calculations from the pyrolysis results applied in this study include the Production Yield ($PY=S_1 + S_2$) and the Production Index ($PI=S_1/S_1+S_2$)

The paleodepositional environment of the Hoiho source rock is evaluated through the application of biomarker data from the Hoiho-1C and Kawau-1A wells. Biomarker data and important derivations were interpreted according to studies done by Rodriguez and Philp [22], Abdullah *et al.* [23] and Ayinla *et al.* [24]. Studying the environment where the Hoiho source rock was deposited provides a background understanding and confirmation of the kerogen types generated in the Hoiho Formation. In addition to the paleodepositional environment, using biomarkers and their derivations such as the pristane/phytane ratio, isoprenoid/n-alkanes ratio, concentration of regular steranes (C_{27} , C_{28} and C_{29}), and the carbon preference index (CPI) can be used to determine the quality and thermal maturity of the source rock.

In assessing the Hoiho source rock's burial and thermal maturity histories, the utilization of the PetroMod software is necessary. Relevant input parameters for one-dimensional basin modelling are derived from completion reports, composite logs, and the well card summary for all wells in the study. These parameters include the formations detected in each well, formation thickness (metres), formation age (Ma), measured borehole temperature ($^{\circ}C$), and measured vitrinite reflectance ($\%R_o$). It is also important to identify individual petroleum system elements for every stratigraphic sequence detected in each well. For the studied source rock, other geochemical parameters such as TOC and HI are required.

Calibrating measured and calculated values for borehole temperature and vitrinite reflectance was performed to examine the quality of data used in this study. Prior to calibration, every borehole temperature extracted from composite logs must be corrected to eliminate inaccuracies attributed to the lack of equilibrium between the formation temperatures and those of the drilling mud. In this study, borehole temperature correction was done based on the studies by Waples and Ramly [25], Waples and Ramly [26], Peters and Nelson [27] and Bullard [28]. Modelled vitrinite reflectance values are calculated using the EASY $\%R_o$ model [29]. The 1-D modelling of the formation is expected to constrain the burial history, thermal maturity history, and timing of hydrocarbon generation in the Hoiho Formation. Only the Kawau-1A, Toroa-1 and Tara-1 wells were used for modelling.

4. Results and discussion

4.1. TOC and rock-eval pyrolysis results

Based on this study, the Hoiho Formation has S_1 values that range from 0.36 to 15.76 mg HC/g. T_{max} values are recorded to be between $421^{\circ}C$ to $472^{\circ}C$, which provide S_2 values for the source rocks. All wells generate good to excellent S_2 values, ranging from 5.95 to 174.79 mg HC/g rock, and S_3 values are documented ranging from 0.44 to 15.15 mg CO_2 /g rock. Source rocks contain TOC values range from 4.21% to 77.03%, making the Hoiho Formation a promising potential source rock with excellent quantity of organic matter, based on the TOC classification introduced by Peters [20]. PI values for source rocks range from 0.04 to 0.11. Derived OI values of 2.71 to 25.53 mg CO_2 /g TOC were recorded in this formation and calculated HI values range from 9.52 to 293.3 mg HC/g TOC.

PY values are between 6.33 and 190.6 mg HC/g TOC and vitrinite reflectance ($\%R_o$) values range from 0.36 to 1.42% R_o . The results of rock-eval pyrolysis and other parameters calculated are summarized in Table 1.

The S_1 versus TOC plot is used to investigate the origin of the hydrocarbon found in the source rocks (Fig. 3). In this cross-plot, it is found that the hydrocarbon from all wells is uncontaminated or autochthonous, which means that the hydrocarbon hosted by the source rocks did not migrate from elsewhere. PY can be plotted with TOC (Fig. 4) to estimate the hydrocarbon generation potential [30-34]. Figure 4 demonstrates the good to excellent capability of the Hoiho Formation to generate hydrocarbon.

Table 1 Rock-eval pyrolysis results used in this study

Well name	Depth (m)	Lithology	S ₁	S ₂	S ₃	TOC	OI	HI	PI	S ₂ /S ₃	S ₁ +S ₂ =PY	T _{max}
Hoiho-1C	1975	Coal	7.8	107.3	8.25	36.57	22.6	293.3	0.07	13.0	115.1	421
	2286	Coal	4.78	93.9	15.15	59.35	25.5	158.3	0.05	6.20	98.7	423
	2286	Shaly coal	2.17	48.2	7.63	34.37	22.2	140.3	0.04	6.32	50.4	423
Kawau-1A	3299	Coal	11.92	168.6	3.12	77.03	4.05	218.8	0.07	54.0	180.5	443
	3299	Shaly coal	4.35	64.9	1.59	28.71	5.54	226.2	0.06	40.8	69.3	441
	3299	Mudstone	0.38	5.95	0.44	4.73	9.30	125.8	0.06	13.5	6.33	437
	3303	Coal	15.76	174.8	3	79.8	3.76	219.0	0.08	58.3	190.6	446
	3303	Shaly coal	5.51	78.2	1.61	36.11	4.46	216.4	0.07	48.5	83.7	442
	3303	Mudstone	0.36	4.95	0.44	4.21	10.5	117.6	0.07	11.3	5.31	439
Tara-1	4310	Mudstone	6.6	52.5	3.3	27.2	12.1	193.0	0.11	15.9	59.1	456
	4365	Coal	9.3	89.6	9.5	57	16.7	157.2	0.09	9.43	98.9	456
	4365	Mudstone	4.9	47.3	2.3	24	9.58	197.1	0.09	20.6	52.2	458
Toroa-1	4327	Coal	4.23	86.0	2.22	67.31	3.30	127.8	0.05	38.7	90.2	468
	4494	Coal	4.38	83.3	2.04	75.15	2.71	110.8	0.05	40.8	87.7	472

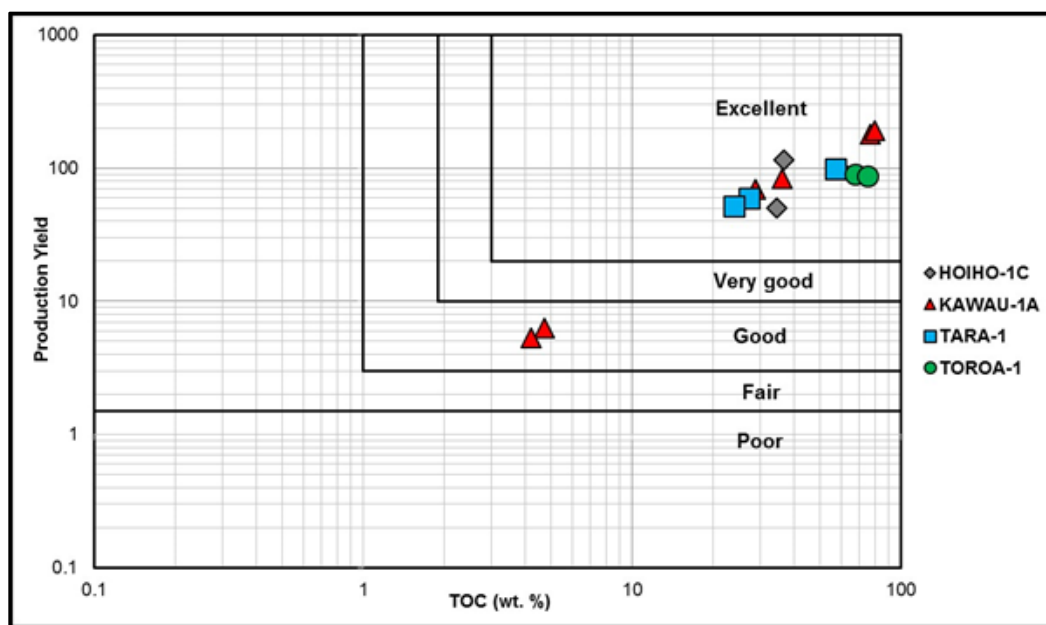


Figure 4. A cross-plot of PY versus TOC to demonstrate the generating potential of the Hoiho Formation

4.2. Types of organic matter

Accurate identification of genetic organic matter type is required to determine the characteristics of the hydrocarbon discharged and this is achievable using various pyrolysis results.

A S₂-TOC cross plot (Fig. 5) is used to investigate the hydrocarbon quality and quantity. The result suggests excellent organic matter quantity based on the TOC concentration in the

source rock, and a good to excellent hydrocarbon quality. Plotting S_2 versus TOC as done by Langford and Blanc-Valleron [35] (Fig. 6) also shows that most samples contain a mixture of kerogen type II-III and kerogen type III, although the organic matter in Toroa-1 shows only gas prone source rock of kerogen type III.

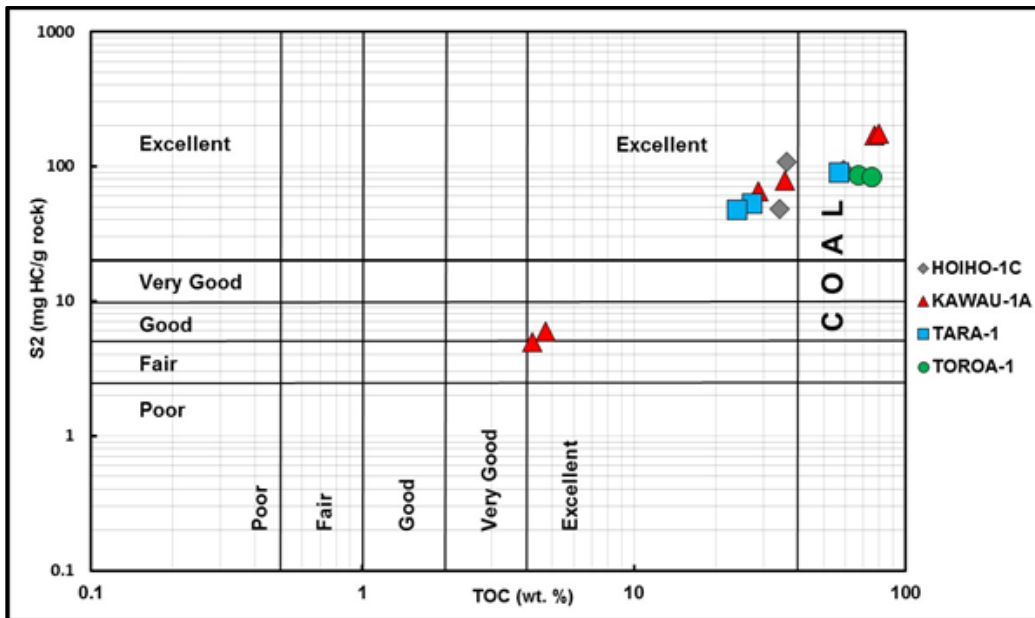


Figure 5. A cross-plot of S_2 versus TOC to demonstrate the quality and quantity of hydrocarbon (Espitalié et al. [36])

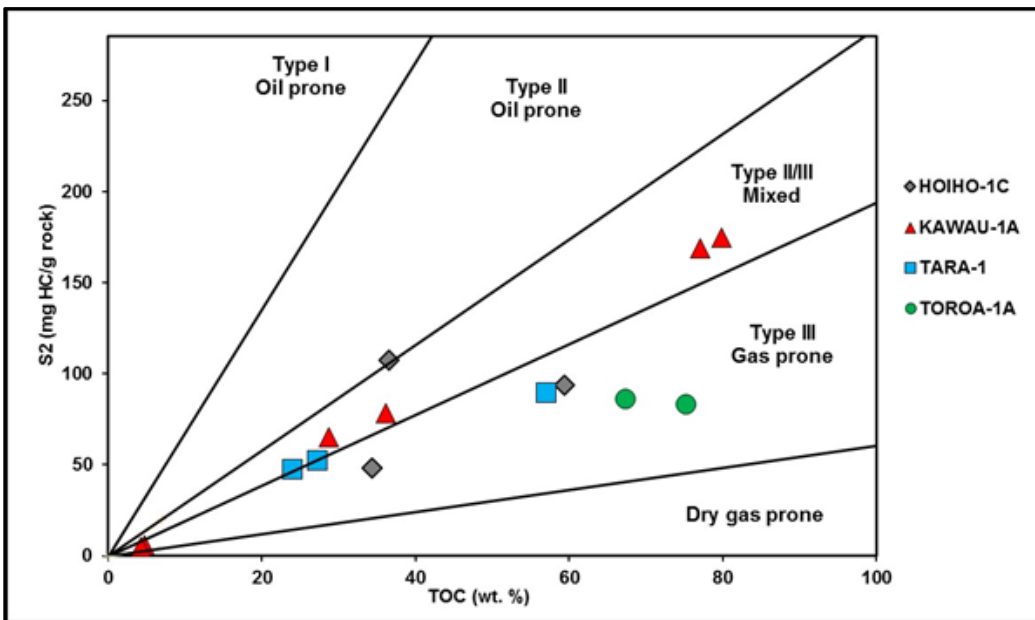


Figure 6. A cross-plot of S_2 versus TOC to identify the type of hydrocarbon produced from every wells (Langford and Blanc-Valleron [35])

The Van Krevelen diagram (Fig. 7) shows the relationship between HI (mg HC/g TOC) and OI (mg CO₂/g TOC) [19,36-38]. HI and OI are defined through the formulae (HI = $S_2/TOC \times 100$) and (OI = $S_3/TOC \times 100$) respectively. These parameters consider the amount of hydrogen and oxygen with respect to the hydrocarbon produced by the source rock [20]. The modified Van Krevelen diagram (Fig. 7) shows HI values for the study ranging from 140.26 to 293.3

mg HC/g TOC. The outcome of the correlation between these values indicates the presence of kerogen II-III (oil and gas prone) and kerogen type III (gas prone) [38]. This result provides a confirmation of the results from the S_2 -TOC cross plot in Figure 6.

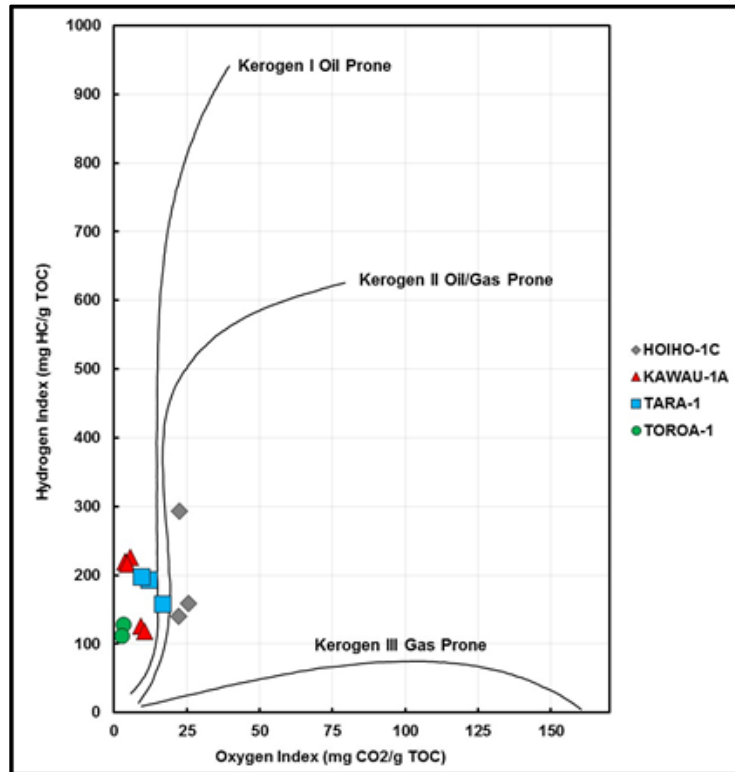


Figure 7. A cross-plot of HI versus OI in the modified Van Krevelen diagram shows the type of kerogen available in the source rock (Espitalié et al. [36])

4.3. Thermal maturity and hydrocarbon generation potential

Thermal maturity is an important factor in source rock evaluation. Indicators of thermal maturity include T_{max} , R_o , and PI, which will be correlated with the other pyrolysis results to demonstrate the evolution of Hoiho source rock maturity.

By definition, T_{max} is the pyrolysis temperature which produces the maximum amount of hydrocarbon from the thermal degradation of kerogen [39], and an increase in T_{max} values indicates increasing organic matter evolution [21,40]. A classification introduced by Peters [20] relating to hydrocarbon type and T_{max} marks the temperature range of 430°C–445°C as the beginning of the mature oil window. At 470°C, oil is no longer produced and gas generation is initiated.

A cross-plot between T_{max} and HI (Fig. 8) shows that the organic matter in Hoiho-1C well is thermally immature. All points belonging to Kawau-1A well are located within the mature oil window, with T_{max} values ranging from 437°C to 446°C. Tara-1 and Toroa-1 contain points that lie at the early and late ends of the condensate wet gas window respectively, making the organic matter in Toroa-1 almost thermally over-mature with a T_{max} of 468°C and 472°C. Figure 8 also shows good agreement with Figures 6 and 7, confirming the kerogen type present in the Hoiho Formation as kerogen type II-III and kerogen type III.

Vitrinite reflectance is the proportion of normal incident light reflected by a plane polished surface of vitrinite, which alters according to the level of maturation [41]. Similar to T_{max} , more mature samples reflect higher % R_o values, therefore an increase in % R_o is expected with increasing depth [42]. However, these values are only available if the samples originate from a continental source, therefore only coal samples in this study were tested for vitrinite reflectance [43]. The cross-plot of T_{max} and % R_o can be used to further understand the thermal

maturity of the source rock, as displayed in Figure 9 [44]. This figure shows a positive correlation between both indices, and indicates thermally immature source rock in Hoiho-1C, mature source rocks in Kawau-1A and Tara-1, an almost over-mature organic matter in Toroa-1. Values for vitrinite reflectance together with their respective well names are summarized in Table 2.

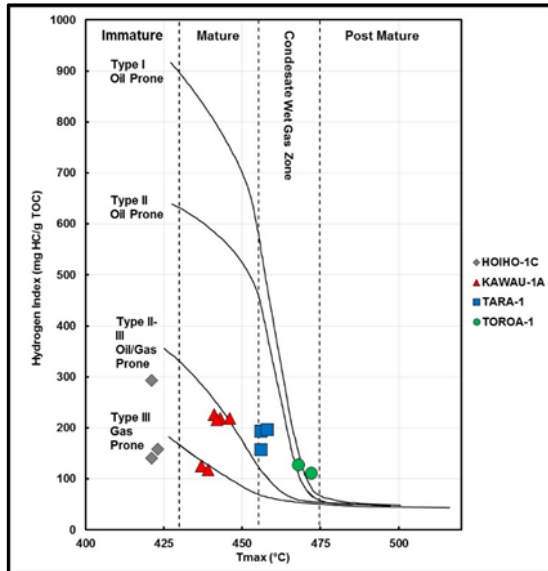


Figure 8. A cross-plot of HI versus T_{max} to indicate source rock thermal maturity

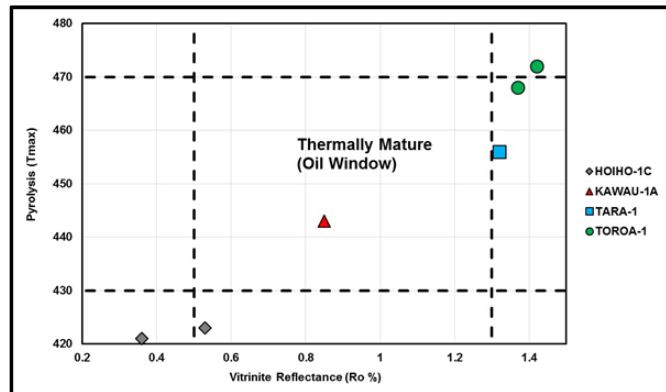


Figure 9. A cross-plot of T_{max} versus R_o to indicate source rock thermal maturity

Table 2. Vitrinite reflectance values used in this study

Well name	Depth (m)	% Ro	Well name	Depth (m)	% Ro
Tara-1	944.8	0.34	Toroa-1	1938.2	0.36
	1188.7	0.39		2621.2	0.62
	1341.1	0.35		3169.8	0.72
	1584.9	0.38		3291.2	0.85
	1676.3	0.37		4327	1.37
	1859.2	0.37		4327.9	1.12
	2011.6	0.46		4358.4	1.17
	2438.3	0.45		4388.9	1.19
	2468.8	0.53		4419.4	1.2
	2834.5	0.58		4449.9	1.2
	3047.9	0.6		4480.3	1.22
	3169.8	0.65		4494	1.42
	3169.8	0.7		4510.8	1.24
	3474.6	0.7		4541.3	1.26
3840.3	0.83	4551.4	1.27		
4145.1	0.89				
4365					
1.32					

PI can be used to determine thermal maturity [20,30-34]. PI is the proportion of the amount of the free hydrocarbons already generated to the total amount of hydrocarbon that the organic matter is capable of generating [19,38]. The plot of PI versus T_{max} (Fig. 10) shows that the organic matter for the Hoiho Formation in the four wells grade from immature to over-mature with values ranging from 0.04 to 0.11. This cross-plot is in good agreement with Figure 9, demonstrating the presence of organic matter in several thermal maturity stages for Hoiho source rocks.

On the other hand, the Toroa-1 well has a lower PI value (0.05). The data indicating over maturity in this well, T_{max} (468-472°C) and vitrinite reflectance $R_o\%$ (1.37-1.42%), are inconsistent with the PI value. The reason for this is well described by Abdullah *et al.* [56]; it can be due to different lithology, nature of kerogen, or even the preservation condition of organic matter.

A cross-plot of TOC versus depth from different wells (Fig. 11) shows that majority of the Hoiho Formation contains an excellent hydrocarbon quantity regardless of the formation's depth. However, depth affects the organic matter quality and thermal maturity (Figs. 12-13).

The Hoiho Formation is encountered at a shallow depth in Hoiho-1C well, at a depth of 1966 to 2286 metres, compared to the other wells. Conversely, the formation is found to be over-mature in Toroa-1 well, as the condensate gas window is already reached at greater depths with high T_{max} (Figs. 12-13).

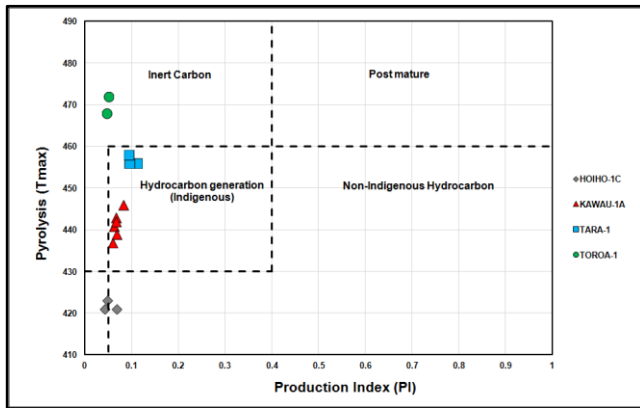


Figure 10. A cross-plot of T_{max} versus PI to identify source rock maturity

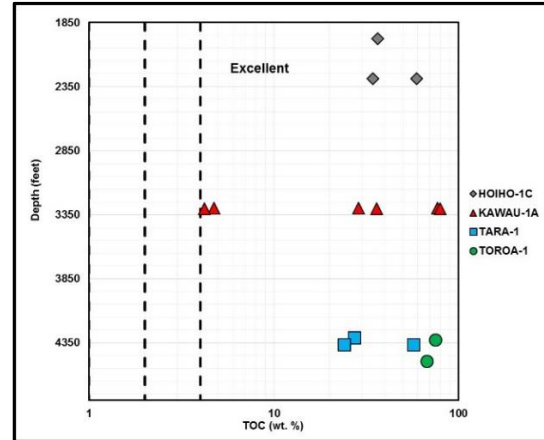


Figure 11. Cross-plot of TOC versus depth to demonstrate the distribution of the parameter with increasing depth (Shalaby *et al.* [33])

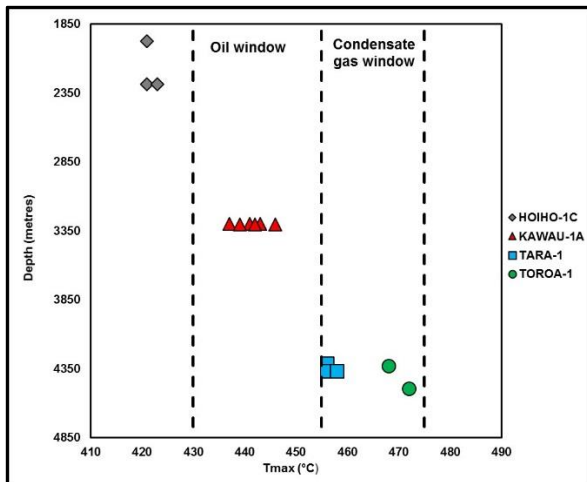


Figure 12. Cross-plot of T_{max} versus depth to demonstrate the distribution of the parameter with increasing depth (Shalaby *et al.* [33])

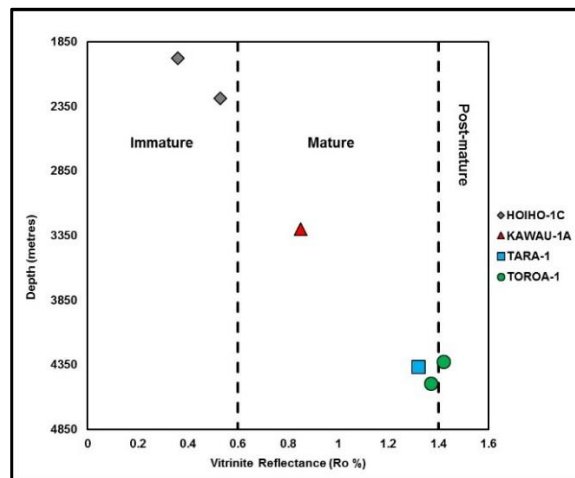


Figure 13. Cross-plot of R_o versus depth to demonstrate the distribution of the parameter with increasing depth (Shalaby *et al.* [33])

Difference in thermal maturity recorded in all four wells is attributed to the positions of these wells in the Great South Basin. Thermal maturation of the Hoiho Formation encountered in Kawau-1A, Toroa-1 and Tara-1 wells is resulted from to the positions of these wells at the Central Graben of the Great South Basin, where sediments are the thickest.

Good homogeneity is shown for all four wells, whereby a gradation of maturity-measuring parameters, such as T_{max} and % R_o , is recorded as the Hoiho Formation is encountered at varying depths across the wells.

4.4. Paleodepositional environment

Biomarkers are one of the important means to assess a source rock's paleodepositional environment. They are ubiquitous in nature and can be distinct when evaluating a specific source rock depositional facies [45]. Biomarkers utilized for evaluating source rocks are derived from organic compounds of previous living organisms [46]. Different biomarker parameters and their derivations can be correlated together to give accurate results constraining the paleodepositional environment and thermal maturity, as well as the quality of a source rock.

4.4.1. Pristane/phytane ratio (Pr/Ph)

The conditions of a source rock's depositional environment can be evaluated by the ratio of two alkanes: pristane (2, 6, 10, 14-tetramethyl pentadecane) and phytane (2, 6, 10, 14-tetramethyl hexadecane) [45,47]. The range of values for the Pr/Ph ratio indicates a variation in the redox conditions underwent by the source rock [48-49]. For the Hoiho Formation, the Pr/Ph ratio ranges from 3.9 to 7.0, reflecting the presence of mostly oxidizing terrestrial sediments (Table 3).

Table 3. Geochemical data, n-alkane and isoprenoid biomarker ratios

Well name	Hydrocarbons		n-alkane and isoprenoid biomarker ratios			
	TOC (wt. %)	EOM (ppm)	Pr/Ph	Pr/nC ₁₇	Ph/nC ₁₈	CPI
Hoiho-1C	61.23	3740.5	5.17	1.93	0.50	1.16
Kawau-1A	51.18	5936.3	3.93	0.48	0.13	1.01
	77.03	7407.7	6.00	1.29	0.21	1.03
	79.80	7463	7.15	1.35	0.19	0.98

Well name	Regular steranes		Steranes		
	C ₂₇	C ₂₈	C ₂₉	C ₂₇ /(C ₂₇ + C ₂₉)	C ₂₉ /(C ₂₉ +C ₂₇)
Hoiho-1C	4.41	8.64	87.0	0.47	0.53
Kawau-1A	7.16	19.4	73.5	0.62	0.38
	0	21.5	78.5	0.60	0.40
	6.18	20.6	73.2	0.60	0.40

Key to biomarker abbreviation: **Pr**- 2,6,10,14-tetramethyl pentadecane; **Ph** -2,6,10,14-tetramethyl hexadecane; **IP** -C₂₀H₃₆; **dh** -18β-de-E-hopane

4.4.2. Isoprenoid/n-alkanes ratio

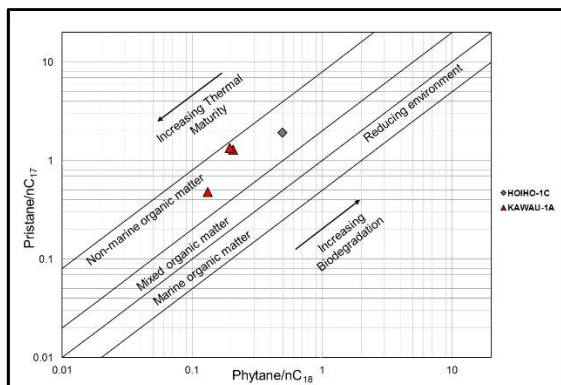


Figure 14. Graph of pristane/nC₁₇ ratio versus phytane/ nC₁₈ ratio calculated from gas chromatograms of maltene fraction of the Hoiho Formation (adapted from Peters et al., 2005)

The isoprenoids/n-alkanes ratios used in this study are the Pr/nC₁₇ and Ph/nC₁₈ ratios. These two parameters can indicate the biodegradation, maturation, and diagenetic state of a source rock. A correlation of these two ratios, as shown in Figure 14, indicates that the Hoiho Formation is dominantly made up of non-marine oxidizing organic matter. This agrees with the previously mentioned Pr/Ph ratio in 4.4.1.

4.4.3. Concentration of sterane biomarkers

The regular sterane biomarkers used for this study are C₂₇, C₂₈ and C₂₉. Together, these steranes can indicate the origin of the organic matter making up the hydrocarbon. High concentrations of C₂₇ sterane signify a marine origin for the organic matter. A dominance of C₂₈ is caused by high levels of lacustrine algae and C₂₉ dominance indicates a terrestrial origin. Volkman [50] stated that relying on steranes concentration to investigate the origin of organic matter is not always reliable. C₂₉ sterane, which is originally thought to be derived from vascular plants, can also be found in sediments generated from a marine environment. A combination of results from other biomarkers derived from higher plants is therefore necessary to have a comprehensive understanding of the source of organic matter, especially from coals.

A ternary diagram, shown in Figure 15, has been constructed using C₂₇, C₂₈ and C₂₉ steranes to study the origin of organic matter (adapted after Huang and Meinschein [51]). Figure 15 shows that the organic matter of the Hoiho Formation is primarily terrestrial due to the dominance of the C₂₉ sterane.

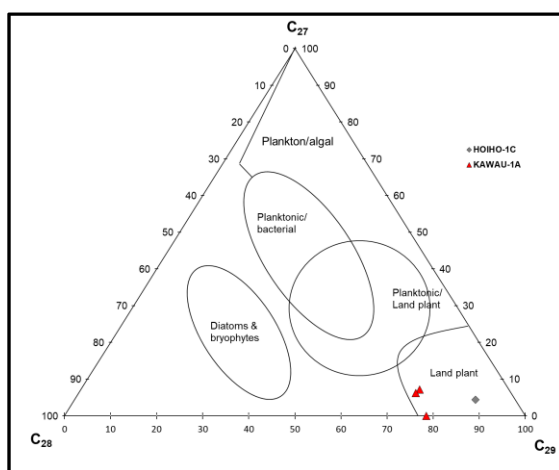


Figure 15. Ternary diagram of regular steranes for the Hoiho Formation (adapted from Huang and Meinschein, 1979)

4.4.4. Ratio of sterane and Pr/Ph

Conditions of the paleodepositional environment of the source rock were evaluated using a graph of C₂₇/(C₂₇+C₂₉) sterane versus Pr/Ph. Figure 16 indicates that the organic matter was deposited in a terrestrial and oxic environment.

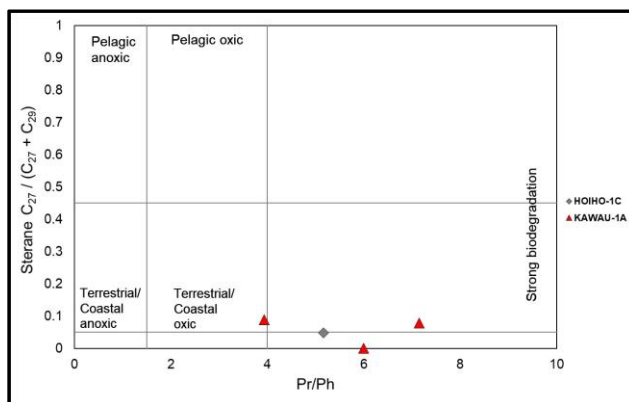


Figure 16. Cross-plots of C₂₇ / (C₂₇ + C₂₉) versus pristane/phytane ratio for the Hoiho Formation (adapted from Hossain et al., 2009)

4.4.5. Carbon Preference Index (CPI)

The Carbon Preference Index (CPI) of organic matter is defined as the ratio between the sum of odd-numbered carbon alkanes to the sum of even-numbered carbon alkanes. This parameter gives an indication of the state of a source rock's thermal maturity and the source of the organic matter [19]. A thermally immature source rock is indicated by CPI values that are significantly high or containing values that are less than 1.0 [47]. In this study, samples from the Hoiho Formation contain CPI values ranging from 1.0 to 1.2, indicating the organic matter of the Hoiho Formation is thermally mature and originates from a terrestrial source, which is in good agreement with figure 14 (Table 3).

4.4.6. Total organic carbon content (TOC) versus extractable organic matter (EOM)

Extractable organic matter derived from biomarkers can be used to assess the quality of source rock. In the cross-plot of total organic carbon (TOC) versus extractable organic matter (EOM), as shown in Figure 17, it is evident that the Hoiho source rock is of excellent quality and confirms the geochemical results as shown in Figures 4–5.

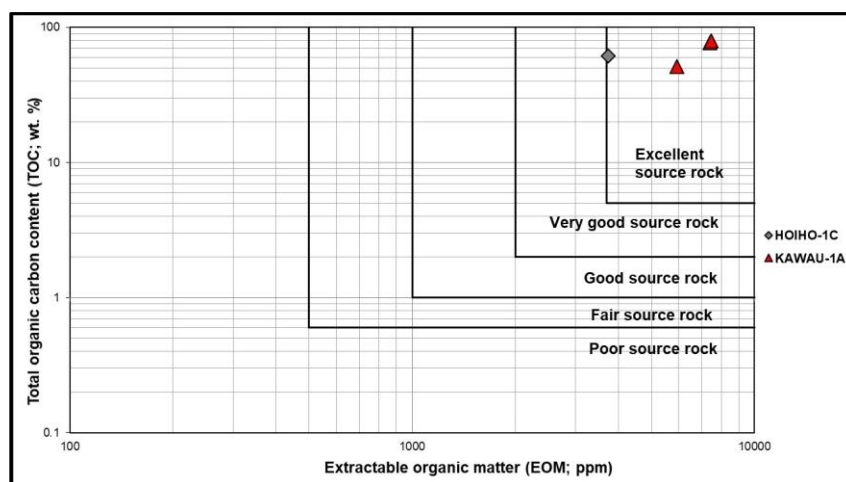


Figure 17. A cross-plot of TOC versus EOM to demonstrate the source rock quality

4.5. Burial history and Basin modelling

4.5.1. Subsidence and burial history

Through one-dimensional basin modelling using PetroMod software, several important factors can be assessed for the Hoiho source rock, including the burial history, sedimentation rate, thermal maturity history, maturation of source rock, and timing, as well as exact depth of hydrocarbon generation.

A total of eight formations are encountered in Kawau-1A well. The metamorphic basement is overlain by 442.5 m of the Late Cretaceous Hoiho Formation, which was deposited from 100.2 Ma for a duration of 13.7 Ma. Overlying this formation is the Kawau Sandstone, which was deposited from 86.5 Ma to 84.0 Ma, and serves as the reservoir for the underlying Hoiho Formation. Deposition of the Wickliffe Formation then follows for a duration of 18.5 Ma, producing a 955 m thick of sandy shale. The Waipawa Black Shale was deposited for a relatively short time, generating a thickness of 49 m. The Laing Formation is dominantly shale and was deposited from 55.8 Ma to 53.3 Ma to produce a layer of 157 m thick. The Tucker Cove Formation that lies above the Laing Formation consists primarily of shaley limestone. It has a present thickness 513 m and was deposited from 53.3 Ma to 34.5 Ma. Following the deposition of Tucker Cove Formation is the deposition of the Penrod Formation that has a duration of 18.6 Ma. From 15.9 Ma to the present, recent sediments are still being deposited

with shale as the main lithology (Fig. 18). Summary of the stratigraphic sequence for Kawau-1A well is found in Table 4.

Table 4. Input parameters for 1-D modelling of Well Kawau-1A

Formation name	Age (Ma)	Top (metres)	Bottom (metres)	Thickness (metres)	Lithology	Petroleum System Elements
Recent sediments	0-15.9	0	1100	1100	Shale	Overburden rock
Penrod Formation	15.9-34.5	1100	1550	450	Limestone	Overburden rock
Tucker Cove Formation	34.5-53.3	1550	2063	513	Shaly limestone	Overburden rock
Laing Formation	53.3-55.8	2063	2220	157	Shale	Overburden rock
Waipawa Black Shale	55.8-65.5	2220	2269	49	Shale	Overburden rock
Wickliffe Formation	65.5-84.0	2269	3224	955	Sandy shale	Seal rock
Kawau Sandstone	84.0-86.5	3224	3259.5	35.5	Sandy	Reservoir rock
Hoiho Formation	86.5-100.2	3259.5	3702	442.5	Shaly coal	Source rock

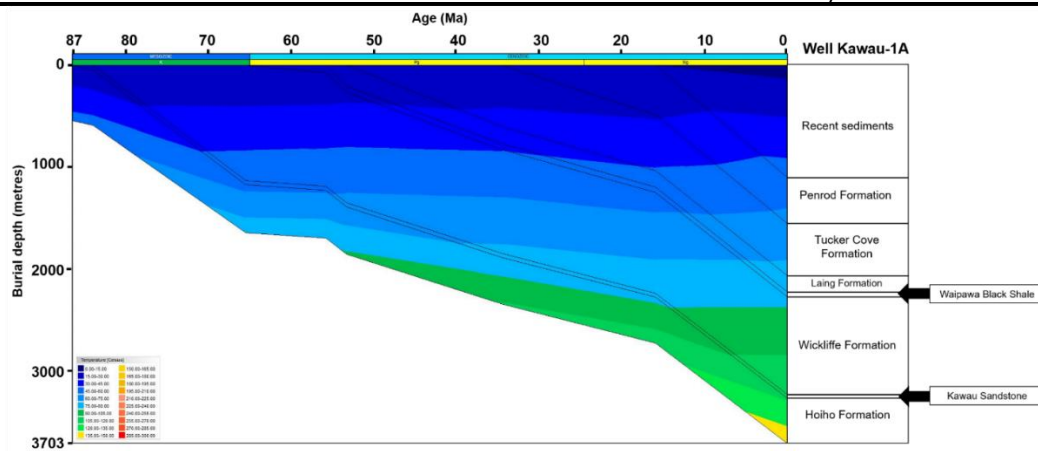


Figure 18. Burial history with temperature variations for Well Kawau-1A

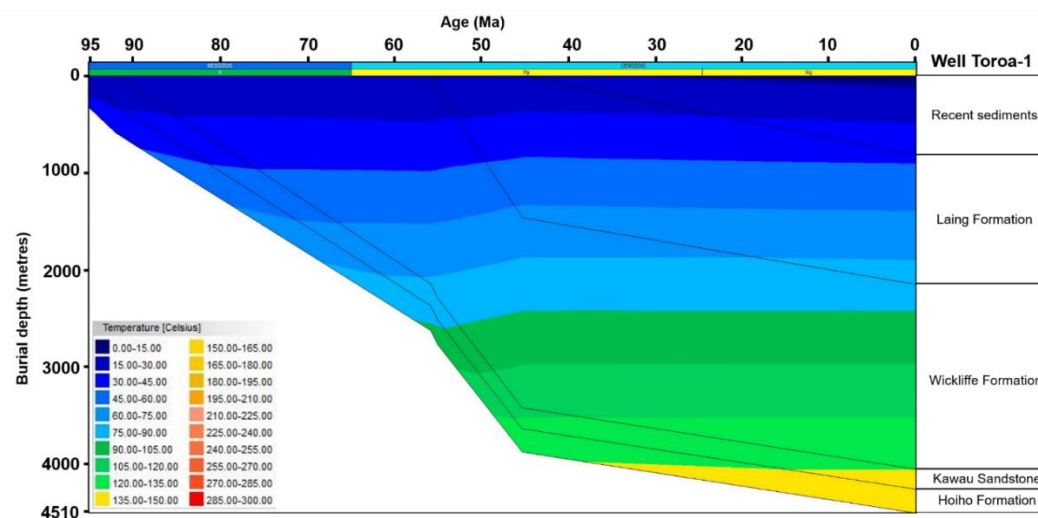


Figure 19. Burial history with temperature variations for Well Toroa-1

In the Toroa-1 well, the Late Cretaceous Hoiho Formation was deposited on top of the metamorphic basement from 100.2 Ma for a duration of 5 Ma. Overlying the Hoiho Formation is the Kawau Sandstone, which was deposited from 95.2 Ma to 92.1 Ma. Deposition of sandstone belonging to the Wickliffe Formation then occurred for 37.1 Ma, overlying the Kawau Sandstone. The Eocene Waipawa Black Shale is deposited afterwards with a thickness of 40 m from 55 Ma to 55.8 Ma. From 55.8 Ma to 45.3 Ma, the shale was further overlain by

the deposition of the Laing Formation, for which shale and sandstone are the main lithology. Following this is the deposition of recent sediments from 45.3 Ma to the present (Fig. 19). Table 5 indicates the succession of formation in Toroa-1 well.

Table 5. Input parameters for 1-D modelling of Well Toroa-1

Formation name	Age (Ma)	Top (metres)	Bottom (metres)	Thickness (metres)	Lithology	Petroleum System Elements
Recent sediments	0-45.3	0	823	823	Shale	Overburden rock
Laing Formation	45.3-55.0	823	2155	1332	Shale and Sandstone	Overburden rock
Waipawa Black Shale	55.0-55.8	2155	2195	40	Shale	Seal rock
Wickliffe Formation	55.8-92.1	2195	4100	1905	Sandstone	Reservoir rock
Kawau Sandstone	92.1-95.2	4100	4310	210	Sandstone	Reservoir rock
Hoiho Formation	95.2-100.2	4310	4551.5	241.5	Sandy coal	Source rock

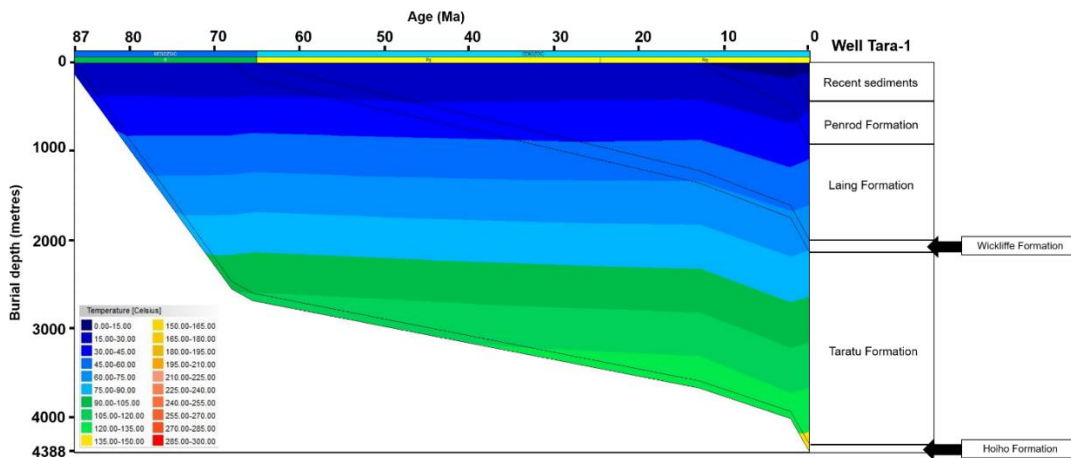


Figure 20. Burial history with temperature variations of Well Tara-1

The metamorphic basement of Tara-1 well is overlain by the Hoiho Formation which was deposited from 89.1 Ma to 86.5 Ma. Following this is the deposition of the Taratu Formation, which distinguishes Tara-1 well from the other two wells. With a thickness of 2165 m, the Paleocene and Late Cretaceous Taratu Formation was deposited from 86.5 Ma to 68 Ma. Overlying this is the sandy shale Wickliffe Formation that was deposited for a duration of 2.5 Ma. Deposition of Laing Formation then follows, from 65.5 Ma to 12.98 Ma to produce a 1086 m thick of sand and shale layer. Overlying the Laing Formation is the Penrod Formation, which was deposited 12.98 Ma to 2.2 Ma, with limestone as the main lithology. Recent sediments are then deposited from 2.2 Ma to the present (Fig. 20). Stratigraphy in Tara-1 well can be summarized in Table 6.

Table 6. Input parameters for 1-D modelling of Well Tara-1

Formation name	Age (Ma)	Top (metres)	Bottom (metres)	Thickness (metres)	Lithology	Petroleum System Elements
Recent sediments	0-2.2	0	442	442	Shale	Overburden rock
Penrod Formation	2.2-12.98	442	920	478	Limestone	Overburden rock
Laing Formation	12.98-65.5	920	2006	1086	Sandstone and shale	Overburden rock
Wickliffe Formation	65.5-68.0	2006	2139	133	Sandy shale	Seal rock
Taratu Formation	68.0-86.5	2139	4304	2165	Shaly sand	Reservoir rock
Hoiho Formation	86.5-89.1	4304	4387	83	Sandy coal	Source rock

4.5.2. Data calibration and thermal history

In the Great South Basin, heat flow is found to be more than 80 mW/m² [52] and is relatively higher than other basins, such as the Taranaki Basin, which has a heat flow ranging from less

than 50 mW/m² to more than 70 mW/m². The elevated heat flow found in the Great South Basin will influence the maturity of source rocks and hydrocarbon generation. According to Uruski and Ilg [13], there is an elevated heat flow value of approximately 90 mW/m² due to a heat flow anomaly towards the area around Dunedin.

Borehole temperature (BHT) values recorded do not reflect accurate formation values as the readings are taken before temperature equilibrium between the drilling mud and the formation is reached. For this reason, raw BHT readings are considerably lower than actual formation temperatures and must be corrected. In this study, corrections of BHT are performed based on studies by Waples and Ramly [25], Waples and Ramly [26], Peters and Nelson [27] and Bullard [28]. Corrected temperatures are compared with modelled temperature values for calibration purposes, and a best fit between those two values indicates excellent data quality. Similarly, calibration was undertaken between measured vitrinite reflectance and calculated values based on the EASY%R_o model [29] are undertaken.

For Kawau-1A, Toroa-1 and Tara-1 wells, calibration of temperature and vitrinite reflectance at all depths display a generally good fit with each other. A minor offset in temperature calibration is detected in Kawau-1A well (Fig. 21) but there is an excellent fit for modelled and measured vitrinite reflectance values (Fig. 22). In Figures 23 to 25, an excellent fit for measured and modelled temperature as well as vitrinite reflectance values are detected for both Toroa-1 and Tara-1 wells.

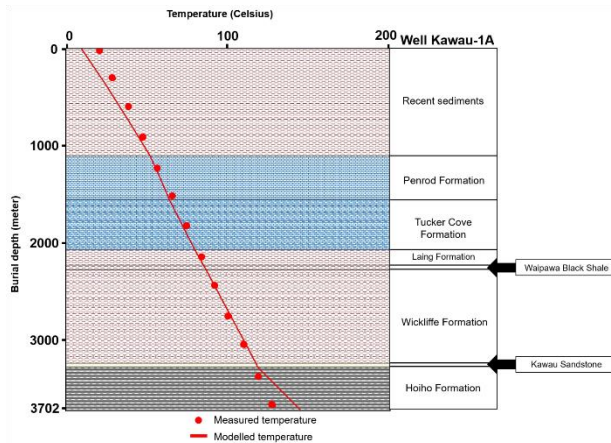


Figure 21. Calibration of measured and modelled temperature for Well Kawau-1A

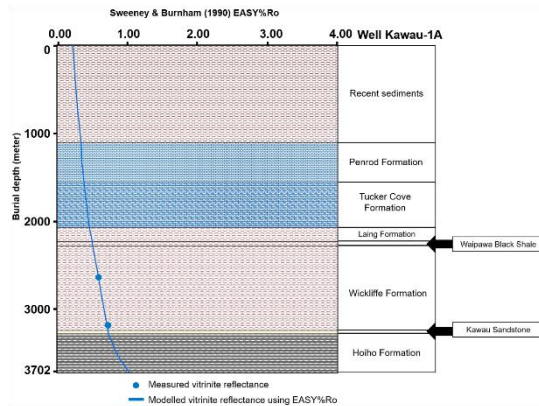


Figure 22. Calibration of measured and modelled vitrinite reflectance values for Well Kawau-1A

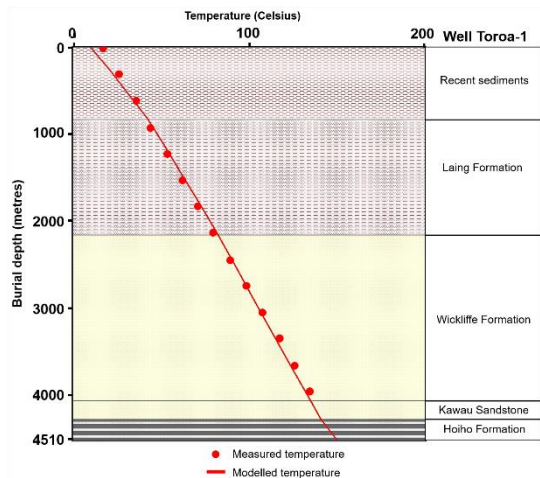


Figure 23. Calibration of measured and modelled temperature for Well Toroa-1

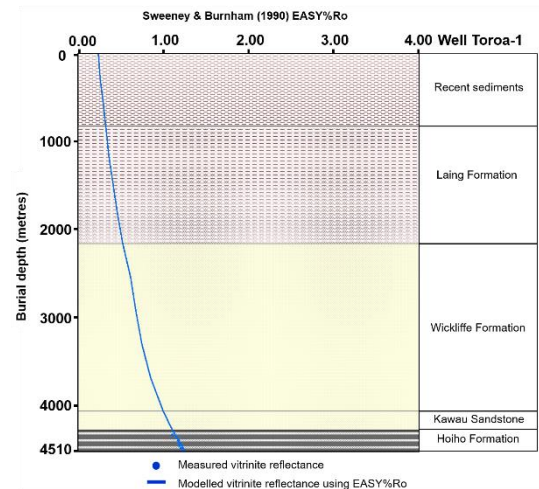


Figure 24. Calibration of measured and modelled vitrinite reflectance values for Well Toroa-1

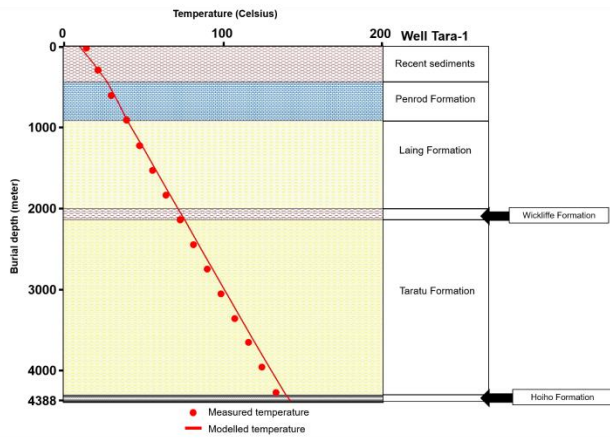


Figure 25. Calibration of measured and modelled temperature for Well Tara-1

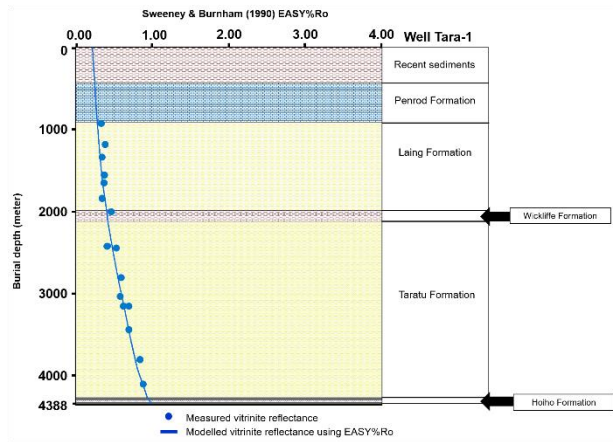


Figure 26. Calibration of measured and modelled temperature for Well Toroa-1

4.5.3. Timing of hydrocarbon generation and expulsion in the Hoiho Formation

1-D modelling from all wells permits the identification of the exact timing and depth of hydrocarbon generation and expulsion for the Hoiho source rocks. This was done based on formation temperature and maturation history [44]. Figures 26 to 31 show the hydrocarbon generation models for Kawau-1A, Toroa-1 and Tara-1 wells, with reference to the study by Burnham [53], together with their respective hydrocarbon multi-component ratio model.

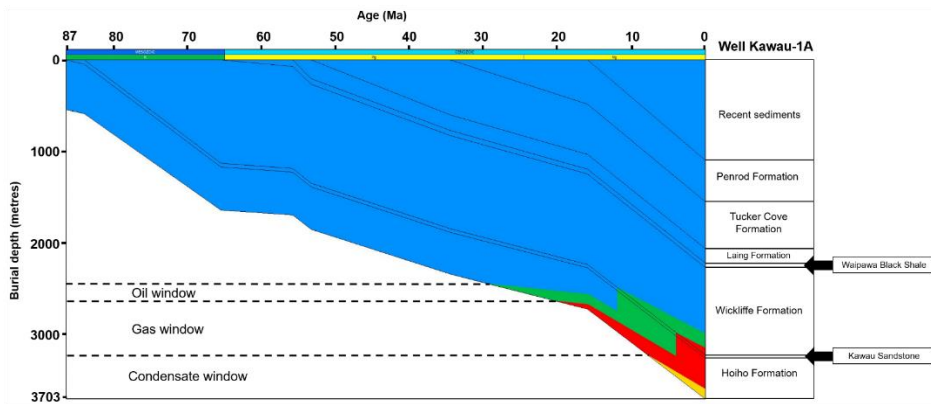


Figure 27. Hydrocarbon generation model indicating oil, gas and overmaturation windows for Well Kawau-1A

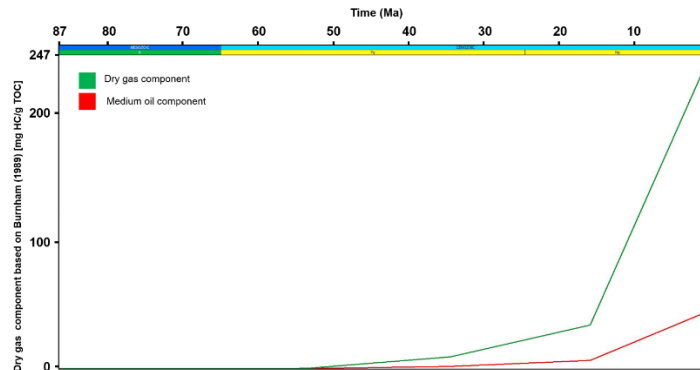


Figure 28. Hydrocarbon multi-component ratios for Well Kawau-1A

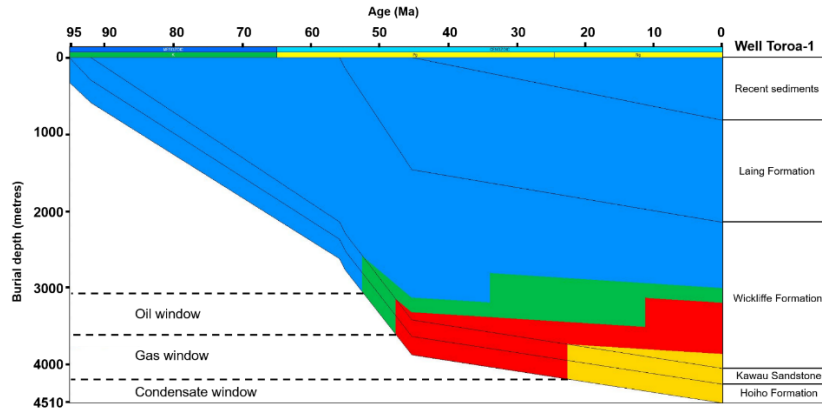


Figure 29. Hydrocarbon generation model indicating oil, gas and overmaturation windows for Well Toroa-1

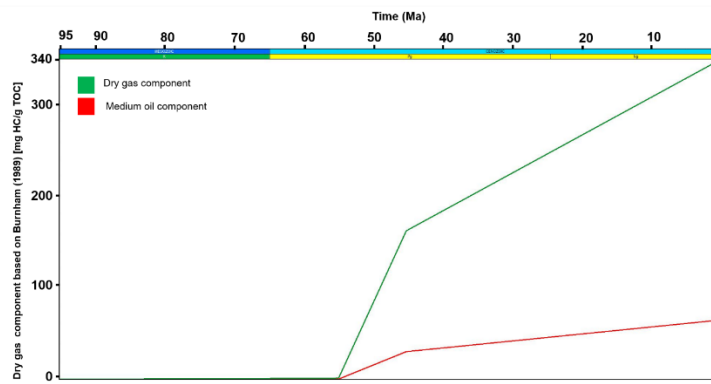


Figure 30. Hydrocarbon multi-component for Well Toroa-1

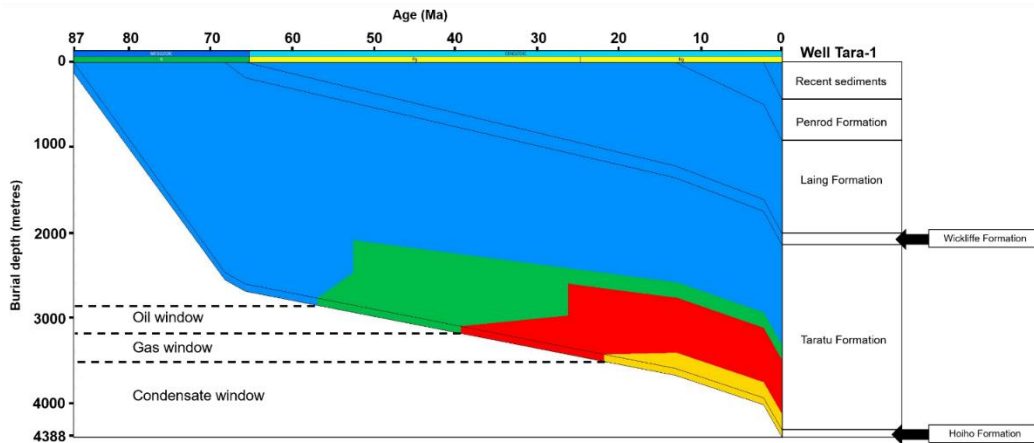


Figure 31. Hydrocarbon generation model indicating oil, gas and overmaturation windows for Well Tara-1

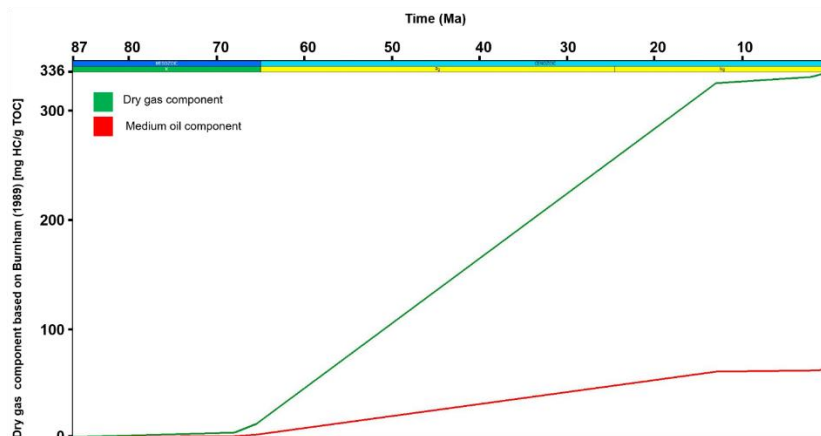


Figure 32. Hydrocarbon multi-component for Well Tara-1

In Kawau-1A, the top of oil window of the Hoiho Formation was achieved 29 Ma ago at a depth of 2448 m and in 20 Ma, the hydrocarbon matures to gas at 2634 m depth (Fig. 26). Over maturity for the Hoiho Formation in this well was reached at 3227 m depth in 8 Ma. At the present, oil and gas is still being generated in Kawau-1A well as shown in Figure 27.

The oil generation window for the Hoiho source rock began at 53 Ma at a depth of 3056 m for Toroa-1. At 48 Ma, the top of gas window was reached at a depth of 3601 m. In this well, over maturity of organic matter was attained at 23 Ma ago at a depth of 4206 m (Fig. 28). At the present, 340 mg HC/g TOC of dry gas has been produced and the generation of liquid hydrocarbon has not yet reached its peak (Fig. 29).

At a depth of 2853 m, the oil generation window for the Hoiho Formation was reached in 57 Ma for Tara-1 well. The top of gas window for this well is reached at a depth of 3183 m in 39 Ma and overmaturity is reached at 3508 m in 22 Ma (Fig. 30). For Tara-1 well, there is a rapid generation of gas for a duration of 55 Ma with a concentration of 325 mg HC/g TOC (Fig. 31).

5. Conclusions

This study demonstrates the excellent potential of the Hoiho Formation in the Great South Basin of New Zealand as a promising source rock that may generate excellent hydrocarbon quality and quantity. In pyrolysis performed on rock samples belonging to four wells, high TOC with moderate HI readings are produced, indicating the presence of kerogen types II-III and kerogen type III. Studying thermal maturity in terms of T_{max} , vitrinite reflectance and other pyrolysis results indicates that the source rock is generally thermally mature but can be immature when drilled at a relatively shallower depths of approximately less than 2500 m. At greater depths of more than 4400 m, the organic matter is thermally over-mature. The results also show that maturity of the Hoiho source rock is higher at only three out of four studied wells due to the positions of these wells in the Great South Basins. One-dimensional basin modelling of the Hoiho source rock for Kawau-1A, Toroa-1 and Tara-1 provide an understanding of the burial and thermal maturity history of the formation. The results show that a best-fit between measured and calculated/modelled values for vitrinite reflectance and borehole temperatures in both wells. The top of oil window was reached earlier in Kawau-1A (approximately 29 Ma) while Toroa-1 and Tara-1 began to generate liquid hydrocarbon at approximately 53 Ma and 57 Ma respectively. Biomarker parameters used together with their derivations all confirm that the paleodepositional environment of the Hoiho source rock was originally non-marine and possibly located in a coastal swamp environment where marine influence is present.

Acknowledgement

The authors would like to express their gratitude to New Zealand Petroleum and Minerals, Ministry of Business, Innovation & Employment and GNS Science for providing the data for this study. Thanks and appreciations are also extended to University Brunei Darussalam for providing all facilities and support to complete this research.

References

- [1] Schiøler P, Rogers K, Sykes R, Hollis CJ, Ilg B, Meadows D, Roncaglia L and Uruski C. Palynofacies, organic geochemistry and depositional environment of the Tartan Formation (Late Paleocene), a potential source rock in the Great South Basin, New Zealand. *Mar. Pet. Geol.* 2009; 27(2): 351-369.
- [2] Evans PR. Petroleum potential of New Zealand. *J. Pet. Geol.* 1982; 5(1) 89-96.
- [3] Beggs JM. Depositional and tectonic history of the Great South Basin. *South Pacific sedimentary basins. Sedimentary basins of the World.* 1993; (2) 93-107.
- [4] Cook RA, Sutherland R and Zhu H. Cretaceous-Cenozoic Geology and Petroleum Systems of the Great South Basin, New Zealand. Institute of Geological & Nuclear Sciences. 1999; 20.
- [5] Lipski PS. Evidence for an oil play fairway on the inner shelf of the Great South Basin, New Zealand. *New Zealand Petroleum Conference Proceedings.* 2004; 7-10.
- [6] Kuehnert HA. Source rock potential of Hunt's Kawau-1A, New Zealand. *Petroleum report.* 1977; 737.
- [7] Gibbons MJ and Jackson RG. A geochemical review of the Great South Basin (incorporating previously unreported data for Kawau-1 and Toroa-1). *Petroleum report.* 1980; 902.
- [8] Anderton PW, Holloway NH, Engstrom JC, Ahmad HM and Chong B. Evaluation of the geology and hydrocarbon potential of the Great South and Campbell Basins. *Petroleum report.* 1982; 828.
- [9] Killops SD, Cook RA, Sykes R and Boudou JP. Petroleum potential and oil-source correlation in the Great South and Canterbury Basins. *N. Z. J. Geol. Geophys.* 1997; 40: 405-423.
- [10] New Zealand Petroleum and Minerals. *New Zealand Petroleum Basins.* Ministry of Business, Innovation and Employment. New Zealand: New Zealand Petroleum and Minerals, New Zealand. 2014.
- [11] Uruski CI and Baillie P. Petroleum potential of New Zealand's deepwater basins. *PESA Eastern Australasia Basins Symposium.* 2001; 151-158.
- [12] Pearson AR. The Great South Basin-Antrim International's Exploration Strategy. *Proceedings of the 1998 New Zealand Petroleum Conference.* Ministry of Commerce, Wellington. 1998; 123-139.
- [13] Uruski CI and Ilg B. Preliminary Interpretation and Structural Modelling of DUN06 Seismic Reflection Data from Great South Basin, Offshore New Zealand, Ministry of Economic Development New Zealand Unpublished Petroleum Report PR3450. 2006.
- [14] McMillan SG and Wilson GJ. Allostratigraphy of coastal south and east Otago: a stratigraphic framework for interpretation of the Great South Basin, New Zealand. *N. Z. J. Geol. Geophys.* 1997; 40(1): 91-107.
- [15] Constable RM, Langdale S and Allan TMH. Development of a sequence stratigraphic framework in the Great South Basin. *Advantage NZ: 2013 Petroleum Conference, Wellington.* 2013; 1-21.
- [16] Laird MG and Bradshaw JD. The break-up of a long-term relationship: the Cretaceous separation of New Zealand from Gondwana. *Gondwana Res.* 2004; 7 (1): 273-286.
- [17] Laird M. Mid and early Late Cretaceous break-up basins of the South Island, New Zealand. In *Geological Society of Australia Abstracts. Geological Society of Australia.* 1996; 43: 329-336.
- [18] King PR. Tectonic reconstructions of New Zealand: 40 Ma to the present. *N. Z. J. Geol. Geophys.* 2000; 43(4): 611-638.
- [19] Tissot BP and Welte DH. *Petroleum Formation and Occurrence: A New Approach to Oil and Gas Exploration.* Berlin: Springer-Verlag. 1978; 538.
- [20] Peters KE. Guidelines for evaluating petroleum source rock using programmed pyrolysis. *AAPG Bull.* 1986; 70(3): 318-329.
- [21] Espitalié J, Madec M, Tissot, B., Mennig JJ and Leplat P. Source rock characterization method for petroleum exploration. *Offshore Technology Conference.* 1977.
- [22] Rodriguez ND and Philp RP. Source rock facies distribution predicted from oil geochemistry in the Central Sumatra Basin, Indonesia. *AAPG Bull.* 2015; 99(11): 2005-2022.
- [23] Abdullah WH, Togunwa OS, Makeen YM, Hakimi MH, Mustapha KA, Baharuddin MH, Sia S-G and Tongkul F. Hydrocarbon source potential of Eocene-Miocene sequence of Western Sabah, Malaysia. *Mar. Pet. Geol.* 2017; 83: 345-361.

- [24] Ayinla HA, Abdullah WH, Makeen YM, Abubakar MB, Jauro A, Yandoka BMS, Mustapha KA and Abidin NSZ. Source rock characteristics, depositional setting and hydrocarbon generation potential of Cretaceous coals and organic rich mudstones from Gombe Formation, Gongola Sub-basin, Northern Benue Trough, NE Nigeria. *International Journal of Coal Geology* 2017; 173: 212-226.
- [25] Waples DW and Ramly M. A simple statistical method for correcting and standardizing heat flows and subsurface temperatures derived from log and test data. *Bulletin of the Geological Society of Malaysia, Special Publication*. 1994; 37: 253-267.
- [26] Waples DW and Ramly M. A statistical method for correcting log-derived temperatures. *Pet. Geosci.* 2001; 7(3): 231-240.
- [27] Criteria to determine borehole formation temperatures for calibration of basin and petroleum system models. *Thermal history analysis of sedimentary basin: Methods and applications: SEPM Special Publication*. 2013; 103: 5-16.
- [28] Bullard EC. The time necessary for a bore hole to attain temperature equilibrium. *Geophys. J. Int.* 1947; 5(5): 127-130.
- [29] Sweeney JJ and Burnham AK. Evaluation of a simple model of vitrinite reflectance based on chemical kinetics (1). *AAPG Bull.* 1990; 74(10): 1559-1570.
- [30] Shalaby MR, Hakimi MH and Abdullah WH. Geochemical characteristics and hydrocarbon generation modeling of the Jurassic source rocks in the Shoushan Basin, north Western Desert, Egypt. *Mar. Pet. Geol.* 2011; 28(9): 1611-1624.
- [31] Shalaby MR, Hakimi MH and Abdullah WH. Modeling of gas generation from the Alam El-Bueib formation in the Shoushan Basin, northern Western Desert of Egypt. *Int. J. Earth Sci.* 2012a; 102(1): 319-332.
- [32] Shalaby MR, Hakimi MH and Abdullah WH. Organic geochemical characteristics and interpreted depositional environment of the Khatatba Formation, northern Western Desert, Egypt. *AAPG Bull.* 2012b; 96: 2019-2036.
- [33] Shalaby MR, Hakimi MH and Abdullah WH. Geochemical characterization of solid bitumen (migrabitumen) in the Jurassic sandstone reservoir of the Tut Field, Shoushan Basin, northern Western Desert of Egypt. *International Journal of Coal Geology*. 2012c; 100: 26-39.
- [34] El Nady MM, Ramadan FS, Hammad MM and Lotfy NM. Evaluation of organic matters, hydrocarbon potential and thermal maturity of source rocks based on geochemical and statistical methods: Case study of source rocks in Ras Gharib oilfield, central Gulf of Suez, Egypt. *Egypt. J. Pet.* 2015; 24(2): 203-211.
- [35] Langford FF and Blanc-Valleron MM. Interpreting Rock-Eval pyrolysis data using graphs of pyrolyzable hydrocarbons vs. total organic carbon (1). *AAPG Bull.* 1990; 74(6): 799-804.
- [36] Espitalié J, Deroo G and Marquis F. Rock-Eval pyrolysis and its applications. *Revue De L Institut Francais Du Petrole* 1985; 40(5): 563-579.
- [37] Waples DW. *Geochemistry in petroleum exploration*, D. Reidel Publishing Co.: Dordrecht-Boston-Lancaster, 1985; pp. 1-232.
- [38] Peters KE and Cassa MR. *Applied source-rock geochemistry*, Magoon, L.B., Dow, W.G., Eds.; The Petroleum System—From Source to Trap. *AAPG Mem.* 1994; 60: 93-120.
- [39] Espitalié J. Use of Tmax as a maturation index for different types of organic matter, Burrus, J., Ed.: Editions Technip Paris, 1986; pp. 475-496.
- [40] Barker C. Pyrolysis techniques for source-rock evaluation. *AAPG Bull.* 1974; 58(11): 2349-2361.
- [41] Mukhopadhyay PK. Vitrinite reflectance as a maturity parameter. 1994; 570: 1-24.
- [42] Stach E, Mackowsky MT, Teichmüller M, Taylor GH, Chandra D and Teichmüller R. *Stach's textbook of coal petrography*. Borntraeger, Berlin. 1982; pp. 1-535.
- [43] Price LC and Barker CE. Suppression of vitrinite reflectance in amorphous rich kerogen--a major unrecognized problem. *J. Pet. Geol.* 1985; 8(1): 59-84.
- [44] Qadri ST, Shalaby MR, Islam MA and Hoon LL. Source rock characterization and hydrocarbon generation modeling of the Middle to Late Eocene Mangahewa Formation in Taranaki Basin, New Zealand. *Arabian J. Geosci.* 2016; 9(10): 559, 8-9.
- [45] Moustafa YM and Morsi RE. Biomarkers. *Chromatography and its Applications*. InTech. 2012.
- [46] Mobarakabad AF, Bechtel A, Gratzner R, Mohsenian E and Sachsenhofer RF. Geochemistry and origin of crude oils and condensates from the Central Persian Gulf, Offshore Iran. *J. Pet. Geol.* 2011; 34(3): 261-275.
- [47] Peters K, Walters C and Moldowan J. *The Biomarker Guide: Biomarkers and isotopes in petroleum systems and Earth history*. Cambridge University press, New York. 2005; 2(2).

- [48] Powell TG and McKirdy DM. Relationship between ratio of pristane to phytane, crude oil composition and geological environment in Australia. *Nature*. 1973; 243(124): 37-39.
- [49] Didyk BM. Organic geochemical indicators of palaeoenvironmental conditions of sedimentation. *Nature*. 1978; 272: 216-222.
- [50] Volkman JK. A review of sterol markers for marine and terrigenous organic matter. *Org. Geochem*. 1986; 9(2): 83-99.
- [51] Huang WY and Meinschein WG. Sterols as ecological indicators. *Geochim. Cosmochim. Acta* 1979; 43(5): 739-745.
- [52] Townend J. Heat flow through the west coast, South Island, New Zealand. *N. Z. J. Geol. Geophys*. 1999; 42(1): 21-31.
- [53] Burnham AK. A simple kinetic model of petroleum formation and cracking. Lawrence Livermore National Lab, California; 1989.
- [54] Fakhri M, Tabatabaei H and Amiri A. Comparing the Potential of Hydrocarbon Generation of Kazhdomi and Pabdeh Formations in Bangestan Anticline (Zagros Basin) According To Rock-Eval Pyrolysis Data. *J. Earth Sci. Clim. Change*. 2013; 4(157).
- [55] Hossain HZ, Sampei Y and Roser BP. Characterization of organic matter and depositional environment of Tertiary mudstones from the Sylhet Basin, Bangladesh. *Org. Geochem*. 2009; 40(7): 743-754.

To whom correspondence should be addressed: Liyana N. Oslı, Department of Geology, Faculty of Science, Universiti Brunei Darussalam, Jalan Tungku Link, BE 1410, Brunei Darussalam, anadiyah.osli@gmail.com

THE USE OF SPECTRAL DECOMPOSITION AS A HYDROCARBON INDICATOR IN THE NIGER DELTA OILFIELD

Michael Emenike Egbunike

Department of Geology, Chukwuemeka Odumegwu Ojukwu University, Uli, Nigeria.

Received December 20, 2017; Accepted March 19, 2018

Abstract

The use of frequency analysis had been known in the petroleum industry for decades. The present study was born out of the need to demonstrate the applicability of spectral analysis in the search for hydrocarbon in the Niger Delta Basin. The objectives of the study were to show the presence of hydrocarbon and demonstrate the use of frequency analysis in the determination of the fluid contact. The spectral analysis of the D6.2 reservoir in KC field was performed using ndi software. The Short Time Fourier Transform (STFT) method is used with the specified frequency range of 5 - 50 Hz. The analysis was done over a time interval of 1500 – 4000ms. The window length and the taper used is 256ms and 20% respectively. The location of the calibration well-39 on the gas leg is at track 8600 and the bin is at 4784. The location of well-32 on the brine leg is at track 8426 while the bin is at 4854. Moreover, the seismic / frequency / amplitude generated is extracted from both the gas leg and the brine leg respectively. The result of the spectral decomposition shows the presence of hydrocarbon in the D6.2 reservoir and establishes a possible hydrocarbon contact. The hydrocarbon contact at 2690ms shown by the frequency maps agreed with the contact established in the amplitude versus time cross plot.

Keywords: *Hydrocarbon; Spectral; Analysis; Contact; Amplitude.*

1. Introduction

The spectral decomposition was done in the D6.2 reservoir in KC field in the Niger Delta Basin. This method utilizes wavelet transforms to obtain frequency spectral with high temporal resolution without the windowing problem associated with traditional Fourier analysis. Spectral decomposition transforms the seismic data (time domain) into the frequency domain. Spectral analysis produces a continuous time-frequency analysis of a seismic trace [1]. Thus, a frequency spectrum is output for each time sample of the seismic trace. Spectral decomposition has been used for a variety of applications including layer thickness determination [2-5] and stratigraphic visualisation [5]. The purpose of this study is to show that spectral decomposition has the capacity to uncover the effects of hydrocarbon accumulation on seismic data acquired from the Niger Delta Basin. The analysis revealed the presence of hydrocarbon and used to determine the hydrocarbon contact in the D6.2 reservoir. This result ordinarily could not have been resolved using the conventional Fourier-based spectral decomposition methods [7-9]. Knowledge of the exact location of the hydrocarbon contact in a reservoir is very necessary for hydrocarbon column determination which is an important parameter in calculating the volume of petroleum in the field.

The objectives of the study were to (i) show the presence of hydrocarbon (ii) demonstrate the use of frequency analysis in the determination of the fluid contact.

2. Location, historical background and geology of the field

The KC field is in the seasonally flooded land area of the Eastern Division in OML-28, about 75 km west of Port Harcourt (Fig.1). The field was discovered in May, 1971 by well 1, it lies within

the central swamp. The field has shallow gas bearing reservoirs with the E2.000x being the only oil-bearing reservoir with a total of twenty-five drainage points [10]. The 2D geological model of the field is a fault rollover structure bounded to the north by a major growth fault to the south by a system of faults, with dip-closed eastern and western boundaries. The D sand consists of six reservoirs and is gas bearing from 9,200 – 11,570 ft.ss. At the E2.000x level, a major E-W trending synthetic crestal fault separates the field into a main upthrown and downthrown block. The sand is hydrocarbon bearing within 11,300 – 11,900ft.ss with an oil rim of 200ft overlain by a large gas cap. The E2.000x reservoir consists of deltaic package of barrier sheets and channel sands deposited in five cycles. The sand quality improves towards the north with the channel sands. Poor sand development and system of faults limit aquifer into the reservoir. The field has 39 wells drilled to date. Thirty-five of these penetrated the E2.000x reservoir. The field came on stream in 1973 and in June 1974 peaked at a production rate of 43,000 barrels of oil per day.

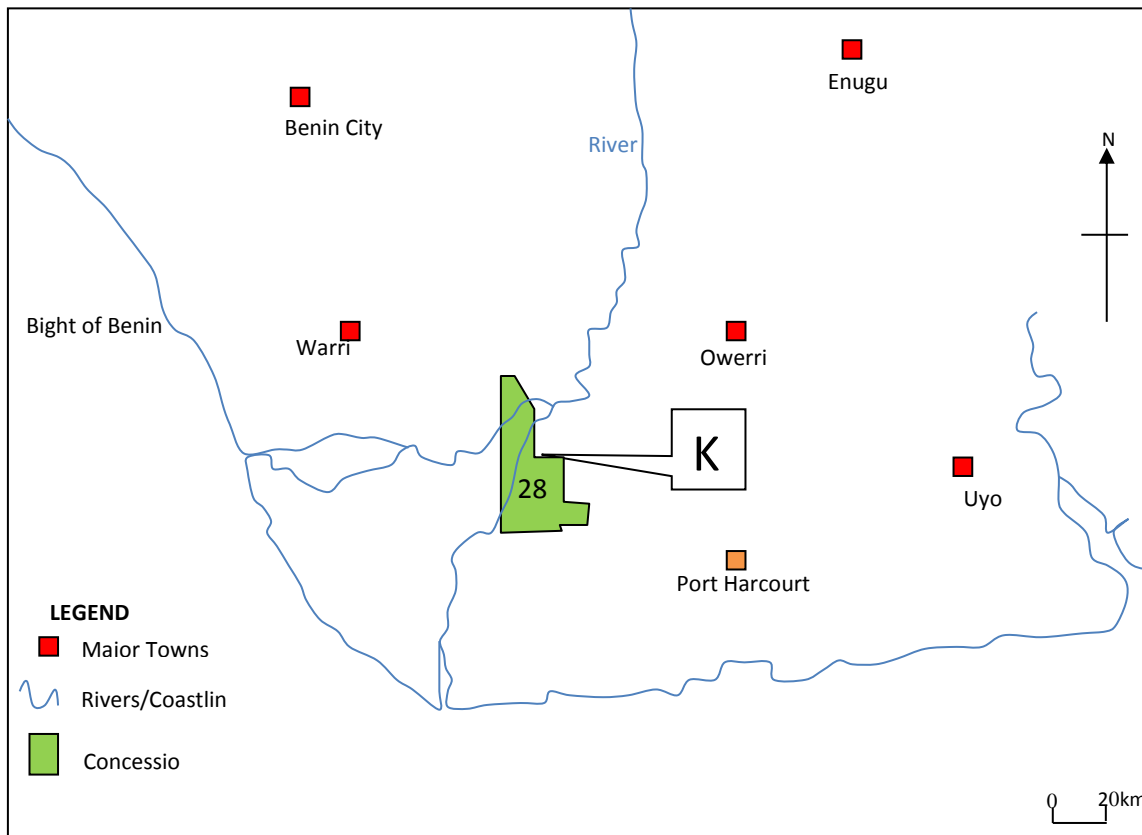


Fig.1. Location map showing the KC field

The main structural features of the KC E2000x and D6200 reservoirs show that the structure is NW – SE trending rollover collapsed-crest anticline constrained to the North by the KC boundary fault. The crest of the structure has low relief with the flanks becoming steeper. Crestal faulting is intense with the general pattern being along the structural strike thereby presenting an essentially open fault system. Flank faulting is also significant but occurs at a lower frequency than at the crest. Hydrocarbons are mainly dip trapped with the northern boundary fault providing the major fault-assisted trapping to the north – east of the structure [11].

3. Methodology

The spectral decomposition of the D6.2 reservoir in KC field was carried out using ndi software. The ndi software is Shell Petroleum Development Company (SPDC) software. The

method used is the Short Time Fourier Transform (STFT) and the specified frequency range is 5-50 Hz. The analysis was performed over a time interval of 1500 – 4000ms. The window length is 256ms and the taper is 20%.

The location of the calibration well-39 on the gas leg is at track 8600 and the bin is at 4784. The location of well – 32 on the brine leg is at track 8426 while the bin is at 4854. In the gas leg, the seismic trace/frequency/amplitude is extracted (Figs. 2 and 3) while from the brine leg, the seismic trace/frequency/amplitude is extracted as shown in Fig.4. The top and base of the reservoir at the gas leg is determined at 2644ms and 3025ms respectively from the well data or seismic interpretation. The top of the reservoir at the brine leg is at 2716ms.

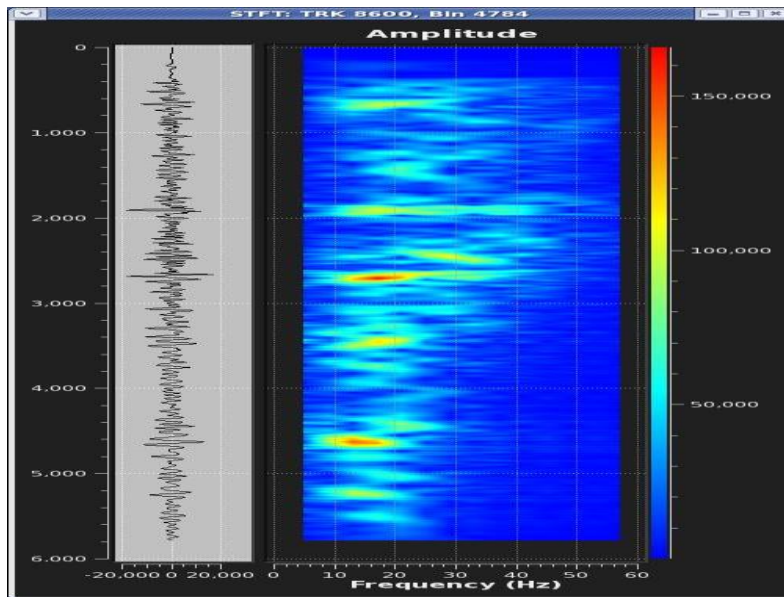


Fig.2. Extracted seismic trace/frequency/amplitude at the gas leg. The diagram shows very high amplitude occurring at low frequency range of 8 – 22.9Hz

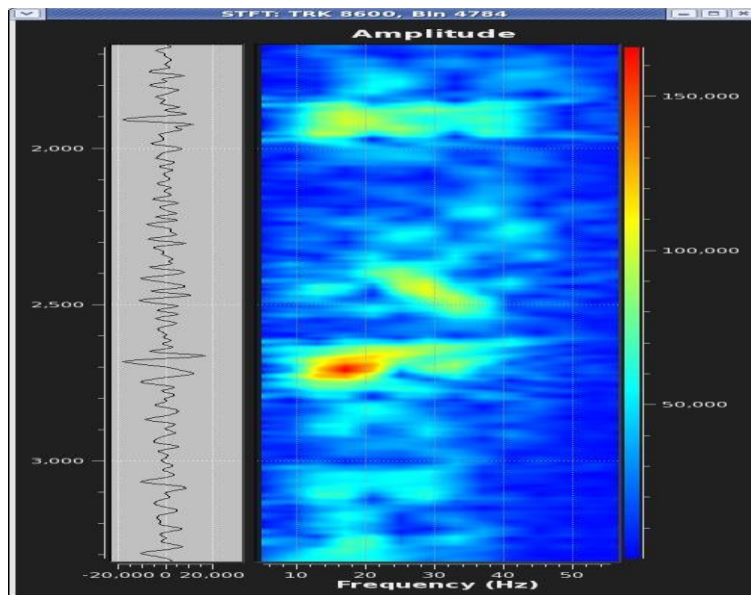


Fig.3. Zoomed extracted seismic trace/frequency/amplitude at the gas leg. The diagram shows very high amplitude at a low frequency range of 8 – 22.9Hz

4. Results and discussions

The result of the spectral decomposition or frequency analysis shows the presence of hydrocarbon in the D6.2 reservoir and establishes a possible hydrocarbon contact. The dominant frequency range for gas leg is 8 – 22.9 Hz (Figs. 2 and 3) while the dominant frequency range for brine leg is at 24 – 36 Hz (Fig.4).

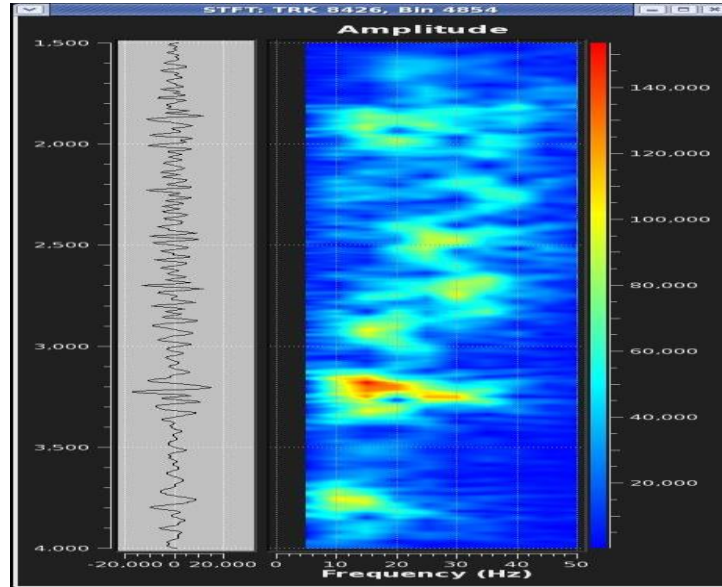


Fig.4. Extracted seismic trace/frequency/amplitude at the brine leg. This shows low amplitude response occurring at very high frequency range of 24 – 36Hz

The dominant frequency range for both gas leg and brine leg conforms to the results obtained from the frequency maps (Fig.5, Fig.6, Fig.7, Fig.8 and Fig.9).

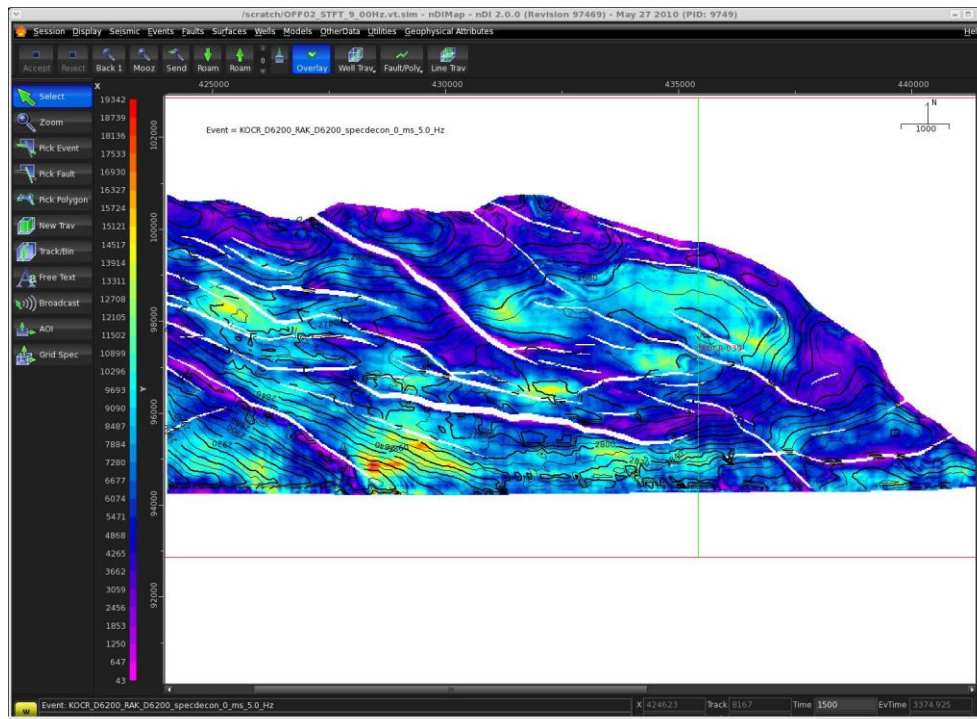


Fig.5. Frequency map generated at 5Hz. The 5Hz frequency could not separate the brine from the gas

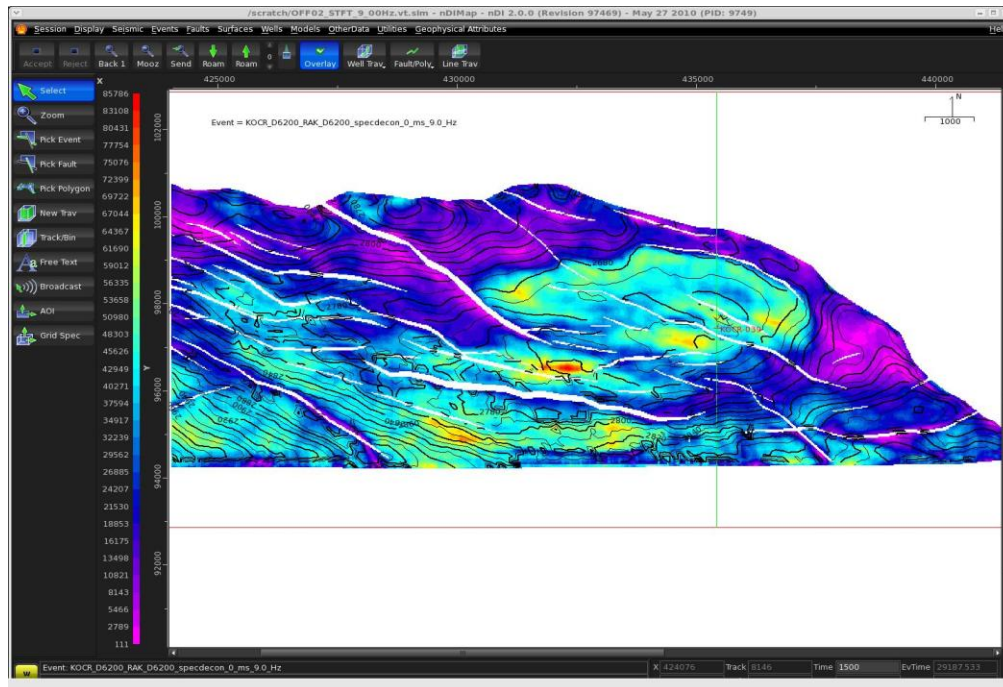


Fig.6. Frequency map generated at 9Hz. The 9Hz frequency gives the best separation of the brine from the gas and the best conformable amplitude to structure

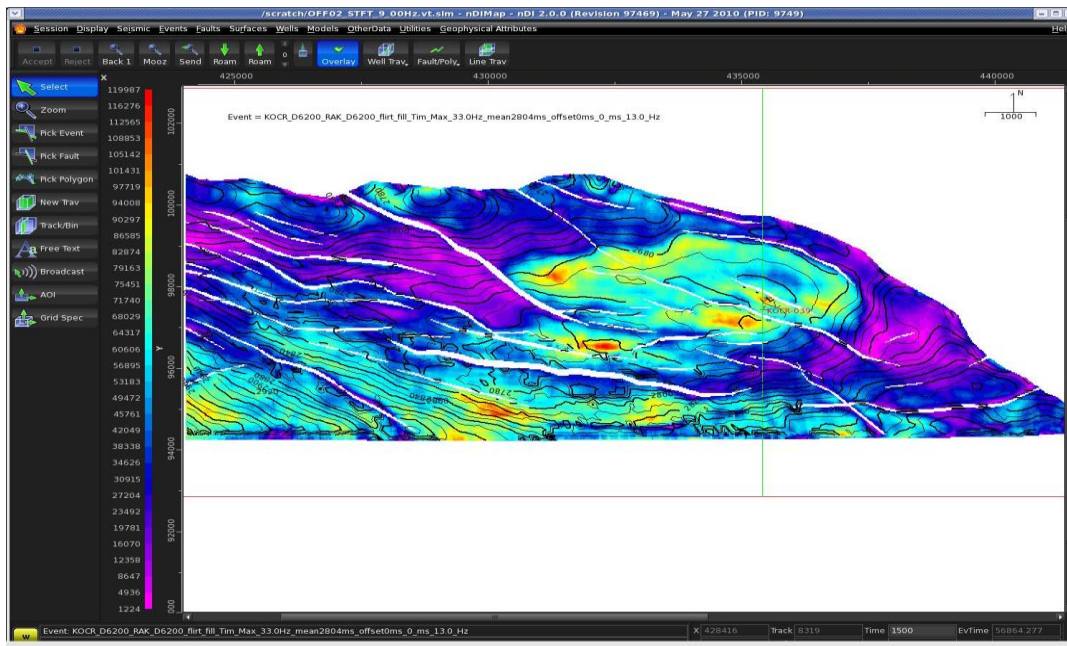


Fig. 7. Frequency map generated at 13Hz. The 13Hz frequency shows the separation of the brine from the gas

It has been observed that using the dominant frequency ranges between 9 – 15 Hz gives the best isolation of the gas from the brine. The 9Hz frequency gives the best conformable amplitude to structure and calibrated contact as measured in the KC field. The extracted seismic trace/frequency/amplitude at the gas leg in well-39 shows very high amplitude at a low frequency range of 8-22.9Hz. The high amplitude response (amplitude boom) occurring at low frequency range was due to the effect of hydrocarbon (gas) in the reservoir. However,

the extracted seismic trace/frequency/amplitude at the brine leg in well-32 depicts much lower amplitude occurring at higher frequency ranges of 24-36Hz. The low amplitude response occurring very high frequency range is interpreted as a result of the presence of brine-water in the reservoir.

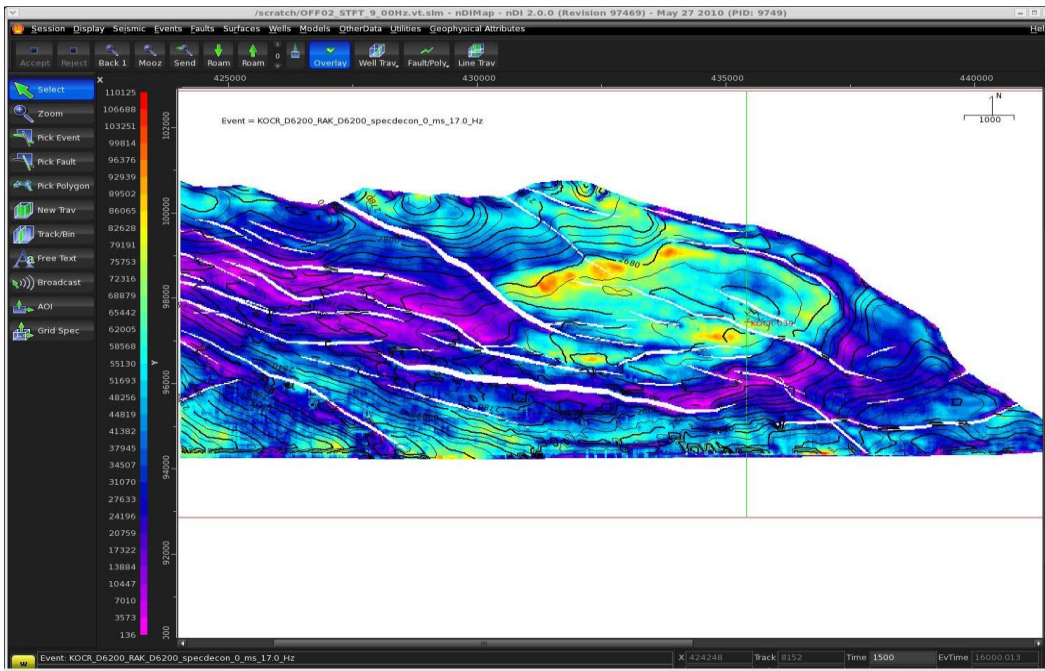


Fig. 8. Frequency map generated at 17Hz. High frequency of 17Hz becomes difficult to show contact or the separation between the brine and the gas

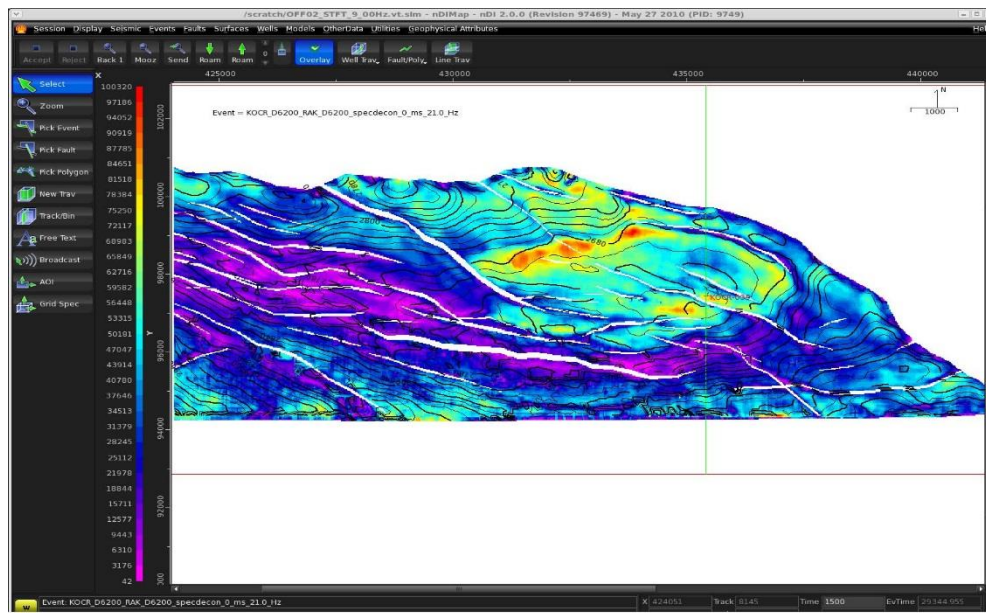


Fig. 9. Frequency map generated at 21Hz. At high frequency of 21Hz showed that it was difficult to separate the brine from the gas or define the contact

The contact shown by the frequency maps (Figs.6 and 7) also agrees with the contact established in the amplitude versus time cross plot (Fig.10).

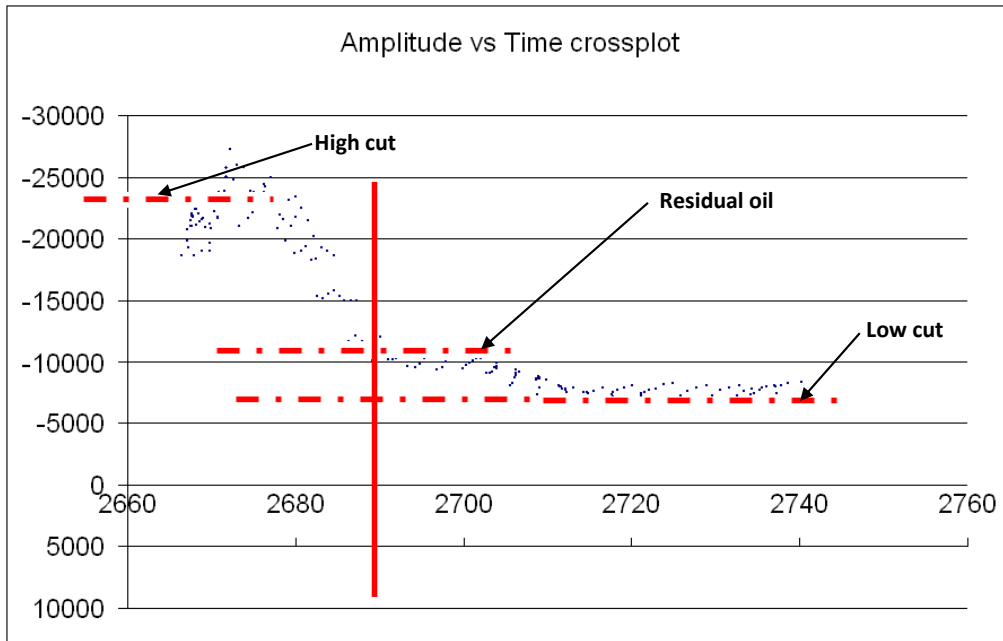


Fig. 10. Amplitude versus time (milliseconds) cross plot. The graph clearly defines the separation of high amplitude from the low amplitude values at 2690ms. The dots represent different values of amplitude at different time values

The separation of amplitudes between the brine and gas is clearly demonstrated in the frequency maps generated at 9Hz and 13Hz frequencies which define the hydrocarbon contact at 2690ms. This result agrees with the hydrocarbon contact established in the amplitude versus time cross plot (Fig.10). At higher frequency of 17Hz and above it could no longer separate the brine from the gas fluid. Therefore, at higher frequency the hydrocarbon contact could not be visible again or becomes difficult to define the contact.

5. Conclusion

The spectral analysis showed the presence of hydrocarbon in the D6.2 reservoir. This is shown by the dominant frequency range for gas leg at 8-22.9 Hz while 24-36 Hz is the dominant frequency range for brine leg. The hydrocarbon contact was established at 2690ms and found to be gas-water contact. The dominant frequency between the ranges of 9-15 Hz gives the best isolation of the gas leg amplitude from the brine leg amplitude. The 9Hz frequency gives the best conformable amplitude to structure and calibrated contact in the KC field.

References

- [1] Castagna JP and Sun S. 2006. Comparison of spectral decomposition methods. *First break*, 2006; 24: 75-79.
- [2] Burnett MD, Castagna JP, Mendez-Hernandez E, Rodriguez GZ, Garcia LF, Vazquez JTM, Aviles MT and Villasenor RV. Application of spectra decomposition to gas basins in Mexico. *The Leading Edge*, 2003; 2: 1130-1134.
- [3] Gridley J, and Partyka G. Processing and interpretational aspects of spectral decomposition. *Society of Exploration Geophysicists expanded abstracts*, 1997: 1055-1058.
- [4] Partyka GJ, Gridley J and Lope, J.1999. Interpretational applications of spectral decomposition in reservoir characterization. *The Leading Edge*, 1999; 18: 353-360.
- [5] Sun S, Castagna JP and Seigfried RW. Examples of wavelet transform time-frequency analysis in direct hydrocarbon detection. 72nd Annual International Meeting of Society of Exploration Geophysicists 2002, Salt Lake City, Utah, USA.

- [6] Marfurt KJ and Kirlin RL.2001. Narrow-band spectral analysis and thin-bed tuning. J. of Geophysics, 2001; 66: 1274-1283.
- [7] Castagna JP, Sun S and Siegfried RW. The Use of Spectral Decomposition as a Hydrocarbon Indicator. GasTIPS, 2002: 24-27.
- [8] Castagna JP, Sun S and Siegfried RW.2003. Instantaneous spectral analysis: Detection of low-frequency shadows associated with hydrocarbons. The Leading Edge, 2003; 22: 127-129.
- [9] Sinha S, Routh PS, Anno PD and Castagna JP. Spectral decomposition of seismic data with continuous-wavelet transforms. J. of Geophysics,2005; 70: 19-25.
- [10] Onyejekwe C. Kolo Creek 15.9Ma Exploration Well Proposal. SPDC, EPX-G-XNEG, Report no.01BXE0002, 2005: 6-16.
- [11] Egele P. Kolo Creek Field Development Plan. SPDC, DPE-ISS, DPE/2003/RPT/06, 2003: 34-36.

To whom correspondence should be addressed: Assoc. prof. Michael Emenike Egbunike, Department of Geology, Chukwuemeka Odumegwu Ojukwu University, Uli, Nigeria, me_egbunike2006@yahoo.com

PURE CO₂-OIL SYSTEM MINIMUM MISCIBILITY PRESSURE PREDICTION USING OPTIMIZED ARTIFICIAL NEURAL NETWORK BY DIFFERENTIAL EVOLUTION

Menad Nait Amar, Nourddine Zeraibi and Kheireddine Redouane

Department of Mining and Petroleum Engineering, Faculty of Hydrocarbons and Chemistry, University M'hamed Bougara- Boumerdes, 35000 Algeria

Received December 15, 2017; Accepted March 19, 2018

Abstract

Miscible CO₂ flooding is one of the most attractive enhanced oil recovery options thanks to its microscopic efficiency improvement. A successful implementation of this method depends mainly on the accurate estimation of minimum miscibility pressure (MMP) of the CO₂-oil system. As the determination of MMP through experimental tests (slim tube, and rising bubble apparatus (RBA)) is very expensive and time consuming, many correlations have been developed. However, all these correlations are based on limited set of experimental data and specified range of conditions, thus making their accuracies questionable. In this research, we propose to build robust, fast and cheap approach to predict MMP for pure CO₂-oil by applying hybridization of artificial neural networks with differential evolution (DE). DE is used to find best initial weights and biases of neural network. Four parameters that affecting the MMP are chosen as input variables: reservoir temperature, mole fraction of volatile-oil components, mole fraction of intermediate-oil components and molecular weight of components C₅₊. 105 MMP data covering wide range of conditions are considered from the published literature to establish the model. The obtained results demonstrate that our approach outperforms all the published correlations in term of accuracy and reliability.

Keywords: Pure CO₂ minimum miscibility pressure; carbon dioxide injection, artificial neural networks, differential evolution.

1. Introduction

With the technological advancement worldwide, demand for energy (mainly fuel energy) is growing exponentially thus requiring the creation of effective methods for tertiary recovery of the residual oil before the stage of reservoirs abandonment. Miscible gas injection, especially miscible CO₂ flooding, is one of well-established enhance oil recovery methods (EOR) during recent decades. This method is able to improve recovery of original oil in place over of 20% [1]. The right parametric design of miscible CO₂ injection depends greatly on a key factor: minimum miscible pressure (MMP), which is defined as the lowest pressure at which the flood changes from immiscible (multiple phase flow) to miscible (single phase flow) [2-4]. Hence an accurate estimation of MMP seems to be necessary.

MMP can be estimated using experimental tests such as slim tube [5], rising bubble apparatus (RBA) [6], multi-contact mixing-cell experiment [4] or the vanishing interfacial tension (VIT) technique [7]. Although the accuracy of these tests, all of them are very expensive and time consuming. An alternative way which is practicable on the slightest costs to calculate the MMP of CO₂-oil systems is insured by the available empirical/analytical correlations. However, as all these correlations have been developed under experimental data of CO₂-oil systems, they have certain constraints and conditions of application. Holm and Josendal first graphical MMP correlation for pure CO₂-oil [8] has been developed using crude oils with molecular weight of C₅₊ elements (MW_{C₅₊}) ranged between 180 g/mol and 240 g/mol, their experiment temperatures were between 32.2 °C and 82.5°C, and ranges of the MMP were between 9.65 MPa

and 22 MPa. Cronquist correlation [9] has been established with tested oil gravity ranged from 23.7 to 44.8°API, temperature ranged from 21.67 to 120.8°C and experimental MMP ranged from 7.4 to 34.5 MPa. Yellig & Metcalfe correlation [10] and Orr & Jensen correlation [11] were only suitable for reservoir temperatures of $(35\text{ }^{\circ}\text{C} \leq T_R \leq 88.9\text{ }^{\circ}\text{C})$ and $(T_R < 49\text{ }^{\circ}\text{C})$ respectively. Emera-Sarma correlation [12] was limited to $40.8\text{ }^{\circ}\text{C} < T_R < 112.2\text{ }^{\circ}\text{C}$, $8.28 < \text{MMP} < 30.2\text{ MPa}$ and $166.2\text{ g/mol} < MW_{C5+} < 267.5\text{ g/mol}$. Shokir correlation [13] was elaborated under $32.2\text{ }^{\circ}\text{C} < T_R < 112.2\text{ }^{\circ}\text{C}$, $6.9 < \text{MMP} < 30.28\text{ MPa}$ and $185\text{ g/mol} < MW_{C5+} < 268\text{ g/mol}$. Other correlations such as Alston *et al.* [14], Orr and Silva [15], Glaso's [16], Lee [17], and Yuan *et al.* [18] have focused directly to a specific oil reservoirs, and this, cannot satisfy the level of comprehensiveness and generalization required by various other oil reservoirs where the characteristics are different.

Recently, Artificial Intelligence (AI) has been widely applied in the petroleum field to solve many conventional and unconventional problems [19-21]. Among AI methods, artificial neural networks (ANNs) is the famous one thanks to its effectiveness. ANNs create models that can recognize highly complex and non-straight-forward problems. As the miscibility concept is a high complex problem and as ANN is a robust tool in mapping input to output of complex relationship, this technique provides an integrated way for predicting CO₂ MMP.

ANN models can present some obvious defects and inaccuracies caused by the defaulted training algorithms (like backpropagation BP) that trap in local minima. Hence, in this paper, we propose to optimize the weights and thresholds of the neural networks with differential evolution algorithm (DE) (which belongs to global meta heuristic optimization algorithms) to comprehensively predict MMP in pure CO₂-oil systems. On other words, this approach consists in building a hybrid ANN-DE-BP with minimum error function. Four parameters are considered as the influence factors (inputs) of MMP pure CO₂-oil systems: the mole percentage of volatiles x_{vol} (includes C1 and N2), the mole percentage of intermediates x_{int} (contains C2-C4, CO₂ and H₂S), the molecular weight of C5+ oil components (MW_{C5+}) and reservoir temperature (T_R). The model is developed and tested using 105 data collected from published literature and covering a wide range of variables. The accuracy of the ANN-DE-BP model is compared with MMP values calculated from the ANN-BP (artificial neural network with defaulted back propagation learning) and some well-known correlations. In additions, several statistical indexes and graphical error analysis are performed to better judge the robustness and the reliability of ANN-DE-BP to predict MMP of pure CO₂-oil system.

2. Artificial Neural Network (ANN)

In order to find relationship between the input and output data derived from experimental works, a more powerful method than the traditional ones are necessary. Artificial Neural Network (ANN) is an especially efficient algorithm to approximate any function with finite number of discontinuities by learning the relationships between input and output vectors. ANN is a mathematical model inspired by the biological neural networks. It is a non-linear mapping model and has been successfully applied in many domains [19,22].

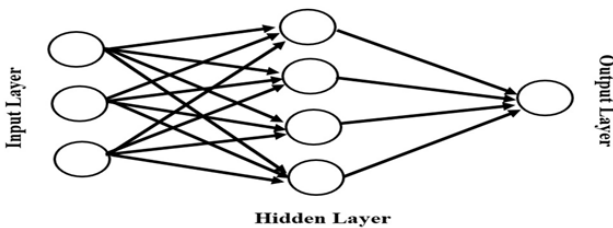


Fig. 1. An example of an ANN structure

It consists of many calculating units called nodes, these nodes are inside the layers: input data enter the first layer and output data exit the last layer. The layers between input and output layers are called hidden layers. For modeling purposes, the commonly used feed-forward ANN architecture namely multi-layer perceptron (MLP) may be employed. MLP involves an input layer, an output layer, and one (or more) hidden layer (s) with different roles. Each connecting line has an associated weight. Fig. 1 shows an example of typical 3-layer MLP.

The output from a given neuron is calculated by applying a transfer function to a weighted summation of its input to give an output, which can serve as input to other neurons, as follows [19]:

$$a_{jk} = g_k \left(\sum_{i=1}^{N_{k-1}} w_{ijk} a_{i(k-1)} + b_{jk} \right) \quad (1)$$

where a_{jk} are j th neuron outputs from k th layer and b_{jk} is the bias weight for neuron j in layer k . The model fitting parameters w_{ijk} are the connection weights. The nonlinear activation transfer functions g_k may have many different forms. The classical ones are threshold, sigmoid, Gaussian and linear function [23].

MLP training procedure aims at obtaining suitable weight set w_{ijk} and biases that minimizes a pre-specified error function such average absolute relative deviation percent (AARD %). The back propagation learning algorithm is the most commonly used algorithm. Several back-propagations training methodologies exist, which include the quasi-Newton backpropagation (BFGS), the Powell -Beale conjugate gradient, the Levenberge-Marguardt Algorithm (LMA) and others [19]. During the training, both the inputs and the outputs are provided. The network then processes the inputs and compares its resulting outputs against the desired outputs. Errors are then propagated back through the system, causing the system to adjust the weights which control the network. This process occurs over and over as the weights are continually tweaked.

According to [24-25], the convergence of the BP algorithm is highly dependent on the initial values of weights and biases. In the literature, using novel heuristic optimization methods or evolutionary algorithms is a popular solution to enhance the problems of BP-based learning algorithms.

3. Differential Evolution (DE)

Differential Evolution (DE) is a stochastic, population-based optimization algorithm introduced by Storn and Price in 1996 [26-27]. It is also one of the evolutionary algorithms. DE uses the similar genetic algorithm operators: crossover, mutation and selection. The main difference in constructing better solutions is that genetic algorithms rely on crossover while DE uses mutation operation as a search mechanism and selection operation to direct the search toward the prospective regions in the search space. The main steps of this algorithm are summarized as follows:

- *Initialization*: An optimization task consisting of D parameters can be represented by a D -dimensional vector. In DE, a population of NP solution vectors is randomly created at the start.

- *Mutation*: For each individual i of a generation G : $x_{i,G}$, a mutant vector is produced by:

$$v_{i,G+1} = x_{r1,G} + F * (x_{r2,G} - x_{r3,G}) \quad (2)$$

where $i, r1, r2, r3 \in \{1, 2, \dots, NP: Population\ size\}$ are randomly chosen and must be different from each other. F is called the mutation factor: it is a random number from $[0, 2]$; and $v_{i,G+1}$ is called donor vector.

- *Recombination (crossover)*: The parent vector is mixed with the mutated (donor) vector to produce a trial vector $u_{ji,G+1}$

$$u_{ji,G+1} = \begin{cases} v_{i,G+1}, & \text{if } (rand_{ij} \leq CR) \text{ or } j = I_{rand} \\ x_{ji,G}, & \text{if } (rand_{ij} > CR) \text{ and } j \neq I_{rand} \end{cases} \quad (3)$$

where $j = 1, 2, \dots, D$; $rand_{ij} \in [0, 1]$ is the random number; CR is crossover constant $\in [0, 1]$ and $I_{rand} \in \{1, 2, \dots, D\}$ is a randomly chosen index.

- *Selection*: The child produced after the mutation and crossover operations is evaluated. Then, the performance of the child vector and its parent is compared and the better one is selected. If the parent is still better, it is retained in the population.

$$x_{i,G+1} = \begin{cases} u_{i,G+1}, & \text{if } f(u_{i,G+1}) \leq f(x_{i,G}) \\ x_{i,G}, & \text{otherwise} \end{cases} \quad (4)$$

where f is the fitness function (the case shown in the equation 4 corresponds to minimize the fitness function).

The implementation of the differential evolution algorithm to optimize the weights and biases of ANN is illustrated in Fig. 2.

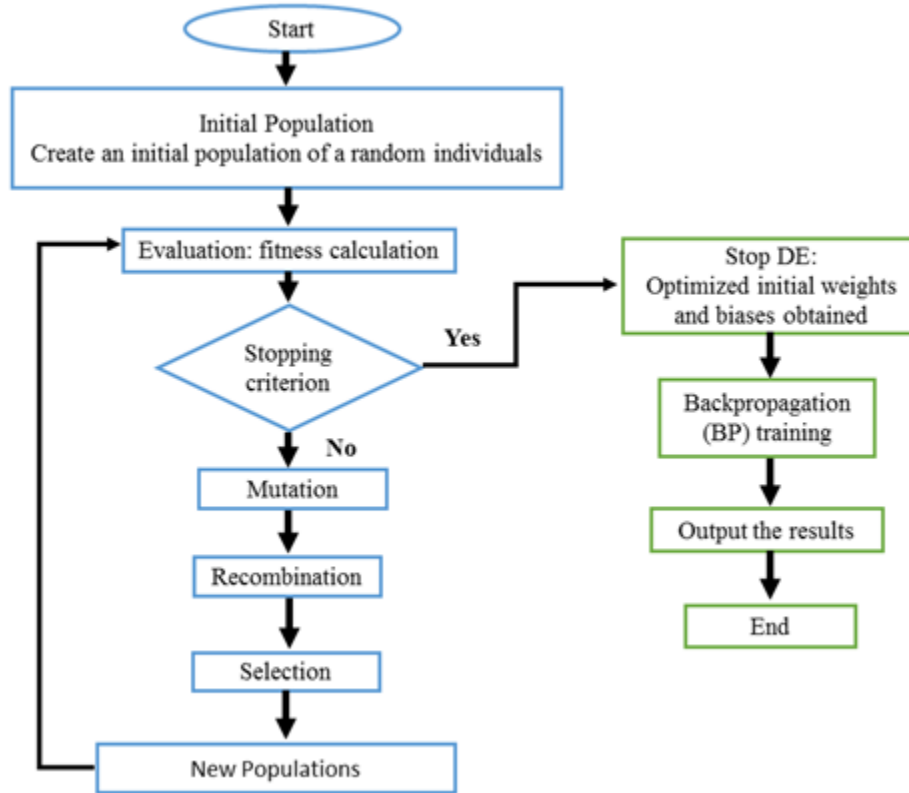


Fig. 2. Implementation of DE to MMP ANN's training

4. Data analysis

105 data sets are collected from published literature [9-18, 28-34] with a wide range of temperatures and oil compositions. Reservoir temperature for this dataset ranged from 34.4 to 137.2°C, while the molecular weight of the C5+ fraction varied from 136.26 to 391 g/mol. Table 1 shows a full statistical description of the collected and used data in the development of the model.

Table 1. Ranges and their corresponding statistical parameters of the input/output data used for developing the model

	Variables	Max	Min	Mean	SD
Output	MMP (MPa)	38.5	7.93	17.40	6.99
	MW _{C5+} (g/mol)	391	136.26	205.43	39.65
Inputs	T _R (°C)	137.22	34.4	74.38	26.11
	x _{vol} (%)	54.3	0	20.43	15.65
	x _{int} (%)	43.5	0	18.77	12.33

To demonstrate the correlation between MMP and the used independent variables, the correlation matrix is implemented [35]. This matrix illustrates the power of a linear relationship between two different variables in multi-variables system [35]. The coefficient between two variables x and y, is defined by the following formula:

$$r_{xy} = \frac{\sigma_{xy}}{\sigma_x \sigma_y} \quad (5)$$

where σ_x and σ_y are the sample standard deviations, and σ_{xy} is the sample covariance.

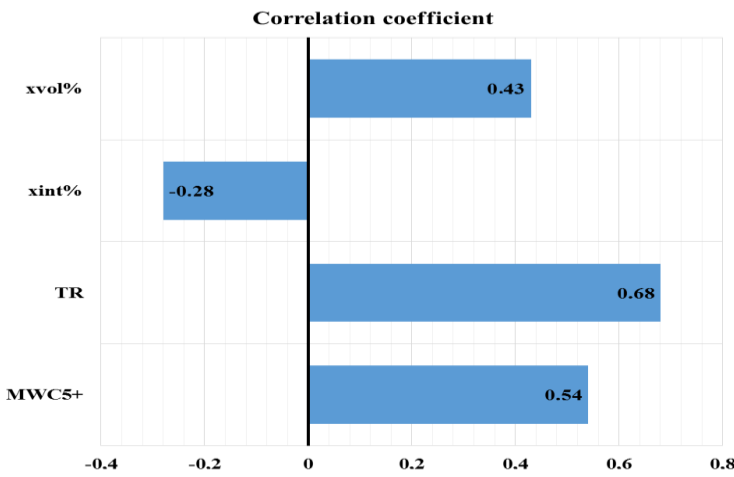


Fig. 3. Correlation coefficient of the independent variables

Its values are between [-1 1]. Two variables are said to be positively linearly related if their correlation coefficient is close to 1 and negatively linearly if it is close to -1. For values nearby zero, it would indicate a weak linear relationship between the variables. The obtained results are shown in Fig. 3.

The graph certifies that reservoir temperature (T_R) has the highest linearly relation with MMP (0.68). Then Molecular Weight (MW) of the C5 + and x_{vol} % by 0.54 and 0.43, respectively. Furthermore, it can be deduced that molar

fraction of the intermediate elements (x_{int}) has a negative linearly relation with MMP which means that MMP is high, if x_{int} is low.

5. Model development

To improve the convergence conditions during the development of the model, the used data are normalized at the interval [-1 1] according to the following equation:

$$x_{normalized} = \frac{2(x_i - x_{min})}{(x_{max} - x_{min})} - 1 \quad (6)$$

where $x_{normalized}$ is the normalized value of x_i , x_{max} and x_{min} are the maximum and minimum values of the variable x respectively (as shown in Table 1).

The first step to establish an ANN-DE-BP model to estimate MMP of pure CO₂-oil systems consists in achieving to a best ANN topology. One hidden layer is employed in our study, as it is proven in the literature [36] that a MLP network having only one hidden layer can estimate most of nonlinear systems. The number of neurons in the hidden layer is established using trial and error method: after a series of optimization processes by monitoring the performance of the network until the best network structure is accomplished. The radial basis activation function is used as the transfer function from input layer to hidden layer, and the linear function is taken as the activation function in the last layer. Then the problem is formulated as an optimization problem to find a set of weights and biases of the ANNs that minimizes the difference between the predictions and the target values in the training set of data using differential evolution algorithm (by following flowchart of Fig. 2). 88 points of the 105 are selected randomly and employed in the training process while the remain 17 are used to test the model. The features of implemented algorithm are summarized as follows: population size: 50, max number of generation: 100 and crossover's constant: 0.8. All the programming tasks developed in this work are carried out using MATLAB® 2016-a computing environment [37].

To evaluate the developed model and its predictive performances, it must be compared against existing correlations and approaches. This is done through cross plots and a group error analysis, using the average absolute percent error (AARD%), standard deviation (SD), the correlation factor (R^2) and the root mean square error (RMSE). These statistical indexes can be mathematically expressed by the following equations:

$$AARD\% = \frac{1}{N} \sum_{i=1}^N \left| \frac{MMP_i^{exp} - MMP_i^{cal}}{MMP_i^{exp}} \right| \times 100 \quad (7)$$

$$SD = \sqrt{1/(N - 1) \sum_{i=1}^N \left(\frac{MMP_i^{exp} - MMP_i^{cal}}{MMP_i^{exp}} \right)^2} \quad (8)$$

$$R^2 = 1 - \frac{\sum_{i=1}^N (MMP_i^{exp} - MMP_i^{cal})^2}{\sum_{i=1}^N (MMP_i^{cal} - \overline{MMP})^2} \quad (9)$$

$$RMSE = \sqrt{\frac{1}{N} \sum_{i=1}^N (MMP_i^{exp} - MMP_i^{cal})^2} \quad (10)$$

where N represents the number of the measured information, MMP_i^{exp} is the experimental minimum miscibility pressure values, while MMP_i^{cal} is the calculated MMP values which are predicted by the developed model. Average value of the MMP data is shown by \overline{MMP} .

6. Results and discussion

Table 2 shows the results of performed sensitivity analysis for investigation of the number of neurons in the hidden layer for ANN-BP. In this table, only topologies which have been trained several times and show a high degree of accuracy are presented. The optimal configuration has been selected by finding the structure which has a high accuracy based on the statistical error analysis. It can be clearly seen that 16 is the best number of neurons in the hidden layer, and the configuration $4 \times 16 \times 1$ (one input layer containing the inputs showed in Table 1, one hidden layer with 16 nodes and one output layer containing one node which is MMP) can be considered as an optimal topology in this study.

Table 2. Sensitivity analysis for various ANN topologies (training data)

Number of hidden neurons	AARE (%)	R ²	SD	RMSE
9	8.46	0.9607	0.11	1.87
10	6.91	0.9743	0.097	1.82
12	6.99	0.9719	0.093	1.89
15	7.52	0.9604	0.11	1.88
16	6.16	0.9681	0.085	1.72
19	6.37	0.970	0.089	1.74

Cross plots between output and target values for training and test data of ANN-DE-BP and ANN-BP models are illustrated in Fig. 4. For each model, all the predicted values are sketched against the experimental values, and therefore across plot is created and compared against a unit slope line that shows the perfect model line: the closer the plotted data to this line, the higher is the reliability of the model. According to these cross plots, ANN-DE-BP model has closer match to the real values. For a deep comparison, Table 3 presents the results of performance evaluation through the aforementioned statistical indicators. According to this table, ANN-DE-BP has a reliable ability to predict MMP with a total AARD% of 5.92%, RMSE of 1.47, high correlation coefficient (R²=0.9808) and low standard deviation (SD=0.0817). Furthermore, this table depicts that ANN-DE-BP outperforms largely ANN-BP model.

Table 3. Performance analysis of ANN-BP and ANN-DE-BP

		R ²	AARD (%)	RMSE	SD
ANN-BP	Training (88 data)	0.9681	6.16	1.72	0.085
	Test (17 data)	0.9491	13.88	3.26	0.1681
	All (105 data)	0.9650	7.41	1.97	0.098
ANN-DE-BP	Training (88 data)	0.9807	5.17	1.33	0.0745
	Test (17 data)	0.9811	9.81	2.23	0.12
	All (105 data)	0.9808	5.92	1.47	0.0817

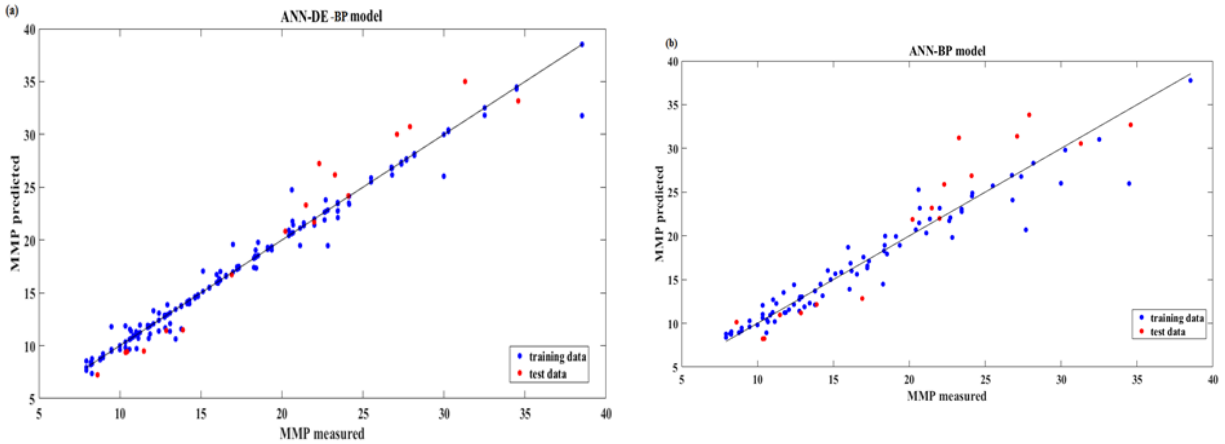


Fig. 4. Cross-Plots of the Results: (a) MMP measured vs MMP ANN-DE-BP (training + test); (b) MMP measured vs MMP ANN-BP (training + test)

To find better comprehension on the performance of the model, cumulative distribution function (CDF) plot of the predicted errors is shown in Fig. 5. In this figure, the error is the percent relative error (PRE%) which measures the relative deviation of predicted data from the experimental data. Also, details of this figure are presented in Table 4 using concept of the probability distributions of the errors. Table 4 and Fig. 5 reveal that 80 % of the ANN-DE-BP prediction values have an absolute error less than 10%, and only 3% with an absolute error up to 20%.

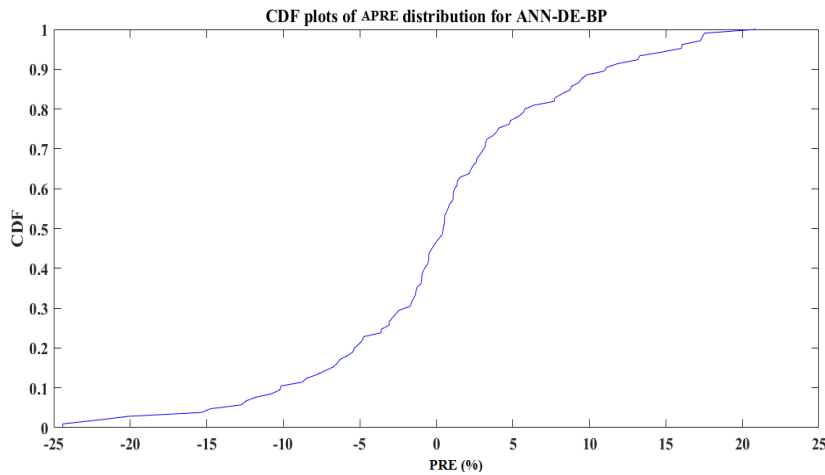


Fig. 5. CDF plot of APRE of ANN-DE-BP

Table 4. Probability distribution of the simple errors for used data

Error	ANN-DE-BP	Error	ANN-DE-BP
$ APRE < 0.16$	0.019	$ APRE < 7.80$	0.70
$ APRE < 0.53$	0.10	$ APRE < 10.00$	0.80
$ APRE < 1.00$	0.21	$ APRE < 14.75$	0.90
$ APRE < 1.50$	0.30	$ APRE < 17.38$	0.95
$ APRE < 2.65$	0.40	$ APRE < 20.00$	0.97
$ APRE < 3.70$	0.50	$ APRE < 24.40$	1
$ APRE < 5.45$	0.60		

To investigate and to provide more insight into the validity of the proposed model for MMP estimation in pure CO₂-oil systems, seven of well-known correlations have been selected for comparison. Table 5 shows the results. It can be seen from the analysis of comparison that

ANN-DE-BP proves its ability in MMP prediction of the pure CO₂-oil systems with high precision and lowest average absolute deviation among all correlations and ANN with backpropagation learning.

Table 5. Comparison of ANN-DE-BP performances against existing correlations

Model / correlation	R ²	AARD (%)	RMSE	SD	Max AARD (%)
ANN-DE-BP	0.9808	5.92	1.47	0.0817	24.40
ANN-BP	0.9650	7.41	1.97	0.098	34.10
Cronquist	0.9043	16.42	4.23	0.2085	69.13
Lee	0.6393	19.73	6.05	0.2782	98.68
Yelling Metcalfe	0.6771	18.01	6.06	0.2341	66.09
Orr-Jensen	0.6331	20.17	6.71	0.2548	78.71
Alston et al.	0.8546	19.15	6.05	0.2640	91.54
Emera-Sarma	0.8868	14.02	3.92	0.1867	56.82
Shokir	0.8574	12.58	3.45	0.1674	57.94

Finally, for utilizing of our best-established model (i.e. ANN-DE-BP) and exact reproducing its results, the detailed information (its weight and bias matrixes) are reported in Table 6. This model contains one input layer (containing the inputs as arranged in Table 1), one hidden layer (it contains 16 nodes) and one output layer (contains one node) which is MMP. The radial basis activation function is used as the transfer function from input layer to hidden layer, and the linear function is taken as the activation function in the last layer. The normalization of dataset followed is expressed in equation (6) with respect to the bounds shown in Table 1.

Table 6. Weights and biases of the ANN-DE-BP

Neurons	Weight values of connections between input and hidden layer				
1	-2.6435	-2.8768	-0.4822	0.3454	
2	-2.4828	-0.6234	-0.8255	0.3686	
3	0.1751	-0.6750	3.6811	-0.6295	
4	2.3005	-2.4885	-1.1044	-1.3275	
5	0.3134	0.6956	-3.1345	0.9178	
6	-2.6354	-0.1521	1.5074	-2.2200	
7	0.0636	-0.2535	0.3671	-1.0719	
8	-2.4234	-0.3067	-0.6915	1.0496	
9	3.9934	-2.9587	-0.1020	0.9007	
10	2.5631	-2.6922	-0.8403	-0.4032	
11	0.2141	0.3385	-0.8303	-1.1127	
12	3.3936	3.5477	0.2842	0.3107	
13	-1.0396	1.0211	-0.1439	-2.7147	
14	4.1151	2.8660	0.5029	1.7354	
15	1.4882	-1.8420	-3.7362	-1.2947	
16	2.1720	0.9226	1.8268	0.0507	

Weight values of connections between hidden and output layer															
-0.5965	0.3559	1.1612	-0.3095	-1.5506	-0.3876	2.9475	-0.9274	0.0064	1.2707	3.9655	2.4085	-1.5664	-0.3002	-0.3924	-1.8314
Biases of the hidden layer															
-2.8664	3.4227	2.0303	-1.9878	-1.6632	0.7837	0.9189	-1.8503	2.1158	-0.7092	-1.5149	2.3326	2.5369	3.5869	0.3510	3.3695
Biases of the output layer															
-0.8889															

7. Conclusion

In this study, a new approach to predict MMP of pure CO₂-oil systems is proposed by optimizing artificial neural network with differential evolution (DE). This latter is used to optimize weights and biases of a pre-established neural networks. The results generated by this model i.e. ANN-DE-BP, are then compared with the experimental results, those generated by neural network with backpropagation learning and those generated by the existing approaches. The results show an excellent agreement between the model predictions and experimental data ($R^2 > 0.98$), and this model outperforms all other approaches. Furthermore, ANN-DE-BP provides a considerable improvement over previous proposed correlation with broader applicability in terms of accuracy and independent variable ranges.

List of symbols

<i>MMP</i>	<i>minimum miscibility pressure (MPa)</i>
<i>MW_{C5+}</i>	<i>molecular weight of C5+ elements (g/mol)</i>
<i>X_{vol}</i>	<i>mole percentage of volatiles (includes C1 and N2)</i>
<i>X_{int}</i>	<i>mole percentage of intermediates (contains C2–C4, CO₂ and H₂S)</i>
<i>T_R</i>	<i>reservoir temperature (°C)</i>
<i>ANN</i>	<i>artificial neural network</i>
<i>DE</i>	<i>differential evolution</i>
<i>BP</i>	<i>back propagation</i>
<i>AARD</i>	<i>average absolute percent error (%)</i>
<i>SD</i>	<i>standard deviation</i>
<i>R²</i>	<i>the correlation factor</i>
<i>RMSE</i>	<i>root mean square error</i>

References

- [1] Grigg RB, Schechter DS. State of the Industry in CO₂ Floods. in: SPE Annu. Tech. Conf. Exhib., Society of Petroleum Engineers, 1997. doi:10.2118/38849-MS.
- [2] Benmekki EH, Mansoori GA. Minimum miscibility pressure prediction with equations of state. SPE (Society Pet. Eng. Reserv. Eng.; (United States). 1988; 3:2.
- [3] Fazlali A, Nikookar M, Agha-Aminiha A, Mohammadi AH. Prediction of minimum miscibility pressure in oil reservoirs using a modified SAFT equation of state. Fuel, 2013; 108: 675–681.
- [4] Jaubert J-N, Wolff L, Neau E, Avaullee L. A Very Simple Multiple Mixing Cell Calculation To Compute the Minimum Miscibility Pressure Whatever the Displacement Mechanism. Ind. Eng. Chem. Res., 1998; 37: 4854–4859.
- [5] Wu RS, Batycky JP. Evaluation of Miscibility from Slim Tube Tests. J. Can. Pet. Technol., 1990; 29(6): doi.org/10.2118/90-06-06.
- [6] Christiansen RL, Haines HK. Rapid Measurement of Minimum Miscibility Pressure With the Rising-Bubble Apparatus, SPE Reserv. Eng., 1987; 2: 523–527.
- [7] Orr FM, Jessen K. An analysis of the vanishing interfacial tension technique for determination of minimum miscibility pressure, Fluid Phase Equilib., 2007; 255: 99–109.
- [8] Holm LW, Josendal VA. Mechanisms of Oil Displacement by Carbon Dioxide, J. Pet. Technol., 1974; 26:1427–1438.
- [9] Cronquist C. Carbon dioxide dynamic miscibility with light reservoir oils, in: Proc. 4th Annu. U.S. DOE Symp., 1978: pp. 28–30.
- [10] Yellig WF, Metcalfe RS. Determination and Prediction of CO₂ Minimum Miscibility Pressures (includes associated paper 8876, J. Pet. Technol., 1980; 32: 160–168.
- [11] Orr FM, Jensen CM. Interpretation of Pressure-Composition Phase Diagrams for CO₂/Crude-Oil Systems, Soc. Pet. Eng. J., 1984; 24: 485–497.
- [12] Emera MK, Sarma HK. Use of genetic algorithm to estimate CO₂-oil minimum miscibility pressure—a key parameter in design of CO₂ miscible flood, J. Pet. Sci. Eng., 2005; 46: 37–52.
- [13] Shokir EME-M. CO₂-oil minimum miscibility pressure model for impure and pure CO₂ streams, J. Pet. Sci. Eng., 2007; 58: 173–185.
- [14] RB Alston, GP Kokolis, CF. James, CO₂ Minimum Miscibility Pressure: A Correlation for Impure CO₂ Streams and Live Oil Systems, Soc. Pet. Eng. J., 1985; 25: 268–274.
- [15] Orr FM, Silva MK. Effect of Oil Composition on Minimum Miscibility Pressure-Part 2: Correlation, SPE Reserv. Eng., 1987; 2: 479–491.

- [16] Glaso O. Generalized Minimum Miscibility Pressure Correlation (includes associated papers 15845 and 16287), Soc. Pet. Eng. J.,1985; 25: 927–934.
- [17] Lee JI. Effectiveness of carbon dioxide displacement under miscible and immiscible conditions, Rep. RR-40, Pet. Recover. Inst., Calgary. (1979).
- [18] Yuan H, Johns RT, Egwuenu AM, Dindoruk B. Improved MMP Correlation for CO₂ Floods Using Analytical Theory, SPE Reserv. Eval. Eng., 2005; 8: 418–425.
- [19] Gharbi RBC., Mansoori GA. An introduction to artificial intelligence applications in petroleum exploration and production, J. Pet. Sci. Eng.,2005; 49: 93–96.
- [20] Vaferi B, Eslamloueyan R, Ayatollahi S. Automatic recognition of oil reservoir models from well testing data by using multi-layer perceptron networks, J. Pet. Sci. Eng., 2011; 77: 254–262.
- [21] Vafaei MT, Eslamloueyan R, Ayatollahi S. Simulation of steam distillation process using neural networks, Chem. Eng. Res. Des.,2009; 87: 997–1002.
- [22] Hornik K, Stinchcombe M, White H. Multilayer feedforward networks are universal approximators, Neural Networks.,1989; 2: 359–366.
- [23] Bulsari AB. Neural networks for chemical engineers, Elsevier, 1995.
- [24] Zhang J-R, Zhang J, Lok T-M, Lyu MR. A hybrid particle swarm optimization–back-propagation algorithm for feedforward neural network training, Appl. Math. Comput., 2007; 185: 1026–1037.
- [25] Mirjalili S, Mohd Hashim SZ, Sardroudi HM. Training feedforward neural networks using hybrid particle swarm optimization and gravitational search algorithm, Appl. Math. Comput., 2012; 218: 11125–11137.
- [26] Storn R, Price K. Differential Evolution – A Simple and Efficient Heuristic for global Optimization over Continuous Spaces, J. Glob. Optim.,1997; 11: 341–359.
- [27] Storn R. Differential evolution design of an IIR-filter, in: IEEE Int. Conf. Evol. Comput., IEEE, 1996: 268–273.
- [28] H Zhang, D Hou, Li K. An improved CO₂-crude oil minimum miscibility pressure correlation, J. Chem., 2015;2015: Article ID 175940, <http://dx.doi.org/10.1155/2015/175940>
- [29] Adekunle O. Experimental approach to investigate minimum miscibility pressures in the Bakken, (2014).
- [30] Adyani WN, Kechut NI. Advanced Technology for Rapid Minimum Miscibility Pressure Determination (Part 1), in: Asia Pacific Oil Gas Conf. Exhib., Society of Petroleum Engineers, 2007. doi:10.2118/110265-MS.
- [31] Dicharry RM, Perryman TL, Ronquille JD. Evaluation and Design of a CO₂ Miscible Flood Project-SACROC Unit, Kelly-Snyder Field, J. Pet. Technol., 1973; 25: 1309–1318.
- [32] Dong M, Huang S, Dyer SB., Mourits FM. A comparison of CO₂ minimum miscibility pressure determinations for Weyburn crude oil, J. Pet. Sci. Eng.,2001; 31: 13–22.
- [33] Elsharkawy AM, Poettmann FH, Christiansen RL. Measuring Minimum Miscibility Pressure: Slim-Tube or Rising-Bubble Method?, in: SPE/DOE Enhanc. Oil Recover. Symp., Society of Petroleum Engineers, 1992. doi:10.2118/24114-MS.
- [34] Winzinger R, Brink JL, Patel KS, Davenport CB, Patel YR, Thakur GC. Design of a Major CO₂ Flood, North Ward Estes Field, Ward County, Texas, SPE Reserv. Eng., 1991; 6: 11–16.
- [35] Vaferi B, Samimi F, Pakgohar E, Mowla D. Artificial neural network approach for prediction of thermal behavior of nanofluids flowing through circular tubes. Powder Technol.,2014; 267. 1–10.
- [36] Cybenko G. Approximation by superpositions of a sigmoidal function. Math. Control. Signals, Syst. 1992; 5: 455.
- [37] MATLAB®, MathWorks, Inc, 2016a, (n.d.).

To whom correspondence should be addressed: Menad Nait Amar, Faculty of Hydrocarbon and Chemistry University M'hamed Bougara- Avenue de l'indépendance, Boumerdes,3500, Algeria, manad1753@gmail.com

DETERMINATION OF INFLOW PERFORMANCE RELATIONSHIP FOR A VERTICAL WELL IN NATURALLY FRACTURED OIL RESERVOIRS: NUMERICAL SIMULATION STUDY

Reda Abdel Azim, Melissa Ramirez, and Mohammad R, Awal

American University of Ras Al Khaimah, United Arab Emirates, Ras Al Khaimah

Received December 24, 2017; Accepted March 19, 2018

Abstract

The Inflow Performance Relationship (IPR) of a well is a relation between the oil or gas production rate and the flowing bottom-hole pressure. This relationship serves as an important tool for petroleum engineers to understand and predict well performance. The IPR correlations are used to design and evaluate well completion, optimize well production, and design artificial lift method. There are several IPR correlations reported in the literature, mostly for homogeneous and isotropic reservoirs.

For naturally fractured reservoirs (NFR), which account for almost half of the world's remaining oil reserves, the challenge of predicting reservoir as well as well flow performances is daunting due to the heterogeneous flow in the complex fracture networks. Recently some IPR correlations have been reported for both naturally and hydraulically fractured reservoirs using analytical methods. However, the analytical methods do not represent the complex fractures networks in the NFRs, and the best practice has been, for addressing reservoir flow performance, numerical reservoir simulation approach to model the complex fracture networks as well as model the relative permeability functions of the flowing fluid phases.

In this work, therefore, numerical reservoir simulation approach is adopted in order to develop a new IPR model for oil wells in a NFR. The new model is semi-analytical: first, a 3D black-oil reservoir simulator developed by the lead author is used to develop the oil mobility function (OMF) that captures the complex fluid flow in the fracture networks; then the OMF is used to analytically compute the IPR function. The simulation runs are set up with data from well test analysis along with permeability and pressure-volume-temperature data in the fluid flow equations. In the numerical simulation runs, four different oil flow rates are used to generate the oil saturation and corresponding relative permeability in the naturally fractured reservoir. Comparisons between the new method and two popular correlations for non-fractured reservoirs indicate the necessity for developing and using an IPR correlation specifically developed for a fractured reservoir.

Keywords: *inflow performance relationship; mobility function; naturally fractured reservoir; well test analysis.*

1. Introduction

The Inflow Performance Relationship (IPR) of a well is a non-linear equation between the oil or gas volumetric production rate (q_o or q_g) and the flowing bottom-hole pressure (p_{wf}) that represents the reservoir pressure at the well-reservoir interface. IPR analysis is used to develop optimum reservoir flow rate and flowing bottom hole reservoir pressure for oil and gas wells in various types of reservoir systems, especially during the prolonged pseudo steady-state flow period. The relationship can be derived from the classical diffusivity equation, as originally developed by Muskat and Evinger [1] attempted to account for the observed nonlinear flow relationship (q_o vs p_{wf}) during the pseudo steady-state flow of oil as follows:

$$q_o = \frac{kh}{141.2 \left[\ln \left(\frac{r_e}{r_w} \right) - 0.75 + s \right]} \int_{p_{wf}}^{p_R} \frac{k_{ro}}{\mu_o B_o} dp \quad (1)$$

Equation (1) is valid for a homogeneous and isotropic reservoir, for radial flow in a circular reservoir with a fully penetrating vertical well at the center. The integrand is defined as the

transmissibility function, $T_f(k_{ro}, \mu_o, B_o)$, which is a function of oil-phase saturation (s_o), and the pressure-dependent oil PVT properties (μ_o, B_o):

$$T_f(k_{ro}, \mu_o, B_o) = \frac{k_{ro}}{\mu_o B_o}$$

Given that reservoir pressure changes with time, coupled with obtaining a single permeability value to represent the entire reservoir domain, and the relative permeability term being dependent on oil saturation (s_o) which vary with time and from the drainage boundary to the wellbore, Equation (1) is anything but practical for practicing production engineers in order to predict well productivity as a function of time.

To circumvent the problem, Vogel [2] introduced an easy-to-use method for predicting the performance of a vertical oil well producing oil and associated gas from a solution-gas drive reservoirs. His empirical inflow performance relationship (IPR) is based on computer simulation results and is given by. The correlation between dimensionless pressure, $\left(\frac{p_{wf}}{P_r}\right)$, and dimensionless oil flow rate, $\left(\frac{q}{q_{max}}\right)$, was found to be valid for a range of common rock and fluid properties:

$$\frac{q}{q_{max}} = 1 - b \left(\frac{p_{wf}}{P_r}\right) - (1 - b) \left(\frac{p_{wf}}{P_r}\right)^2 \quad (2)$$

where, $b = 0.2$. The unknown parameter, q_{max} , is specific for a given reservoir, and encapsulates the effects of such flow conditions as formation damage or stimulation (negative, or positive skin effect, respectively), and needs to be estimated by conducting a stabilized production flow test.

It is to be noted that the purpose of using a numerical reservoir simulator (NRS) by these authors was to develop a large data set for production rate (q) and corresponding flowing bottomhole pressure (FBHP, p_{wf}) in the well, which overcomes the practical problem of obtaining representative FBHP along with oil flow rates without the effect of wellbore damage, hydraulic fracturing stimulation, well inclination, etc. Fetkovich [3] used well test data (Isochronal test method) to correlate FBHP with oil flow rate, which can also be rearranged in terms of Vogel's dimensionless variables, and the resulting empirical IPR model, which introduces a second parameter, n (flow exponent), and therefore, requires two well test data at different flow rates:

$$\frac{q}{q_{max}} = \left[1 - \left(\frac{p_{wf}}{P_r}\right)\right]^n \quad (3)$$

Several researchers extended Vogel's work to develop reservoir simulation-based empirical IPR models for homogenous, solution-gas drive reservoirs, in order to include such cases as well inclination, flow of water and solids, etc. For example, Cheng [4] employed Vogel's NRS technique to develop the IPR equation for a horizontal well:

$$\frac{q}{q_{max}} = 1 + 0.2055 \left(\frac{p_{wf}}{P_r}\right) - 1.1818 \left(\frac{p_{wf}}{P_r}\right)^2 \quad (4)$$

Wiggins [5] extended the work of Vogel [2] to include flow of reservoir and solid particles in the flow rate variable, q :

$$\frac{q}{q_{max}} = 1 - 0.52 \left(\frac{p_{wf}}{P_r}\right) - 0.48 \left(\frac{p_{wf}}{P_r}\right)^2 \quad (5)$$

Interested readers may find in Elias *et al.* [6] and Shahri *et al.* [7] a summary of various Vogel-type IPRs.

The Vogel-type IPR correlations are, are valid for isotropic and homogenous reservoirs. These are not valid for naturally fractured reservoirs, where fluid flow path is more complex due to matrix as well as fracture flow. As much as half of the remaining oil reserves in the world is located in NFRs, especially the carbonate reservoirs, and sometimes in igneous basement rocks [8]. The fracture networks provide a higher permeability flow path than the interconnected pores in the matrix. Therefore, using the Vogel-type IPR correlations would under-predict a well's production potential and performance. Only recently this problem was addressed, e.g., Jahanbani & Shadzadeh [9], who presented an analytical IPR model for a

naturally fractured, solution-gas drive reservoir. They used the well-known equation (1), in which the relative permeability term, k_{ro} , is obtained from laboratory measured values using a core obtained from the NFR under consideration. However, it is a common knowledge that a NFR is quite heterogeneous in respect of fracture characteristics, from fracture dimensions, and distribution over the flow domain. Therefore, a limited, lab-based relative permeability function, as used by Jahanbani & Shadizadeh [9], may not be representative of flow characteristics from reservoir outer boundary to the inner boundary (*i.e.*, the wellbore) in a NFR. Therefore, we adopt numerical reservoir simulation approach to evaluate the integral function in equation (1).

2. The new semi-analytical IPR model

In a saturated NFR, a matrix block is saturated with oil and partially by gas, where capillary pressure plays a significant role in oil recovery process.

Therefore, the design objective was to construct a reservoir flow model based on a commercial simulator to generate flow data as a function of pressure. Using the simulation generated data, we develop a correlation between oil mobility and average reservoir pressure. The oil mobility function is a key variable in the IPR equation.

The pseudo-steady state flow in a cylindrical naturally fractured reservoir (NFR) with a vertical well at the center of the drainage area is represented by the following equation.

$$p_{wf} = p_R - \frac{141.2 qB}{T_f} \left[\ln \left(\frac{r_e}{r_w} \right) + s - 0.75 \right] \quad (6)$$

$$\text{where, } T_f = \frac{162.6 qB}{m} = \frac{k_f h}{\mu} \quad m = \frac{162.6 qB}{T_f}$$

T_f (Fracture transmissibility) is calculated from the slope, m , of two parallel lines of the in a semi-log plot of pressure versus logarithm of time (data from transient test: drawdown and buildup tests from a well producing in a finite, naturally fractured reservoirs). Various equations and type curves have been presented in the literature to analyze such transient flow and pressure buildup tests.

When two-phase flow conditions prevail, Eq. (1) for oil phase flow can be approximated, by evaluating the fluid properties μ_o and B_o and relative permeability k_{ro} are evaluated at the average reservoir pressure, $p_{av} = \frac{p_{wf} + p_R}{2}$, as,

$$p_{wf} = p_R - \frac{141.2 q_o B_o}{T_f} \left[\ln \left(\frac{r_e}{r_w} \right) + s - 0.75 \right] \quad (7)$$

Substituting for T_f into the above equation gives, we obtain oil flow rate as follows:

$$q_o = \frac{0.00708 k_f h (p_r - p_{wf})}{\left[\ln \left(\frac{r_e}{r_w} \right) + s - 0.75 \right]} \left(\frac{k_{rf,o}}{\mu_o B_o} \right) p_{av} \quad (8)$$

In case of our studied reservoir, the drainage boundary is a square and not circular. Eq (8) is therefore adjusted to incorporate the reservoir shape factor, C_A , as follow:

$$q_o = \frac{0.00708 k_f h (p_r - p_{wf})}{\left[\frac{1}{2} \ln \left(\frac{4A}{\gamma C_A r_w^2} \right) + s \right]} \left(\frac{k_{rf,o}}{\mu_o B_o} \right) p_{av} \quad (9)$$

where: γ = Euler's constant = 1.78; A = drainage area; C_A = reservoir shape factor = 30.9 for square drainage boundary.

The objective now is how to find relationship between the mobility function, T_f , and the average reservoir pressure, p_{av} , as a function of time, in order to evaluate at a specific point of time the oil production rate from a vertical well at the center of a naturally fractured reservoir (NFR) of constant thickness and rectangular drainage boundary. The first step is to evaluate the permeability value, k_f , that represent the combined effect of matrix and fracture channel permeability for a given fracture aperture and distribution. Toward that end, we construct a 3D reservoir simulation model, which contains fracture map and permeability tensor. The workflow is described in detail by Abdelazim and Rahman [10], and Abdelazim [11]; therefore we present only an outline of the methodology here.

3. Generation of subsurface network fracture map

Fracture data analysis is the first step in reservoir characterization process. The analysis consists of the determination of types of fractures or fracture parameters that control the distribution and quality of flow zones. Borehole images and production data are used to identify a set of variables such as dip, azimuth, aperture, or density that controlling hydrocarbon flow. Fracture indicators such as production rates are combined with borehole images to flag the flow contributing fracture zones. This technique has been used successfully in fractured basement reservoirs [12-13]. The fracture sets are defined based on fractures dip, length, and azimuth. The initial data of fractures length and dip angles ranging from 9 m to 60 m and 70° to 90° respectively and the fracture aperture ranges from 0.004 mm to 0.04 mm. Once the fracture set has been identified, it is used in the form of a fracture intensity curve.

For flow simulation in the NFR, we divide the rectangular reservoir flow domain in to number of grid blocks. We use a hybrid methodology to simulate fluid flow, combining the single continuum and the discrete fracture approach. The 3D discrete fracture network is created that consists of two sets of fractures: (i) small to medium fractures (length < 40 m), and (ii) long fractures (length > 40 m), along with their density, orientations and locations. These fractures are considered as part of the matrix (in the form of *permeability tensor*, which can be contributing to local vertical heterogeneity).

Fracture intensity map is extracted from geological interpretations of reservoirs. Fractures are distributed stochastically with different radius, dip and azimuth angles using fracture intensity value of 0.1 m⁻¹. The fracture intensity is calculated by dividing the studied reservoir (500m x 500m x 30m) into different grid blocks and fractures that cut each block are well-defined. Fracture intensity is expressed as:

$$Fracture\ intensity = \frac{\sum_{i=1}^N Area}{Volume} \tag{10}$$

where, N is the total number of fractures that intersect the corresponding grid block.

The grid block along with small and medium fractures uses tetrahedral elements in 3D domain for matrix and triangular elements in 2D domain for fractures. Once the block-based permeability tensors (3D) are calculated, the reservoir domain along with long fractures are discretized by tetrahedral elements for matrix as well as triangular elements for fractures.

A threshold value for fracture length is defined by trial and error. The threshold length is selected depends on the effect of different fracture length on the reservoir performance. Fractures with length smaller than the threshold value are used to generate the grid-based *permeability tensor* in 3D, while fractures with length longer than the threshold value are explicitly discretized in the domain by using tetrahedral elements.

4. Estimation of block-based permeability tensor

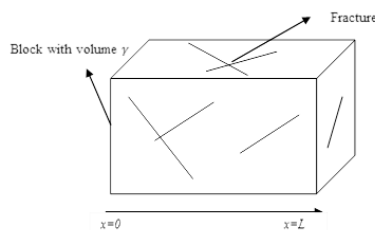


Figure 1. 3D cube used for permeability tensor calculations

In order to calculate the effective permeability tensors which represents an average permeability for the two structures, 3D cube is used to represent the matrix and fractures porous media (Fig.1).

The fractured porous media is bounded in an impermeable cover with boundary conditions for pressures (P₁ and P₂).

The boundary conditions are:

$$p(x = 0) = p_1, p(x = L) = p_2, J.n = 0 \text{ and } v = 0 \text{ on } s_1$$

The seepage velocity calculated based on the flow rate integration over fracture surfaces and matrix porous media and by using total volume of the block.

$$v = -\frac{k_m}{\mu} \nabla p \tag{11}$$

where μ the fluid viscosity and p is the pressure and the continuity equation for local seepage velocity in the matrix read as:

$$\nabla \cdot v = 0 \quad (12)$$

The hydraulic properties of fracture can be characterized by fracture transmissivity (aperture) and main flow rate is set parallel and normal to fracture plane. The flow rate J in fractures is usually defined by unit width of fracture and can be expressed by:

$$J = -\frac{k_{eff}}{\mu} \nabla_s p \quad (13)$$

In case of the flow is parallel to fracture plane, the seepage velocity normal to the fracture induces a pressure drop expressed by:

$$v = -\frac{1}{\mu} \nabla p \quad (14)$$

The effective fracture permeability of fracture can be describing by its aperture b as (in case the fractures are empty):

$$k_{eff} = -\frac{b^3}{12} \quad (15)$$

The mass conservation equation for the flow in a fracture is:

$$\nabla_s \cdot J = -\left(\vec{v}^+ + -\vec{v}^-\right) \cdot n \quad (16)$$

where n the unit vector is normal to fracture plane, \vec{v}^+ is the seepage velocity in the matrix on the side of n and \vec{v}^- is the seepage velocity on the opposite side.

This transport equation is implemented with the above-mentioned boundary conditions to calculate the permeability tensors.

Therefore, the total seepage velocity over the block is obtained by integrating the flow rates over fracture surfaces and matrix porous media. Then the results divided by the total block volume to calculate the block effective permeability tensor.

$$v_x = \frac{1}{\gamma} \left\{ \int_{\gamma_m}^- v_x dv + \int_{sf}^- J_x ds \right\} = \frac{-k_{eff}}{\mu} \frac{\partial p}{\partial x} \quad (17)$$

where, sf is the surface for all fractures and γ is the matrix volume.

5. Simulation of fluid flow in NFR

Currently, there are three major approaches to simulate fluid flow through naturally fractured reservoirs which include: continuum, dual porosity/dual permeability, and flow through discrete fracture network. Recently studies revolving the use of pressure Transient data for characterizing naturally fractured reservoir through Inversion of well test data [14]. In this paper, pressure transient data from the NFR is used to evaluate the fracture map which is generated by statistical analysis of field data as per Doonechaly and Rahman [15]. This is carried out in two inversion steps.

Step 1. The reservoir is divided into a number of grid blocks and the block-based permeability tensors are estimated by considering all fractures that are intersected by the blocks. Fluid flow is simulated (forward modelling by single continuum approach, therefore the permeability tensors) to estimate change in pressure and pressure derivatives. The simulated pressure data is compared with that obtained from well test to estimate error. The gradient based technique is utilized to repeat the forward modelling for different realizations of block-based fracture permeability tensors until the error is reduced to a minimum. The optimized permeability tensors are then correlated to fracture properties of the corresponding blocks.

Step 2. In the next inversion step, different subsurface fracture maps are realized based on the correlation and the forward modelling carried out by using single continuum and discrete fracture approach, which was developed by Gholizadeh and Abdelazim *et al.* [16] until an optimized fracture map is obtained (see Fig.2 and Table.1).

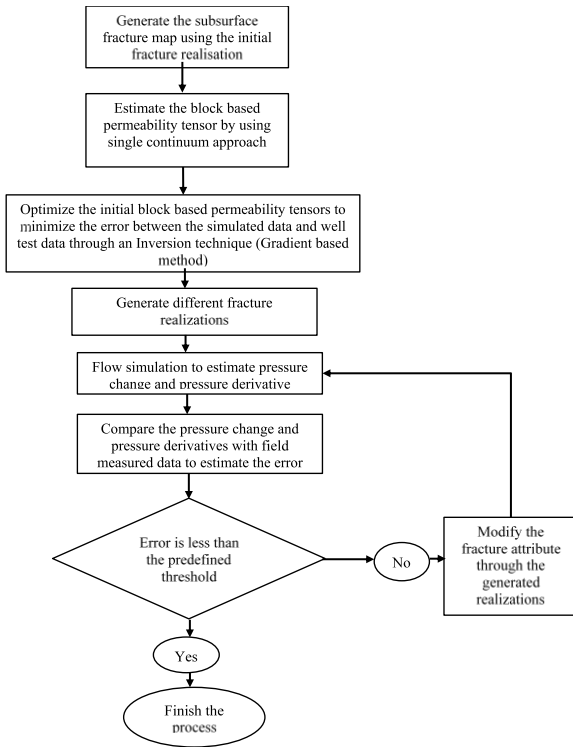


Fig. 2: The different steps used in optimizing the subsurface fracture map

Table 1. Reservoir inputs parameters for permeability tensor calculations

Parameter	Value
Reservoir dimensions	500m×500m×250m
Matrix permeability	0.0095 mD
Matrix porosity	2%
Fracture aperture	7.06×10^{-3} mm
Initial fracture intensity	0.15m^{-1}
Initial reservoir pressure	34.9 MPa, 5,063psia)
Injection pressure (injection case)	54.9 MPa, (7963.65psia)
Fluid viscosity	1.38cp
Fluid compressibility	10^{-8}MPa^{-1}
Production time before shut in (t_p)	72hrs
Production flow rate before shut in	5571bbl/d

We simulate the single-phase flow by coupling permeability tensors and flow through discrete fractures. The reservoir fracture map and grid blocks are shown in Fig. 3a, with short to medium fractures that cut these blocks. The calculated *permeability tensors* are shown in Fig. 3b.

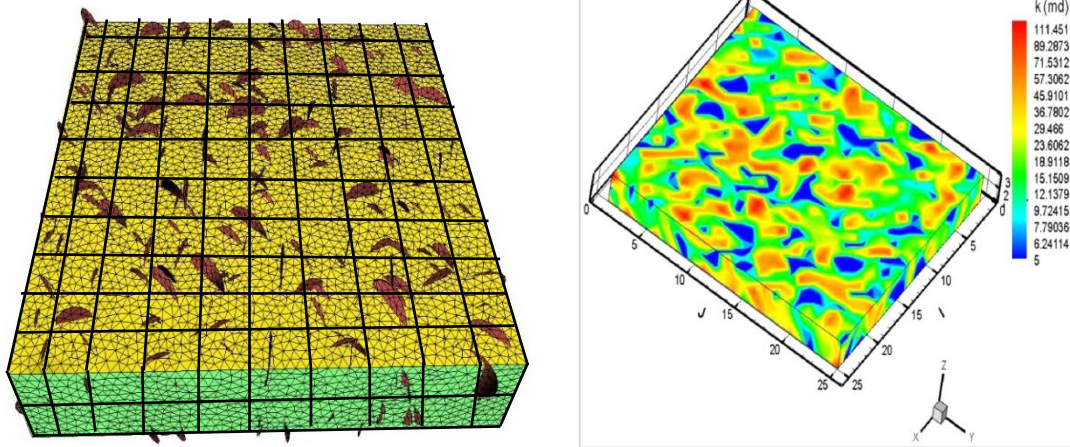


Fig. 3(a) Reservoir domain showing 3D optimized fracture map generated using the block-based permeability tensors; (b) 3D block-based permeability tensor map of the reservoir

5.1. Reservoir simulation workflow

Having optimized the fracture map, flow simulation is conducted at four different oil flow rates for 20 years (1990 – 2010): 5, 10, 15, and 20 MSTB/d. Figure 4 shows the relative permeability data used during the simulation process. Table 2 shows the calculated oil mobility

function (T_f) as a function of average reservoir pressure (p_{av}). Figure 5 shows the oil saturation changes over the simulation period. As can be seen from this figure that oil saturation changing drastically inside the fractures as the fractures considered the main source for oil in this case.

Table 2. Calculated oil mobility function data: $T_f(p_{av})$

Year	S_o	k_{ro}	p_{av} (psia)	μ_o	B_o	$T_f = k_{ro}/\mu_o B_o$
1990	0.53	0.09	5370	0.13	1.5	0.46153846
1991	0.526	0.089	2297	0.13	1.5	0.45641026
1992	0.531	0.095	2000	0.13	1.5	0.48717949
1993	0.531	0.095	1861	0.13	1.5	0.48717949
1994	0.531	0.095	1759	0.13	1.5	0.48717949
1995	0.532	0.09	1681	0.13	1.5	0.46153846
1996	0.5323	0.096	1621	0.13	1.5	0.49230769
1997	0.533	0.097	1567	0.13	1.5	0.49743590
1998	0.5328	0.0964	1518	0.13	1.5	0.49435897
1999	0.5325	0.0962	1475	0.13	1.5	0.49333333
2000	0.532	0.0957	1436	0.13	1.5	0.49076923
2001	0.531	0.0947	1398	0.13	1.5	0.48564103
2002	0.529	0.0928	1394	0.13	1.5	0.47589744
2003	0.528	0.0918	1331	0.13	1.5	0.47076923
2004	0.526	0.0899	1300	0.13	1.5	0.46102564
2005	0.524	0.0879	1271	0.13	1.5	0.45076923
2006	0.522	0.0861	1243	0.13	1.5	0.44153846
2007	0.5197	0.0838	1217	0.13	1.5	0.42974359
2008	0.518	0.0822	1193	0.13	1.5	0.42153846
2009	0.515	0.0793	1169	0.13	1.5	0.40666667
2010	0.513	0.0774	1147	0.13	1.5	0.39692308

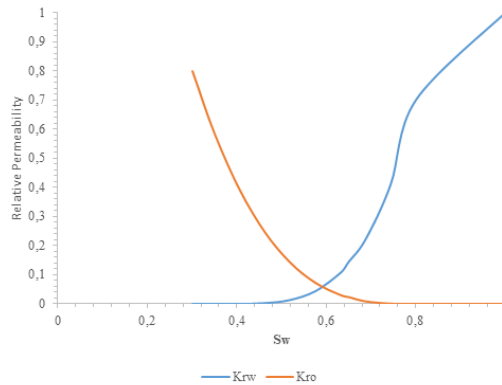


Figure 4. Relative permeability curve used in the simulation work

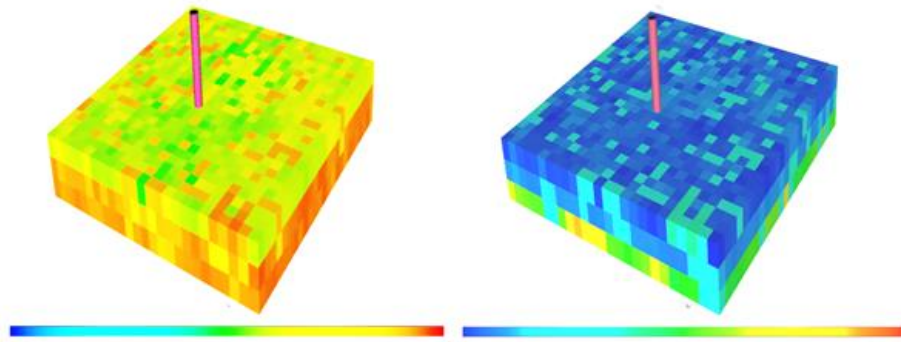


Figure 5. Reservoir simulation model. Oil saturation distribution: (a) After 4 years of oil production, and (b) after 20 years of oil production

6. Results

Data from the four different flow rate runs was combined in Table 3:

Table 3. Mobility Function (T_f) at average reservoir pressure at different flow rate

p_{av} (psia)	T_f at $q_o = 20$ STB/d	T_f at $q_o = 15$ STB/d	T_f at $q_o = 10$ STB/d	T_f at $q_o = 5$ STB/d
2297	0.4564	0.4808	0.4610	0.3772
2000	0.4872	0.4906	0.4906	0.4265
1861	0.4872	0.4906	0.4906	0.4512
1759	0.4872	0.4906	0.4901	0.4610
1681	0.4615	0.4956	0.4921	0.4660
1621	0.4923	0.4956	0.4956	0.4709
1567	0.4974	0.5005	0.4956	0.4758
1518	0.4944	0.4956	0.4956	0.4808
1475	0.4933	0.4946	0.4946	0.4857
1436	0.4908	0.4906	0.4906	0.4827
1398	0.4856	0.4857	0.4857	0.4788
1394	0.4759	0.4758	0.4758	0.4734
1331	0.4708	0.4699	0.4709	0.4660
1300	0.4610	0.4600	0.4610	0.4591
1271	0.4508	0.4497	0.4512	0.4512
1243	0.4415	0.4395	0.4413	0.4413
1217	0.4297	0.4265	0.4265	0.4314
1193	0.4215	0.4186	0.4167	0.4167
1169	0.4067	0.4068	0.4068	0.4068
1147	0.3969	0.3969	0.3969	0.4019

After collecting all data available, we plot the mobility oil function with respect of average by quadratic regression the following equation were obtained:

$$\frac{k_{rf,o}}{\mu_o \beta_o} = -2 \times 10^{-7} P_{av}^2 + 0.0007 P_{av} - 0.165 \tag{18}$$

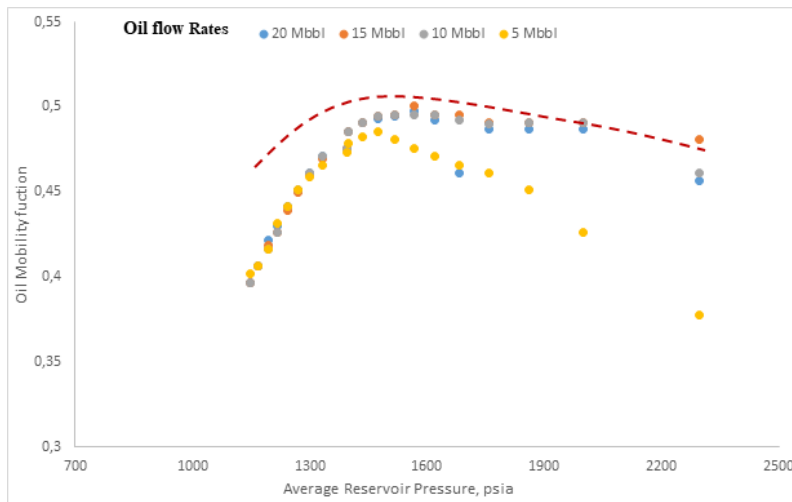


Figure 6. Oil mobility vs Average Reservoir Pressure

7. Discussions

After introducing the new mobility function to the IPR equation an IPR curve is obtained.

$$q_o = \frac{0.00708 k_f h (p_r - p_{wf})}{\left[\frac{1}{2} \ln \left(\frac{4A}{\gamma C_A r_w^2} \right) + s \right]} \left(\frac{k_{rf,o}}{\mu_o B_o} \right) p_{av} \tag{19}$$

where,

$$\frac{k_{rfo}}{\mu_o \beta_o} = -2.0 \times 10^{-7} P_{av}^2 + 0.0007 P_{av} - 0.165 \quad (20)$$

Our new correlation was compared with Vogel's and Wiggins' IPRs based on flow data used from a real well [17]. The results are shown in Fig.7. It was found that our new IPR curve gives more reliable results than the other two methods, which are not applicable to a fracture reservoir. Firstly, the well's test point data are respected by the new correlation, whereas the two other correlations significantly deviate from the test point. Secondly, the methods by Vogel and Wiggins underestimate the absolute open flow potential that a fractured reservoir (with high negative skin) can deliver.

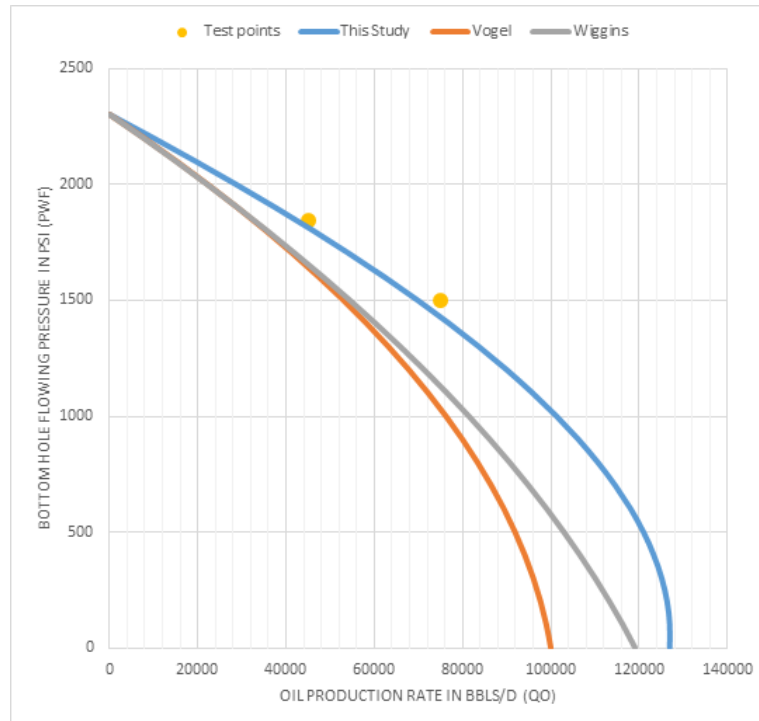


Figure 7. Inflow performance relationship curve using test well data (Jahanbani et al. [9])

8. Conclusions

The objective of this study was to develop reservoir inflow performance relationship (IPR) equation that predicts volumetric production rate as a function of average reservoir pressure in a saturated, fractured reservoir. Several IPR correlations developed in the past are not applicable for the case of a fractured reservoir.

Therefore, a new IPR equation is developed in this study based on extensive numerical reservoir simulation runs that captures fluid flow rates as a function of reservoir pressure over time.

The newly developed IPR equation is compared with two well-known IPR equations (Vogel, and Wiggins). The significant difference of oil production rate as a function of wellbore pressure underscores the fact that an IPR developed for fluid flow in non-fractured reservoir rock cannot be used for a fractured reservoir. As expected, the use of the two existing correlations for multiphase flow in fractured reservoir underestimate production rate by a wide margin.

The new IPR equation can serve as an important tool for routine reservoir flow performance by practicing engineers using a simple spreadsheet.

Nomenclature

$FBHP$	absolute open flow potential (volumetric oil flow rate at zero FBHP)
p_r	static reservoir pressure
p_{wf}	flowing bottom hole pressure (FBHP)

q	<i>volumetric oil flow rate</i>
q_{max}	<i>absolute open flow potential (volumetric oil flow rate at zero FBHP)</i>
m	<i>semi-log straight line slope, psia/cycle</i>
p	<i>pressure, psia</i>
p_{av}	<i>average pressure, psia</i>
p_i	<i>initial reservoir pressure, psia</i>
p_R	<i>average reservoir pressure, psia</i>
p_{wf}	<i>flowing wellbore pressure, psia</i>
r_e	<i>drainage radius, ft</i>
R_p	<i>cumulative produced gas/oil ratio, scf/STB</i>
R_s	<i>solution gas/oil ratio, scf/STB</i>
R_w	<i>wellbore radius, ft</i>
S	<i>skin factor</i>
S	<i>storage, ft/psia</i>
S_o	<i>oil saturation, fraction</i>
S_w	<i>water saturation, fraction</i>
t	<i>time, hours</i>
T_f	<i>fracture transmissibility, mD. Ft/cp</i>
B_g	<i>gas formation volume factor, bbl/scf</i>
B_o	<i>oil formation volume factor, bbl/STB</i>
B_t	<i>total formation volume factor, bbl/STB</i>
C_e	<i>effective compressibility, psia⁻¹</i>
C_{mt}	<i>total matrix compressibility, psia⁻¹</i>
c_o	<i>oil compressibility, psia⁻¹</i>
c_r	<i>rock compressibility, psia⁻¹</i>
c_w	<i>water compressibility, psia⁻¹</i>
h	<i>formation thickness, ft</i>
h_m	<i>matrix thickness (height), ft</i>
k_f	<i>fracture bulk permeability, md</i>
k_o	<i>effective oil permeability, md</i>
k_{ro}	<i>oil relative permeability, dimensionless</i>

References

- [1] Muskat M, and Evinger HH. Calculations of Theoretical Productivity Factor. Trans. AIME, 1942; 146: 126–139.
- [2] Vogel JV. 1968, Inflow Performance Relationships for Solution-Gas Drive Wells. J. Pet. Technol., 1968; 20(1): 83–92.
- [3] Fetkovich MJ. The Isochronal Testing of Oil Wells, Paper SPE 4529 presented at the 1973 SPE Annual Meeting, Las Vegas, Nevada, 30 September–3 October 1973.
- [4] Cheng AM. Inflow performance relationships for solution-gas-drive slanted/horizontal wells. In SPE Annual Technical Conference and Exhibition 1990. Society of Petroleum Engineers.
- [5] Wiggins ML. 1994, Generalized Inflow Performance Relationships for Three-Phase Flow. SPE Res Eng., SPE-25458-PA, 1994; 9 (3): 181-182.
- [6] Elias M, El-Banbi HA, Fattah KA and El-Tayeb ESA. New Inflow Performance Relationship for Solution-Gas Drive Oil Reservoirs. SPE/EAGE Reservoir Characterization & Simulation Conference 2009.
- [7]. Shahri MP, Shi ZR, Zhang HQ, Akbari B, Firoozabad MRM. Generalized Inflow Performance Relationship (IPR) for Horizontal Wells. In SPE Eastern Regional Meeting, Pittsburgh, PA, 2013: 20-22.
- [8] Abdelazim RA. Integration of static and dynamic reservoir data to optimize the generation of subsurface fracture map. Journal of Petroleum Exploration and Production Technology, 2016; 6(4): 691-703.
- [9] Jahanbani GA, Torsæter O and Moradi M. Inflow Performance Relationship for Horizontal Oil Wells in Fractured Reservoirs. 7th EAGE Saint Petersburg International Conference and Exhibition. November 2016.
- [10] Abdelazim R, and Rahman SS. Estimation of permeability of naturally fractured reservoirs by pressure transient analysis: An innovative reservoir characterization and flow simulation. Journal of Petroleum Science and Engineering, 2016; 145: 404-422

- [11] Abdelazim R. Prediction of Naturally Fractured Reservoir Performance using Novel Integrated Workflow. *International Journal of Advanced Computer Science and Applications*, 2017; 8(4): 115-122.
- [12] Luthi SM. Fractured reservoir analysis using modern geophysical well techniques: application to basement reservoirs in Vietnam. Geological Society, London, Special Publications, 2005; 240(1): 95-106.
- [13] Tarahhom F, Sepehrnoori K, Marcondes F. A novel approach to integrate dual porosity model and full permeability tensor representation in fractures. Paper presented at the SPE Reservoir Simulation Symposium 2009.
- [14] Morton KL, Nogueira PDB, Booth R, Kuchu, FJ. Integrated interpretation for pressure transient tests in discretely fractured reservoirs. In SPE Europec/EAGE Annual Conference. Society of Petroleum Engineers 2012.
- [15] Doonechaly NG, Rahman S. 3D hybrid tectono-stochastic modelling of naturally fractured reservoir: Application of finite element method and stochastic simulation technique. *Tectonophysics*, 2012; 541: 43-56.
- [16] Gholizadeh Doonechaly N, Abdel Azim RR, Rahman SS (2016). A study of permeability changes due to cold fluid circulation in fractured geothermal reservoirs. *Groundwater*, 2016; 54(3): 325-335.
- [17] Janban, A, Shadizadeh SR. Determination of the Inflow Performance Relationship in Naturally Fractured Oil Reservoirs: Analytical Considerations. *Energy Sources, Part A: Recovery, Utilization, and Environmental Effects*, 2013; 35(8): 762-777.

To whom correspondence should be addressed: Assoc. prof. Reda Abdel Azim, American University of Ras Al Khaimah, United Arab Emirates, Ras Al Khaimah, Reda.abdelazim@aurak.ac.ae

ANALYSIS OF PETROLEUM SYSTEM FOR EXPLORATION AND RISK REDUCTION IN THE SOUTH-EASTERN INLAND BASINS OF NIGERIA

Chidozie I. Princeton Dim^{1*}, K. Mosto Onuoha¹, Okwudiri A. Anyiam¹, Ikenna C. Okwara¹, Ifeanyi A. Oha¹, Ikenna A. Okonkwo¹, Chukwudike G. Okeugo¹, Elijah E. Nkitnam², Bertram M. Ozumba³

¹ Department of Geology, Faculty of Physical Sciences, University of Nigeria, Nsukka, Enugu State, Nigeria

² Department of Geology and Geophysics, Federal University of Ndufu-Alike Ikwo, Ebonyi State, Nigeria

³ Department of Geology, Federal University of Technology, Owerri, Imo State, Nigeria

Received December 30, 2017; Accepted March 19, 2018

Abstract

Although several acreages exist within the inland basins of southeastern Nigeria, the distribution of key petroleum system elements and associated generation, migration and accumulation processes have not been fully understood. This has hindered extensive exploration and subsequent development plans within these important hydrocarbon provinces. In this paper, outcrop, well logs and seismic data have been integrated with sequence stratigraphic and geochemical modelling techniques to allow for better understanding of the petroleum system elements and processes within the inland basins. Results from petroleum system analysis reveal the existence of two key petroleum systems namely, the Albian-Santonian system of the Abakaliki Basin and the Campano-Maastrichtian system of the Anambra Basin. Integrated analytical studies using sequence stratigraphic and geochemical modelling techniques unravelled the presence and distribution of source, reservoir, seal packages and associated generation, migration and accumulation processes. Structurally, the presence of hanging walls, footwalls, horst blocks and collapsed crest trapping systems provided both possible hydrocarbon migration pathways for generated hydrocarbons and good entrapment for hydrocarbon accumulation. Common Risk Segment (CRS) maps indicate zones of low, moderate and high risks intervals, which are prospective and favourable for hydrocarbon exploration. This study thus, provides a guide to oil and gas exploration and potential in the inland basins of Nigeria.

Keywords: Albian-Santonian system; Campano-Maastrichtian system; Abakaliki Basin; Anambra Basin; Common Risk Segment Maps.

1. Introduction

Studies have shown that a petroleum system exists wherever all the essential elements and processes are known to occur or are thought to have a reasonable chance of occurring [1-2]. Exploration for petroleum in Nigeria's inland basins dates back to the colonial era, when reports of hydrocarbon shows (seeps and smell) by geologists of Shell-BP and preindependence Geological Survey of Nigeria, spurred initial oil prospecting efforts in the Abakaliki Basin of the southern Benue Trough, Anambra Basins and Niger Delta Basin [3]. These exploration studies were limited due to little or no subsurface data. However, with an array of recently acquired data from various sources, there is now a better understanding of the petroleum system elements and processes of Nigeria's inland basins. This paper aims at integrating data from outcrop, well and seismic with sequence stratigraphic and burial history analysis, to better understand the petroleum system and establish prospective and favourable zones that will provide suitable guide for hydrocarbon exploration and production in Anambra and Abakaliki basins of southeastern Nigeria. The key objectives are to identify the key petro-

leum system elements that will aid in generating an Event Chart and further insight on the existing petroleum systems and reconstruct a common risk segment map using information from map extent of key petroleum system elements to unravel prospective and favourable zone.

2. Geologic framework

The initiation and evolution of the sedimentary basins of southeastern Nigeria is well documented in several studies [4-7]. From the Albian to Santonian, the depositional centre was the NE-SW trending Abakaliki-Benue Trough, which was terminated during the Santonian inversion event. With the folding of the Benue Trough into the Abakaliki Anticlinorium and the Afikpo and Anambra Synclines, deposition shifted to the south-eastern, southern and western flanks of the structure, forming the Anambra Basin [8-9]. The study area lies within Abakaliki Basin (Southern Benue Trough) and Anambra Basin, which consists predominantly of Early to Mid-Cretaceous (Albian to Santonian) and Upper Cretaceous (Campanian-Maastrichtian) clastic sediments [10-11] (Figs. 1; 2; 3a and 3b). The Abakaliki Basin consists of three groups, namely: i) Asu-River Group (Middle Albian to Lower Cenomanian age), related to the earliest stages of the basin's formation [12-13]; ii) Eze-Aku Group (Cenomanian to Late Turonian age) consisting of shallow marine sandstones, shales and limestones [14-15]; and iii) Awgu Group (Coniacian to Santonian age), which records the beginning of the regression that culminated in the uplift that ended the first tectonic phase [12]. Sedimentation in the Anambra Basin began with the deposition of the Campanian Nkporo Group (Owelli, Nkporo, and Enugu formations), succeeded by the Late Campanian to Maastrichtian Mamu Formation, Ajali Formation, and ended with the late Maastrichtian age Nsukka Formation [16]. The sediment packages were deposited during an overall regressive cycle within fluvio-tidal, deltaic, shelfal and marine settings [17-18].

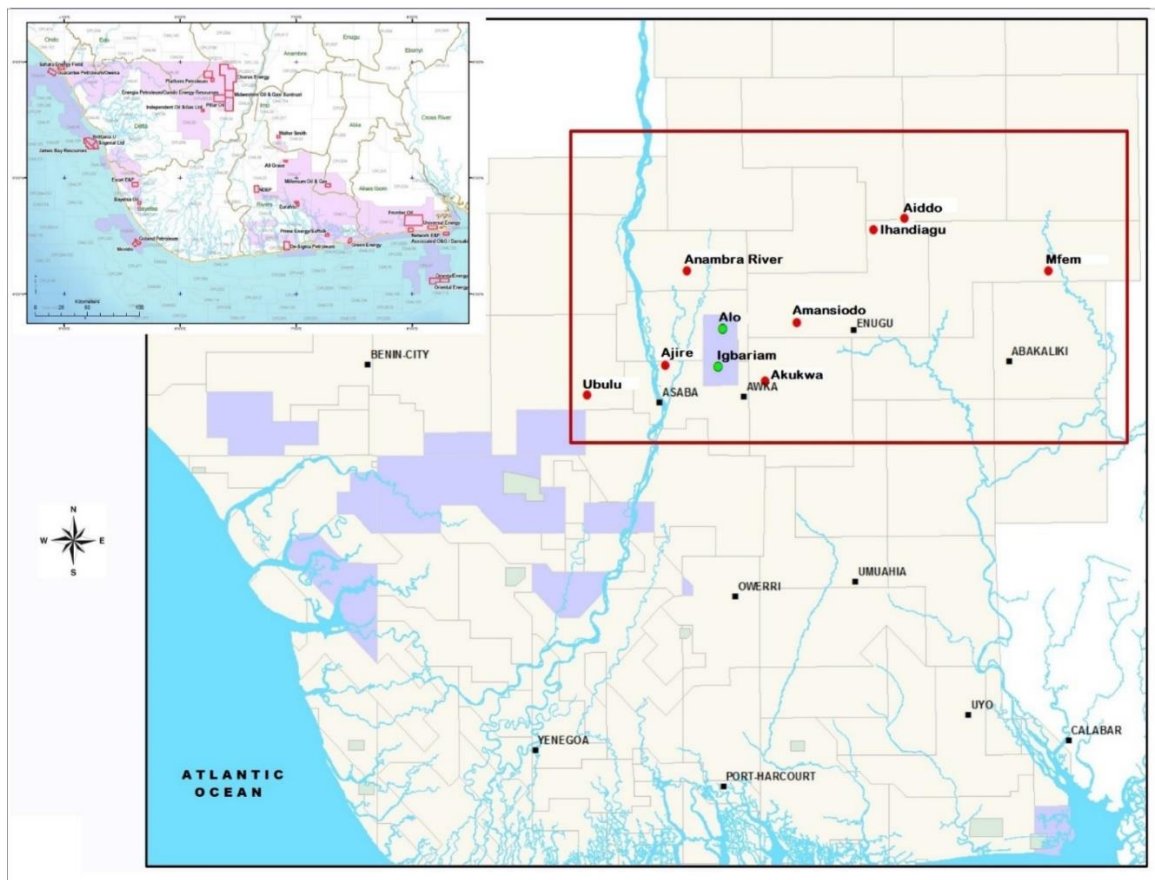


Fig. 1. Concession map of the southern Nigeria showing the well bore distribution in the study area (within the red box)

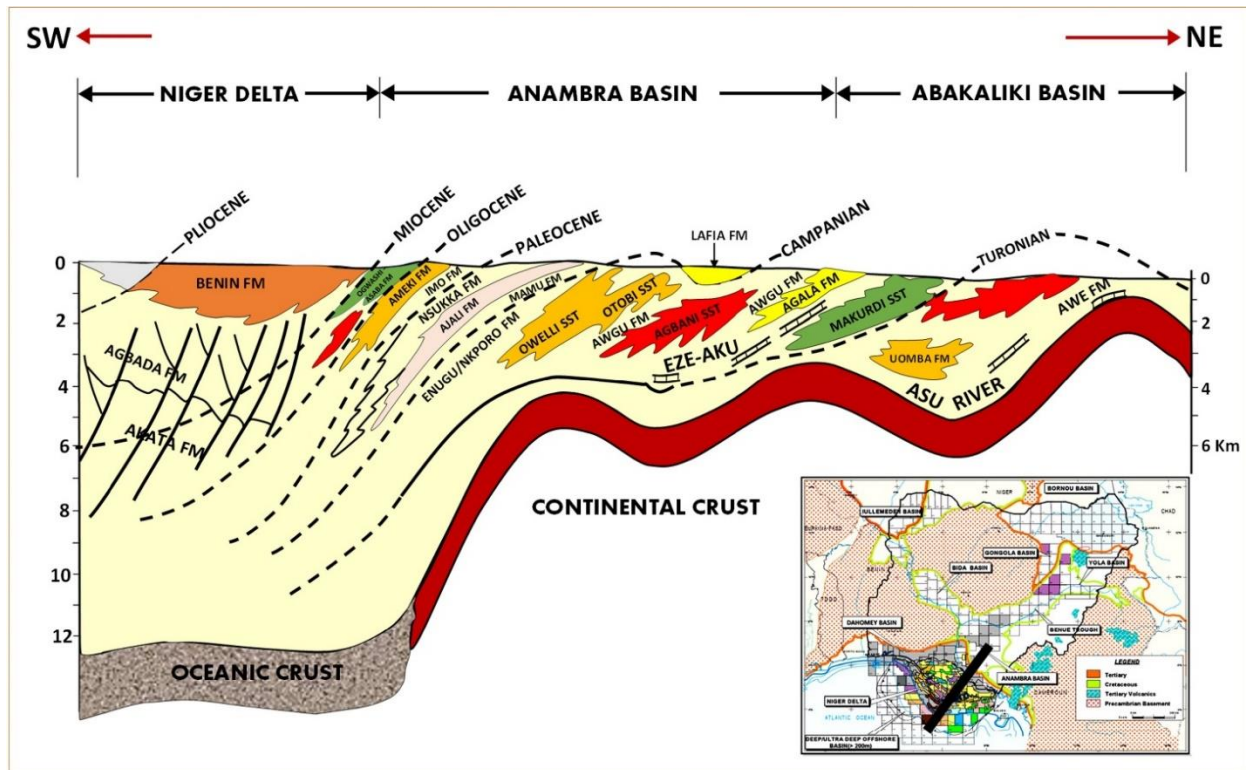


Fig. 3b. Cross section of the showing lithostratigraphic units of Abakaliliki, Anambra and Niger Delta Basins (after Benkhellil [11])

3. Methodology

This study integrates data from outcrops, well, and seismic to generate a sequence stratigraphic framework and geochemical model of the basin. Representative outcrops within the Anambra and Abakaliki basins were mapped, to document rock units and structural features that constitute potential elements of petroleum system. Well log sequence stratigraphic correlation was also carried out, constrained by biostratigraphic data [19-20]. Region-wide correlation was also carried out across the study area to understand the behaviour of sediment packages within lithostratigraphic unit. Lithological thicknesses were estimated for each formation at various intervals of occurrence in all the wells to enable better understanding of subsurface sand-shale thickness distributions across various geologic ages. Information obtained from published geochemical data was used to reconstruct burial history and model hydrocarbon generation. 2D seismic sections were interpreted to highlight key stratigraphic packages and structural configuration. A common risk segment map was also generated to better define hydrocarbon prospective areas.

4. Results and discussion

4.1. Outcrop and Lithostratigraphic Studies

Outcrop studies indicate the lithostratigraphic units of the Abakaliki Basin are seen in quarry, road-cut and river-cut sections (Fig. 4a-4m). Asu-River Group consists mainly of arkosic, non-fossiliferous fanglomerates, shales, limestones and sandstones [12-14]. The Eze-Aku Group consists of sandstones, shales and limestones. The Amaseri Sandstone and Eze-Aku Shale, which belong to the Eze-Aku Group are well exposed in the Amaseri area of Afikpo, southeastern Nigeria (Fig. 4a and 4b). The Awgu Group (Agbani Sandstone and Awgu Shale) are well exposed in the southeastern part of Nigeria. Generally, the lithostratigraphic units of the Abakaliki Basin were affected by the Santonian tectonic event that led to sediment deformation. Hence, exposed stratigraphic packages in the basin are tilted fold limbs with high

dips (Fig. 4a). On the other hand, the lithostratigraphic units of the Anambra Basin that were deposited after the Santonian event, show little or no tectonic dip. The Nkporo Group, which is the oldest lithostratigraphic unit in this basin, consists of carbonaceous shales and sandstone members of deltaic origin [17] (Fig. 4d and 4e). This unit is overlain by the coal-bearing Mamu Formation that consists of alternating sandstones, sandy shales, mudstones, and sub-bituminous coal seams [16]. The outcrop of the Mamu Formation is well exposed on the Udi Bypass and Miliken/Onyeama Hills in Enugu, southeastern Nigeria. Overlying the Mamu Formation is the Ajali Formation, which comprises predominantly of sandstones with interbeds of clay laminae (Fig. 4h). The Nsukka Formation, which is the youngest lithostratigraphic unit in the basin consists of dark shales and sandstones, with thin coal seams (Fig. 4k; 4l and 4m).

Basin wide correlation carried out using well log data reveals that the oldest formation (the Nkporo Formation) consists of a 300 – 600 m thick sediment package while the overlying Mamu Formation consists of 600 – 1200 m thick sediments that are in turn overlain by 400 – 600 m thick unit of the Ajali Formation (Fig. 5). Sediments of the overlying Nsukka Formation are 20 – 50 m thick. The distribution of shale units across the area shows that the Campano-Maastrichtian shale package of the Lower Mamu Formation and the Enugu Shale constitute the thickest shale play of 200 – 860 m (Fig. 6a-6j and 7). Relatively high are the thicknesses of shales of Turonian - Cenomanian and Paleocene ages. Well correlation further reveals that sediment thicknesses are thin at the flanks and thicker towards the central part of the study area. The basin-wards thickening of sediment package observed in well correlation are probably evidence of structural influence (faulting) on stratigraphy (Fig. 5 and 8). These near vertical fault structures offer possible hydrocarbon migration pathways for generated hydrocarbons within the basin and could provide good entrapment mechanism for hydrocarbon accumulation, as proven in the prolific neighbouring Niger Delta Basin [21].

4.2. Sequence stratigraphic correlation and framework

Interpretation of well logs have shown that the study area consists of over 4 km (12000 ft) thick sediment package (Fig 5; 8a-8 and 9a). Thirteen chrono-stratigraphic surfaces (six maximum flooding surfaces - MFSs and seven sequence boundaries - SBs). The MFSs mark regional seals that cap reservoir units across the entire area. Well log sequence stratigraphic correlation using these stratigraphic surfaces along NE-SW dip section shows that the shallow and deepest depositional sequences (SEQ 1 and SEQ 6) are discontinuous, whereas the intermediate sequences (SEQ 3 - SEQ 4) are continuous. Depositional sequences which are defined by SBs [19-20] are associated with reservoir, source and seal packages (key petroleum system elements) belonging to various systems tracts that include the lowstand system tracts (LST), transgressive system tracts (TST) and highstand system tracts (HST) that are laterally continuous and quite correlatable even at deeper stratigraphic intervals, which have not yet been penetrated (Fig. 5b). Depositional sequence thickness decreases at younger intervals, from about 3500 ft (1200 m) to about 1000 ft (350 m). This probably indicates sediment packages deposited rapidly during high-frequency, fluvio-deltaic-eustatic sea level oscillations. Genetic units or systems tracts show variable thicknesses across wells from the northeast to southwest. In addition, stratigraphic sequences generally dip southerly and sediment packages thicken down-dip (in basinward direction). This basinward thickening of sediment, observed in well correlation and seismic mapping, could be attributed to high rate of subsidence and deposition associated with syndepositional structural influence on stratigraphy [18, 21] (Fig. 9a and 10). Sequence stratigraphic analysis based on transgressive-regressive cycle, reflects a second-order cycle (ca. 44 My) composed of two transgressive-regressive parasequence pairs, reflecting relative sea level fluctuations [17]. However, a more in-depth interpretation reveals a subdivision into third-order packages (0.3-5 My), whose constituent sequence form the systems tracts, reflecting six repetitive patterns of transgressive-regressive packages with thirteen (13) delineated chrono-stratigraphic surfaces (seven SBs and six MFSs).



Fig. 4. Representative outcrop of various geologic formations in the inland basin. a) Fold limb with thick sediment package of well-stratified fine to coarse-grained sandstone unit in northwest of Afikpo town, off Amoso-Amaseri Road (outcrop exposure on the Amaseri Sandstone (Abakaliki Basin) ridge at Crush Stone Industry quarry site). b) Interstratification of sandstone and shale unit showing a thinning-upward sand and thickening-upward shale package exposed on Ibi Sandstone ridge (Marlum Civil Engineering quarry site) of Akpoha-Afikpo road, Afikpo, c) Oil seep in Owelli Sandstone at the foot of Enugu Cuesta, near Ugwueme village – thought to have been sourced from shales of Awgu Formation of Abakaliki Basin (after Nwajide [13]). d) A road-cut exposure of the thick shale characterized by siltstone/sandstone interstratification in the Enugu Formation, near Onitsha road flyover in Enugu. Note the heterolithic (interstratification of sandstone, siltstone and shale) package at the middle section with evidence of a listric fault, typical of growth fault system. e) Road cut exposure of the Enugu Formation showing normal fault on thick shale with siltstone interbeds, geologists positioned on the hanging wall and footwall (outcrop at Amagu along Enugu – Port Harcourt expressway). f) Normal faulting of thin siltstone/ironstone and shale package in Enugu Formation exposed at a road cut exposure at Four Corner, Ozalla Junction, along Enugu-Port Harcourt expressway. g) The middle section of Fig. 3d showing a heterolithic interval with well-developed growth fault in the Enugu Formation exposed near Onitsha road flyover in Enugu, southeastern Nigeria (Note rollover structures on both hanging wall and the footwall). h) Very thick sandstone characterized by interstratified thin clay bands exposed at a quarry section in Alabama Hills, behind ABSU, off Okigwe - Afikpo road. i) Normal fault structure in Nsukka Formation showing the down-thrown (hanging wall) and up-thrown (footwall) block exposed at Ikpankwo quarry, off Enugu – Port Harcourt express expressway. j) Anastomosing joint structures that could serve as pathway for fluid migration, occurring within the basal shale unit of the Enugu Formation. k) Coal seam (indicated by yellow line) occurring with carbonaceous laminated sandstone units in the Mamu Formation exposed at Onyeama Mine section, along Enugu – Onitsha Express Road. l) Normal fault at Ikpankwo quarry, off Enugu – Port Harcourt express expressway. Arrow indicates displaced/juxtaposed fault blocks. m) Coal bed of Mamu Formation exposed at the base of thick carbonaceous sandstone at Udi By-pass, SE Nigeria. Note persons (approximately 1.8 m) and geologic hammer (30 cm) for scale

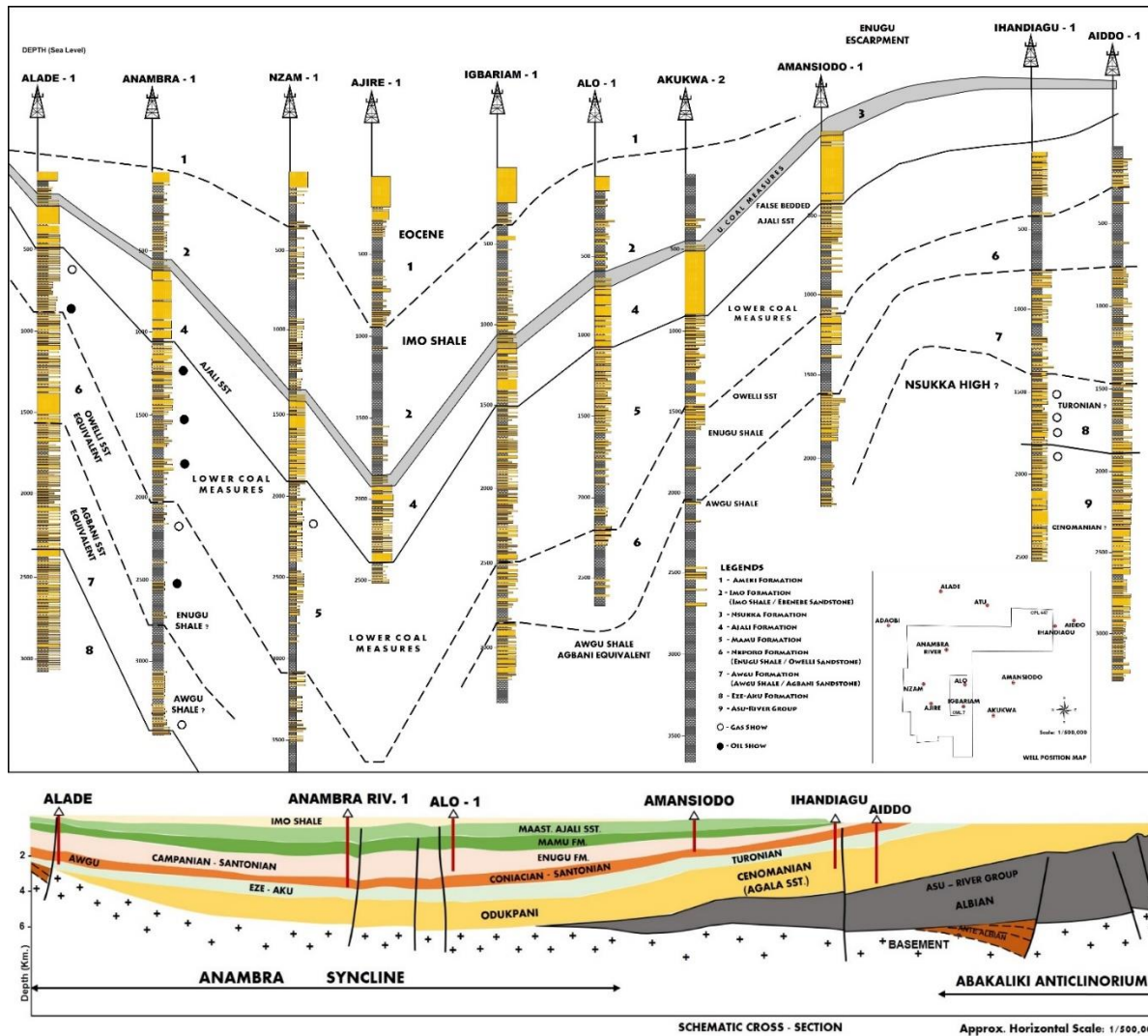


Fig. 5. Multiple dip line correlation section showing lithostratigraphic units and hydrocarbon shows in the Southern Benue Trough (Turonian-Santonian), Anambra Basin (Campanian-Lower Paleocene?) and Niger Delta (Paleocene); Aiddo-1, Ihandiagu-1, Amansiodo-1, Akukwa-2, Alo-1, Igbariam-1, Ajire-1, Nzam-1, Anambra River-1 and Alade-1 with a schematic cross section showing wellbore and sediment package with possible associated near vertical faults. Inset map is the study area showing the spatial distribution of wellbores (after Onuoha and Dim [21])

4.3. Petroleum system elements and processes

Studies have shown the existence of two petroleum systems namely; a) the Albian-Santonian (early to mid-Cretaceous) system of the Abakaliki Basin (Southern Benue Trough). The potential hydrocarbon source or charge in the Abakaliki Basin are the mature Turonian Eze-Aku and Coniacian Awgu shales [22-23]. The reservoir type in the basin is essentially of clastic sandstones, which comprise mainly of interbedded sandstone bodies of Eze-Aku Formation (Amaseri Sandstone) and Agbani Sandstone (Awgu Formation) that have poor to moderately hydro-carbon reservoir quality [15]. Entrapment mechanisms were formed during the Aptian-Albian rifting, which may have created basement normal faults whose throw continues to increase as subsidence increases. These faults formed structural traps which were reactivated and enhanced in the Turonian renewed rifting. In addition, the early Cenomanian post rift and later Santonian deformation led to the formation of folds and fault that serves as structural styles within the basin.

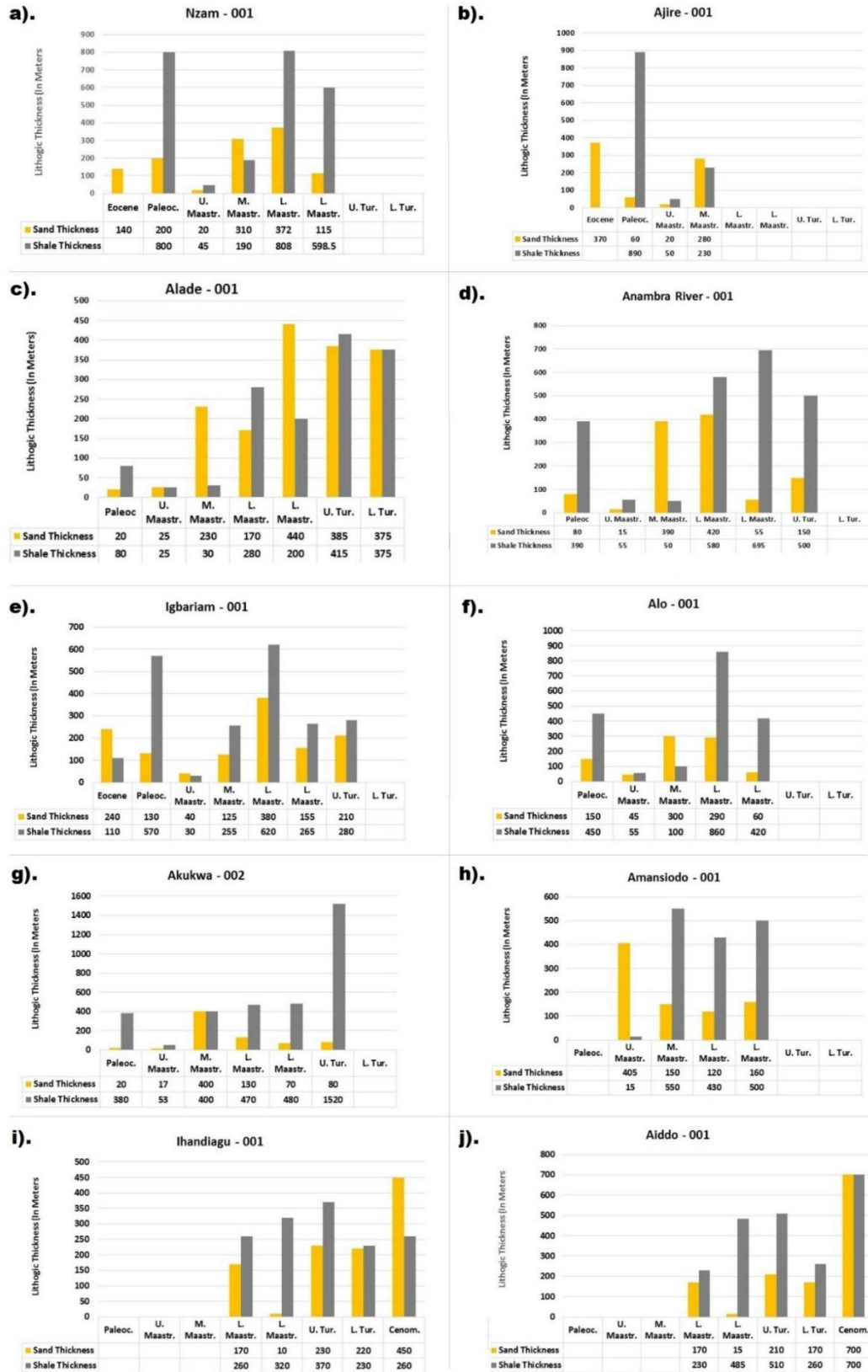


Fig. 6. Distribution of sand-to-shale percent across ages, across several wells (after Onuoha and Dim [21])

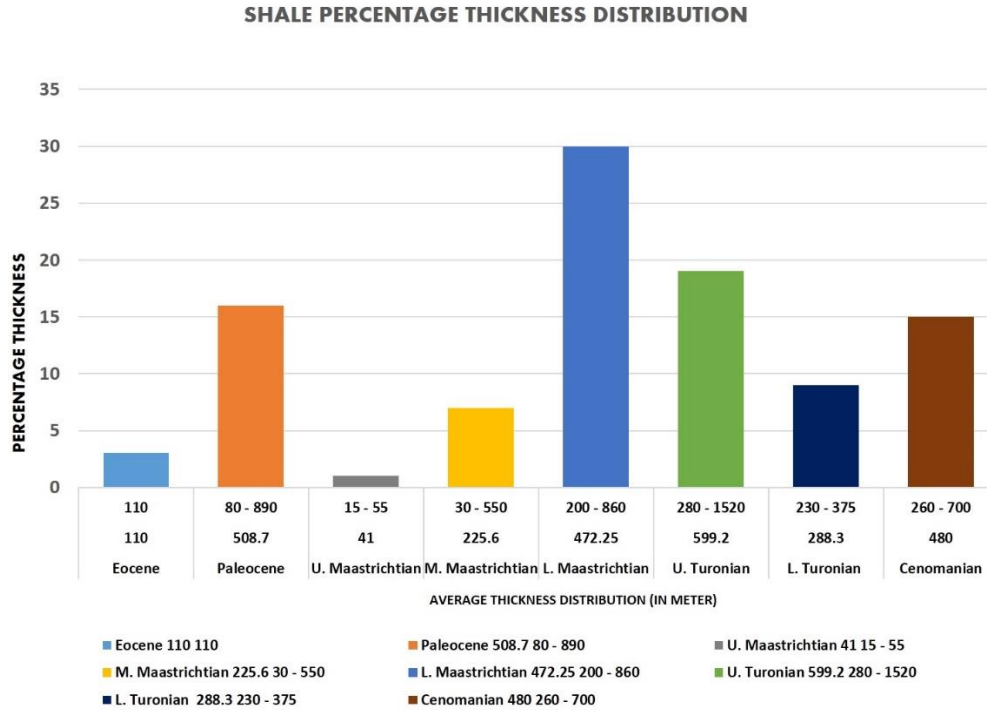


Fig. 7. Gross shale thickness distribution chart by age across the Anambra Basin estimated from subsurface well data (after Onuoha and Dim [21])

The major seals in the basin are mainly the interbedded shales and mudstones of Awgu and overlying Nkporo formations. b) the Campano-Maastrichtian (Late Cretaceous) system of the Anambra Basin that has its major charge from the marginally mature shales of Nkporo with terrigenous inputs from Mamu Shales and Coals, which have been proven to be viable source rocks with fair to good geochemical parameters - kerogen type, total organic carbon (TOC), and Hydrogen Index [22, 24]. The reservoirs in the Anambra Basin are clastic sandstones, which comprise mainly of interbedded sandstone bodies of Nkporo, Mamu and Ajali formations that have adequate hydrocarbon reservoir quality [17, 23]. Traps within the basin were formed possibly due to south-westward stacking of sediment which created differential subsidence basinward [5]. This could have caused the development of syndepositional growth faults during the Campanian renewed thermal subsidence in the Anambra Basin. The presence of the growth faults and associated rollover anticlinal structures offer possible traps for hydrocarbon accumulation. The seal packages are mainly the shales of Nkporo, Mamu and Nsukka the overlying Imo Formation (Paleogene) of the Niger Delta Basin, which have not undergone any regional deformation.

Reconstruction of the burial and thermal histories of sediments in the basin (Fig. 11a-11c), reveals the occurrence of three major episodes in the basins. a) The subsidence in the Turonian time that corresponds to the second phase of renewed rifting in the basin, which is of less magnitude relative to initial rifting and basin opening of the Aptian-Albian times. This subsidence gave rise to the deposition of marine shales of Eze-Aku in the Turonian and Awgu Shales in the Coniancian. b) The compressional uplift (inversion) in the Santonian, that gave rise to the Abakaliki Anticlinorium, the thermal subsidence of the western platform (Anambra Basin) and eastern (Afikpo Syncline). c) Thermal subsidence in the Campanian-Maastrichtian time, which brought about the erosion of the Abakaliki fold belts and deposition of the erosion materials on the rapidly subsiding western and eastern basins. From the burial history charts and plots, the onset of hydrocarbon generation from all the source rocks buried in the deepest parts of the basin as well as those buried to intermediate depths extended over a narrow range of 53 my – starting at 83 my for the Eze-Aku Shale to 30 my for the Nkporo Shale [25].

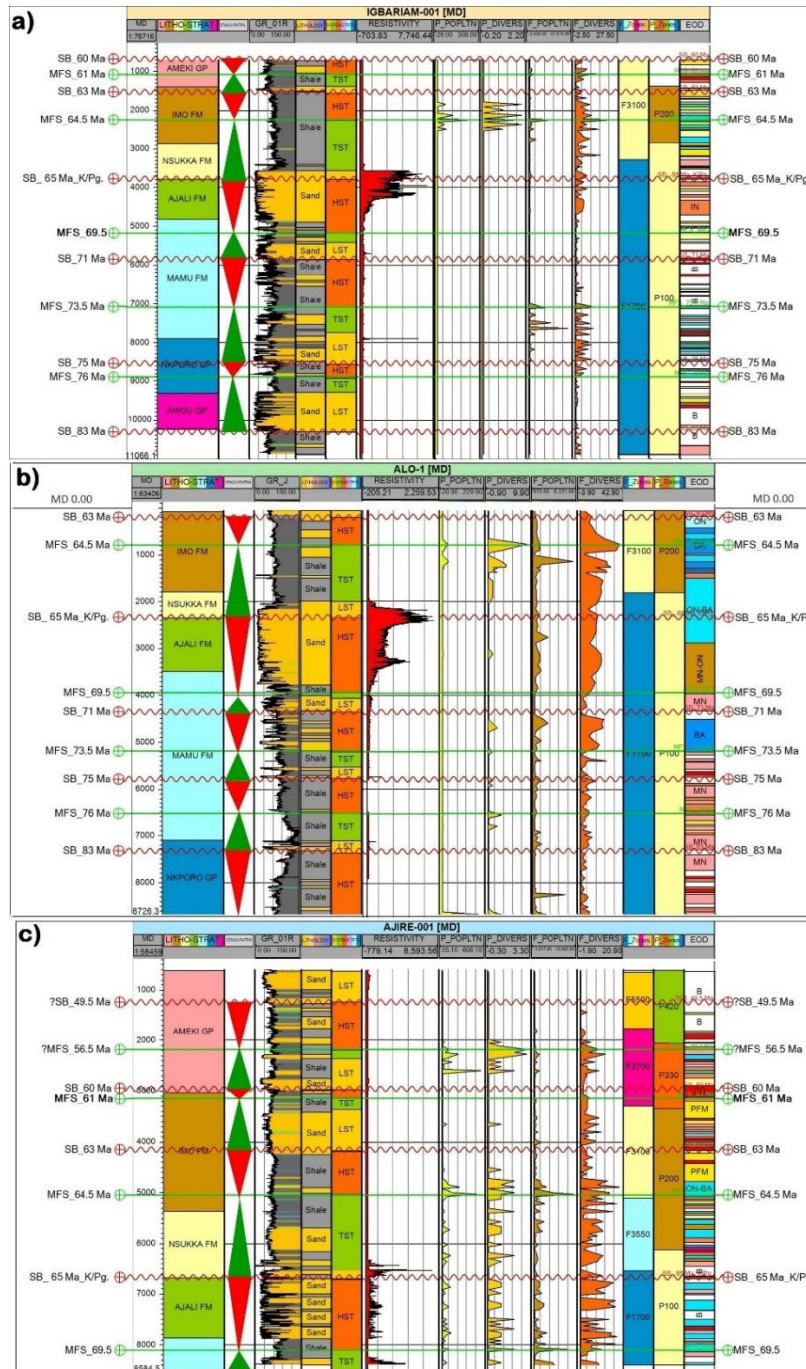


Fig. 8. a) Well log sequence stratigraphic correlation and interpretation of Ajire-001 well study (NB: the occurrence of eight stratigraphic bounding surfaces (four sequence boundaries and four maximum flooding surfaces). b) Well log sequence stratigraphic correlation and interpretation of Alo - 001 well study (NB: the occurrence of nine stratigraphic bounding surfaces, five sequence boundaries and four maximum flooding surfaces). c) Well log sequence stratigraphic correlation and interpretation of Igbariam-001 well study (NB: the occurrence of eleven stratigraphic bounding surfaces e six sequence boundaries and five maximum flooding surfaces). d) Well log sequence stratigraphic correlation (on dip section) and interpretation showing thirteen (13) stratigraphic bounding surfaces (6 MFSs and SBs) and six (6) depositional sequences. NB: Sediment packages thickens down-dip due to structural (Fault e F) influence on stratigraphy (after Dim, et al. [18])

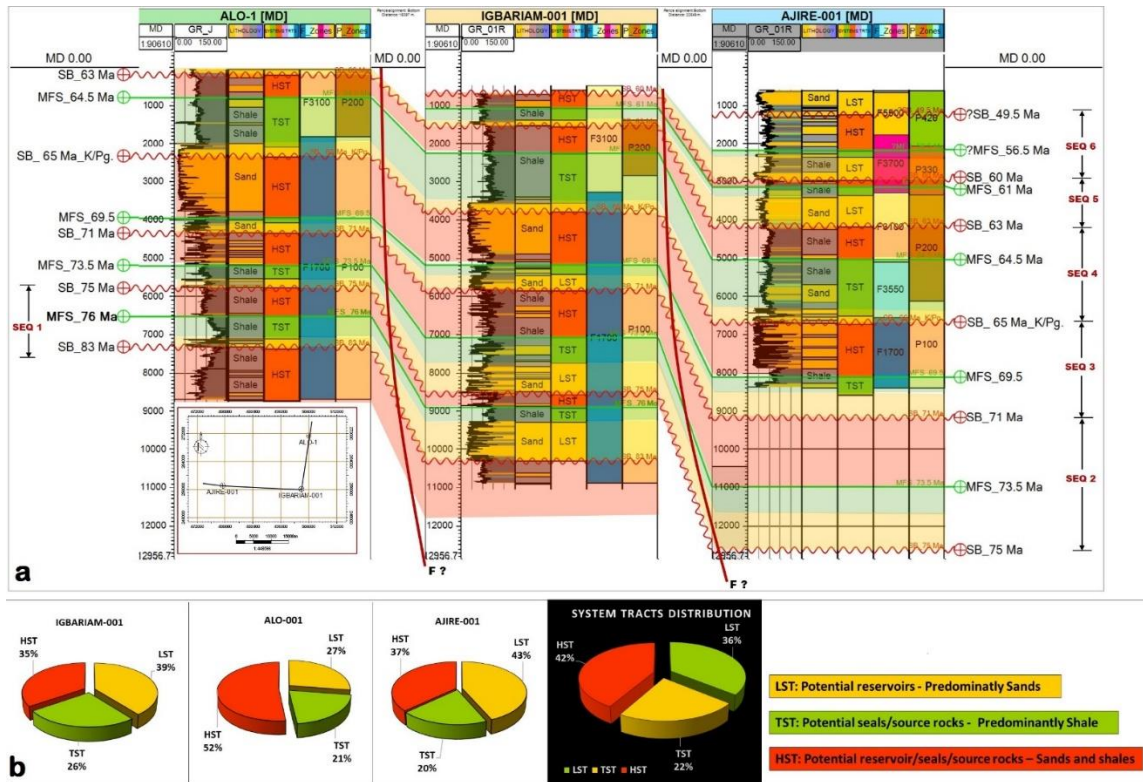


Fig. 9. a) Well log sequence stratigraphic correlation (on dip section) and interpretation showing thirteen (13) stratigraphic bounding surfaces (6 MFSs and 7 SBs) and six (6) depositional sequences (SEQ 1 - SEQ 6). Note that sediment packages thicken down-dip due to structural (Fault - F) influence on stratigraphy. b) Pie chart showing the distribution of potential reservoir, seal and source rocks within the systems tracts across wells (after Dim et al. [18])

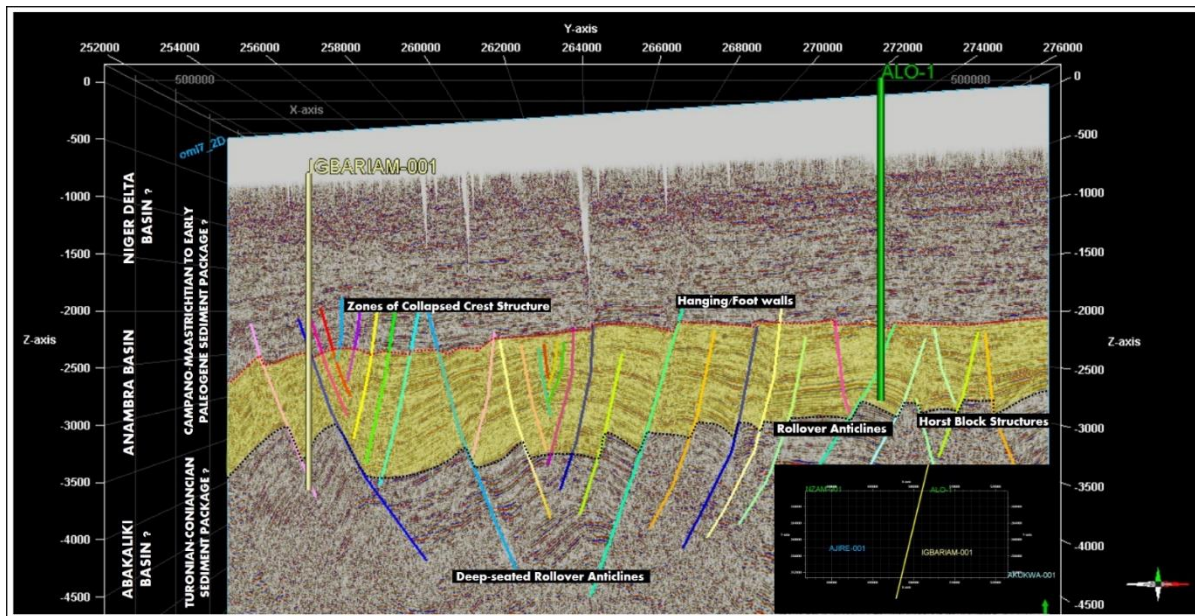


Fig. 10. 2D Seismic section with wellbores in the Anambra basin showing sediment packages and interpreted fault structures which could act as possible migratory pathways and entrapment mechanism. Inset is map view of 2D seismic line (after Dim et al. [18])

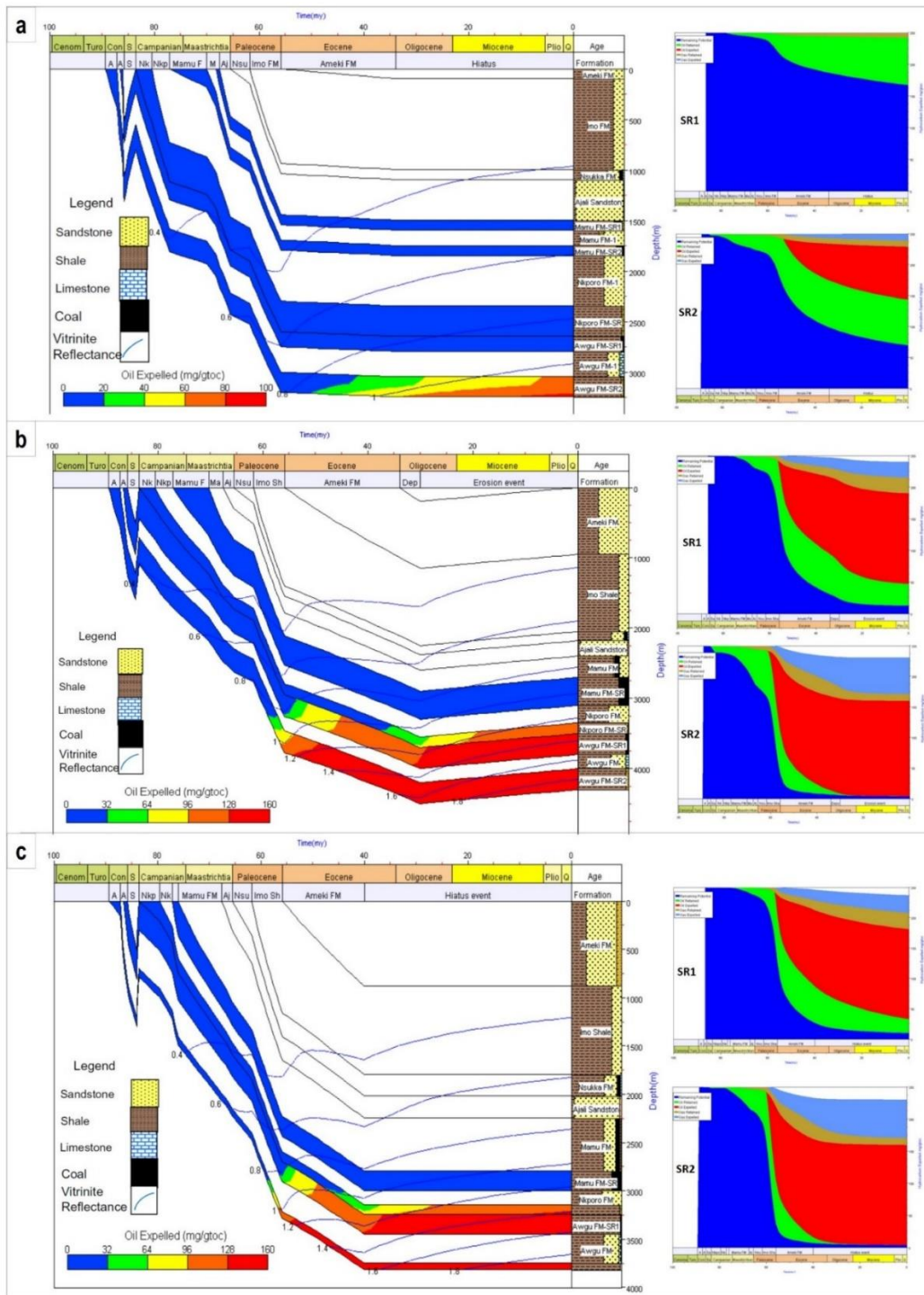


Fig. 11. a) Burial history of the Igbariam-1 well (key well) – with applied variable heat-flow. Expelled, retained and residual hydrocarbons chart for upper source unit SR1 and lower source unit SR2 source unit in Igbariam-1 well (Key Well). b) Burial history chart for Iji-1 well (Pseudo 1), with the buried source units in heavy colours. Expelled, retained and residual hydrocarbons chart for upper source unit (SR1) and lower source unit (SR2) in Iji-1 well (Pseudo 1). c) Burial history chart for Ajire-1 well (Pseudo 2), with the buried source units in heavy colours. Expelled, retained and residual hydrocarbons chart for upper source unit (SR1) and (b) lower source unit (SR2) in Ajire-1 well (Pseudo 2) (after Anyiam, et al., [25]).

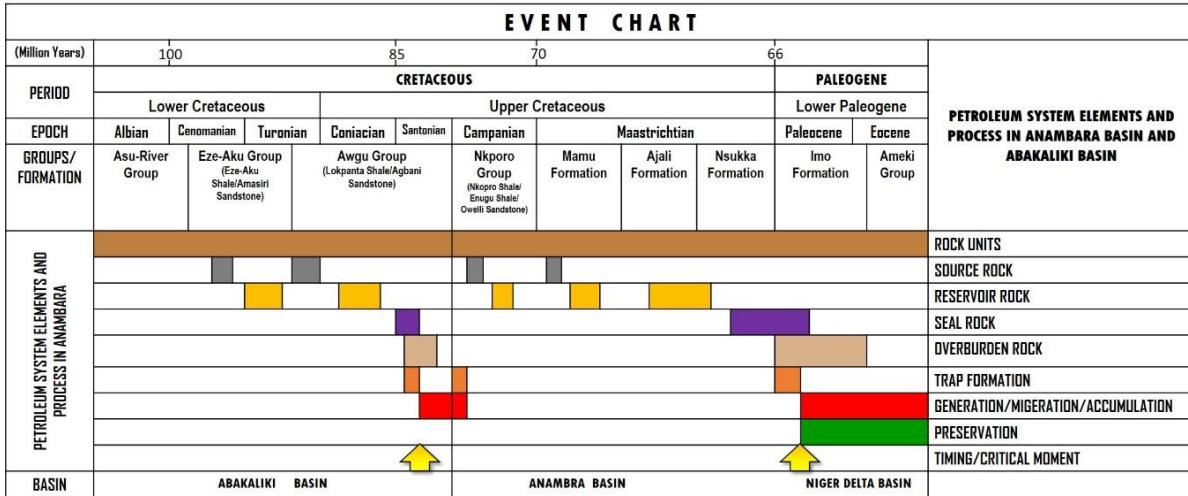


Fig. 12. Petroleum System Chart of Albian-Santonian and Campano-Maastrichtian (Cretaceous) Hydrocarbon Systems in the Anambra Basin and Abakaliki Basin respectively.

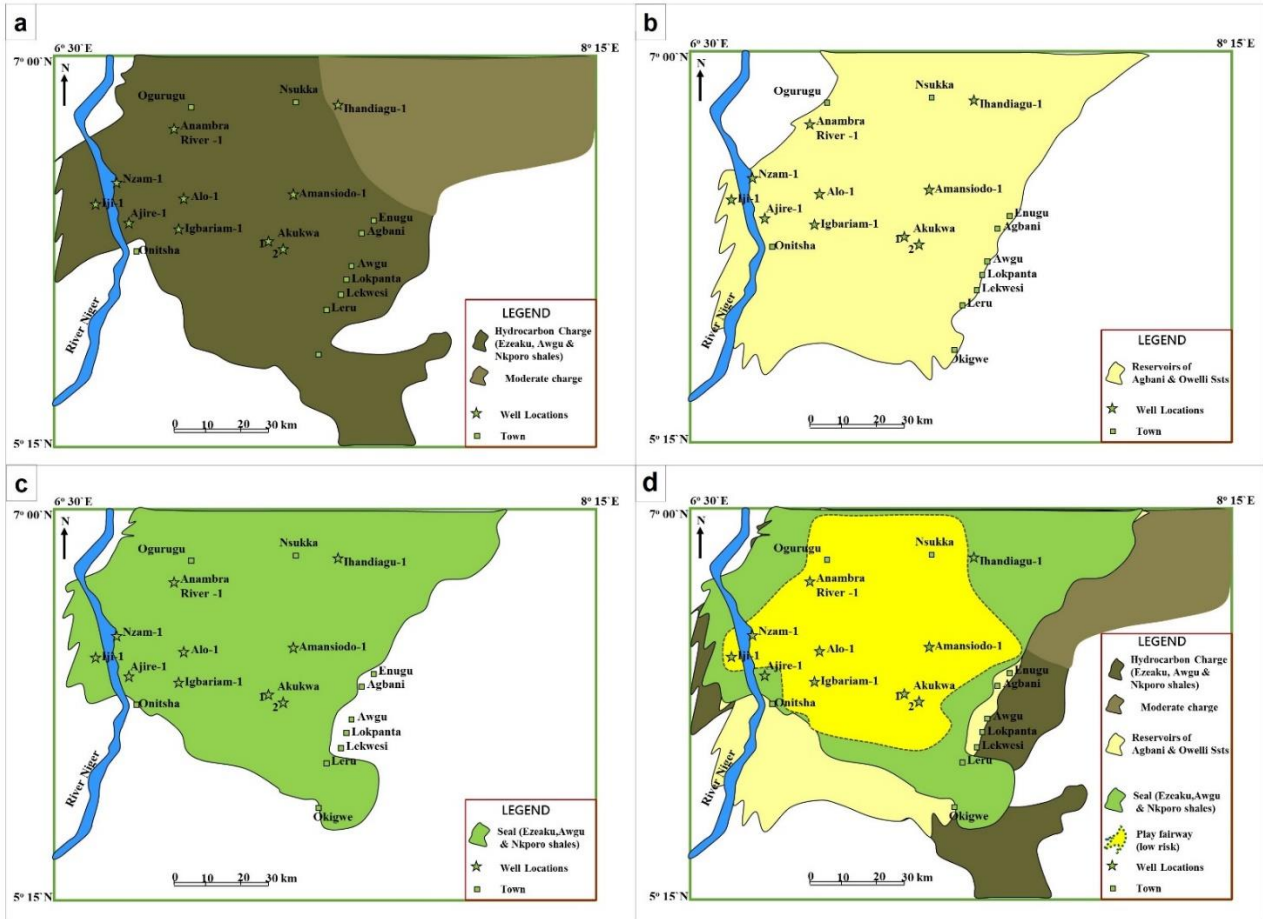


Fig. 13. a) Subsurface hydrocarbon charge for Eze-Aku, Awgu, and Nkpore source rocks in the play. b) Subsurface reservoir distribution for Owelli and Agbani Sandstones in the play. c) Subsurface top and lateral seal for Awgu and Nkpore interbedded shales in the play. d) Composite common risk segment map showing the southern Benue Trough (Abakaliki Basin) and Anambra Basin play fairway. Note the low-risk zone to the west of the area (after Anyiam et al. [28])

Studies have shown that during the pre-Campanian period, enormous volumes of hydrocarbons generated by the Cenomanian-Turonian source rocks (underlying Awgu Group and Lokpanta Shales of the Abakaliki Basin) before the Santonian uplift, might have migrated through these structures probably to shallower horizons, part of which may be contributing to the Niger Delta reserves [3, 26]. There is also evidence of oil shows associated with the Lokpanta Shale exposure in the basin, one of which has been correlated with the oil seepage from the Owelli Formation (reservoir package) of the Nkporo Group [24-25, 27]. The presence of key petroleum system elements and processes in both Abakaliki and Anambra basins is a good indication of the existence of two petroleum systems that span from lower Cretaceous to upper Cretaceous (Fig. 12).

Determination of the most prospective sections of the basin favourable for hydrocarbon exploration and exploitation was deciphered from generated common risk segment maps (Fig. 13a-13c). Evaluation of play fairway and risk analysis through overlying the various play elements maps such as source (charge), reservoir, and seal rocks integrated with other petroleum system processes (timing, trap formation, hydrocarbon generation and migration) reveal that there exists a zone of low risk that should be viable, not only for conventional, but also for unconventional petroleum resources [28] (Fig. 13d). Thus, applying risk analysis to the play fairway level in frontier basins permits channelling of exploration effort into the most prospective parts of the Basins.

5. Conclusion

Integrating outcrop, well logs and seismic data has allowed for better understanding of the petroleum system elements and processes within the inland basins of southeastern Nigeria. Outcrop data indicates the presence of reservoir (sandstone packages), source/seal (shale packages), and associated structural styles for hydrocarbon accumulation. Sequence stratigraphic analysis suggests the existence of depositional sequences that comprise genetic units (LST, TST and HST). The LST and HST sandstones of the Mamu and Ajali formations constitute the reservoir package, whereas TST shales of the Imo Formation offers good seal rock package for the region. These genetic units make up the poor to good reservoirs with favourable thickness, mature to marginally source and laterally extensive seal packages. Studies revealed that presence of seeps possibly due to the updip migration of hydrocarbon from Eze-Aku and Awgu source rocks into the Owelli Sandstone (Nkporo Formation) in the Ugwueme area of southeastern Nigeria, which have been attributed to Santonian unconformity that lies between the pre-Santonian deposits and the Campano-Maastrichtian deposits in the Abakaliki Basin. This constitute a major risk which affected the sealing capacity

Structural styles such as hanging walls, footwalls, horst blocks, and collapsed crest structures (are also evident in seismic section) provide possible hydrocarbon migration pathways for generated hydrocarbons and good entrapment mechanism for hydrocarbon accumulation, as proven in the prolific neighbouring Niger Delta Basin. Hence, a valid petroleum system exists within the Anambra and Abakaliki basins, with the highly bituminous Lokpanta Member of the Eze-Aku Shale Group and the Nkporo Shales identified as targets for commercially viable hydrocarbon resources. Generated common risk segment maps indicate a low risk zone for the southwestern part of the study area. These results confirm that the southwestern part of the study area is the most prospective section, i.e. the section most favourable for hydrocarbon exploration and exploitation.

Acknowledgements

The authors are grateful to the management of Shell Petroleum Companies in Nigeria (SPDCiN), for provision of well log and seismic data and also the team of professionals in the Basin Analysis and Reservoir Geology – Research Group (BARG-RG) of the Department of Geology, University of Nigeria, for their technical support.

References

- [1] Magoon LB and Dow W G. The petroleum system: From source to trap. American Association of Petroleum Geologists Memoir, 1994; 60: 655 p.
- [2] Magoon LB and Beaumont EA. Petroleum Systems. Chapter 3 In: Exploring for Oil and Gas Traps, AAPG Treatise of Petroleum Geology, Handbook of Petroleum Geology 1999, ed. Edward A. Beaumont and Norman H. Foster, 1-3.
- [3] Ekweozor CM. Searching for petroleum in the Anambra basin, Nigeria. In Okogbue, C. O (Ed.), Hydrocarbon Potentials of the Anambra Basin. Proceedings of the First Seminar organized by the Petroleum Technology Development Fund (PTDF) Chair in Geology, 2005; University of Nigeria. 83-110.
- [4] Burke KC, Dessauvage TF J and Whiteman AJ., Opening of the Gulf of Guinea and geological history of the Benue Depression and Niger delta. Nat. Phys. Sci., 1971; 233: 51-55.
- [5] Murat RC. Stratigraphy and palaeogeography of the cretaceous and lower tertiary in Southern Nigeria. In: F. J. Dessauvage, A. J. Whiteman (Eds), African Geology. University of Ibadan Press, Ibadan, Nigeria, 1972: 251-266.
- [6] Benkheilil J. Benue Trough and Benue Chain. Geological Magazine, 1982;119(2): 155-168.
- [7] Benkheilil J, Guiraud M, Ponsard JF and Saugy L. The Bornu-Benue Trough, the Niger Delta and its offshore: Tectono-sedimentary reconstruction during the Cretaceous and Tertiary from geophysical data and geology. In Geology of Nigeria. 2nd edn.1989 Rock view Ltd Jos, Nigeria.
- [8] Benkheilil J. The origin and evolution of the Cretaceous Benue Trough (Nigeria). Journal of African Earth Sciences (and the Middle East), 1989; 8(2-4): 251-282.
- [9] Onuoha KM. Structural features of Nigeria's coastal margin: an assessment based on age data from wells. Journal of African Earth Sciences, 1999; 29(3): 485-499.
- [10] Ozumba BM. Nigeria Sedimentary Basins. In: B. M. Ozumba, Geology of the Niger Delta - An Overview for Geophysics Processors. University Liaison Portfolio, Guest Lecture Program (GLP) 2011 by Shell Companies in Nigeria.
- [11] Benkheilil J. Structure et évolution géodynamique du bassin intracontinental de la Bénoué (Nigeria). 3^e Thèse, University Nice, 1986, 226p.
- [12] Ojoh KA. The southern part of the Benue Trough (Nigeria) Cretaceous stratigraphy, basin analysis, paleo-oceanography and geodynamic evolution in the Equatorial domain of the South Atlantic. Nigerian Association of Petroleum Explorationists' Bulletin,1992; 7(2): 131-152.
- [13] Nwajide CS. Geology of Nigeria's Sedimentary Basins. CSS Bookshops Ltd. 2013, Lagos, 565 p.
- [14] Reyment RA. Aspects of the geology of Nigeria. The stratigraphy of the Cretaceous and Cenozoic deposits. Ibadan University Press 1965, Ibadan, 145 p.
- [15] Banerjee I. A subtidal bar model for the Eze-Aku sandstones, Nigeria. Sedimentary Geology, 1980; 25(4): 291-309.
- [16] Akande SO, Ogunmeyero IB, Peterson HI and Nytoft HP. Source rock evaluation of coals from the Lower Maastrichtian Mamu Formation, SE Nigeria. Journal of Petroleum Geology, 2007; 30(4): 303-324.
- [17] Nwajide CS and Reijers TJ A. Geology of the southern Anambra Basin. In: Reijers, T. J. A. (Ed.), Selected Chapters on Geology. SPDC, Warri, 1996: 133-148.
- [18] Dim CIP, Onuoha KM, Okeugo CG and Ozumba BM. Petroleum system elements within the Late Cretaceous and Early Paleogene sediments of Nigeria's inland basins: An integrated sequence stratigraphic approach. Journal of African Earth Sciences, 2017; 130: 76-86.
- [19] van Wagoner JC, Posamentier HW, Mitchum RM, Vail PR, Sarg JF, Loutit TS, Hardenbol J. An overview of sequence stratigraphy and key definitions. In: Wilgus CK, Hastings BS., Kendall CG, Posamentier HW, Ross CA, van Wagoner JC. (Eds.), Sea Level Changes: An Integrated Approach, vol. 42. 1988 Society of Economic Paleontologists and Mineralogist, Special Publication, pp. 39-45.
- [20] van Wagoner JC, Mitchum RM, Campion KM, Rahmanian VD. Siliciclastic Sequence Stratigraphy in Well Logs, Cores, and Outcrops. American Association of Petroleum Geologists 1990, Tulsa, p. 55.
- [21] Onuoha KM and Dim CIP. Developing Unconventional Petroleum Resources in Nigeria: An Assessment of Shale Gas and Shale Oil Prospects and Challenges in the Inland Anambra Basin. In: Onuoha KM. (Ed.), Advances in Petroleum Geoscience Research in Nigeria, (pp. 313-328). Edition 2017: 1, Chapter: 16, ISBN 978-1-4276-5590-5.

- [22] Obaje NG, Wehner H, Scheede, G, Abubakar MB and Jauro A. Hydrocarbon prospectivity of Nigeria's inland basins from the viewpoint of organic geochemistry and organic petrology. *American Association of Petroleum Geologists Bulletin*, 2004; 88: 325-353.
- [23] Ladipo KO, Nwajide CS and Akande SO. Cretaceous and Paleogene sequences in the Abakaliki and Anambra basins, south eastern Nigeria: A field guide. Port Harcourt: International Symposium on Geology of Deltas 1992.
- [24] Unomah GI and Ekweozor CM. Application of Vitrinite Reflectance in Reconstruction of Tectonic Features in Anambra Basin, Nigeria: Implication for Petroleum Potential. *American Association of Petroleum Geologists, Bulletin*. 1993; 77: 436-451.
- [25] Anyiam OA and Onuoha KM. A study of hydrocarbon generation and expulsion of the Nkporo Shales in Anambra Basin, Nigeria. *Arabian Journal of Geosciences*, 2014; 7(9): 3779-3790.
- [26] Ekweozor CM and Gormly JR. Petroleum geochemistry of late Cretaceous and early Tertiary shales penetrated by Akukwa-2 well in the Anambra Basin, Southern Nigeria. *Journal Pet Geol.*, 1983; 6: 207-216.
- [27] Agagu OK, Ekweozor CM. Source-rock characteristics of Senonian shales in the Anambra syncline, Nigeria. *J. Min. Geol.*, 1982; 19 (1): 132-140.
- [28] Anyiam OA, Onuoha, KM and Jolly BA. Play fairway evaluation of the Anambra Basin, Southeast Nigeria. *Arabian Journal of Geosciences*, 2015; 8: 539-546.

To whom correspondence should be addressed: Chidozie I. Princeton Dim, Department of Geology, Faculty of Physical Sciences, University of Nigeria, Nsukka, Enugu State, Nigeria, princeton.dim@gmail.com; princeton.dim@unn.edu.ng

SPECTROSCOPIC AND PETROGRAPHIC CHARACTERIZATION OF SHALE FROM KUBANG PASU FORMATION, MALAYSIA

Syed Muhammad Ibad, Eswaran Padmanabhan

Department of Geosciences, Faculty of Geoscience and Petroleum Engineering, Universiti Teknologi PETRONAS, Bandar Seri Iskandar, 31750 Tronoh, Perak, Malaysia.

Received December 18, 2017; Accepted March 3, 2018

Abstract

Shale samples from Kubang Pasu (KP) Formation has been taken from two small hills in the Beseri area of Perlis: Bukit Chondong and Kampung Guar Jentik, Kedah, and accounted for spectroscopic and petrographic characterization during this study to provide an opportunity to explore the organic matter quality and quantity, hydrocarbon bonds distribution and texture and structure characteristics present in these shale. Determining these properties of KP will help establish relationships between the total organic carbon (TOC) with humic acid. This is achieved by determining the organic carbon content and humic spectroscopic UV-visible ratio (E4/E6). The calculated UV-visible ratios of E4/E6 for both outcrops indicate the dominance of humic acids over fulvic acids indicating a strong possibility of terrestrial origin. The attenuated total reflectance (ATR) fourier transform infrared spectroscopy (FTIR) was used in the assessment of hydrocarbon present in rocks. Analysis with the ATR-FTIR shows that the aromatic OPCH stretching (690-900 cm^{-1}) hydrocarbon and aromatic IPCH stretching (600-700 cm^{-1}) hydrocarbon groups (both occur in the finger print region) absorbance are more in KP Formation as compare to other hydrocarbon bands. OH groups stretching vibration, alkyne C-H bending bands and alkane C-H bending band in aliphatic hydrocarbons and absorption spectrum of aromatic C=C stretching and aromatic OPCH are found in the FTIR spectra of KP shales. The petrographic analysis results show that KP shale samples consist mainly of dark to light grey, silty, micaceous, massive, discontinuous wavy parallel laminated, brownish massive, parallel laminated and non-calcareous mudstone.

Keywords: Aromatic Hydrocarbons; Total organic carbon; Spectroscopy; Shale; Humic spectroscopic ratio (E4/E6).

1. Introduction

Spectroscopy techniques such as Ultraviolet-Visible Spectroscopy (UV-Vis) and Attenuated total reflectance (ATR) Fourier transform infrared spectroscopy (FTIR) have been well used for the identification of hydrocarbon functional groups and type of humic substance in shale [1-2]. For the organic chemist UV-Vis is mostly concerned in conjugated systems with electronic transitions; the intensities and positions of the absorption band largely depend to a greater extent on the specific system under consideration. The electronic transitions are mostly sensitive to changes in structure and reveal the strains executed on the system by electronic and steric interactions. Unlike infrared spectroscopy functional group absorptions cannot be assigned to fixed and specific regions of the ultraviolet visible wavelength scale, and considerable experience is required in the interpretation of the spectra [3]. Like UV-Vis, FTIR is certainly one of the most important analytical techniques available to today's scientists. One of the great advantages of infrared spectroscopy is that virtually any sample in virtually any state may be studied. Chemical characterization from FTIR can deliver important information on the molecular structure of inorganic and organic components. From the past few decades FTIR has been used extensively for the assessment of hydrocarbon bond distribution of geological samples such as shale, coal, silicate glass, microfossils, fluid and melt inclusions and minerals [4]. Mostly, its use in the characterization of geochemistry and thermal matu-

ration of organic matter in coal and shale is well known. In FTIR analysis, when a photon collides to a molecule and excites it to a higher energy state, absorption of IR radiation takes place. The excited states consequence in the vibrations of molecular bonds (i.e., twisting, stretching, rocking bending, out-of-plane deformation, in-plane deformation and wagging) taking place at variable frequencies (or wavenumbers) in the IR region of the light spectrum [5].

Macroscopic sedimentary characteristics such as shale texture and structure characteristics can interpret by the petrographical characterization. Shale is a fine-grained sedimentary rock that forms from the compaction of silt and clay-size mineral particles. In this study shale has been taken from Kubang Pasu (KP) formation, as this formation comprises very thick sequences of shale which might be a potential energy source ($\pm 3400\text{m}$ thickness). Although, there is no available literature present, that focused on the spectroscopic and petrographic characterization of the shales in the KP formation. Therefore, this study was designed to address, for the first time, the hydrocarbon bonds distribution, organic matter quality and texture and structure characteristics present in these shale. Furthermore, the processes controlling the level of humic substance in the shale are complex. One of the most important factors is the concentration of TOC in shale [6]. However, no study is also focused on the relationship between humic acid and organic carbon in shale, and its needs to be established.

2. Study area

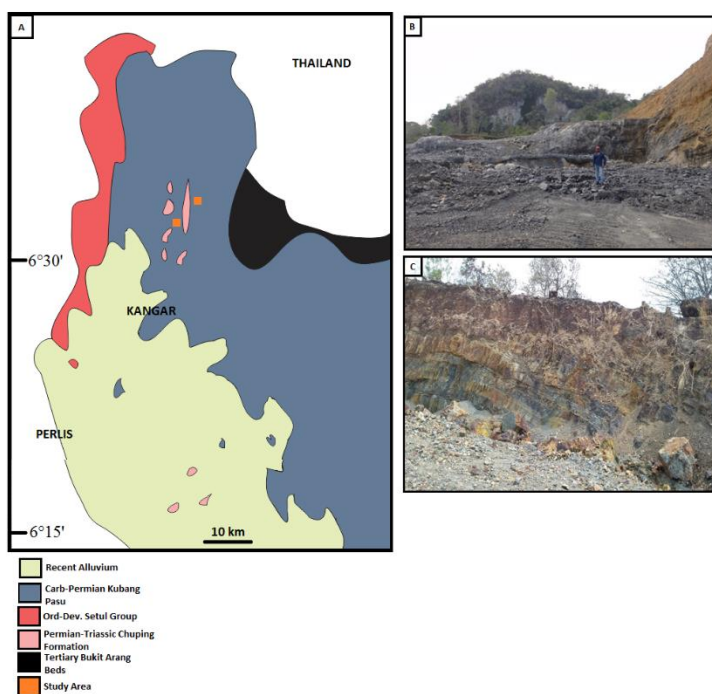


Figure 1. Study area. (A) General Geological Map. (B) Bukit Chondong outcrop. (C) Kampung Guar Jentik outcrop

Shale samples have been taken from two small hills in the Beseri area of Perlis: Bukit Chondong ($6^{\circ}33'18.2''\text{N}$ $100^{\circ}12'20.5''\text{E}$) and Kampung Guar Jentik ($6^{\circ}33'08.7''\text{N}$ $100^{\circ}14'10.4''\text{E}$) (Fig. 1-2). The uppermost Kubang Pasu Formation is exposed at both hills, where they are conformably overlain by the Chuping Formation. Bukit Chondong hill is located in Kampung Padang Malau and in Kampung Guar Jentik, the best exposure has been found in hilly ridge known as Sanai Hill. The age of the basal unit of the Kubang Pasu Formation is Early Carboniferous (Tournaisian--Visean) [6]. The basal unit of the Kubang Pasu Formation is represented by a thick unit of blackish grey-red shale interbedded with sandstone.

In this study shale sample has been collected from the basal unit of Kubang Pasu formation.

3. Samples and methods

In Kubang Pasu formation, ten shale samples were collected by using method mentioned in [7]. Two shale samples (KP-1&2) have been taken from Kampung Guar Jentik and eight samples (KP-3 to 10) from Bukit Chondong. All samples were ensured that weathered exposures are removed by eliminating the surface material. The rock samples were all air dried to remove any moisture present in the sample. In Kampung Guar Jentik, the colors of shale are varying from medium light gray to dark. While in Bukit Chondong shales are mostly medium gray. All of the ten samples were crushed into fine grains (2mm). Coning and

quartering sub-sampling method were used to homogenize all of the sample following the procedure outlined by Gerlach and Dobb [8]. Sub-sampling method reduces biased result and increase the accuracy of the data [9]. Furthermore, duplication of all analysis is done and less than 3% percentage of error has been achieved.

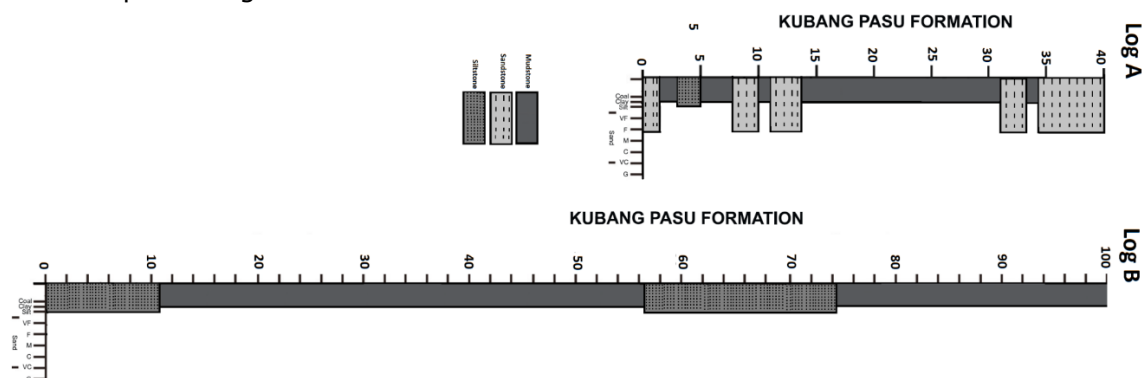


Figure 2. Logged stratigraphic sections of the Kubang Pasu Formation. Log A: Kampung Guar Jentik outcrop. Log B: Bukit Chondong outcrop

3.1. Fourier transform infrared spectroscopy (FTIR)

Infrared measurements were made using a Cary 660 Series FTIR Spectrometer equipped with PIKE MIRACLE diamond attenuated total reflectance spectroscopy (ATR). Data collection was done using the Resolutions Pro software package which was also used for background and automatic baseline correction of all spectra. Spectra were acquired and converted to absorbance mode from 16 coded scans between 4000 and 400 cm^{-1} at a resolution of 4 cm^{-1} , then area normalized prior to further analysis. The limit of detection of the instrument is 0.08%. Background scans were collected using the same settings as the sample analyses. Replicate spectra collected on selected samples showed consistent peak positions and absorbance intensities. The area percentage of hydrocarbon functional groups was calculated by summing the absorbance intensities between the respected wavelength [10-11].

3.2. Total Organic Carbon Analysis

The total carbon test was used to measure the total organic carbon content in the samples. It is the relative dry weight percentage of organic carbon in the sediments [12]. In this study, 1.0g of each powdered samples were measured and placed in beakers. The samples were acidified with 10ml of hydrochloric acid of 37% concentration to remove inorganic carbon fraction from the samples. They were then left for 12 hours in the fume chamber before being rinsed with reverse osmosis water for 3 times and dried in the oven at 60°C for 24 hours. After drying, 60mg of each sample were being weight and placed on ceramic boats. Percentage of organic carbon was measured using multi n/c 3100. The measurements were run in duplicate, and the results were averaged.

3.3. Ultraviolet-visible (UV-Vis) spectroscopy

In this study E4 (465nm) and E6 (665nm) were the primary focus to determine the aromaticity of the samples based on E4/E6 ratio. For extraction of humic substance the U.S. EPA method 3550 was optimized using ultrasonic extraction with Methanol as solvent. In a glass flask with cap, 2 g was weighed of each shale sample. The samples were then submitted to three consecutive extractions with 8mL of Methanol each time, by 3 minutes of ultrasonic stirring (Thornton Unique 1450USC ultrasonic cleaner) and 5 minutes of centrifugation at 2500 rpm (Janetzki T23 centrifuge). The UV-VIS technique analysis of the Methanol extract solution was performed using Perkinelmer lambda 750 UV Vis Spectrophotometer with the liquid samples placed in quartz cells. The scanning wavelength range was 200–800 nm.

3.4. Petrography

Petrographic analysis of the samples were obtained from thin sections prepared in Quality thin sections (QTS), USA. Plane and cross transmitted light optical photomicrographs with a spatial resolution of 500 μm were taken of all thin sections using a LEICA DM 750P attached with a LEICA MC170 HD camera at Universiti Teknologi PETRONAS.

4. Results

4.1. Fourier transform infrared spectroscopy (FTIR)

The FTIR analysis was conducted to characterize the functional groups in the shale. The FTIR spectra of different shale exhibited similar absorption bands and characteristic absorption peaks, based on the vibration of the atoms in a molecule and the spectrum obtained depends on what fraction of the incident radiation is absorbed at a particular energy as shown in Table 1 and Figure 3 [13-14]. Compared to the FTIR spectrum of coal, shale's spectrum normally shows much weaker vibrational bands of aliphatic C-H at 3000–2800 cm^{-1} , but features strong IR absorbance from aromatics at 600-1250 cm^{-1} (Fig. 3).

Table 1. Functional groups identified through FTIR spectra of the shale in the Kubang Pasu formation.

Samples	Aromatic C=C stretching 1430-1650 Absorbance	Alkane APH 720 C-H bending Absorbance	Aromatic bending 1275-1000 In-plane C-H bending Absorbance	Aromatic bending 900-690 Out-of-plane C-H bending Absorbance	Alkyne APH 700-600 =C-H bending Absorbance	-OH Stretching 3600-3000 Absorbance
KP-1	0.03	0.05	0.58	0.17		0.05
KP-2	0.03		0.67	0.18		0.01
KP-3			0.55	0.13	0.10	0.01
KP-4			0.52	0.13	0.10	0.02
KP-5			0.55	0.22	0.06	0.01
KP-6			0.52	0.19	0.07	0.01
KP-7			0.44	0.20	0.09	0.02
KP-8	0.01	0.06	0.41	0.09	0.05	0.02
KP-9	0.01	0.07	0.46	0.74	0.06	0.05
KP-10	0.01	0.11	0.58	0.13	0.09	0.05

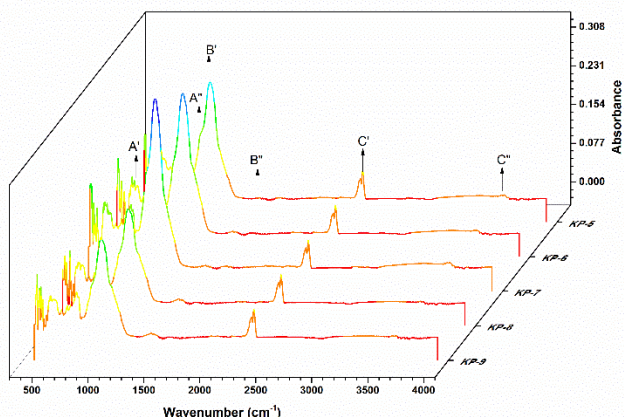


Figure 3. FTIR spectra of few shale samples (from the KP formations) in the frequency interval 4000-400 cm^{-1} showing the Aromatic bending OPCH (represented by the arrows A' and A'' at approximately 694 and 827 cm^{-1} respectively), Aromatic bending OPCH (represented by the arrows B' and B'' at approximately 1001 and 1429 cm^{-1} respectively), ATR Diamond (represented by the arrows C') and -OH Stretching bands (represented by the arrows C'' at approximately 3623)

The FTIR spectra of the shale samples can be divided into three zones, -OH groups stretching vibration, Alkyne C-H bending bands and Alkane C-H bending band in Aliphatic hydrocarbons and absorption spectrum of Aromatic C=C stretching and Aromatic out of plane

C–H bending. Strong intensity peak of free OH-compounds are detected in the region of 3700–3200 cm^{-1} [12,15-16] and seen in all the samples of the KP formation.

4.2. Total Organic Carbon (TOC)

From the Table 2, it is shown that all shale from the KP formation has low total organic carbon. The measured concentration of total organic carbon content in the shale ranged from 0.36% to 1.42%. KP-4 and KP-5 have the highest TOC content compare to other sample. Moreover, shale sample which has been taken from Bukit Chondong outcrop hill have higher total organic carbon content as compared to Kampung Guar Jentik outcrop.

Table 2. TOC results of shale from Kubang Pasu formation

Sample	A	B	Average	Error %
KP-1	0.365	0.354	0.3595	1.529903
KP-2	0.36	0.34	0.35	2.857143
KP-3	0.856	0.811	0.8335	2.69946
KP-4	0.893	0.878	0.8855	0.846979
KP-5	1.62	1.59	1.605	0.934579
KP-6	0.475	0.45	0.4625	2.702703
KP-7	0.869	0.838	0.8535	1.816052
KP-8	0.544	0.537	0.5405	0.647549
KP-9	0.49	0.46	0.475	3.157895
KP-10	0.54	0.51	0.525	2.857143

4.3 Ultraviolet-Visible spectroscopy

Ultraviolet-Visible spectroscopy, already used to quantify and to evaluate the quality of humic substances [11]. Ultraviolet-visible spectroscopy is a rapid and well known used method for the estimation of humic substance in shale. The light absorption of humic substances seems to rise with an increase of degree of condensation of the aromatic rings that these substances contain, total C content, molecular weight and in the ratio of C in aromatic ring to C in aliphatic side chains.

The value of E4 and E6 that are treated with methanol are range from 0.014 to 1.56 and 0.013-1.447 respectively (Table 3). Almost equal values of E4 and E6 also indicate the presence of humic acid in Kubang Pasu formation which indicates that shale have a strong possibility of terrestrial origin (Table 4).

Table 3. UV-Vis results of nine samples of shale from Kubang Pasu formation treated with methanol

Sample	Absorbance At (Methanol) $\lambda = 465 \text{ nm}$ (E4)				Absorbance At (Methanol) $\lambda = 665 \text{ nm}$ (E6)			
	E4(A)	E4(B)	Average	Percentage Error (%)	E6(A)	E6(B)	Average	Percentage Error (%)
KPP-1	1.5766	1.5450	1.5608	1.0123	1.4745	1.4200	1.4473	1.8829
KPP-2	0.1195	0.1168	0.1182	1.1426	0.1163	0.1139	0.1151	1.0426
KPP-3	0.3398	0.3273	0.3336	1.8738	0.2506	0.2449	0.2478	1.1504
KPP-4	0.8604	0.8329	0.8467	1.6240	0.7338	0.7100	0.7219	1.6484
KPP-5	0.0260	0.0250	0.0255	1.9608	0.0149	0.0145	0.0147	1.3605
KPP-6	0.0251	0.0246	0.0249	1.0060	0.0236	0.0229	0.0233	1.5054
KPP-7	0.4682	0.4584	0.4633	1.0576	0.4170	0.4070	0.4120	1.2136
KPP-8	0.0175	0.0169	0.0172	1.7442	0.0159	0.0159	0.0159	0.0943
KPP-9	0.0143	0.0139	0.0141	1.4184	0.0132	0.0131	0.0132	0.2659
KPP-10	0.0159	0.0153	0.0156	1.9231	0.0149	0.0147	0.0148	0.7417

Table 4. E4/E6 ratio of UV-Vis results based on ten samples of shale from Kubang Pasu formation treated with methanol

Sample	E4:E6 (A)	E4:E6 (B)	E4:E6 (Average)
KPP-1	1.0692	1.0880	1.0786
KPP-2	1.0275	1.0255	1.0265
KPP-3	1.3559	1.3365	1.3462
KPP-4	1.1725	1.1731	1.1728
KPP-5	1.7450	1.7241	1.7346
KPP-6	1.0636	1.0742	1.0689
KPP-7	1.1228	1.1263	1.1245
KPP-8	1.0992	1.0636	1.0814
KPP-9	1.0833	1.0586	1.0710
KPP-10	1.0643	1.0394	1.0518

4.4. Petrography

Lithological and sedimentological features of the rock such as stratification, texture, color, grain size and components can be identified by petrography analysis [17]. The petrographic analysis results show that KP shale samples consist mainly of dark to light grey, silty (Fig .4 A-F), micaceous (Fig .4 C, E), Massive (Fig .4 A, F), discontinuous wavy parallel laminated (Fig .4 C, E), brownish massive (Fig .4 A), parallel laminated (Fig. 4 B) and non-calcareous mudstone.

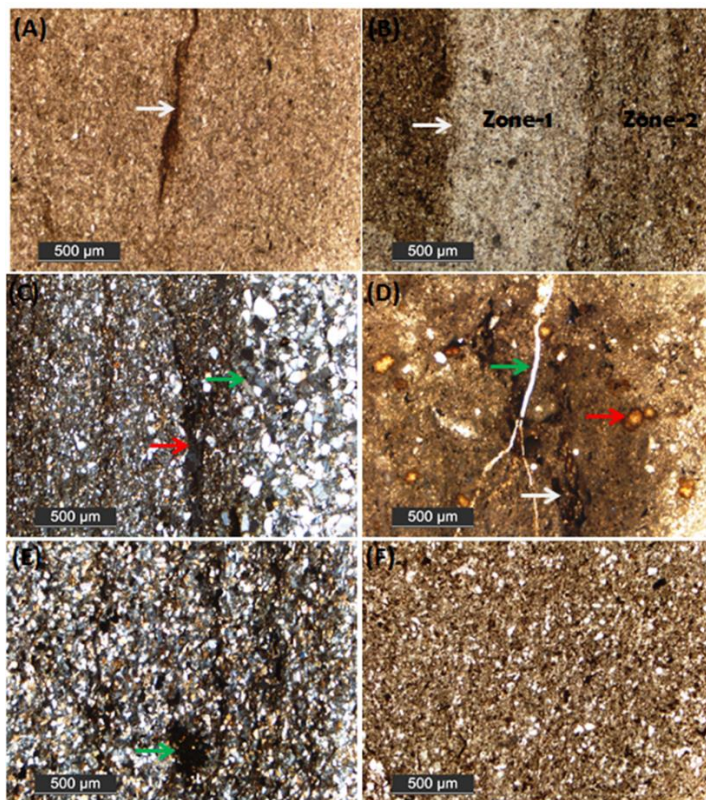


Figure 4. Sedimentologi characteristic of Kubang Pasu shale samples. (A) Brownish, structureless, massive and non-laminated fabric with dominating clay particles. Fissures filled with organic material (white arrow), (B) Thin section of the contact between zones 1 and 2 (white arrow). Zone 1 is dominated by coarser silt particles and zone 2 is dominated by silt and organic rich clay layers, (C) Sharp contact between coarse silt particles and organic rich clay layer (green arrow). Organic material filled in fissures (red arrow) and preferential alignment of mica flakes detected by cross polarized light (D) Abundant fossils fragments (red arrow) and carbonaceous fragment with frayed edge (white arrows). Quartz vein also present (green arrow), (E) Carbonaceous lump in silty shale (green arrow). Wavy-crinkly laminae that contrast with the more planar laminae. Mica flakes also observes parallel to bedding detected by cross polarized light (F) Massive brownish shale with abundant fine to medium size silt particles are present which is surrounded by clay cement

5. Discussions

5.1. Saturated and unsaturated aliphatic hydrocarbon

The C-H stretch vibrations for methyl and methylene are the most characteristic in terms of recognizing the compound as an organic compound. The bending vibrations help to tell more about the basic structure. For example, a band at 725–720 cm^{-1} (methylene rocking vibration) is indicative of a long-chain linear aliphatic structure. Samples 1, 7, 8 and 9 of KP formation contains a band at 720 cm^{-1} which indicates a long-chain compound, and is attributed to crystallinity and a high degree of regularity for the linear backbone structure. The critical region of the infrared spectrum for assessing Alkyne C-H bending bands (unsaturated) in aliphatic hydrocarbon is 600–700 cm^{-1} . Absence of Alkyne C-H bending bands has been observed in shale samples collected from Kampung Guar Jentik.

5.2. Aromatic hydrocarbon

The Aromatic In-plane C–H bending and Aromatic out of plane C–H bending appear in the regions 1275–1000 cm^{-1} and 900–690 cm^{-1} . Aromatic C=C stretching can be observed in 1430–1600 cm^{-1} . Five samples comprises Aromatic C=C stretching. All samples of shale from KP formation contain Aromatic out of plane C–H bending and Aromatic In-plane C–H bending (Table 1).

5.3. TOC and humic acid relationship

Biodegradation of organic matter causes humic substances which are the major components of the natural organic matter in soil and water as well as in geological organic deposits such as lake sediments, peats, brown coals and shales. Humic substances can be subdivided into three major fractions (1) Humin, (2) Humic acid, and (3) Fulvic acids. Humic acids (HAs) comprise a mixture of weak aliphatic (carbon chains) and aromatic (carbon rings). On average 35% of the humic acid (HA) molecules are aromatic (carbon rings), while the remaining components are in the form of aliphatic (carbon chains) molecules. It is suggested that values of the relationship E4/E6 for humic acid is smaller than 5.0 and between 6.0 and 8.0 for fulvic acids [18]. Higher degree of aromaticity of humic acid in shale was evidenced by lower E4/E6 ratio value (1.05–1.73) in Kubang Pasu formation extracted by methanol.

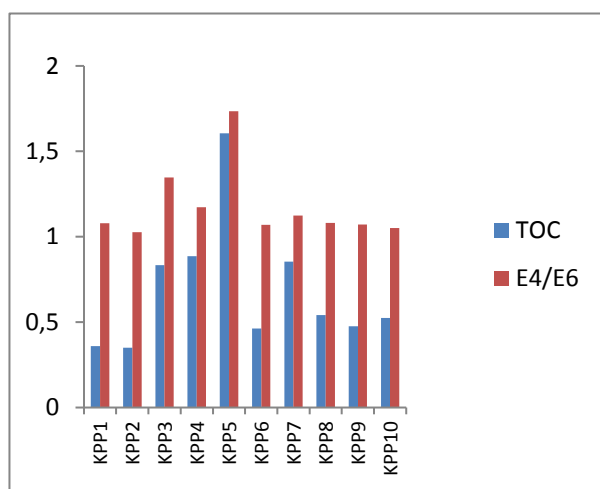


Figure 5. TOC and E4/E6 values in studied shale sample

Preservation and accumulation of organic carbon is different in shale as compared to soil organic carbon. In soils, absorbance of organic carbon increases with increase in the structure of humic substances [19]. However, this phenomenon is not clearly understood in shale. In this study, we proposed that same phenomenon has been observed in studied shale sample of KP formation as by evidence of increase in TOC values with humic substance (Figure 5). This association led us to speculate that, humic substances and organic carbon relationship in is not effected by the grey shale specially with low organic carbon preservation and accumulation conditions.

The performed investigations allowed the formulation of the linear relationship between the humic spectroscopic UV-visible ratio (E4/E6) and total organic carbon concentration. The correlation coefficient calculated for this linear relationship of TOC and E4/E6 is equal to

$R^2=0.873$ (Figure 6). It can be observed that as concentration of organic carbon increases E4/E6 ratio also increases which shows that in the distribution of humic acid in shale, organic carbon may be one of the most important factors.

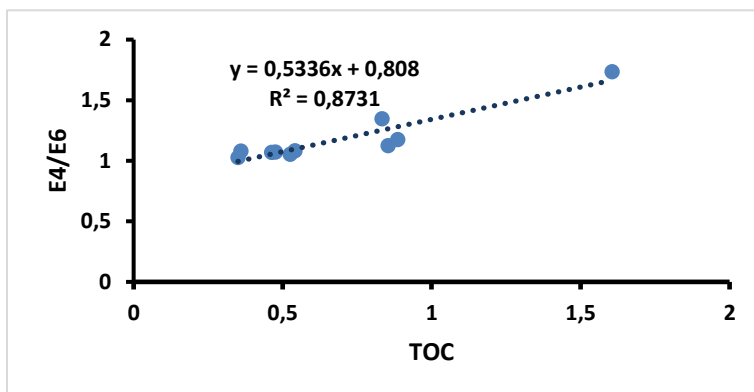


Figure 6. TOC and E4/E6 relationship

6. Conclusion

Three division has been made in FTIR spectra of the shale samples from KP Formation: - OH groups stretching vibration, Alkyne C-H bending bands and Alkane C-H bending band in Aliphatic hydrocarbons and absorption spectrum of Aromatic C=C stretching and Aromatic out of plane C-H bending. Dominance of humic acid and aromatic hydrocarbon by UV-Vis and ATR-FTIR analysis in shale samples indicates possibility the terrestrial origin of deposition. This study also explore that the obtained concentration of TOC in the shale of Kubang Pasu formations shows low values indicating the oxidation of organic matter in both outcrops. Petrographic studies reveal that the studied samples consist mainly of dark to light grey, silty, micaceous, massive, discontinuous wavy parallel laminated, brownish massive, parallel laminated and non-calcareous mudstone. This study also shows the significance of spectroscopic techniques to determine the type of humic substance and their relationship with the total organic carbon in shale. Positive correlation ($r^2=0.873$) between total organic carbons with humic acid suggested that if shale enriched in organic carbon had the more powerful absorption of humic acid and it also indicates that TOC plays an important role in controlling the humic acid level in shale.

Acknowledgment

This work was supported by the PETRONAS Research Fund (PRF) grant awarded to E. Padmanabhan.

References

- [1] Wright MC, and Court RW. A new rapid method for shale oil and shale gas assessment. *Fuel*, 2015; 153: 231–239.
- [2] B Hazra and AK Varma FTIR, XRF, XRD and SEM characteristics of Permian shales, India., *Journal of Natural Gas Science and Engineering*, 2016; 32: 239-255.
- [3] Scheinmann F. An introduction to spectroscopic methods for the identification of organic compounds: Mass spectrometry, ultraviolet spectroscopy, electron spin resonance spectroscopy, nuclear magnetic resonance spectroscopy (recent developments), use of various spectral methods together, and documentation of molecular spectra. 2013: Elsevier.
- [4] Chen Y and Zou C. Applications of Micro-Fourier Transform Infrared Spectroscopy (FTIR) in the Geological Sciences—A Review. *Int. J. Mol. Sci.* 2015; 16: 30223–30250.
- [5] Eglinton G. Applications of Infrared Spectroscopy to Organic Chemistry. An Introduction to Spectroscopic Methods for the Identification of Organic Compounds. Volume 2.
- [6] Yang G.-P. Polycyclic aromatic hydrocarbons in the sediments of the South China Sea. *Environmental Pollution*, 2000; 108(2): 163-171.

- [7] Hassan MHA, Aung A-K, Becker RT, Rahman NAA, Ng TF, Ghani AA, Shuib MK. Stratigraphy and palaeoenvironmental evolution of the mid- to upper Palaeozoic succession in Northwest Peninsular Malaysia. *Journal of Asian Earth Sciences*, 2014; 83: 60-79.
- [8] Coe AL. *Geological Field Techniques*. 2010: John Wiley & Sons.
- [9] Gerlach RW, Dobb DE, Raab GA, Nocerino JM. Gy sampling theory in environmental studies. 1. Assessing soil splitting protocols. *Journal of Chemometrics*, 2002;16(7): 321-328.
- [10] Washburn KE and Birdwell JE. Multivariate analysis of ATR-FTIR spectra for assessment of oil shale organic geochemical properties. *Organic Geochemistry*, 213; 63: 1-7
- [11] Mahmoodi I, Padmanabhan E. Exploring the relationship between hydrocarbons with total carbon and organic carbon in black shale from Perak, Malaysia. *Pet Coal*, 2017; 59(6): 933-943
- [12] Song H, Liu G, Zhang J, Wu J. Pyrolysis characteristics and kinetics of low rank coals by TG-FTIR method. *Fuel Processing Technology*, 2017; 156: 454-460.
- [13] Stuart B. *Modern Infrared Spectroscopy*, 1996.
- [14] Coates J. Interpretation of Infrared Spectra, A Practical Approach, in *Encyclopedia of Analytical Chemistry*. 2006, John Wiley & Sons, Ltd.
- [15] Zodrow EL, Mastalerz M, Werner-Zwanziger U, D'Angelo JA. Medullosalean fusain trunk from the roof rocks of a coal seam: Insight from FTIR and NMR (Pennsylvanian Sydney Coalfield, Canada). *International Journal of Coal Geology*, 2010; 82(1-2): 116-124.
- [16] Mahmoodi SMI and Padmanabhan E. Hydrocarbon Bond Variation in Some Shales from Batu Gajah, Malaysia, in *ICIPEG 2016: Proceedings of the International Conference on Integrated Petroleum Engineering and Geosciences*, M. Awang, et al., Editors. 2017, Springer Singapore: Singapore. p. 363-371.
- [17] MO. Abouelresha An integrated characterization of the porosity in Qusaiba Shale, Saudi Arabia. *Journal of Petroleum Science and Engineering* 149 (2017) 75–87.
- [18] Cunha T. Spectroscopy Characterization of Humic Acids Isolated from Amazonian Dark Earth Soils (Terra Preta De Índio), in *Amazonian Dark Earths: Wim Sombroek's Vision*, W.I. Woods, et al., Editors. 2009, Springer Netherlands: Dordrecht. p. 363-372.
- [19] Schnitzer M. Soil organic matter—the next 75 years. *Soil Science*, 1991. 151(1): p. 41-58.

To whom correspondence should be addressed: Syed Muhammad Ibad, Department of Geosciences, Faculty of Geoscience and Petroleum Engineering, Universiti Teknologi PETRONAS, Bandar Seri Iskandar, 31750 Tronoh, Perak, Malaysia, s.muhammadibad@gmail.com

PORE STRUCTURE CHARACTERIZATION OF A LOW PERMEABILITY RESERVOIR USING NUCLEAR MAGNETIC RESONANCE, NITROGEN ADSORPTION AND MERCURY INTRUSION CAPILLARY PRESSURE

Bello Lawal Toro^{1}, Zhiping Li¹, Caspar Daniel Adenutsi¹, Samira Mohammed Abdullahi²*

¹ School of Energy Resources, China University of Geosciences, Beijing, 100083, P.R. China Beijing Key Laboratory of Unconventional Natural Gas Geology Evaluation and Development Engineering, Beijing, 100083, P.R. China

² Walden University 100 Washington Avenue South Minneapolis, Minnesota 55401

Received September 18, 2017; Accepted December 1, 2017

Abstract

Low permeability core is analyzed using a combination of Nuclear magnetic resonance, Nitrogen adsorption, and Mercury injection capillary pressure. The material's surface area and pore size distributions were determined using Brunauer-Emmett-Teller and Barrett-Joyner-Halenda methods, respectively. Results indicate pores in the 2~ 10nm size ranges have a high percentage. The core displayed high irreducible saturation due to the volume of small pores. Mesopore of type V was identified from study carried out. Capillary pressure correlation between nuclear magnetic resonance and mercury injection show good agreement, however discrepancy in total pore volume was observed.

Keywords: Low permeability; Pore size distribution; Nuclear Magnetic Resonance; Nitrogen Adsorption; Mercury Injection Capillary Pressure.

1. Introduction

One of the major challenges engineers face in the development of Oil and gas fields is the characterization of the reservoir. Detailed knowledge of the field translates to a successful recovery operation therefore, reservoir characterization is very vital in enhancing the remaining untapped hydrocarbons in a formation. It helps to identify those crucial elements of the formation which sometimes operate unpredictably. Such elements include the porosity, permeability and relative permeability, pore size distribution and other major factors that will influence production. In essence reservoir characterization is critical in building an integrated reservoir model for conducting a suitable performance analysis and ultimate recovery calculations.

The pore structure characterization refers to the geometry, distribution, size, porosity, specific surface area and characteristics of rock pore. These parameters are crucial in modeling geophysical and petrophysical behavior of any porous media. Recently, more advanced techniques are developed to determine the pore structures characterization. Chalmers *et al.* [1], Curtis *et al.*, [2]; Milliken *et al.*, [3] characterized mudrocks with advanced imaging techniques which reveals a nanometer-scale pore structure within their inorganic and organic components. One limitation to that is the analysis can only provide visual image of the mudrock's porosity but pore-structure profile cannot be obtained directly. Another limitation to that is pores smaller than 5nm cannot be obtained therefore a portion of the pore structure cannot be investigated [4].

Pore characterization is normally estimated by nuclear magnetic resonance (NMR), mercury intrusion capillary pressure (MICP) or nitrogen adsorption-desorption method (N₂). Consequently, the pore size distribution can be used to examine the fluid flow characteristics of reservoir rocks.

Most researchers use either one or two methods to analyze and characterize the results. Such as Shimokawara *et al.* [5] characterized the pore size distribution by mercury injection

and NMR T_2 relaxation time distribution; Jamal Hassan [6] used the nitrogen adsorption-desorption and NMR technique, to determine the pore size distribution of nano-silica material MCM-41; Sørland *et al.*, [7] used the NMR technique to determine the pore size distribution of core samples. In this study a combination of the three methods to characterize a low permeability rock.

2. Methodology

For the purpose of this entire study, sample of a core was collected for a low permeability reservoir. The sample is in a cylindrical shape. Prior to the NMR experiment the sample was fully saturated in brine for 48 hours under a pressure of 30 MPa. The high pressure was selected because of the very low permeability nature of the sample

2.1. Nuclear magnetic resonance (NMR)

The NMR laboratory measurement was performed using a SPEC PMR machine. The machine operates at a resonance frequency of 21.89 MHz. The measurement was done at echo numbers of 1024 and environment temperature of 32°C. Other parameters are scanning numbers of 64; waiting time is 1s and echo spacing of 1ms. The brine saturated sample was wrapped in a plastic wrap and placed in the machine for the test. In NMR analysis test, samples are scanned when fully saturated with a fluid. This will give the pore size distribution of the sample represented by T_2 . NMR tools are also used to determine the petrophysical properties of reservoir rocks such as permeability, porosity, irreducible water saturation etc. This is a fast and non destructive technique that analyzes the chemical and physical properties of a material. Normally, the relaxation rate $1/T_2$ is proportional to the surface to volume ratio of the pore space and the surface relaxivity in a porous system given in equation 1.

$$\frac{1}{T_2} = \rho_2 \left(\frac{S}{V} \right) \quad (1)$$

where the relaxation rate $1/T_2$ is in 1/ms, surface to volume S/V is in $(1/\mu\text{m})$ and the surface relaxivity ρ_2 is in $(\mu\text{m/s})$.

2.2. Mercury injection capillary pressure

Before the mercury injection experiment was carried out, the sample was dried in an oven for 48 hours, at 110°C to remove all brine from the interconnected pores. Mercury injection test was performed by Quantachrome Poremaster automatic pore size analyzer. The sample was weighed and placed into a penetrometer and loaded into the pressure chamber of the machine. The equipment is capable of injecting mercury through the penetrometer into a dried core plug or cut sample with incrementally increasing the pressure up to 33,000psi (227MPa). The volume of the injected mercury at each pressure increment is recorded until the maximum pore volume mercury saturation is achieved. The pressure is plotted against incremental mercury saturation to achieve a drainage curve. This process can be reversed to generate a non-wetting phase imbibitions curve. Mercury porosimetry is based on the capillary law governing liquid penetration into small pores. Capillary forces in the reservoir and seal are functions of surface and interfacial liquid tensions, pore-throat size and shape, and the wetting properties of the rock. The pore throat radius can be determined by Washburn equation:

$$r = \frac{2\sigma\cos\theta}{P_c} \quad (2)$$

where r is the pore throat radius; θ is the contact angle; σ is the interfacial tension (dynes/cm) and P_c is the capillary pressure.

2.3. Nitrogen adsorption/desorption method

The machine used in the study is a specific surface and pore size analysis instrument, manufactured by Beishide instrument technology Beijing Co. Ltd. This instrument works upon the principle of physical adsorption and has provision to use a few gases, viz. nitrogen, argon, krypton, as adsorbate on various adsorbents.

The experiment was conducted using the same core that was used in the NMR and MICP experiment. The sample was dried in an oven at 110°C for 48 hours. The sample was then

crushed using minimal energy to pass through a sieve. Approximately 4g of the material was used for the test. This is based on the methodology proposed by McCarty [9] because it is effective in producing mineralogically and chemically homogenous splits. Prior to the start of the adsorption process, the sample was degassed under vacuum to remove any unwanted vapors and gases adsorbed on the sample surface. The temperature for degassing was set to 200°C.

3. Results

3.1. NMR

NMR tools provide information on the amount of fluids present in cores, and also the size of pores that are filled with the fluids. This is one of the features that distinguish it from other logging devices. The NMR pore size distribution for the core sample is shown in figure 1. The result of the T_2 spectrum shows a bi-modal distribution showing the T_2 distribution of all pores in the core sample representing the pore size distribution. The population is situated around 1.86ms. The NMR spectrum clearly shows one peak much larger in space and amplitude. The area covered by the larger peak is the BVI (Bulk volume immoveable) with a massive proportion of about 82% of Irreducible water saturation (Swirr) leaving a low proportion for Free fluid index (FFI). This indicates that there are poor pore size distributions within the core.

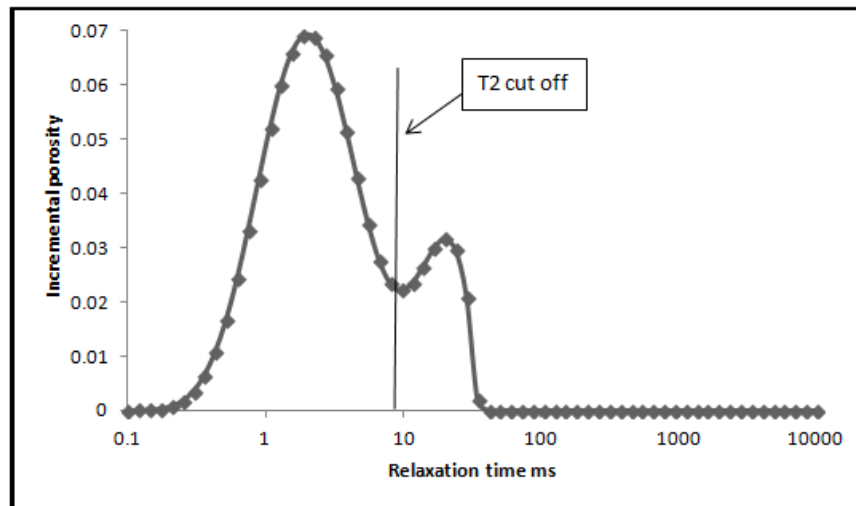


Figure 1. NMR spectrum for sample

The NMR test was able to measure and identify the fully saturated and bound fluid. Results show that the core consists of large proportion of micropore body which is typical of low permeability reservoirs. The spectrum reveals that large proportion of the total volume consist of small pores characterized by small matrix grains. This will cause high irreducible water saturation (Swirr) in the formation. In order to improve the reliability of the formation, it is imperative to measure the Swirr. Determining Swirr on the NMR spectrum requires a T_2 cutoff mark to be identified. The T_2 cutoff mark will define the proportion of Bulk Volume Irreducible (BVI), and Bulk Volume Moveable (BVM) this is also known as Free Fluid Index (FFI). The standard T_2 cutoff for sandstone reservoirs is 22ms [10]. In low permeability sandstones and shale gas fields, the T_2 cutoff mark is around 10msec. The traditional clay bound cut value of 2.5msec are typically too low as well. A value around 1ms is more representative for these types of rocks [11]. This is a common method for determining the Swirr from the NMR by identifying the T_2 cutoff on the log [12].

3.1.1. Estimating permeability from NMR logs

Different empirical equations are suggested for estimating permeability of a porous media using NMR. Many authors presented works on estimation of permeability from NMR [13-16]. However, Coates model [17] is the most widely used. This model can be applied on formations containing water and/or hydrocarbons. The Coates model is used in computing permeability [14]:

$$K = \left[\left(\frac{\phi}{C} \right)^2 \left(\frac{FFI}{BVI} \right) \right]^2 \quad (3)$$

where, k = permeability; with ϕ for total porosity (%); C=10 or can be determined from laboratory measurements on cores; FFI= the free fluid index and BVI = the bulk volume of irreducible water.

Rezaee *et al.* [18] did a study on some cores and came up with a new correlation for estimating permeability. They proposed that using NMR T₂ dominant peak or T₂ peak and multi-regression analysis, permeability can be estimated with high accuracy. The multi-regression analysis resulted in the following equation for permeability estimation using T₂ peak and porosity:

$$K = -0.0461 - 0.0601T_{2peak} + 4.37\phi \quad (4)$$

where k is permeability (mD), T_{2peak} is dominant T₂ on the T₂ spectrum (ms), and ϕ is porosity (fraction). Using this equation, permeability was estimated to be 0.2mD.

3.1.2. Estimating pseudo-capillary pressure curves using NMR logs

Research has been and it is still carried out on how to manipulate the NMR spectrum to determine the properties of hydrocarbon formation and give a proper evaluation. Volokitin *et al.* [19] was among the pioneers of researching how to convert NMR spectrum to pseudo-capillary pressure curve. Later on so many research was carried out on using the logs to derive the pseudo Pc curve [20-23]. Volokitin *et al.* [19] method is commonly used in the characterizing the pore structure. However, Liang Xiao *et al.* [23] carried out test using the same method and discovered that the method is not applicable on the formation in China and tight sandstone reservoirs. They also stated that the conventional linear function proposed cannot be used adequately to predict Pc curves from NMR logs. They proposed a whole new method based on formation classification in their research named Classified Piecewise Power Function (CPPF). In their research the NMR reverse cumulative curves was used to construct the PC curves (Details of the procedure is explained in their paper). The capillary pressure using NMR reverse cumulative curve is calculated as proposed by Liang Xiao *et al.* [23] using the CPPF method. The curve is correlated to that of MICP for validation as illustrated in figure 2b. Good agreement was obtained from the capillary pressure measured from the two methods. This further shows a good relationship between the two experimental methods.

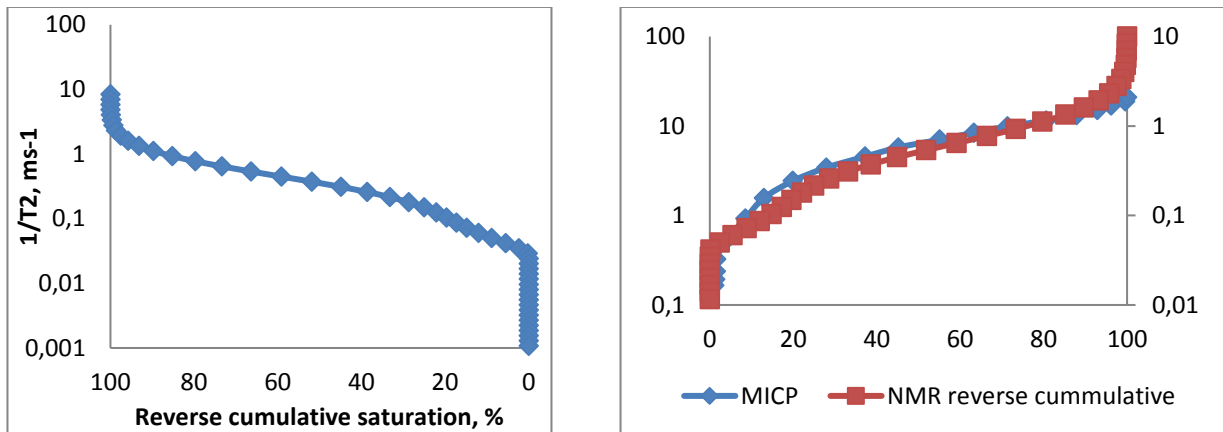


Figure 2. (a) NMR reverse cumulative curve

(b) Pc curve comparison between MICP and NMR

3.2 MICP

Mercury was injected at a high pressure of 10,000psi on the sample. Drainage capillary pressure and pore throat distribution were produced as shown in figure 3. Due to the low permeability nature of the core, the capillary pressure is high. The minimum pressure (P_d), also known as the displacement pressure, the threshold pressure is determined by the size of the largest pores connected to the surface of the medium [24]. In this case the entry pressure is 0.52mPa. The inflection point corresponds to 9.19 mPa at 8.52 saturation of mercury. The Washburn equation (Equation 2) was used to convert capillary pressure into estimated throat radius. Pore throat distribution curve (figure 3b) suggest significant pore volume in micro pores with a bi modal PSD for the sample. Dan J. Hartman and Edward A. Beaumont [25] classified pore sizes as nanopores < 0.1 μm , micropores 0.1-0.5 μm , mesopores 0.5-2 μm , macropores 2-10 μm and megapores > 10 μm . Majority of the pore throat sizes fall between 0.1-1 μm indicating that the core falls within the range of micropores and mesopores. It should be noted that mercury injection experiments doesn't measure all pore throats but only throat accessible to the mercury.

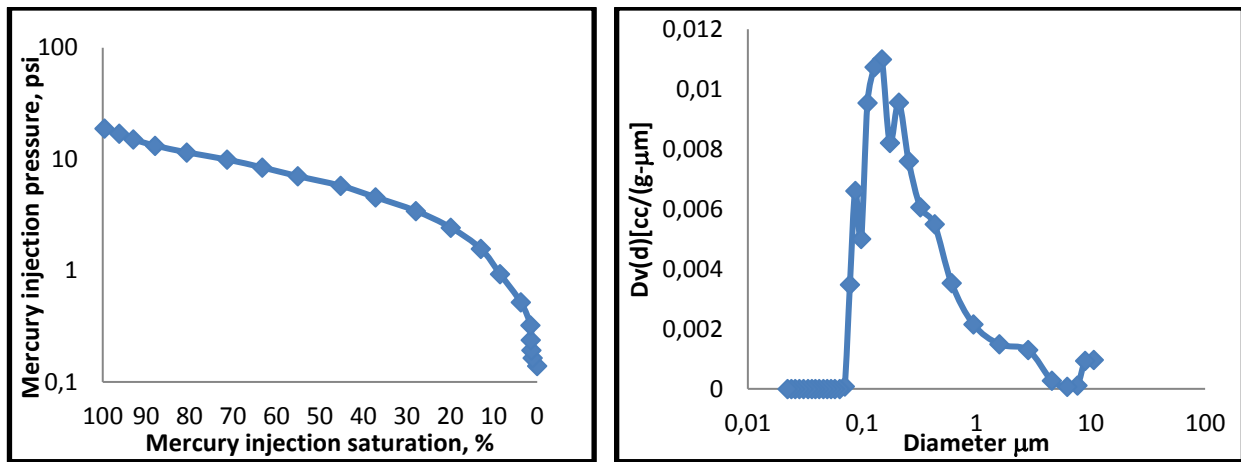


Figure 3. (a) Capillary pressure curve

(b) Pore throat distribution

3.2.1. Relative permeability

Relative permeability is of central importance to soil science, petroleum engineering, and many other industries but may be difficult to measure in some cases. Such cases include extremely low permeability rocks and special fluid systems in which there are phase transformation and mass transfer between the two phases as pressure changes [26]. There are different studies done on computing relative permeability from capillary pressure to [27-30]. Brooks and Corey's model for calculating relative permeability is a method widely used for calculating relative permeability. Brooks and Corey [31] modified Corey's capillary pressure model (equation (5)) and presented a new capillary pressure function model based on evaluations from several drainage capillary pressure curves from consolidated porous media as follows:

$$P_c = P_e (S_w^*)^{-\frac{1}{\lambda}} \tag{4}$$

where: λ pore size distribution index; P_e = entry capillary pressure; P_c = capillary pressure as a function of S_w .

Finally, they derived equation (6) and equation (7) to calculate the true relative permeability curve for the wetting and non-wetting phase.

$$K_{rw} = (S_w^*)^{\frac{2+3\lambda}{\lambda}} \tag{5}$$

$$K_{rnw} = (1 - S_w^*)^2 \left[1 - (S_w^*)^{\frac{2+\lambda}{\lambda}} \right] \tag{6}$$

where: K_{rw} is the relative permeability of the wetting phase; K_{rnw} is the non-wetting phase relative permeability at the irreducible wetting phase saturation; S_w^* is the normalized wetting phase saturation, which could be expressed as follows:

$$S_w^* = \frac{S_w - S_{wi}}{1 - S_{wi}} \quad (7)$$

where: S_{wi} is the irreducible wetting phase saturation.

In this study the Brooks and Corey [31] relative permeability model is used to calculate relative permeability from the capillary pressure data and the result is presented in figure 4.

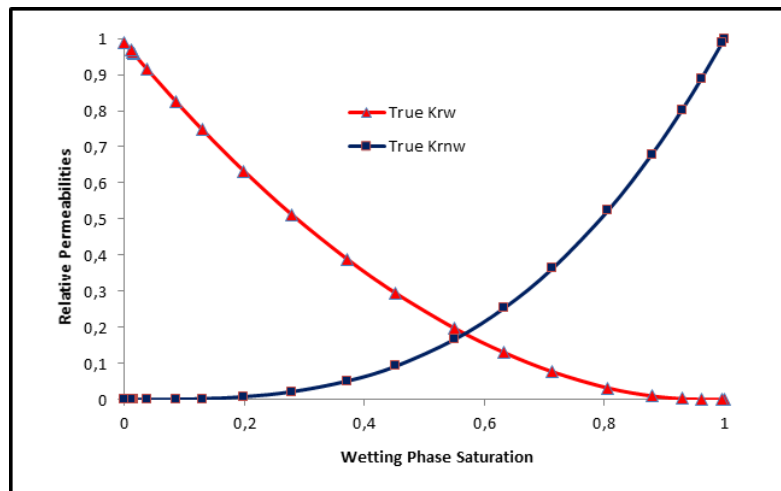


Figure 4. Relative permeability curves

3.3. Nitrogen adsorption/desorption method

The BET (Brunauer, Emmet and Teller) method was used to calculate the surface area of the samples. This technique is universally employed for determining surface area of porous materials because of its simplicity, its definitiveness and its ability to accommodate each of the five isotherm types [32].

Isotherm is the first significant information that is obtained from a physisorption experiment about surface area and porosity of porous materials. During the BET test, there is capillary condensation of liquid nitrogen around the pores and computation of the amount of nitrogen absorbed at a given relative pressure of the sorption isotherm.

The adsorption and desorption isotherms for the sample is shown on figure 5. During the adsorption isotherm process, the monolayer adsorption is formed at low relative pressure. At high relative pressure, the adsorption in mesopores will cause the multilayer formation until the capillary condensation occurs. As the relative pressure starts to increase there's gradual increase of adsorption as well. With the increase in relative pressure the pores are filled with nitrogen and condense. This causes the diameter of the pore filled with the nitrogen to increase gradually. The results shows the adsorption/desorption curves are smooth and give a good hysteresis showing a capillary condensation transition. Based on the IUPAC classification of sorption isotherms by Brunauer, Demming, Deming, and Teller (BDDT), the curves suggest that of type V. The curves show pore condensation and hysteresis which closes at relative pressure of 0.4-0.45 P/Po. As relative pressure reaches 0.98, the core sample absorbed the highest volume of N₂ of 4.36ml/g. The surface area is 1.080m²/g. The curves indicate weak attractive interactions between the adsorbate and adsorbent.

The BJH (Barret, Joyner and Halenda) method was used to determine the pore size distribution of the samples. This method of calculating pore size distribution is from the experimental isotherms using the Kelvin model of pore filling. The BJH computation method starts from higher pressures, hence larger pore sizes, with lower pressures (smaller pore sizes)

in the later steps. Figures 6 show the curves of the pore size distribution in the process of the BJH adsorption and desorption. According to the pore size distribution curves of the BJH, the pores are mainly distributed and centered between 2-10nm. Therefore, according to the classification of pores by the International Union of Pure and Applied Chemistry (IUPAC), the samples are classified as mesopores. The total pore volume determined by BJH is 0.0068 ml/g.

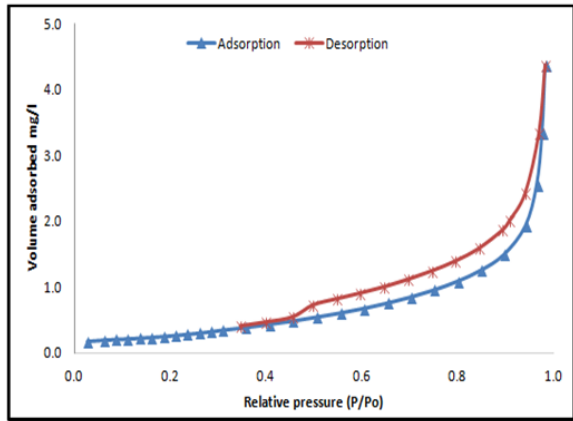


Fig. 5. Adsorption/desorption isotherm for sample

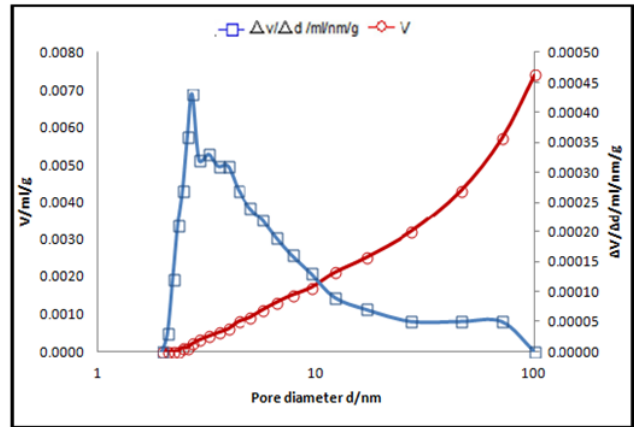


Fig. 6. BJH pore size distribution for sample

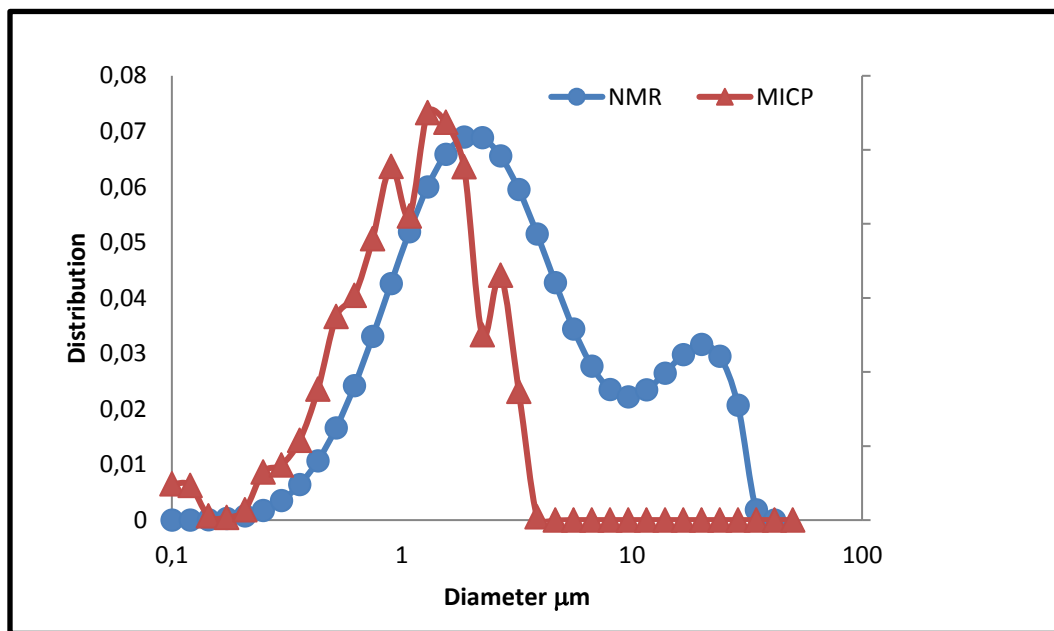


Figure 7. PSD correlations between NMR and MICP

4. Discussion

MICP has a limited disadvantage compared to the N_2 . Its pore diameter range is from 3nm and above, while that of N_2 has the ability to measure pores that are less. However, the MICP covers higher range pore diameters measurement compared to N_2 . For materials containing large pores, the MICP is a preferred technique. Due to its high pressure ability, it is suitable for core of high, medium and low permeability. However, in most cases the mercury injection pressure is not high enough to access small pores. Estimating pore diameters greater than 350nm are rarely used from the gas sorption method. The operational procedures for MICP and N_2 is different while the former first measures larger pores at intrusion phase and the latter first measure smallest pores at the adsorption phase. Surface area of the sample

estimated by MICP is lower than the N_2 . According to Milburn and Davis [33] correlation between surface area obtained from MICP and N_2 is poor if the samples have low surface area. The combination of these three methods for pore characterization is an effective way for understanding the petrophysical properties of the low permeability reservoirs.

Pore size distribution for NMR and MICP are correlated and shown in figure 7. There is a fair agreement between the spectrums. When the PSD curves are fitted, they overlay the distribution with a matching peak. They also show a similar distribution. Experimental work on NMR is much faster than the other methods followed by MICP. Total pore volume calculated by NMR is a bit higher than that measured by N_2 . This may be due to the reason that NMR measures both dead end pores with only one entry to the main pore channel and the interconnected pores that support the flow of fluids.

5. Conclusion

In this study pore structure characterization of a low permeability core was reviewed using Nuclear Magnetic Resonance (NMR), Mercury injection capillary pressure (MICP), and Nitrogen adsorption (N_2).

Results for the permeability, total pore volume, surface area, were obtained. Pore throat distribution using MICP indicate dominant of the pores lie within 0.1-1 μ m making them fall within the micro and mesopore range. Capillary pressure curve of MICP and NMR was correlated and show good agreement. However, there was discrepancy of Total pore volume between NMR and N_2 . Type V mesopore of IUPAC classification of sorption isotherm was identified using the N_2 adsorption method.

Relative permeability was obtained using Brooks and Corey method. Ideally, low permeability cores should have low flow rates. By applying low flow rates to the core, some difficulties are likely to occur like low pressure changes which are intricate to measure and long duration of experiments which in some cases might take days. Therefore using the Brooks Corey method will be less time consuming and less complex.

Acknowledgement

The research was supported by Beijing Municipal Natural Science Foundation (grant number: 3162026). The authors wish to express their sincere appreciation to Dr. Xiao Liang for his guidance and contributions. We would also like to thank Xu Zhi Chao (Jerry) for his assistance in the lab. The authors also thank the reviewers of the manuscript.

Reference

- [1] Chalmers, G. R., R. M. Bustin, and I. M. Power, 2012. Characterization of gas shale pore systems by porosimetry, pycnometry, surface area, and field emission scanning electron microscopy/ transmission electron microscopy image analyses: Examples from the Barnett, Woodford, Haynesville, Marcellus, and Doig units: AAPG Bulletin, 96, no. 6, 1099–1119.
- [2] Curtis, M. E., B. J. Cardott, C. H. Sondergeld, and C. S. Rai, 2012. Development of organic porosity in the Woodford Shale with increasing thermal maturity: International Journal of Coal Geology, 103, 26–31.
- [3] Milliken, K. L., M. Rudnicki, D. N. Awwiller, and T. Zhang, 2013. Organic matter-hosted pore system, Marcellus Formation (Devonian), Pennsylvania: AAPG Bulletin, 97, no. 2, 177–200.
- [4] Kuila U and Prasad M. Colorado School of Mines. Application of nitrogen gas-adsorption technique for characterization of pore structure of mudrocks, December 2013
- [5] Shimokawara M, Kaido H, Mino Y. 2011. Application of NMR for Special Core analysis, iea-eor.ptrc.ca/2011/assets/25_18-10-2011_15-50_Paper.pdf.
- [6] Hassan, Jamal 2012. Pore size distribution calculation from 1H NMR signal and N_2 adsorption desorption techniques, Physica B condensed Matter.
- [7] G.H. Sørland, K. Djurhuus, H. C. Widerøe, J.R. Lien, and A. Skauge. 2007. Absolute pore size distributions from NMR.
- [8] Daniel R, and Kaldi J. 6/8/12. Mercury-injection capillary-pressure analysis store-assets.aapg.org/documents/previews/1044ST60/CHAPTER01.pdf

- [9] McCarty DK. 2002 Quantitative mineral analysis of clay-bearing mixtures. The Reynolds cup contest: IUCr CPD Newsletter, 2002; 27: 12-16.
- [10] Dunn KJ, LaTorraca GA, Warner JL, Bergman DJ. On the Calculation and Interpretation of NMR Relaxation Time Distributions, SPE 69th Annual Technical Conference and Exhibition, New Orleans 1994, SPE28367
- [11] Green DP and Veselinovic D. Analysis of Unconventional Reservoirs using New and Existing NMR Methods, 2010
- [12] Xiao L, Mao Zh, Jin Y. Calculation of Irreducible Water Saturation (Swirr) from NMR Logs in Tight Gas Sands. November 2011
- [13] Kleinberg, R.L., 1996. Utility of NMR T2 distributions, connection with capillary pressure, clay effect, and determination of the surface relaxivity parameter ρ_{02} . Magn. Reson. Imaging 14, 761-767.
- [14] Howard, j., Williams, J., Thorpe, D. 1997. Permeability from nuclear magnetic resonance logging in a gas-condensate field. SPWLA 38th Annual Logging Symposium Transactions.
- [15] Epping, W.j., Eggenkamp, I.M., Reid, I. 1999. Added Value from NMR Measurements to Characterize Gas Reservoirs in the UK Southern North Sea.
- [16] Glove, PW, Zadjali LL, Frew KA. Permeability prediction from MICP and NMR data using an electrokinetic approach, Geophysics, 2006; 71(4): F49-F60.
- [17] Coates GR, Xiao L, Prammer MG. 1999. NMR Logging – Principles and Applications. Halliburton Energy Services, Houston;
- [18] Rezaee R, Saeedi A, Clennell B. December 2011. Tight gas sands permeability estimation from mercury injection capillary pressure and nuclear magnetic resonance data.
- [19] Volokitin Y, Looyestijn WJ, Slijkerman W.J, Hofman JP. A practical approach to obtain 1st drainage capillary pressure curves from NMR core and log data. Paper SCA-9924 presented at the SCA annual symposium 1999.
- [20] Ben Lowden, Res Lab-ART, Suffolk, May 2000. Some simple methods for refining permeability estimates from NMR logs and generating capillary pressure curves.
- [21] Grattoni CA. et al. September 2003. An Improved Technique for Deriving Drainage Capillary Pressure from NMR T2 Distributions. Presented at the International Symposium of the Society of Core Analysts, Pau, France. SCA.
- [22] Shao, W.Z.; Ding, Y.J.; Liu, Y; Liu, S.Q.; Li, Y.Q.; Zhao, J.H. 2009: The application of NMR log data in evaluation of reservoir pore structure. Well Logging Technol. 33(1), 52–56.
- [23] Liang Xiao, Zhi-qiang Mao, Chang-chun Zou, Yan Jin, Ji-chang Zhu 2016. A new methodology of constructing pseudo capillary pressure (P_c) curves from nuclear magnetic resonance (NMR) logs.
- [24] Ekwere J. Peters. 2012. Advanced Petrophysics: Volume 2: Dispersion, Interfacial Phenomena/ Wettability, Capillarity/Capillary Pressure, Relative Permeability.
- [25] Dan J. Hartman and Edward A. 1999. Beaumont Exploring for oil and gas traps.
- [26] Kewen Li and Roland N. Horne 1st Feb, 2006. Comparison of methods to calculate relative permeability from capillary pressure in consolidated water-wet porous media.
- [27] Purcell WR. 1949. Capillary pressures—Their measurement using mercury and the calculation of permeability, Trans. AIME, 186, 39.
- [28] Burdine NT. Relative permeability calculations from pore size distribution data. Trans. AIME, 1953; 198, 71–78.
- [29] Lenhard, R.J., Oostrom, M., A 1998. parametric method for predicting relative permeability saturation–capillary pressure relationships of oil–water systems in porous media with mixed wettability. Transp. Porous Media 31 (1), 109.
- [30] Li, K., Horne, R.N. 2001. An experimental and theoretical study of steam–water capillary pressure. SPEREE 477–482.
- [31] Brooks RH, Corey AT. Properties of porous media affecting fluid flow. J. Irrig. Drain. Div. 1966; 6, 61.
- [32] Lowell S., Shields JE, Thomas MA and Thommes M. Characterization of porous solids and powders: Surface area, pore size and density, Springer 2006.
- [33] Milburn DR and Davis BH. 1993. Comparison of Surface Areas Calculated from Nitrogen Adsorption and Mercury Porosimetry, in A Collection of Papers on Engineering Aspects of Fabrication of Ceramics: Ceramic Engineering and Science Proceedings, 1993; 14(11/12) (ed J. B. Wachtman), John Wiley & Sons, Inc., Hoboken, NJ, USA. doi: 10.1002/9780470314272.ch8.

To whom correspondence should be addressed: Dr. Bello Lawal Toro, School of Energy Resources, China University of Geosciences, Beijing, 100083, P.R. China, bltoro@yahoo.com

APPLICATION OF RESPONSE SURFACE METHODOLOGY (RSM) FOR THE MODELLING AND OPTIMIZATION OF SAND MINIMUM TRANSPORT CONDITION (MTC) IN PIPELINE MULTIPHASE FLOW

Kazeem K. Salam¹, Akeem O. Arinkoola¹, Mohammed D. Aminu^{2,*}

¹ Petroleum Engineering Unit, Department of Chemical Engineering, Ladoke Akintola University of Technology, Ogbomosho, Nigeria.

² Department of Geology, Modibbo Adama University of Technology, Yola, Nigeria.

Received November 20, 2017; Accepted April 16, 2018

Abstract

This study investigated the influence of three operational parameters (liquid viscosity, pipe diameter and sand concentration) and their interactions on sand minimum transport condition (MTC) in multiphase pipelines using response surface methodology (RSM). Historical data: liquid viscosity (A) at 1, 7, 20, 105, 200, 340 cP; pipe diameter (B) at 0.0776 and 0.10 m; sand concentration (C) at 50 and 200 lb of sand per 1000 bbl of fluid, were correlated with the response (MTC). A two-factor interaction (2FI) regression model was developed and validated prior to optimization studies. The effects of the combination of these factors were also ascertained with 3D plots. The result showed that the predicted data had a reasonable agreement with the experimental data with the values of R^2 (0.9941) and $Adj-R^2$ (0.9869). The predicted optimum conditions of the operating parameters were observed at liquid viscosity (335.63 cP), pipe diameter (0.08 m) and sand concentration (115.61 lb/bbl) to achieve minimum sand MTC of 0.130242 m/s which were coherent with the experimental optimum conditions 340 cP liquid viscosity, 0.08 m pipe diameter, 125 lb/1000bbl sand concentrations and 0.130242 m/s MTC. Liquid viscosity and pipe diameter were the most significant operating parameters from the 3D plots. The study revealed that the response surface methodology (RSM) is an efficient statistical technique for providing appropriate empirical model for relating the operational parameters, and predicting the optimum operating conditions affecting sand MTC, a veritable parameter in evaluating sand transport in pipeline multiphase flow.

Keywords: Minimum Transport Condition (MTC); Multiphase Flow; Response Surface Methodology (RSM); Historical Data; Empirical Model, Optimization.

1. Introduction

In the petroleum industry, one of the main problems encountered during production is sand transport through pipelines [1-2]. Sand production occurs usually in oil and gas reservoirs since majority of the reservoirs are unconsolidated. Massive reductions in oil and gas production rates have been experienced over time due to wormholes [3] and sand deposition on surface and downhole equipment [4]. The risks of frictional pressure loss, microbiologically-influenced corrosion and equipment failure are also there to contend with [5]. The processes involved in removing large deposits of sand have also been found to be time consuming. These and other attendant problems concerned with cost of repairs, operational safety and pollution, all aid in drawing the problem to global attention [2]. Hence, the need for studies on the subject matter for elaborate understanding and prediction of sand transport in multiphase flow (involving two or more distinct phases such as gas, oil and water).

An important parameter which can be applied in the evaluation of sand transport in multiphase flows is minimum transport condition (MTC), defined as the minimum average fluid velocity required to prevent bed formation which occurs as a result deposition of sand particles [2]. This according to Thomas [6] is the mean stream velocity required to prevent the accumu-

lation of a layer of sliding sand particles at the bottom of a horizontal pipe. MTC concept is based on the principle that the sand particles in pipelines will not lose their ability to be transported in a fluid since they are fully suspended therein [2,6-8]. Other terms used to describe MTC are critical deposition velocity (CDV), critical transport fluid velocity (CTFV) and critical foam velocity (CFV) [2,9].

In sand resistant production systems, it is of great necessity knowing the actual value of sand MTC in pipelines to prevent sand bed formation [4], and predict objectively the changes that may have occurred and how often pipelines need to be dredged to prevent the havoc associated with blockage and abrasion [10]. Sand MTC in pipeline multiphase flow is dependent on several conditions such as sand particle size, sand concentration, pipe diameter, pipe inclination and fluid viscosity [1]. The high variability of these parameters has made the prediction of sand transport more tasking [11]. The dispersed distribution of sand transport in pipelines is also a militating factor against sand transport estimations [12].

Many of the models which have been developed for this purpose have proven to be a far cry from what is required for the knowledge of sand transport processes [10,13-17]. For instance, Wicks [13] developed correlations on sand transport in which only high solids concentration were considered for analysis. These correlations cannot be applied in the offshore environments where sand concentration was estimated to be between 5 to 40 lb of sand per 1000bbl of liquid [4]. Angelson *et al.* [14] improved on the model by extending it to two-phase flow and the only parameters considered were liquid velocity and hydraulic diameter. Imprecision resulted from the multiphase flow model due to incoherence between experimental data and the model. A general correlation for critical mixture velocity of multiphase flow was also formulated by Salama [15] as shown in **Equation 1** involving various experimentally determined theoretical parameters which cannot be adequately measured.

$$U_{M,C} = U_{SL} + U_{SG} = \left(\frac{U_{SL}}{U_M}\right)^{0.04} d_p^{0.17} v^{-0.09} (s-1)^{0.55} D^{0.47} \quad (1)$$

An empirical model for CDV prediction was put forward by Kökpınar and Göğüş [16] by assuming critical velocity as a function of the parameters given in **Equation 2**.

$$\frac{V_c}{\sqrt{gD}} = 0.055 \left(\frac{d_p}{D}\right)^{-0.6} C_v^{0.27} (s-1)^{0.07} \left(\frac{\rho_1 u_t d_p}{\mu_1}\right)^{0.3} \quad (2)$$

A mechanistic model for CDV (**Equation 3**) was proposed by Al-Mutahar [17] based on turbulent theory and force balance. Estimation of turbulent velocity fluctuations generated by liquid flow and that required to suspend particles as well as assumptions of equality of the required and produced turbulent velocity fluctuations were made.

$$V_c = 5.66 [f(C_v) \sqrt{a_p} g (s-1)]^{8/7} \left(\frac{D \rho_1}{\mu_1}\right)^{1/7} \left(\frac{1}{\Omega}\right)^{8/7} \quad (3)$$

where $\Omega = (1 + 3.64C_v)^{-1}$ for concentrations > 1%; $\Omega = 0.5 (1 + 3.64C_v)^{-1}$ for concentrations < 1%

Yan [1] also developed a theoretical correlation for sand MTC as shown in **Equations (4-6)** for single phase flow.

$$u_o = \left[100 u_t \left(\frac{v_l}{d_p}\right)^{2.71}\right]^{0.269} \quad (4)$$

$$u_c = u_o + 0.092 C_v^{0.271} \text{ for } 0.00000538 \leq C_v \leq 0.3 \frac{v}{v} \quad (5)$$

The fanning factor can be obtained by applying **Equation 7** which was proposed by Chen [18].

$$u_c = \left(\frac{f}{2}\right)^{0.5} \times MTC \quad (6)$$

$$\frac{1}{\sqrt{f}} = -4 \log \left[0.2698 \left(\frac{\varepsilon}{D}\right) - \frac{5.0452}{Re} \log \left(0.3539 \left(\frac{\varepsilon}{D}\right)^{1.1098} + \frac{5.8506}{Re^{0.8981}}\right)\right] \quad (7)$$

Apart from the inconsistency caused by the assumptions, the parameters involved in these correlations are those which cannot but be experimentally determined in accordance with proven mechanistic models. This is one shortcoming that the present study is intended to resolve with the development of an empirical model which will factor in the operational parameters directly affecting sand MTC, and by extension sand transport in pipeline multiphase flow.

In this study, RSM was used to establish the relationship between the response and operational parameters because it is effective in optimizing the response function and predicting future responses after it has developed a regression model statistically from appropriate experimental data [19]. From the several design types available in RSM: Box-Behnken, central-composite, one-factor, optimal and historical data, historical data is the preferred choice for this study as it can accommodate all available data into a blank design layout from an already conducted experiment [20]. Also, it is suitable for conducting multi-factor experiments because it provides information on the influence of factor interactions [21].

Liquid viscosity, pipe diameter and sand concentration have been recognized as important parameters influencing sand MTC in pipeline multiphase flow as reported by Yan [1]. It is the aim of this study to develop an empirical model that will explain explicitly the effect of the interactions of these parameters on sand MTC in pipeline multiphase flow, a feat which has not been reached due to insufficient data, and to improve upon the approach of Yan [1] involving experimental determination of MTC by visual observations and assumptions. The optimum operating conditions will also be evaluated from optimization of the response.

2. Methodology

2.1. Experimental design and model development

RSM of Design Expert software version 6.0.8 (Stat-Ease Inc., Minneapolis, USA) was used in this study. Historical data experimental design, with categorical factor of 0, was employed in modelling and optimizing sand MTC. The three parameters: liquid viscosity, pipe diameter and sand concentration, which are conditions affecting MTC, were operated within two ranges (minimum (-1) and maximum (+1)). The lowest and the highest levels of the variables were: liquid viscosity, 1 and 340 cP; pipe diameter, 0.0776 and 0.1 m; sand concentration, 50 and 200 lb/1000bbl. All experimental data sets of a total of 12 runs were used as the design points for modelling and optimizing the level of chosen variables from the experimental results of Yan [1].

The experimental data of the historical design experiment can be represented in the general form of the two-factor interaction (2FI) model as shown in **Equation 8**, to develop an empirical model which will be used to analyse the effect of factor interactions.

$$Y = b_0 + \sum b_i X_i + \sum b_{ij} X_i X_j + e_i \tag{8}$$

(after Bradley [19]; Ahmad *et al.*, [22]; Fakhri and Adami, [23]).

where Y is the predicted response; n is the number of factors; X_i and X_j are the coded variables; b₀ is the constant coefficient; b_i and b_{ij} are the first-order and interaction coefficients, respectively; i and j are the index numbers for factors; and e_i is the residual error.

The operating parameters, their designated symbols, response and range of conditions are presented in Table 1.

Table 1. Design summary

Operating Parameters	Symbols	Ranges	Low Coded	High Coded
Liquid Viscosity (cP)	A	1 - 340	-1	+1
Pipe Diameter (m)	B	0.0776 - 0.10	-1	+1
Sand Concentration (lb/1000bbl)	C	50 - 200	-1	+1
Response	Symbol	Analysis	Minimum	Maximum
MTC (m/s)	Y1	Polynomial (2FI)	0.070	0.80

The validity of the polynomial model was expressed by the coefficient of determination, R² and coefficient of adjusted determination, Adj-R² while the statistical significance was verified with the F-test and the adequate precision ratio.

2.2. Optimization of sand MTC and operational parameters

Numerical optimization of the model in Equation (2) was done using the Design Expert software to determine the liquid viscosity, pipe diameter and sand concentration at which the

sand MTC of fluid was at maximum. The following steps were taken prior to the optimization in order to identify the criteria of the numerical optimization. First, the goal factors for the operational parameters were set to "is in range" with the exception of liquid viscosity (105 and 340 cP) in consistency with the viscosity of oil [1], while that of sand MTC was set to "minimum". The lower limit of the response was the minimum response obtained from the interactions of the parameters considered.

3. Results and discussion

3.1. Model fitting

The effects of the different process parameters on the value of MTC were investigated. This work contributes immensely to existing knowledge since little or no work has been done on the development of an empirical model and optimization of sand MTC in pipeline multiphase flow. The historical data RSM design and the response for this study can be found in **Table 2**.

Table 2. Historical Data Experimental Design of the Independent Variables and the observed values for the response

Std	Run	Experimental Variables			Response	
		Liquid viscosity (cP)	Pipe diameter (m)	Sand concentration (lb/bbl)	Actual MTC (m/s)	Predicted MTC (m/s)
1	1	1	0.1000	50	0.600	0.630
12	2	7	0.1000	50	0.700	0.670
5	3	20	0.1000	50	0.750	0.750
10	4	105	0.0776	50	0.350	0.350
9	5	200	0.0776	50	0.250	0.240
4	6	340	0.0776	50	0.070	0.075
8	7	1	0.1000	200	0.700	0.700
2	8	7	0.1000	200	0.750	0.740
6	9	20	0.1000	200	0.800	0.820
3	10	105	0.0776	200	0.450	0.430
7	11	200	0.0776	200	0.300	0.330
11	12	340	0.0776	200	0.200	0.190

Polynomial regression analysis was performed on the response to determine the coefficients of the model terms. Model reduction by manual exclusion of larger insignificant terms, were not performed since bulk of the model terms were significant. The predicted response of sand MTC is expressed by **Equation 9** in terms of actual factors.

$$\begin{aligned}
 MTC = & -0.048324 - 0.026382 * Liquid\ Viscosity + 6.53261 * Pipe\ Diameter + 0.000340814 * \\
 & Sand\ Concentration + 0.324 * Liquid\ Viscosity * Pipe\ Diameter + 0.000000967431 * Liquid\ Viscosity * \\
 & Sand\ Concentration + 0.000946007 * Pipe\ Diameter * \\
 & Sand\ Concentration
 \end{aligned}
 \tag{9}$$

The empirical model includes all the factors in consideration, thereby eliminating the need for experimental determination of theoretical parameters required by mechanistic models.

3.2. Analysis of variance (ANOVA) and statistical significance of the model

For the optimization of MTC, Analysis of Variance (ANOVA) values were obtained for the 2FI regression model in Equation 9. The ANOVA results derived from the historical data utilized for this study are listed in Table 3. The p (or prob) values depicted the significance of each coefficient as well the interaction effectiveness between each independent variable. The p-value < .0001 and the model F-value of 139.38 (a large value occurring due to noise) for the 2FI model, suggests that the regression model is statistically significant. The significance of the regression coefficients is also depicted in Table 3. P-values < .05 indicate that the model terms are significant at 95% confidence level.

Table 3. ANOVA for Response Surface 2FI Model

Source	Sum of Squares	Degrees of Freedom	Mean Square	F-Value	Prob > F	Remark
Model	0.702666	6	0.117111	139.3804	< 0.0001	significant
A	0.009451	1	0.009451	11.24802	0.0202	
B	0.027774	1	0.027774	33.05528	0.0022	
C	0.013606	1	0.013606	16.1933	0.0101	
AB	0.019742	1	0.019742	23.49629	0.0047	
AC	0.000296	1	0.000296	0.352615	0.5785	
BC	2.33E-06	1	2.33E-06	0.002771	0.9601	
Residual	0.004201	5	0.00084			
Cor Total	0.706867	11				

From the ANOVA, it can be observed that four (4) of the six (6) model terms (A, B, C and AB) are significant. The significant model terms have synergistic effect on the regression model while insignificant terms have antagonistic effect. Therefore, model factors A, B, C and AB positively contribute to the model equation while AC and BC have negative impact on the developed model. The most influential model parameter was B because it had the least p-value.

3.3. Validation of the model

Since adequate precision measures the signal to noise ratio and a ratio value greater than 4 is desirable, the 2FI model of liquid velocity at sand MTC with adequate precision ratio of 33.505 indicates an adequate signal. The 2FI regression model fitting was regulated by the coefficient of determination, R^2 which gave a high value of 0.9941 for the liquid velocity at sand MTC from the ANOVA results. A reasonable agreement of the R^2 with the adjusted coefficient of determination, $Adj-R^2$, is of great importance. The value of $Adj-R^2$ obtained was 0.9869. Therefore, the proximity of the R^2 and $Adj-R^2$ value to 1.0 indicates a very high correlation between the experimental and the predicted values of the liquid velocity at sand MTC. From the foregoing, the 2FI regression model presents an explicit explanation of the relationship between the independent factors and response.

3.4. Verification of model adequacy

The adequacy of the regression model was also ascertained between the experimental data and the model response with the diagnostic plot shown in Figure 1.

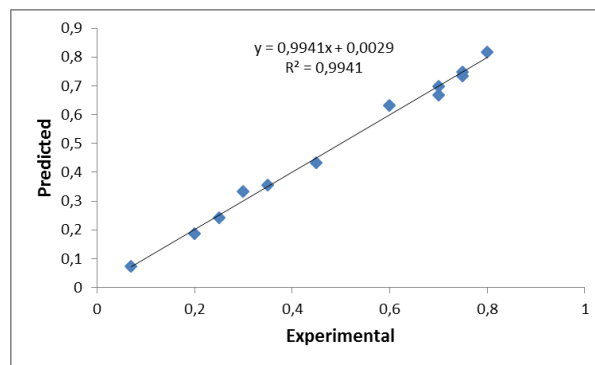


Figure 1. Cross plot between the Experimental and Predicted Values.

It can be observed that the 2FI regression model fits realistically, thereby adequately expressing the experimental range studied. The actual value of sand MTC velocity represents the measured result for each experimental run while the predicted value is evaluated from the independent variables in the regression model.

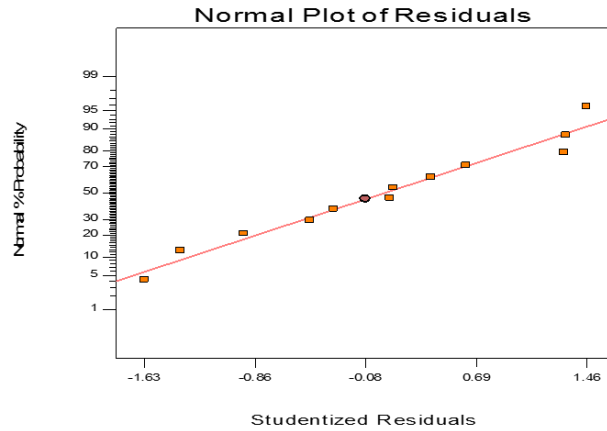


Figure 2. Normal plot of residuals for the model.

The normal plot of residuals depicts the graphical analysis of the model as exhibited by Figure 2. It is obvious that the residuals reflect a normal distribution since virtually all the points follow a straight-line curve. It is also revealed that no further improvement can be done to the model by making changes to the response because the data points are scattered and do not exhibit “S-shaped” curve [20]. The graphs and tables thereby suggest that the model in Equation 9 can be regarded as the best possible model of the historical data RSM design of sand MTC in pipeline multiphase flow. Therefore, these shall be utilized in deriving the optimum values of the operational parameters.

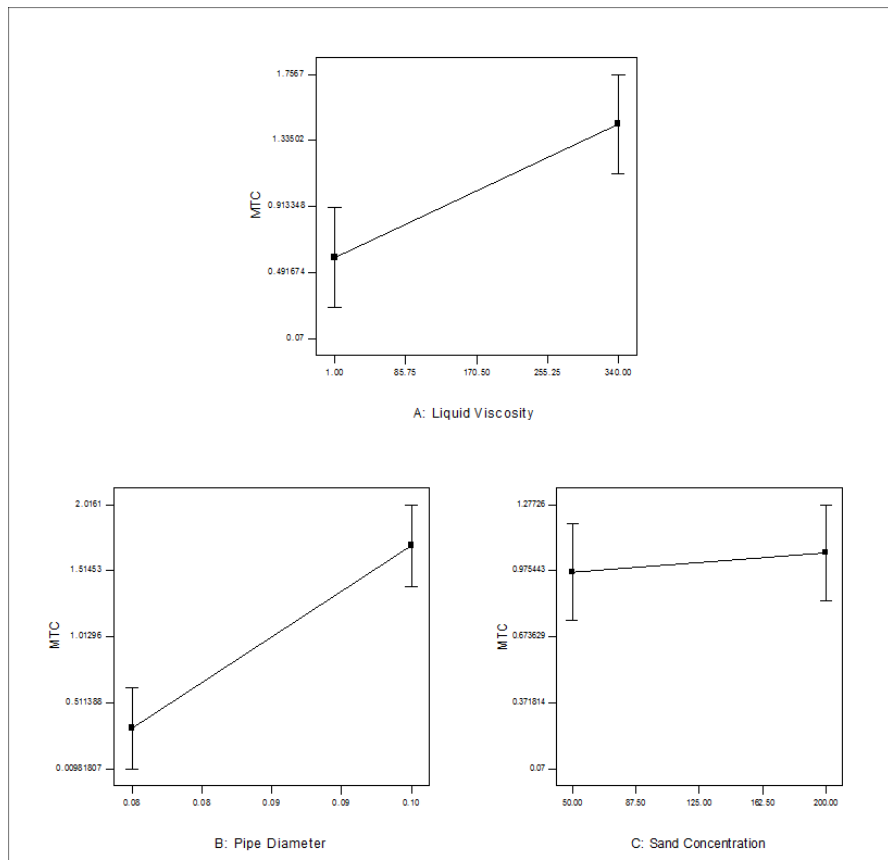


Figure 3. One factor plots.

The individual effects of each operational parameter: liquid viscosity, pipe diameter and sand concentration on the MTC in multiphase pipelines are presented in Figure 3 (i-iv). Figure 3 (i) shows the effect of liquid viscosity on MTC at constant pipe diameter and sand concentration. MTC increased slightly from 0.5874 to 1.4385 m/s with increase in liquid viscosity from 1 to 340 cP, reflecting a direct relationship. Figure 3 (ii) depicts the effect of pipe diameter on MTC at constant liquid viscosity and sand concentration. There was a more pronounced increase in MTC from 0.3198 to 1.7062 m/s when pipe diameter increased from 0.0776 to 0.10 m. Figure 3 (iii) illustrates the effect of sand concentration on MTC at constant liquid viscosity and pipe diameter. The MTC increased slightly from 0.9687 to 1.0572 m/s when sand concentration increased from 50 to 200 lb/1000bbl, depicting the least significant effect on the response. Therefore, the three parameters have a synergistic effect with pipe diameter indicating the greatest main factor effect on MTC in multiphase flow pipelines.

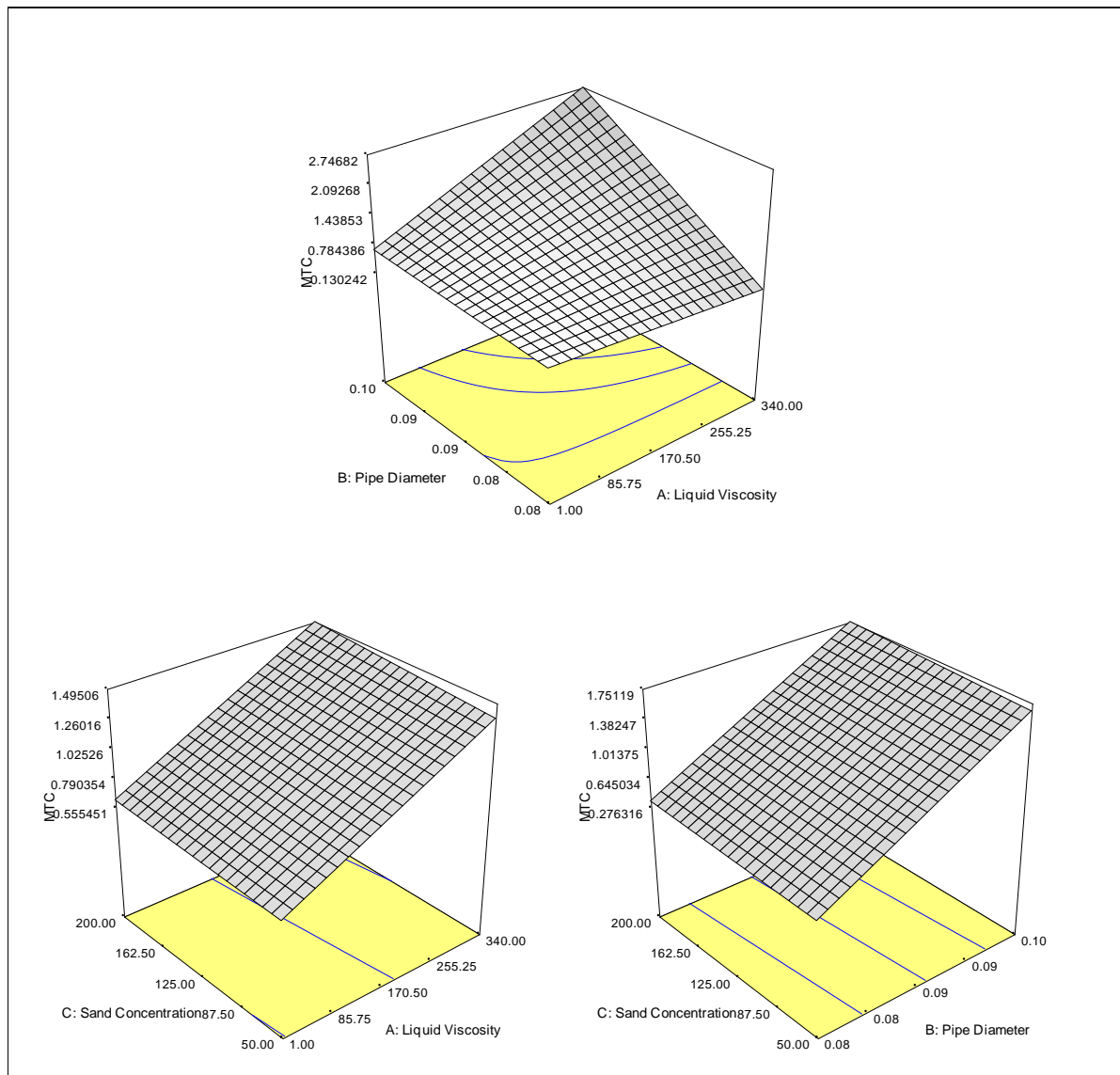


Figure 4. 3D Response surface plots

In this paper, the three dimensional (3D) plots depicted by Figure 4 (i-iii) were studied to investigate the behaviour of the sand MTC from the interactions of the three operating

variables: liquid viscosity, pipe diameter and sand concentration. Two operating variables were analysed in each case while the other variable was kept constant.

The 3D plot showing the effect of the combination of liquid viscosity and pipe diameter on sand MTC when sand concentration was kept constant is presented by Figure 4 (i). The sand MTC velocity increased from 0.67 to 2.75 m/s when liquid viscosity increased from 1 to 340 cP with pipe diameter of 0.1 m. There was however, a slight decrease in sand MTC velocity from 0.51 to 0.13 m/s with equivalent increment in liquid viscosity when a smaller pipe of diameter 0.0776 m was used. These were observed at constant sand concentration of 125 lb/1000bbl. The increase in sand MTC of fluids was more prominent at high liquid viscosity with decrease in pipe diameter than it was at low liquid viscosity.

Figure 4 (ii) depicts the combined effect of liquid viscosity and sand concentration at constant pipe diameter on sand MTC. It is clearly indicated at constant pipe diameter that at sand concentration of 200 lb/bbl, there was a continuous increase in sand MTC from 0.62 to 1.50 m/s when liquid viscosity increased from 1 to 340 cP. A similar trend was observed for sand concentration of 50 lb/bbl with the same increase in liquid viscosity as sand MTC increased from 0.56 to 1.38 m/s. The increase in MTC experienced with increase in liquid viscosity was more appreciable than that experienced with increase in sand concentration, thereby making the effect of latter rather insignificant.

The combined effect of pipe diameter and sand concentration on velocity of sand at MTC when liquid viscosity was kept constant is depicted by the 3D plot shown in Figure 4 (iii). The sand MTC increased from 0.36 to 1.75 m/s at sand concentration of 200 lb/bbl when the pipe diameter was increased from 0.0776 to 0.1 m. The observations at sand concentration of 50 lb/bbl was similar as sand MTC velocity increased from 0.28 to 1.66 m/s when the same increase in pipe diameter was maintained. The effect of increasing pipe diameter in increasing sand MTC of fluids overwhelms that of sand concentration.

It can be inferred from these plots that liquid viscosity and pipe diameter are the most significant parameters influencing MTC of fluids in sand transport multiphase pipelines. The effect of sand concentration is greatly masked and as such can be considered the least significant.

3.5. Validation of model optimization

Figure 5 illustrates the predicted optimum conditions and the response studied in this paper. The predicted optimum operating parameters influencing sand MTC was estimated to be liquid viscosity (335.63 cP), pipe diameter (0.08 m) and sand concentration (115.61 lb/1000bbl). At these optimum conditions, the corresponding predicted volumetric mass transfer coefficient was found to be 0.130242 m/s.

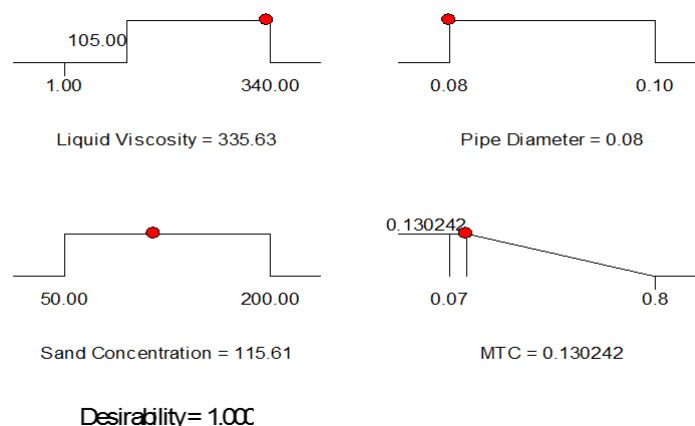


Figure 5. Optimum conditions and response

Experimentally, liquid viscosity (340 cP), pipe diameter (0.08 m) and sand concentration (125 lb/1000bbl) were the values of the operating parameters whose interactive effect gave minimum sand MTC as 0.130242 m/s. Thus, it is evident that the historical data RSM design is an efficient statistical technique for predicting the optimum operating variables for the minimization of sand MTC in pipeline multiphase flow by incorporating all factors under consideration.

4. Conclusion

This study revealed the effectiveness of RSM to successfully develop a suitable empirical model for the prediction of sand MTC in the investigation of sand transport in multiphase pipelines. This model has an advantage over the previously developed mechanistic models because it directly includes the factors under consideration with the aim of studying their interactive effects in contrast to the latter which requires assumptions and experimental determination of factors which only gives estimations of MTC and hence sand transport in multiphase pipelines. The closeness of R^2 (0.9941) and $Adj-R^2$ (0.9869) to 1.0 proved that there was coherence between the experimental and predicted response. 3D response surface plots were employed in explaining the effects of interaction of the operating parameters considered in this study and they revealed that liquid viscosity and pipe diameter are the most significant parameters affecting the response. Numerical optimization showed that the predicted optimum operating parameters observed at liquid viscosity (335.63 cP), pipeline diameter (0.08 m) and sand concentration (115.61 lb/1000bbl) to achieve minimum MTC of 0.130242 m/s were close to the experimental optimum conditions of 340 cP liquid viscosity, 0.08 m pipeline diameter, 125 lb/1000bbl sand concentrations and 0.130242 m/s MTC. Sand MTC minimization is vital for reduction in energy requirement. It can thus be concluded that historical data RSM is a reliable statistical technique for the prediction and optimization of sand MTC in pipeline multiphase flow and that estimation of sand MTC under the conditions considered is crucial for oil pipeline design to provide quality assurance for sand transport during operation.

Nomenclature

C_v	Sand volume fraction	v/v
d_p	Particle diameter	microns
D	Pipe diameter	m
ϵ	Pipe roughness	m
f	Friction factor	
g	Gravitational acceleration	m/s^2
Re	Reynolds number	
s	Ratio of particle to carrier fluid density	
u_o	Friction velocity at minimum transport condition for infinite dilution	m/s
u_t	Terminal settling velocity	m/s
u_c	Friction velocity at minimum transport condition	m/s
ρ_1	Liquid density	kg/m^3
U_M	Mixture velocity	m/s
$U_{M,C}$	Critical mixture velocity	m/s
U_{SG}	Superficial gas velocity	m/s
U_{SL}	Superficial liquid velocity	m/s
μ_1	Liquid dynamic viscosity	Pas
v	Liquid velocity	m/s
ν_1	Liquid kinematic viscosity	m^2/s
V_c	Critical Transport Velocity	m/s

References

- [1] Yan W. Sand transport in multiphase pipelines. Ph.D. thesis, Cranfield University, 2010.
- [2] Udoh R. Sand transport by oil in tubing and pipelines. M.Sc. Thesis, Norwegian University of Science and Technology, 2012.
- [3] Yuan JY, Babchin A, Tremblay B. A model for sand transport through a partially filled wormhole in cold production. *J Can Pet Technol.*, 2002; 41:25–32.
- [4] Danielson TJ. Sand transport modeling in multiphase pipelines. *Offshore Technol. Conf.*, 2007, p. 11. doi:10.4043/18691-MS.
- [5] Akpabio E, Ekott E, Akpan M. Inhibition and control of microbiologically influenced corrosion in oilfield materials. *Environ Res J.*, 2011; 5:59–65.
- [6] Thomas DG. Transport characteristics of suspensions: Part VI. Minimum transport velocity for large particle size suspensions in round horizontal pipes. *AIChE J.*, 1962; 8:373–8.
- [7] Thomas DG. Transport characteristics of suspensions: II. Minimum transport velocity for flocculated suspensions in horizontal pipes. *AIChE J.*, 1961; 7:423–30.
- [8] Thomas DG. Transport characteristics of suspensions: Part IX. Representation of periodic phenomena on a flow regime diagram for dilute suspension transport. *AIChE J.*, 1964; 10:303–8.
- [9] Duan M, Miska SZ, Yu M, Takach NE, Ahmed RM, Zettner CM. Critical conditions for effective sand-sized solids transport in horizontal and high-angle wells. *Soc. Pet. Eng.*, 2009: 10.
- [10] Davies AG, van Rijn LC, Damgaard JS, van de Graaff J, Ribberink JS. Intercomparison of research and practical sand transport models. *Coast Eng.*, 2002; 46:1–23.
- [11] Gambino J. A Comparison of sediment transport models for combined current and wave flows. M.Sc. thesis, Massachusetts Institute of Technology, 1998.
- [12] Haas KA, Hanes DM. Process based modeling of total longshore sediment transport. *J Coast Res* 2004; 20:853–61.
- [13] Wicks M. Transport of solids at low concentration in horizontal pipelines. *Adv Solid-Liquid Flow Pipelines Its Appl.*, 1971:101–24.
- [14] Angelson S, Kvernfold O, Linglem M, Oslén S. Long distance transport of unprocessed hydrocarbon: Sand settling in multiphase flowlines. *Proc 4th Int Conf Multiph Flow*, Pap D2, BHRA, Nice, 1989 Fr 1989.
- [15] Salama MM. Sand production management. *J Energy Resour Technol Trans ASME* 2000; 122:29–33. doi:10.1115/1.483158.
- [16] Kökpinar MA, Göğüş M. Critical flow velocity in slurry transporting horizontal pipelines. *J Hydraul Eng.*, 2001; 127:763–71.
- [17] Al-Mutahar F. Modeling of critical deposition velocity of sand in horizontal and inclined pipes. M.Sc. Thesis, The University of Tulsa, 2006.
- [18] Chen NH. An explicit equation for friction factor in pipe. *Ind Eng Chem Fundam.*, 1979; 18:296–7.
- [19] Bradley N. The response surface methodology. M.Sc. Thesis, Indiana University of South Bend, 2007.
- [20] Jeirani Z, Jan BM, Ali BS, Noor IM, See CH, Saphanuchart W. Prediction of the optimum aqueous phase composition of a triglyceride microemulsion using response surface methodology. *J Ind Eng Chem.*, 2013; 19:1304–9.
- [21] Asmara Y, Ismail M. The use of response surface methodology to predict CO₂ corrosion model empirically. *Int J Mater Sci Innov* 2013; 1:101–14.
- [22] Ahmad R, Al-Shorgani N, Hamid A, Yusoff W, Daud F. Optimization of medium components using response surface methodology (RSM) for mycelium biomass and exopolysaccharide production by *Lentinus squarrosulus*. *Adv Biosci Biotechnol.*, 2013; 4:1079–85.
- [23] Fakhri A, Adami S. Response surface methodology for adsorption of fluoride ion using nanoparticle of zero valent iron from aqueous solution. *J Chem Eng Process Technol.*, 2013; 4.

To whom correspondence should be addressed: Mohammed D. Aminu, Department of Geology, Modibbo Adama University of Technology, Yola, Nigeria, mdaminu@mautech.edu.ng